Structure-Function Analysis of the Pex3-Pex19 Interaction:

An improved Understanding of Peroxisomal Membrane Biogenesis

Struktur-Funktionsanalyse der Pex3-Pex19 Interaktion:

Ein verbessertes Verständnis der peroxisomalen Membranbiogenese

Dissertation

der Mathematisch-Naturwissenschaftlichen Fakultät

der Eberhard Karls Universität Tübingen

zur Erlangung des Grades eines

Doktors der Naturwissenschaften

Dr. rer. nat

vorgelegt von

Friederike Schmidt

aus Basel/CH

Tübingen

2011

Tag der mündlichen Qualifikation: 29.11.2011

Dekan: Prof. Dr. Wolfgang Rosenstiel

1. Berichterstatter: Prof. Dr. G. Dodt

2. Berichterstatter: Prof. Dr. T. Stehle

Nicht der Beginn wird belohnt,
sondern einzig und allein das Durchhalten.
Katharina von Siena

TABLE OF CONTENTS

ABBREVIATIONS

AAA	ATPases associated with various cellular activities
aar	amino acid residue
ABCD	ATP-binding cassette subfamily D
APS	ammonium persulfate
ASU	asymmetric unit
ATP	adenosine triphosphate
BESSY	Berliner Elektronenspeicherringgesellschaft für Synchrotronstrahlung
β-ME	β-mercaptoethanol
Bis-Tris	2-(bis(2-hydroxyethyl)amino)-2-(hydroxymethyl)propane-1,3-diol
BSA	buried surface area
CD	circular dichroism
CoA	coenzyme A
CoIP	Coimmunoprecipitation
COP	coat protein
CV	column volume
DMEM	Dulbecco's modified Eagle's medium
DNA	deoxyribonucleic acid
dNTP	deoxynucleotide triphosphate
DTT	dithiothreitol
ECL	enhanced chemoluminescence
E. coli	*Escherichia coli*
EDTA	ethylenediaminetetraacetate
ER	endoplasmic reticulum
ESI-MS	electrospray ionization mass spectrometry
FCS	fetal calf serum
Fis1	fission protein 1
Get	guided entry of tail-anchored proteins
GFP	green fluorescent protein
HEPES	4-(2-hydroxyethyl)-1-piperazineethanesulfonic acid
HPLC	high performance liquid chromatography
HRP	horseradish peroxidase
IPTG	isopropyl-β-thiogalactopyranoside
IRD	infantile Refsum disease
ITC	isothermal titration calorimetry
LB	Luria Bertani
MALDI-TOF MS	matrix-assisted laser desorption/ionization time of flight mass spectrometry
MES	2-(N-morpholino) ethanesulfonic acid
MHC	major histocompatibility complex
MOM	mitochondrial outer membrane
M_r	molecular mass
mRNA	messenger ribonucleic acid
MWCO	molecular weight cut-off
NALD	neonatal adrenoleukodystrophy
OD_{600}	optical density at 600 nm
PAGE	polyacrylamide gel electrophoresis
PBD	peroxisomal biogenesis disorder
PBS	phosphate buffered saline
PCR	polymerase chain reaction
PEG	polyethylene glycol
PEX	gene coding for a peroxin
PEX	peroxin

PMP	peroxisomal membrane protein
P. pastoris	*Pichia pastoris*
(m)PTS	(membrane) peroxisomal targeting sequence
PVDF	polyvinylidene fluoride
RCDP	rhizomelic chondrodysplasia punctata
RING	really interesting new gene
rmsd	root mean square deviation
ROS	reactive oxygen species
rpm	revolutions per minute
SAM	sorting and assembly machinery
S. cerevisiae	*Saccharomyces cerevisiae*
SDS	sodium dodecyl sulfate
SEC	size exclusion chromatography
SH3	Src homology 3
SLS	Swiss Light Source
SV40	simian virus 40
TA	tail-anchored
TCEP	tris-(2-carboxyethyl)phosphine
TEMED	tetramethylethylenediamine
TEV	tobacco etch virus
TIC	translocase of the inner membrane of chloroplasts
TIM	translocase of the inner mitochondrial membrane
TLS	translation, libration, screw
TM	transmembrane
TNT	transcription and translation
TOB	topogenesis of outer membrane β-barrel proteins
TOC	translocase of the outer membrane of chloroplasts
TOM	translocase of the outer mitochondrial membrane
TPR	tetratricopeptide repeat
TRC	transmembrane recognition complex
Tris	tris-(hydroxymethyl)aminomethane
VLCFA	very long chain fatty acid
WB	western blotting
WD 40	tryptophan-aspartic acid 40
X-ALD	X-linked adrenoleukodystrophy
YFP	yellow fluorescent protein
Y. lipolytica	*Yarrowia lipolytica*
ZS	Zellweger syndrome

1   INTRODUCTION

1.1   Peroxisomes

Peroxisomes have first been described in 1954 by Rhodin [1] and were initially called "microbodies". The presence of several H_2O_2-producing oxidases and the H_2O_2-degrading enzyme catalase within the matrix of these organelles has led to the name peroxisomes in 1966 [2]. Today, peroxisomes and the related organelles in plants and trypanosomes, glyoxisomes and glycosomes, respectively, represent the group of microbodies. In plants, peroxisomes are involved in lipid metabolism, whereas glyoxisomes are mainly found in germinating seeds, where they are part of the glyoxylate cycle [3]. Glycolysis is performed in trypanosomal glycosomes, while it occurs in the cytosol in other species [4]. Thus, glyoxisomes and glycosomes are specialized microbodies that are adapted to specific cellular needs and external influences.
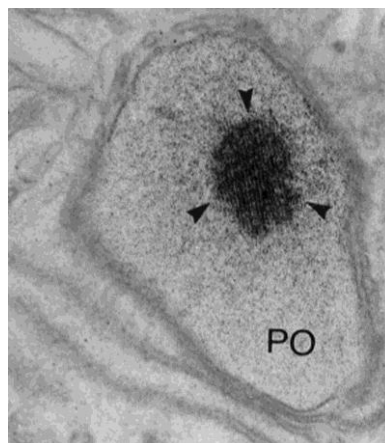
Figure 1.1: Cytochemical staining of the peroxisomal enzyme urate oxidase. Crystalline core of urate oxidase (arrows) within the matrix of a peroxisome (PO) stained with the cerium method [5]. Modified from [6].

Peroxisomes are single membrane-bound organelles that are present in all types of eukaryotic cells and have a diameter in the range of 0.1 – 0.5 μm. In contrast to mitochondria, peroxisomes do not contain DNA; hence, all peroxisomal proteins are synthesized in the cytosol and have to be imported posttranslationally. Dependent on the particular cell type, the number of peroxisomes and their protein contents can be quite variable [7]. Especially in peroxisomes of liver and renal cells, some proteins, such as urate oxidase, are present in such high concentrations that they appear as crystalline inclusions, which can easily be identified in electron micrographs (Figure 1.1, [8, 9]).

1.2   Peroxisomal metabolic pathways

More than 50 peroxisomal enzymes have been identified in human cells to date. In addition to the degradation of H_2O_2 and other reactive oxygen species (ROS), peroxisomes are responsible for oxidative processes especially in lipid metabolism (Figure 1.2). In mammalian cells, the β-oxidation of fatty acids is divided between mitochondria and peroxisomes [10, 11]. While standard fatty acids are oxidized in mitochondria, only peroxisomes can catabolize unusual compounds such as very long chain fatty acids (VLCFA), branched chain fatty acids, or long chain dicarboxylic acids [12]. In these processes, and additionally during the degradation of several D-amino acids (D-proline, D-aspartate) [13] and purine metabolism, ROS (H_2O_2 and epoxides) are produced and have to be degraded by the enzyme catalase. In addition to these catabolic processes, peroxisomes harbor several anabolic functions, including the synthesis of bile acids [14] and plasmalogens [15]. Several steps of cholesterol biosynthesis have also been reported to take place in peroxisomes [16].
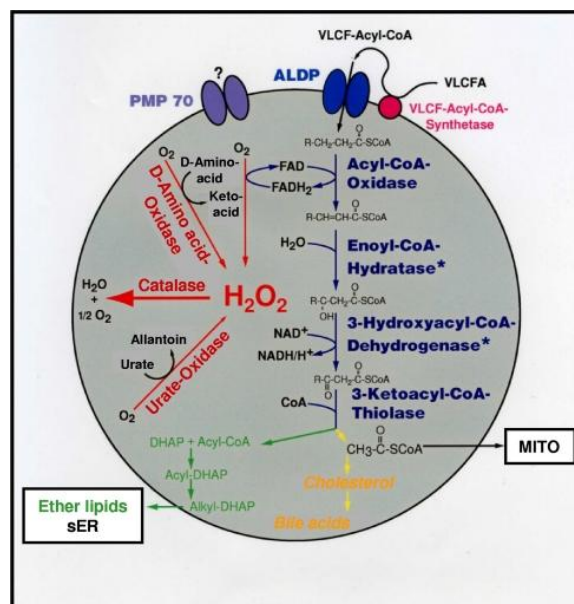
Figure 1.2: Metabolic pathways in the human liver. The products of the β-oxidation of VLCFA are further processed for the biosynthesis of ether lipids, cholesterol and bile acids, or are transferred to mitochondria. The activity of several oxidases results in the production of H_2O_2, which is degraded by the enzyme catalase. Image taken from [6].

1.3   Peroxisomal biogenesis disorders

The central role of peroxisomes in many metabolic pathways explains the appearance of severe inherited diseases in individuals that partially or fully lack peroxisomal functions. These diseases can be classified into two main groups: (i) disorders of peroxisome biogenesis and (ii) single peroxisomal enzyme deficiencies. One example for a single

enzyme defect is X-linked adrenoleukodystrophy (X-ALD), in which the ABC-transporter ABCD1 is no longer able to transport VLCFA or their correspondent acyl-CoA esters into the peroxisomal matrix [17]. This leads to enriched levels of VLCFA in the blood. The patients suffer from strong neurologic dysfunctions, including the demyelination of neurons, which finally lead to death [18]. The autosomal recessive lethal diseases included in the term "peroxisomal biogenesis disorders" (PBDs) are caused by mutations in the *PEX*-genes [19, 20]. 14 *PEX*-genes are known in humans and encode specific proteins, the peroxins, which are all involved in peroxisomal biogenesis [21]. Several phenotypes have been linked to mutations in different peroxins. In cells lacking one of the peroxins PEX3, PEX16 or PEX19, peroxisomal membrane structures cannot be detected at all. Mutations in all other peroxins lead to the formation of empty peroxisomal membrane vesicles, so-called "ghosts", which mostly appear with a lower copy number compared to normal peroxisomes within the cell. An overview of all known peroxins, including their localization and function is given in Table 1. PBDs include Zellweger syndrome (ZS) [22], neonatal adrenoleukodystrophy (NALD) [23], infantile Refsum disease (IRD) [24, 25] and rhizomelic chondrodysplasia punctata type 1 (RCDP) [26], with ZS bearing the most severe features. The patients show retardation in their neurological development including degenerative changes of the white matter combined with severe hepatic or renal dysfunctions and usually die in early or late infancy.

1.4   Peroxisomal biogenesis

Peroxisomal dynamics include the formation, proliferation and degradation of peroxisomes. The formation of peroxisomes can be divided into three steps: 1. formation of the peroxisomal membrane, 2. insertion of peroxisomal membrane proteins, and 3. import of peroxisomal matrix proteins. All peroxisomal membrane and matrix proteins are encoded in the nucleus and have to be inserted into the peroxisome after translation at ribosomes in the cytosol. In contrast to mitochondria and chloroplasts, peroxisomes are additionally able to form *de novo* in cells initially lacking peroxisomes. The proliferation of mature peroxisomes and their degradation (pexophagy) are highly dynamic processes, which can be regulated depending on the presence of specific metabolites or under specific physiological conditions (for reviews see: [6, 27, 28]).

Table 1: Overview of peroxins.

Name	Organism[a]	Localization[b]	Features[c]	Proposed function[d]
PEX1	m, y	c, m	AAA-ATPase	Export of PEX5
PEX2	m, y	m	Integral membrane protein, RING-finger motif	Part of translocation machinery
PEX3	m, y	m	Integral membrane protein	PMP import
PEX4	y	m	Ubiquitin ligase	PEX18/PEX21 turnover, PEX5 recycling
PEX5	m, y	c, p	2 splicing variants in mammals, TPR domains	Receptor for matrix proteins (PTS1), import pore
PEX6	m, y	c, m	AAA-ATPase	Export of PEX5
PEX7	m, y	c, p	WD40 repeats	Receptor for matrix proteins (PTS2)
PEX8	y	m	Integral membrane protein	PEX5-binding
PEX10	m, y	m	Integral membrane protein, RING-finger motif	Part of translocation machinery
PEX11	m, y		Integral membrane protein, 3 isoforms in mammals	Proliferation and fission
PEX12	m, y	m	Integral membrane protein, RING-finger motif	Part of translocation machinery
PEX13	m, y	m	Integral membrane protein, SH3 domain	PEX5 docking complex
PEX14	m, y	m	Integral membrane protein	PEX5 docking complex, import pore
PEX15	s.c.	m	Integral membrane protein, phosphorylated	Anchoring of PEX6 in the membrane
PEX16	m, y.l.	m	Integral membrane protein	PMP import
PEX17	y	m	Integral membrane protein	Docking complex, PMP import
PEX18	s.c.	c, p	Cytoplasmic	PTS2-dependent import
PEX19	m, y	c, p	Farnesylated: CAAX motif	Receptor for PMPs, chaperone
PEX20	y.l.	c, p	Cytoplasmic	Import of thiolase
PEX21	s.c	c, p	Integral membrane protein	PTS2-dependent import
PEX22	y	m	Integral membrane protein	Anchoring of PEX4 in the membrane
PEX23	y.l.	m	Integral membrane protein	Import of matrix proteins
PEX24	y.l.	m	Integral membrane protein	Matrix and membrane protein import
PEX25	s.c.	m	Integral membrane protein	Regulation of number and size of peroxisomes
PEX26	m	m	Integral membrane protein	Anchoring of PEX6 in the membrane
PEX27	s.c.	m	Integral membrane protein	Regulation of number and size of peroxisomes
PEX29	s.c.	m	Integral membrane protein	Regulation of number and size of peroxisomes
PEX30-32	s.c.	m	Dysferlin domain	Regulation of number and size of peroxisomes

[a] Organism: mammals (m), yeast (y), *Saccharomyces cerevisiae* (s.c.), *Yarrowia lypolitica* (y.l.)

[b] Localization: membrane (m), cytosol (c), peroxisome (p)

[c] Features: AAA-ATPase (ATPase associated with diverse cellular activities), RING-finger (really interesting new gene-finger), TPR domain (tetratricopeptide repeat domain), WD40 repeat (Trp Asp 40 repeat), SH3 domain (src homology 3 domain)

[d] Proposed function: PMP (peroxisomal membrane protein), PTS (peroxisomal targeting sequence). Modified from [29].

4

1.4.1 Formation of the peroxisomal membrane

The origin of the peroxisomal membrane is an ongoing matter of debate. In the 1960s, peroxisomes were thought to arise from the endoplasmic reticulum [30]. Based on the observation that peroxisomal membrane proteins (PMPs) are synthesized in the cytosol and have to be imported posttranslationally into peroxisomes [31], Lazarow and Fujiki postulated their "growth and division" theory in the 1980s [32]. This scenario requires a preexisting organelle that multiplies autonomously similar to mitochondria and chloroplasts to serve as a precursor for mature peroxisomes (Figure 1.3). However, this model is challenged by the observation that cells deficient in PEX3, PEX16 or PEX19, and thus lacking any detectable peroxisomes, are able to form peroxisomes *de novo* upon complementation with the missing gene [33-35]. Over the past years, several experiments confirmed the ER as the origin for *de novo* formation of peroxisomes at least in yeast [36-38]. Several peroxins have been reported to be N-glycosylated in *Yarrowia lipolytica* [39] and *Saccharomyces cerevisiae* [40], indicating that these proteins must have passed through the ER. Particularly in yeast, the membrane protein PEX3 initiates budding of preperoxisomal vesicles from a specialized compartment in the ER (Figure 1.3, [38, 41]. This event appears to be independent of the *Sec* machinery [42], but requires the presence of PEX19 [38, 40]. Recently, a cell-free ER-budding assay in *Pichia pastoris* showed a packaging of PEX3 and PEX11 into the budded vesicles [43]. This process was dependent on ATP, temperature, yet undefined cytosolic factors and PEX19. In wildtype yeast, it was shown that peroxisomes multiply mainly by growth and division [44]. However, the concept of ER-dependent peroxisome biogenesis was also expanded to wildtype cells [45]. At least for PEX3, the route via the ER is supported by the observation that PEX3 mRNA colocalizes to the ER in *S. cerevisiae* [46]. It has been shown that the information for *de novo* peroxisome formation is harbored in the cytosolic C-terminal domain of PEX3 [47], which is even able to initiate peroxisome formation from mitochondria when fused to the targeting sequence of the mitochondrial protein TOM20 [48]. Furthermore, a membrane fusion assay in *Y. lipolytica* revealed the dependence of early peroxisomal vesicle fusion on the AAA-ATPases PEX1 and PEX6 [36, 49].

In mammalian cells, the contribution of the ER to peroxisome biogenesis is less evident. In mouse dendritic cells, PEX13 and PMP70 have been identified in ER subdomains using immunocytochemistry [37, 50]. Additionally, PEX3 and PEX16 have been shown to

start from the ER in PEX3- or PEX16-deficient cells, respectively, to generate preperoxisomal membranes [51, 52]. This process does likely not involve the classical COPI/COPII-mediated vesicular transport for developing peroxisomes [53, 54]. However, Sec16B, an ER protein involved in the formation of COPII vesicles, was recently identified to mediate the export of PEX16 from the ER en route to peroxisomes [55]. The contribution of *de novo* formation to peroxisome maintenance in wildtype cells is still a matter of debate in lower and higher eukaryotes.
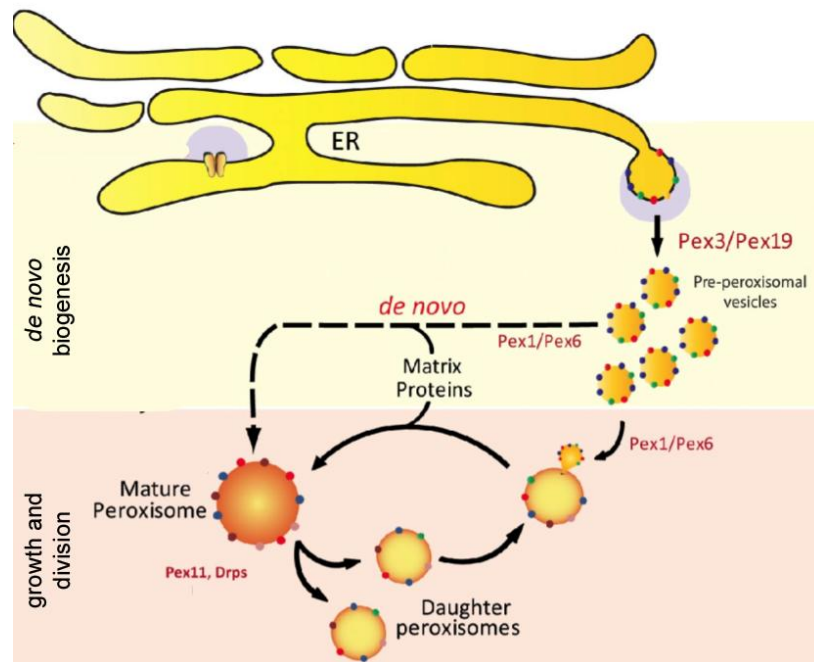
Figure 1.3: Peroxisome biogenesis. Mature peroxisomes proliferate by growth and division (lower panel) and are formed *de novo* via peroxisomal compartments of the ER (upper panel). Here, PEX3 is first localized to a specialized compartement of the ER in order to generate preperoxisomal vesicles that bud from the ER in the presence of PEX19. Image taken from [56].

1.4.2 Insertion of peroxisomal membrane proteins

The peroxins PEX3 and PEX19, and additionally PEX16 in mammals and in the yeast *Y. lipolytica* are absolutely essential for the formation of detectable peroxisomal membrane structures [35, 57]. These three peroxins exhibit important functions in the early stages of peroxisomal biogenesis and *de novo* formation of peroxisomes [58, 59]. This process can be induced in cells lacking one of the three early peroxins after reintroduction of the corresponding gene [33-35]. The import of peroxisomal membrane proteins is completely independent of the import of peroxisomal matrix proteins [60, 61]. PMPs do not possess a defined amino acid sequence that could serve as a sorting signal to peroxisomes [62]. One or two transmembrane segments flanked by a cluster of basic amino acid residues represent the membrane peroxisomal targeting sequence

(mPTS) [63]. The cytosolic protein PEX19 acts as the receptor for class I PMPs, which are directly targeted to peroxisomes [64]. PEX19 binds a multitude of PMPs via their mPTS [63, 65-69], probably during or shortly after protein synthesis at the ribosome [70]. However, within some PMPs, the peroxisomal targeting signal and the PEX19-binding region do not overlap [62, 71].
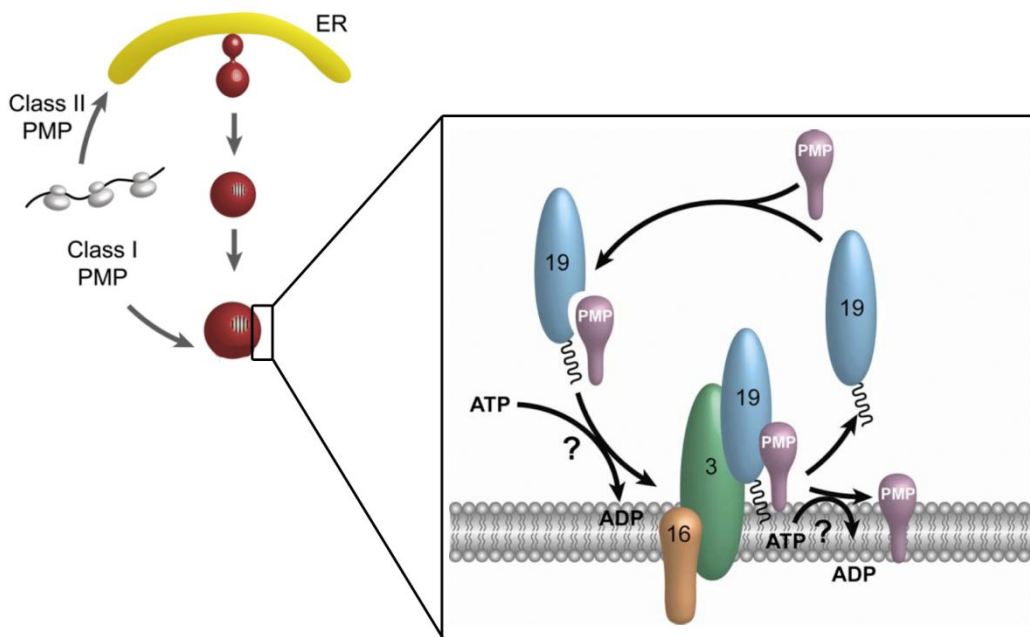
Figure 1.4: Import of peroxisomal membrane proteins. PMPs are either imported directly to peroxisomes with the help of PEX19 (class I PMPs) or are sorted via the ER (class II PMPs) to peroxisomes [72]. PMPs are transported to peroxisomes posttranslationally by the receptor PEX19 that mediates the interaction with PEX3 at the peroxisomal membrane. The PMP insertion into the membrane and the role of ATP remain to be elucidated. Image taken from [64].

The peroxins PEX3 and PEX16 represent class II PMPs, which arrive in peroxisomes after travelling through the ER. While PEX3 acts as the receptor for PEX19 at the peroxisomal membrane [70, 73, 74], PEX16 was shown to be a tethering factor for PEX3 at the peroxisome [52, 75]. The subsequent insertion of the PMP into the lipid phase remains to be elucidated. After PMP release, PEX19 is cycled back to the cytosol to initiate another round of import [76]. The schematic mechanism of PMP import is shown in Figure 1.4. The role of ATP in PMP import is discussed controversially. An *in vitro* import assay showed that the targeting of PEX19 to peroxisomes is more efficient in the presence of ATP [76]. However, a similar cell-free import assay detected that PMP22 is inserted into the peroxisomal membrane independently of ATP [77].

1.4.3 Import of peroxisomal matrix proteins

The import of peroxisomal matrix proteins is the step in peroxisomal biogenesis that is best characterized (Figure 1.5, for review see: [56, 64, 72]). In contrast to mitochondria and the ER, peroxisomal matrix proteins are imported in a folded, co-factor bound and even oligomeric state [78-80]. Most matrix proteins exhibit one of two known peroxisomal targeting signals, PTS1 and PTS2, which are recognized by their corresponding cytosolic receptors PEX5 and PEX7, respectively, in mammals [81, 82]. Nearly 90 % of peroxisomal matrix proteins carry a PTS1 signal represented by a highly conserved C-terminal tripeptide with the sequence **Ser**/Cys/Ala-**Lys**/Arg/His-**Leu** (SKL) [83, 84], which interacts with the cytosolic receptor PEX5 via its TPR domain [85]. Matrix proteins carrying a PTS2 sequence are bound by the cytosolic receptor PEX7. This nonapeptide (Arg/Lys-Leu-X_5-Gln/His-Leu) is located in the N-terminus of the PTS2-protein [86]. Cargo-loaded PEX7 requires a longer isoform of PEX5 (PEX5L) in mammals to be directed to peroxisomes [87-89]. Some peroxisomal proteins are imported into peroxisomes without any evidence for a PTS sequence. These proteins either "piggyback" on a PTS-containing protein [79, 90] or interact with PEX5 without binding to the TPR domain [91].

After cargo recognition in the cytosol (step I), the cargo-loaded receptor complexes are directed to the peroxisomal membrane (step II), where the docking-complex is located [92]. This complex is composed of the integral membrane proteins PEX13 [60] and PEX14 [93]. A transient import pore is formed by the receptor PEX5 and the peroxin PEX14 (step III) [94]. PEX5 can be integrated into the peroxisomal membrane and tends to form oligomers [95] – two prerequisites for the transient pore model. In the translocation process, the size of the pore is highly dynamic and can be influenced by the size of the receptor-cargo-complex [94]. After cargo release (step IV), PEX5 and PEX7 are recycled back to the cytosol to start another round of protein import. PEX5 is mono-ubiquitinated at a highly conserved cysteine residue close to its N-terminus [96, 97]. This modification of PEX5 is essential for its removal from the peroxisomal membrane into the cytosol (step V). This step is ATP-dependent [98] and requires a protein export complex composed of two AAA-ATPases (ATPases associated with diverse cellular activities), PEX1 and PEX6, and its membrane anchor PEX26 [99] [100]. In addition, PEX5 can also be poly-ubiquitinated, which is a signal for proteasomal degradation and may serve as a quality control to remove dysfunctional PEX5 [101, 102].
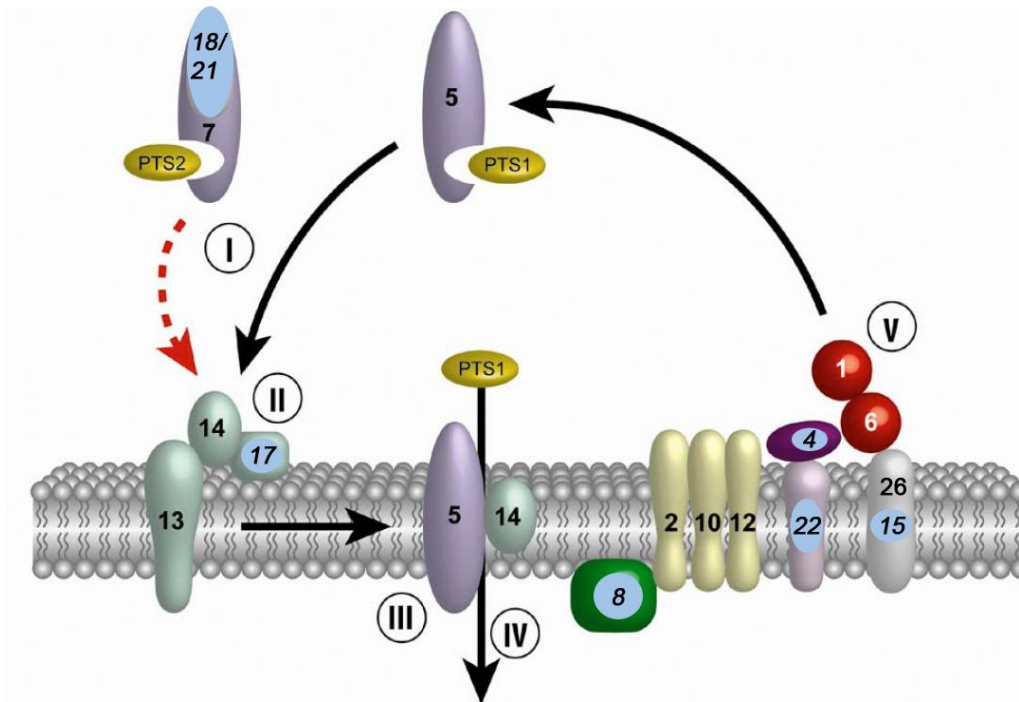
Figure 1.5: Peroxisomal matrix protein import is divided into five steps. Matrix proteins are targeted to peroxisomes with PTS1 and 2 using the cytosolic receptors PEX5 and PEX7, respectively. The docking-complex is composed of PEX13 and PEX14. A transient pore is formed by PEX5 and PEX14, which mediates the translocation across the peroxisomal membrane. After cargo release into the matrix, the receptors are recycled back to the cytosol to start another round of protein import. The peroxins underlayed in blue are additional compounds in *S. cerevisiae*. Image modified from [64].

1.5 Protein translocation and insertion – a comparison of peroxisomes with other cellular membranes

The majority of proteins is synthesized in the cytosol and has to be distributed co- or posttranslationally to their final destination within the cell. Targeting information within the protein sequence, which is recognized by cytosolic or membrane-bound receptors, is often responsible for correct intracellular localization. The protein translocation across or insertion into biological membranes is usually mediated by multi-subunit complexes that manage the crossing of the membrane barrier. In many cases, cytosolic chaperones keep the protein in an import-competent form to translocate the unfolded polypeptide chain, which is subsequently folded to receive its active form. Although these requirements for successful protein translocation are rather universal (Figure 1.6), the import and insertion machineries of the individual cellular compartments differ profoundly in their structures, signal sequences and insertion mechanism.
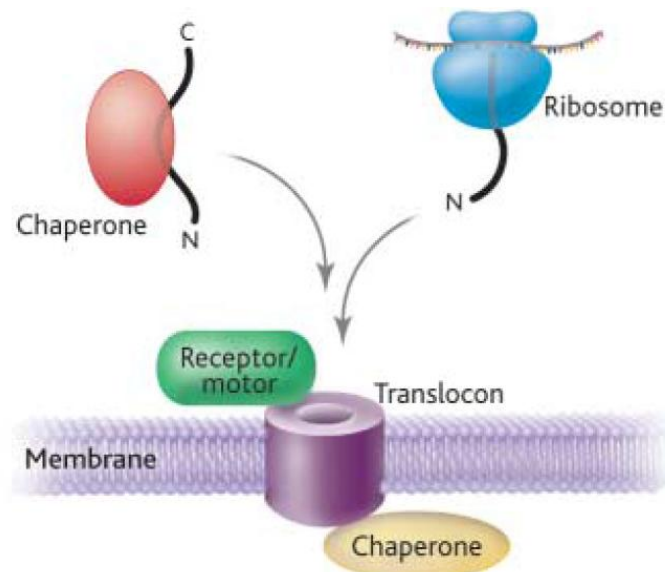
Figure 1.6: General mechanisms of protein translocation across biological membranes. Proteins are either imported cotranslationally from the ribosome (blue) or posttranslationally with the help of chaperones (red). In general, a receptor/motor module (green) mediates insertion into the translocon and translocation across the membrane barrier. Image taken from [103].

1.5.1 Protein translocation processes

In the ER, mitochondria or chloroplasts, the protein translocation machinery is in general linked to the machinery that mediates protein insertion into the corresponding membranes (Figure 1.7). In peroxisomes, however, matrix protein import appears to be strictly separated from peroxisomal membrane protein insertion. The presence of peroxisomal membrane ghosts, which contain PMPs but lack peroxisomal matrix proteins, supports the independence of PMP insertion from peroxisomal matrix protein import [104, 105]. These ghosts are detected in cells with defects in peroxins involved in matrix protein import [106]. Peroxisomal matrix protein import is comparable to protein translocation across the ER, mitochondria or chloroplasts, as all pathways use import pores. These translocons provide an aqueous channel for the proteins to cross the hydrophobic membrane barrier. The Sec61 complex of the ER [107], the TOM/TIM complexes of mitochondria [108] and the TOC/TIC complexes of chloroplasts [109] feature a static pore and translocate the linear polypeptide chain across the corresponding membrane. The proteins destined for the ER matrix, the mitochondrial matrix and the chloroplast matrix are imported as unfolded polypeptide chains with only single secondary structure elements already formed [103]. In peroxisomes, a transient import pore is formed by the cytosolic receptor PEX5 and the PMP PEX14 [94]. As peroxisomes are capable of importing folded and oligomeric proteins, the diameter of the pore can be dynamically adapted to the size of the cargo protein [94]. An additional

example for the import of folded proteins is the TAT (twin arginine translocase) system, which is found in bacterial plasma membranes [110] and in thylakoid membranes of plants [111].
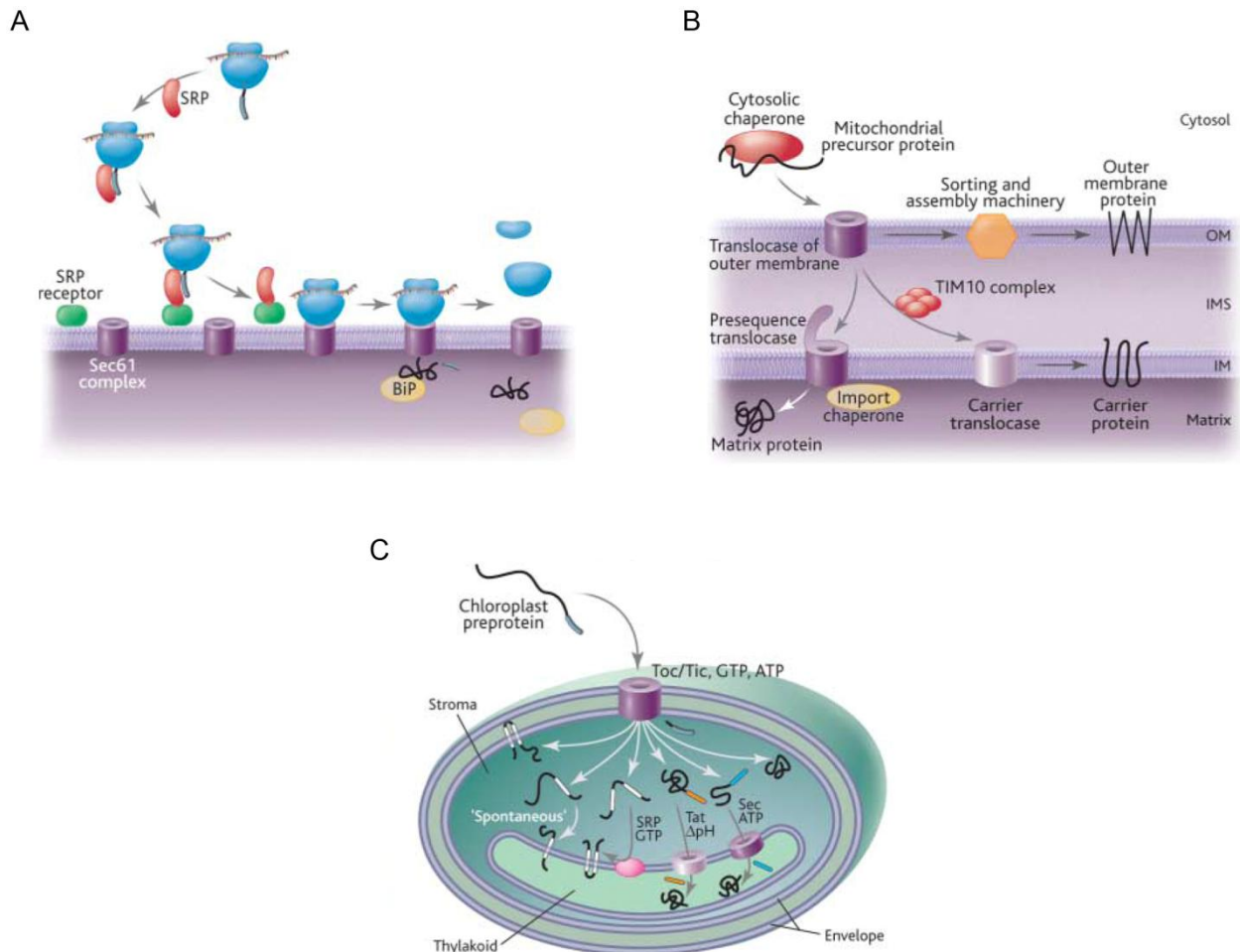
Figure 1.7: Protein translocation processes in (A) the ER, (B) mitochondria and (C) chloroplasts. Image modified from [103].

1.5.2 Protein insertion processes

ER membrane protein insertion initially uses the import pore of the Sec61 complex, but laterally releases the protein into the lipid bilayer by partial opening one side of the channel [107]. Mitochondrial outer membrane proteins are first completely translocated via the TOM complex into the intermembrane space before they are inserted into the mitochondrial outer membrane with the help of the TOB/SAM complex [112]. Proteins destined for the mitochondrial inner membrane also cross the outer membrane via the TOM complex but are then directed to the TIM23 or TIM22 complex. In both cases, membrane proteins are arrested within the pore after entry, which results in a lateral release of the membrane proteins into the lipid phase [113]. In chloroplasts, all

11

membrane proteins are first translocated through the TOC pore into the intermembrane space [114]. Proteins of the outer membrane are then inserted into the chloroplast outer membrane, whereas proteins of the inner membrane are probably first translocated to the stroma via the TIC complex before they are embedded into the chloroplast inner membrane [109]. In contrast, PMP insertion into peroxisomal membranes is isolated from matrix protein import. The targeting of PMPs requires the cytosolic receptor PEX19, which interacts with PEX3 at the peroxisomal membrane. However, the mechanisms of PMP insertion into the peroxisomal membrane remain to be elucidated in detail.

1.5.3 Tail-anchored proteins

Tail-anchored (TA) proteins represent a special class of membrane proteins that can be found in a variety of biological membranes (ER, outer mitochondrial, outer chloroplast, peroxisomal) and that use insertion pathways distinct from the previously described processes. As TA proteins carry a single C-terminal transmembrane domain, which represents the sole targeting signal, they are inserted into the corresponding membranes posttranslationally. The majority of TA proteins destined for the ER follow the TRC40/Get pathway, which relies on the activity of the ATPases TRC40 (transmembrane recognition complex) in mammals and Get3 (guided entry of tail-anchored proteins) in yeast [115]. A distinct insertion pathway for TA proteins to mitochondria has not been established yet. Different mitochondrial TA proteins use different entry systems or are inserted in an unassisted manner into the outer mitochondrial membrane [115]. In peroxisomes, the machinery for inserting peroxisomal membrane proteins and TA proteins (*e.g.* PEX26, Fis1) is the same, both involving the cytosolic receptor PEX19 and its membrane receptor PEX3 [116, 117].

1.6 The peroxins PEX3 and PEX19

1.6.1 A dual function of PEX3 and PEX19

The peroxins PEX3 and PEX19 are conserved throughout all eukaryotic species, which emphasizes their essential role in peroxisomal membrane biogenesis. The insertion of PMPs is thought to occur directly into the peroxisomal membrane after translation on free ribosomes in the cytosol. In this model, PEX19 acts as a cytosolic receptor by generally binding the mPTS of PMPs [68, 69]. Furthermore, PEX19 is considered a chaperone [67, 118] as it shields exposed hydrophobic domains and keeps the PMPs in

an import competent form. This stabilizing effect is supported by the observation, that PMPs are degraded or mislocalized in the absence of PEX19 [67, 69]. The interaction at the peroxisome surface is mediated by PEX3 (Figure 1.4), resulting in a PEX3-PEX19-dependent insertion process [67, 70, 76, 119]. Apart from anchoring cargo-loaded PEX19 at peroxisomes, PEX3 could occupy an active role during PMP insertion, although a direct binding of PEX3 to PMPs has not yet been shown.
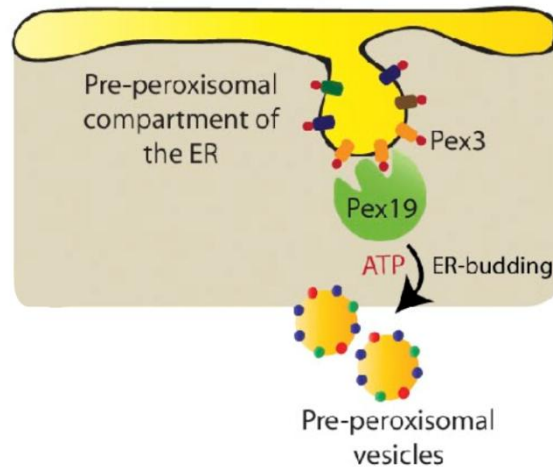
Figure 1.8: ER-dependent biogenesis of peroxisomes in yeast. PEX3 is first localized to a specialized compartment of the ER in order to generate preperoxisomal vesicles that bud from the ER in the presence of PEX19. Image modified from [56].

However, a study in yeast showed that multiple PMPs are first targeted to the ER in wildtype cells as well as in PEX3- and PEX19-deficient cells [43, 45]. The finding that PMPs may be localized cotranslationally to the ER independently of PEX19 and that PEX19 is rather required for the budding of preperoxisomal vesicles from the ER led to a different import model [45, 56]. There, PMPs are not inserted into existing peroxisomes but are in general first localized to the ER to form a preperoxisomal compartment. Budding from the ER in the presence of PEX3 and PEX19 and the subsequent fusion of several small vesicles form peroxisomes, which already contain most if not all PMPs (Figure 1.8).

1.6.2 Biochemical properties of PEX3

The human peroxin PEX3 is a 42 kDa protein composed of 373 amino acid residues, with the N-terminal 33 residues anchoring it into the peroxisomal membrane (Figure 1.9). This transmembrane domain is necessary and sufficient for PEX3 targeting to peroxisomes [120, 121]. PEX3 represents a class II PMP, which is directed to peroxisomes in a PEX19-independent way. The cytosolic domain of PEX3 protrudes into

the cytosol and mediates the interaction with PEX19 [70, 122]. This PEX3-PEX19 interaction is of high affinity and involves a strictly conserved tryptophan residue at position 104 within PEX3 [123]. In addition, a hydrophobic region of PEX3 comprising residues 120-136 was proposed to bind PEX19 [70].
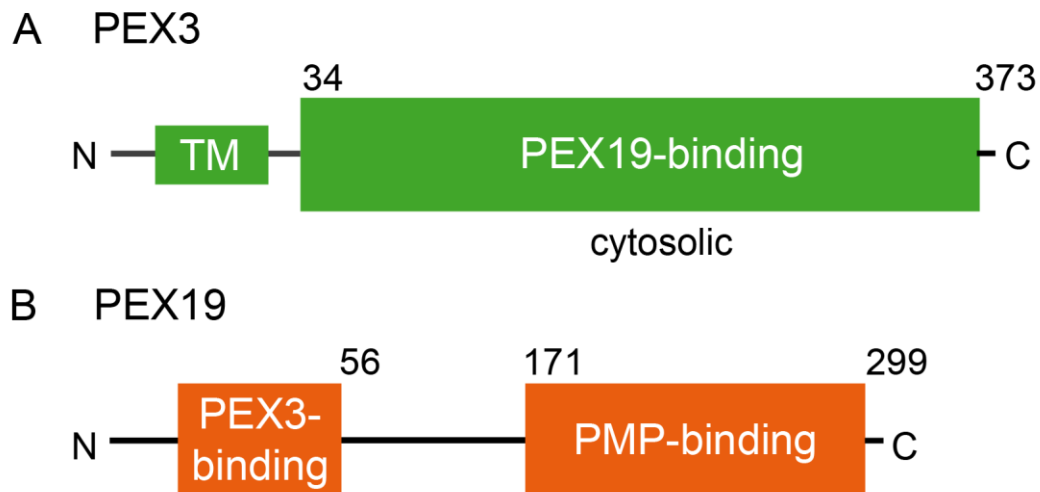
Figure 1.9: Domain topology of the peroxins 3 and 19. (A) The transmembrane domain (TM) at the N-terminus of PEX3 is essential for peroxisome targeting. The rest of the protein projects into the cytosol and is responsible for PEX19 binding. (B) The first N-terminal 56 amino acids of PEX19 are necessary for binding to PEX3 and for localization to peroxisomes. The C-terminal domain mediates the interaction with PMPs.

1.6.3 Biochemical properties of PEX19

PEX19 is mainly localized in the cytosol, but a small amount can also be found at the peroxisomal membrane [59]. The human 299-residue protein adopts a two-domain architecture (Figure 1.9), with a highly flexible N-terminal domain and a folded C-terminal domain [118] that was recently shown to form an all α-helical bundle able to recognize several PMPs [66]. Some data suggest an additional role for the N-terminal part of PEX19 in PMP recognition [76, 118, 124]. The N-terminus of PEX19 comprising residues 1-56 is needed for the localization to peroxisomes, and thus for the interaction with PEX3 [65, 70, 76]. A second PEX3-binding site was proposed to lie within PEX19 residues 124-150 [65]. PEX19 carries a strictly conserved CAAX-box at its very C-terminus, a typical farnesylation motif [125]. The importance of PEX19 farnesylation *in vivo* is discussed controversially [126-128].

1.7 Aim of this work

The major objective of this thesis was to elucidate the parameters underlying the PEX3-PEX19 complex formation. Although both proteins were known to interact and are indispensable for peroxisome biogenesis, no structural information was available on either PEX3 or the N-terminus of PEX19, which mediates the interaction with PEX3. Therefore, structural analyses of PEX3 alone and PEX3 in the presence of its interaction partner PEX19 were undertaken. An available PEX3 construct starting at amino acid 26 was used initially, with limited success [129]. A further truncated PEX3 construct was then designed, and the expressed protein was purified and used to screen for crystallization conditions alone and in the presence of a PEX19-derived peptide fragment. The *in vitro* studies were complemented with *in vivo* experiments in order to achieve a comprehensive structure-function analysis of the PEX3-PEX19 interaction. All experiments in this thesis were designed and performed to address the following questions:

⇒ What are the molecular details of the PEX3-PEX19 interaction?

⇒ What residues are essential for the PEX3-PEX19 complex formation?

⇒ What are the affinity and the molar ratio of the PEX3-PEX19 complex?

⇒ Does PEX19-binding have an effect on the structure or stability of PEX3?

⇒ Are the identified conserved regions on the surface of PEX3 involved in PEX19-binding or other steps in peroxisome biogenesis?

Answering these questions was expected to lead to a more detailed model of PMP import into the peroxisomal membrane by defining the specific function of PEX3 and PEX19 in peroxisome membrane biogenesis.

2 MATERIALS AND METHODS

2.1 Buffers and reagents

All chemicals were purchased from Roth (Karlsruhe, Germany) or Sigma Aldrich (München, Germany). Reagents for molecular biology were from Fermentas (Thermo Fisher Scientific/Fermentas, St. Leon-Roth, Germany).

Table 2: Buffers and reagents used for cloning, protein preparation and protein analysis.

E. coli strains	
DH5α	F⁻φ80lacZΔM15 Δ(lacZYA-argF)U169 recA1 endA1 hsdR17(r_k⁻, m_k⁺) phoA supE44 thi-1 gyrA96 relA λ⁻
BL21 (DE3)	F⁻ ompT hsdS$_B$(r_B⁻ m_B⁻) gal dcm lon λ (DE3)
Rosetta2 (DE3)	F⁻ ompT hsdS$_B$(r_B⁻m_B⁻) gal dcm (DE3) pRARE2 (CAM^R)
Cloning	
6x DNA loading dye	10 mM Tris, 60 % (v/v) glycerol, 60 mM EDTA, 0.03 % (w/v) bromophenol blue, pH 7.6
5x TBE	450 mM Tris, 450 mM boric acid, 10 mM EDTA, pH 8.0
LB medium	1 % (w/v) peptone, 1 % (w/v) NaCl, 0.5 % (w/v) yeast extract
LB-Amp	1 % (w/v) peptone, 1 % (w/v) NaCl, 0.5 % (w/v) yeast extract, 100 µg/mL ampicillin
LB-Amp/Cam	1 % (w/v) peptone, 1 % (w/v) NaCl, 0.5 % (w/v) yeast extract, 100 µg/mL ampicillin, 34 µg/mL chloramphenicol
LB agar	1 % (w/v) peptone, 1 % (w/v) NaCl, 0.5 % (w/v) yeast extract, 1.5 % (w/v) agar
SOC medium	2 % (w/v) peptone, 0.5 % (w/v) yeast extract, 10 mM NaCl, 2.5 mM KCl, 10 mM $MgCl_2$, 10 mM $MgSO_4$, 20 mM glucose
Protein preparation	
HisA	20 mM NaH_2PO_4, 300 mM NaCl, 10 mM imidazole, 5 mM β-ME, pH 8.0
HisB	20 mM NaH_2PO_4, 300 mM NaCl, 500 mM imidazole, 5 mM β-ME, pH 8.0
SEC	50 mM Tris, 200 mM NaCl, 5 mM DTT, pH 8.0
Protein analysis	
SDS- and native PAGE	
2x SDS loading dye	125 mM Tris (pH 6.8), 4 % (w/v) SDS, 10 % (v/v) β-ME, 20 % (v/v) glycerol, 0.02 % (w/v) bromophenol blue

SDS running buffer	25 mM Tris, 192 mM glycine, 0.1 % (w/v) SDS, pH 8.3 (do not adjust)
Coomassie staining solution	30 % (v/v) ethanol, 10 % (v/v) acetic acid, 0.25 % (w/v) Coomassie Brilliant Blue G-250
Coomassie destaining solution	30 % (v/v) ethanol, 10 % (v/v) acetic acid
2x loading dye (native)	125 mM Tris (pH 6.8), 20 % (v/v) glycerol, 0.02 % (w/v) bromophenol blue
Western blotting	
WB buffer	20 mM Tris, 150 mM glycine, 0.05 % (w/v) SDS, 20 % (v/v) methanol
PBS	10 mM Na_2HPO_4, 1.8 mM KH_2PO_4, 140 mM NaCl, 2.7 mM KCl, pH 7.4
PBS-Tween	PBS, 0.1 % Tween-20
PBS-ST	PBS, 0.02 % (w/v) SDS, 0.1 % (v/v) Triton-X-100
Antibodies	
GDA7	antibody against C-terminal human PEX3 peptide (aar 354-371) generated in rabbit; Dodt lab, University of Tübingen
PEX19-1	antibody against recombinant human full-length PEX19 generated in rabbit; Dodt lab/N. Treiber, University of Tübingen
Secondary antibody	α-rabbit IgG coupled to HRP (Sigma Aldrich)
CD spectroscopy	
CD buffer	5 mM Na_2HPO_4, 0.9 mM KH_2PO_4, 70 mM NaCl, 1.35 mM KCl, 0.25 mM TCEP, pH 7.2
T_m buffer	10 mM Na_2HPO_4, 1.8 mM KH_2PO_4, 5 mM NaCl, pH 7.4
ITC experiments	
ITC buffer	10 mM Na_2HPO_4, 1.8 mM KH_2PO_4, 140 mM NaCl, 2.7 mM KCl, 0.5 mM TCEP, pH 7.4
TNT and CoIP	
CoIP A	20 mM HEPES, 110 mM KAc, 5 mM NaAc, 2 mM MgAc, 1 mM EDTA, pH 7.3
CoIP B	20 mM HEPES, 110 mM KAc, 5 mM NaAc, 2 mM MgAc, 1 mM EDTA, pH 7.3; 0.1 % (w/v) BSA
CoIP C	20 mM HEPES, 110 mM KAc, 5 mM NaAc, 2 mM MgAc, 1 mM EDTA, pH 7.3; 0.5 % (v/v) Triton X100 + protease inhibitor cockatil (Sigma Aldrich, 1:200))

2.2 Molecular biology

All enzymes and reagents used for cloning procedures were purchased from Fermentas (St. Leon-Roth, Germany) unless indicated otherwise. Oligonucleotides were synthesized by biomers.net (Ulm, Germany). Chemicals were purchased from Roth (Karslruhe, Germany) or Sigma Aldrich (München, Germany). DNA concentrations were calculated using their absorbance values at 260 nm with a NanoDrop ND-100 (PeqLab, Erlangen, Germany).

2.2.1 Plasmids

The plasmids used in this work are listed in Table 3. Detailed plasmid cards of pNT65, pFS122 and pNT45 can be found in section 0. The DNA and amino acid sequences of sPEX3 and PEX19 are listed in section 9.2.1 and 9.2.2, respectively.

Table 3: Plasmid list.

Plasmid	Basic vector	Description	Protein
Bacterial expression			
pNT65 [129]	pET32a (Merck/Novagen, Darmstadt, Germany)	Human PEX3, aar 26-373, C235S, N-terminal Trx-His$_6$-tag, TEV protease cleavage site	nPEX3
pFS122	pET32a (Merck/Novagen, Darmstadt, Germany)	Human PEX3, aar 41-373, C235S, N-terminal Trx-His$_6$-tag, TEV protease cleavage site	sPEX3
pNT45 [129]	pCold1 (Takara/Bio Europe, St Germain en Laye, France)	Human PEX19, full-length N-terminal His$_6$-tag, TEV protease cleavage site	PEX19
Mammalian expression			
pMS20 [120, 130]	pcDNA3.1zeo (Invitrogen, Darmstadt, Germany)	Human PEX3, full-length C-terminal myc-tag	PEX3-myc
pMS200 [120, 130]	pcDNA3.1zeo (Invitrogen, Darmstadt, Germany)	Human PEX3, aar 1-33 C-terminal GFP-tag	PEX3$^{1-33}$-GFP
pMS218 [120, 130]	pcDNA3.1zeo (Invitrogen, Darmstadt, Germany)	Human PEX3, aar 34-373 C-terminal GFP-tag	PEX3$^{34-373}$-GFP
pPEX3-YFP (A. Muntau) [73]	pcDNA3.1zeo (Invitrogen, Darmstadt, Germany)	Human PEX3, aar 1-373 C-terminal YFP-tag	PEX3$^{1-373}$-YFP
pKB8.1 (K. Bagner; Dodt lab)	pcDNA3.1zeo-myc (Invitrogen, Darmstadt, Germany)	Human PEX16, aar 1-336 C-terminal myc-tag	PEX16-myc

pBG4 (B. Gürke; Dodt lab)	pEYFP-N1 (Takara/ Clontech St Germain en Laye, France)	Human PEX16, aar 1-336 C-terminal YFP-tag	PEX16-YFP
pPMP70-myc (S. Gould; Baltimore)	pcDNA3 (Invitrogen, Darmstadt, Germany)	Human PMP70 C-terminal myc-tag	PMP70-myc
pYFP-PTS1 (A. Muntau, München)	pEYFP-Peroxi (Takara/ Clontech St Germain en Laye, France)	YFP C-terminal PTS1-tag	YFP-PTS1

2.2.2 Cloning

2.2.2.1 General theory

A DNA insert used for cloning into an expression plasmid is amplified from template DNA with specific primers using polymerase chain reaction (PCR, [131]). The PCR product is analyzed with agarose gel electrophoresis. The expression plasmid and the PCR product are digested with restriction endonucleases to obtain suitable DNA fragments for ligation. The produced new plasmid is then transformed into *E. coli* cells, and plasmid-containing cells are selected via antibiotic resistance. Several clones are tested for positive insertion by DNA preparation followed by analytical digestion with restriction endonucleases.

For inserting point mutations within a DNA sequence, the method of site directed mutagenesis is performed [132]. Here, specific primers are designed that contain the desired mutation within the sequence of the oligonucleotide. A subsequent PCR amplifies the complete plasmid carrying the desired mutation. The parental DNA is digested with *Dpn*I. After transformation of the plasmid, DNA is amplified and isolated of *E. coli* cells. In both cases, new DNA constructs are sequenced based on the dideoxy method of Sanger using fluorescence labeled ddNTPs as terminator nucleotides [133].

2.2.2.2 Polymerase chain reaction and agarose gel electrophoresis

For cloning of *sPEX3* into pET32a, the plasmid pNT65 served as template DNA. The forward primer (GD 425) contained in addition the sequence for the TEV protease cleavage site (italics) following the restriction site for *Nco*I (underlined). The reverse primer (GD 426) contained the restriction site for *Sal*I (underlined). The primer sequences were:

GD 425 5´-3´ GC*CCATG*GAAAACCTGTATTTTCAGGGACAGGAAAGGGAGGCTGCAGAATACATTGC

GD 426 5´-3´ GGCGTCGACTCATTTCTCCAGTTGCTGAGGGG

The components and the program for PCR reaction are listed in Table 4. Each PCR product was analyzed by agarose gel electrophoresis. Therefore, 1 µL of 6x DNA loading dye was added to 5 µL of the PCR sample and loaded onto a 1 % (w/v) agarose gel. The gel was produced by melting agarose (Biozym, Hessisch Oldendorf, Germany) in 50 mL 0.5x TBE buffer. Ethidium bromide was added (end concentration: 1 mg/mL) and the gel was cast into a gel chamber. Gels were run for 1 hour at 100 V before DNA was visualized under UV light.

Table 4: PCR reaction batches and PCR program used for amplifying *sPEX3*.

Component	Volume (µL)		Step	Time (min)	Temperature (°C)
pNT65 (100 ng/µL)	1	1	denaturation	3	95
Primer GD 425 (10 pmol/µL)	5	2	denaturation	2	95
Primer GD 426 (10 pmol/µL)	5	3	annealing	2	65
Buffer (10x)	5	4	elongation	5	72
dNTPs (10 mM)	1		Go back to step 2 for 30 times		
Pfu DNA polymerase (2.5 U/µL)	1	5	elongation	15	72
H$_2$O	32	6	hold	pause	4

2.2.2.3 Restriction and ligation

The PCR product was purified using the *mi-PCR Purification Kit* according to the manufacturer's instructions (Metabion, Martinsried, Germany). In order to obtain DNA sequences suitable for ligation, the purified PCR product and the plasmid pNT65 were digested with restriction endonucleases overnight at 37 °C using the following reaction mixture:

DNA	1 µg
*Nco*I	1 µL
*Sal*I	2 µL
Buffer (Tango, 10x)	4 µL
H$_2$O	ad 20 µL

The samples were separated on a 1 % (w/v) agarose gel, and the corresponding bands were cut out. The DNA was eluted from the agarose by centrifugation (16000*g, 10 min, 4 °C) using a filter tube (Costar Spin-X®, Corning, Amsterdam). For ligation, 80 ng of digested plasmid pNT65 were incubated with the insert DNA. Different molar ratios of

insert to vector were used (5:1 and 25:1). The reaction batch was completed with ligase (1 μL) and ligation buffer (10x, 2 μL), and it was filled up with H_2O to 20 μL. The reaction mixtures were incubated at 16 °C for 16 hours in a thermocycler (Biometra, Göttingen, Germany).

2.2.2.4 Transformation and DNA isolation

The ligation batches were dialyzed for 20 minutes against H_2O prior to transformation into *E. coli* DH5α using electroporation. In preparation, the DNA solutions were pipetted on a nitrocellulose filter (0.025 μm VSWP, Merck/Millipore, Darmstadt), floating on 5 mL H_2O in a culture dish. 50 μL of competent bacteria cells were mixed with 10 μL of dialyzed DNA sample on ice. The cell-DNA suspension was transferred to an electroporation cuvette (Biozym, Hessisch Oldendorf, Germany) and exposed to 2500 V for 6 ms using an electroporator (Eppendorf, Hamburg, Germany). Directly after electroporation, cells were treated with 500 μL warm (37°C) SOC medium and incubated at 37 °C with gentle shaking for 30-60 minutes. 100-200 μL of cell suspension was plated on an LB agar plate containing ampicillin (100 μg/mL) and incubated overnight at 37 °C. For DNA preparation, single colonies were transferred into 15 mL of LB-Amp medium and incubated on a bacterial shaker (Infors HT, Basel, Switzerland) at 180 rpm overnight at 37 °C. DNA isolation was carried out with the *mi-Plasmid Miniprep Kit* (Metabion, Martinsried, Germany) according to the manufacturer's instructions. To test for successful ligation, restriction analysis with *Nco*I/*Sal*I was performed and analyzed by agarose gel electrophoresis. Positive clones containing the insert were sequenced at Eurofins MWG Operon (Ebersberg, Germany) using S-tag (5' CGAACGCCAGCACATGGACA 3') and T7 reverse (5' CTAGTTATTGCTCAGCGGT 3') primers.

2.2.2.5 Site directed mutagenesis

For inserting point mutations in *sPEX3* (pFS122), *PEX3-myc* (pMS20) or *PEX3-YFP* (pMS204), site directed mutagenesis was performed by PCR. The primers are listed in Table 5, with the sequences of the corresponding mutations being underlined. Components and the program for mutagenesis PCR are listed in Table 6.

The PCR reaction samples were incubated with 1 μL *Dpn*I at 37 °C overnight to digest methylated template DNA. To verify successful mutagenesis PCR, each sample was analyzed by agarose gel electrophoresis. PCR-positive samples were transformed into *E. coli* DH5α (2 μL DNA + 50 μL electro-competent cells; see section 2.2.2.4) and

21

plasmid-containing clones were selected via ampicillin resistance. 15 mL of LB-Amp medium were inoculated with a single colony and incubated on a shaker overnight at 37 °C and 180 rpm. DNA was isolated with the *mi-Plasmid Miniprep Kit* (Metabion, Martinsried, Germany) according to the manufacturer's instructions and sequenced (Eurofins MWG Operon, Ebersberg, Germany).

Table 5: Primers used for inserting point mutations in *sPEX3* and *PEX3-myc and PEX3-YFP*.

Mutation	Primer forward 5'- 3'	Primer reverse 5'- 3'
L93N	CCGAGAGCCTCACAGCTCTG<u>AAC</u>AAAAACAGGCC	GGCCTGTTTTT<u>GTT</u>CAGAGCTGTAGGCTCTCGG
I140N	CATAATTGGTGGATAT<u>AAC</u>TACCTGGATAATGCAGC	GCTGCATTATCCAGGTA<u>GTT</u>ATATCCACCAATTATG
L165N	CCAACAGCAGTAT<u>AAT</u>TCAAGTATTCAGCACC	GGTGCTGAATACTTGA<u>ATT</u>ATACTGCTGTTGG
E266A	CTATTAAACTTCTCAAT<u>GCA</u>ACTAGAGACATGTTGG	CCAAATGTCTCTAGT<u>TGC</u>ATTGAGAAGTTTAATAG
D275A	GTTGGAAAGCCCA<u>GCT</u>TTTAGTACAGTTTTG	CAAAACTGTACTAAA<u>AGC</u>TGGGCTTTCCAAC
K324A	GTCAGCCTGCCTTTAGCT<u>GCG</u>ATAATTCCAATAG	CTATTGGAATTAT<u>CGC</u>AGCTAAAGGCAGGCTGAC
C235S	GGATCCAAACCTTTATTA<u>AGC</u>CATTATATGATGCC	GGCATCATATAATG<u>GCT</u>TAATAAAGGTTTGGATCC

Table 6: Reaction batches and corresponding temperature program for mutagenesis PCR.

Component	Volume (µL)		Step		Time (min)	Temperature (°C)
pMS20 or pFS122 (100 ng/µL)	1	1	denaturation		2	95
Primer forward (10 pmol/µL)	5	2	denaturation		1	95
Primer reverse (10 pmol/µL)	5	3	annealing		1	60
Buffer (10x)	5	4	elongation		15	72
dNTPs (10 mM)	1			Go back to step 2 for 18 times		
Pfu DNA polymerase (2.5 U/µL)	1	5	elongation		20	72
H₂O	32	6	hold		pause	4

2.3 Protein preparation and protein analysis

All chemicals were purchased from Roth (Karlsruhe, Germany), Fermentas (St. Leon-Roth, Germany) or Sigma Aldrich (München, Germany) unless stated otherwise. Protein purification was carried out on an ÄKTA Purifier system (GE Healthcare, München, Germany) using the supplied Unicorn 5.01 software. Size exclusion chromatography was performed using an FPLC BioLogic Duo Flow system (Bio-Rad, München, Germany). All columns for purification procedures were purchased from GE Healthcare. All purification steps were carried out at 4 °C.

2.3.1 Expression and purification of proteins

2.3.1.1 General remarks

For recombinant expression of proteins in *E. coli*, a plasmid coding for the desired protein sequence with a suitable promoter is first transformed into bacterial cells. Plasmid-containing cells are selected by specific antibiotic resistance. Protein expression can be induced through the presence of specific metabolites, which initiate DNA transcription by activating the corresponding promoter. In this thesis, all bacterial expression plasmids are based on the lac operon, which can be regulated by the addition of isopropyl-β-thiogalactopyranoside (IPTG). The culture conditions (bacterial cell line, temperature, concentration of IPTG) must be optimized for each single protein to obtain soluble protein in an adequate yield.

For purification, the recombinantly expressed protein has to be extracted from the protein pool of the lysed cells. Metal chelate affinity chromatography is based on reversible interactions of histidine residues in proteins with metal ions, usually Ni^{2+}, which are immobilized on a column matrix [134]. After binding to the column, proteins can be eluted with increasing concentrations of imidazole that competes with histidine residues for binding to the Ni^{2+} ions. Size exclusion chromatography separates proteins according to their size and shape using a porous matrix. Each column has to be calibrated with proteins of known molecular mass to estimate the oligomerization state of the protein of interest.

2.3.1.2 Expression of nPEX3 and sPEX3

For protein expression, 100 ng of the different PEX3 constructs were transformed in *E. coli* Rosetta2 (DE3) cells as described in section 2.2.2.4 this time using LB-Amp/Cam medium. 4 mL of the overnight culture were used to inoculate 400 mL of LB-Amp/Cam medium. Cells were incubated in a bacterial shaker at 37 °C and 180 rpm until the OD_{600} reached 0.6-0.9. Then, protein expression was induced with 1 mM IPTG and the temperature was set to 18 °C for 16-20 hours without precooling the bacterial cultures.

2.3.1.3 Expression of PEX19

For PEX19 expression, 100 ng of the vector pNT45 containing the DNA for human PEX19 was transformed into *E. coli* BL21 (DE3) cells (see section 2.2.2.4). 4 mL of the overnight culture were used to inoculate 400 mL of LB-Amp medium. Cells were incubated in a bacterial shaker at 37 °C and 180 rpm until the OD_{600} reached 0.4. Then, the temperature

was lowered to 15 °C for 30-45 minutes before protein expression was further induced with 1 mM IPTG. Cells were then incubated overnight at 15 °C.

2.3.1.4 Cell lysis and protein purification

Cell lysis and protein purification were the same for nPEX3, sPEX3 and PEX19. First, bacterial cells were harvested by centrifugation (8000*g, 10 min, 4 °C). The pellet was resuspended in buffer HisA (10 g pellet in 50 mL buffer) prior to lysis in a French press (Emulsiflex, Avestin, Mannheim, Germany). After centrifugation (28000*g, 45 min, 4 °C), the lysate was filtered (0.45 μm), loaded onto a Ni^{2+}-column (HisTrap™ HP, 5 mL), and target protein was eluted with buffer HisB using the protocol listed in Table 7. The flow-through was collected separately. Five mL fractions were collected during the first two washing steps and 2 mL fractions were collected during the elution steps.

Table 7: Protocol for elution of proteins from Ni^{2+}-columns.

Step	Concentration HisB (%)	Column volume (CV)
Washing 1	0	20
Washing 2	10	25
Elution 1	10-100	25
Elution 2	100	10

The target protein containing fractions were pooled, and 1 mg TEV protease was added to 40 mg of protein. Cleavage was carried out in a membrane tube (MWCO 10 kDa, Spectrumlabs, Breda, The Netherlands) overnight at 4 °C while dialyzing against 1 L buffer HisA. The protein solution was next applied to a second Ni^{2+}-column to remove uncleaved protein, His_6-tags and His_6-tagged TEV protease. The flow-through containing cleaved protein was concentrated using a centrifugal filter unit (Merck/Millipore, Darmstadt, Amicon Ultra®, Ultracell®, MWCO 10 kDa) and applied to a SEC column. Preparative SEC was carried out on a Superdex™ 200 10/300 GL column whereas analytical SEC was done on a Superdex™ 200 PC 3.2/30 with SEC buffer.

2.3.2 Peptide synthesis

PEX19-derived peptides were synthesized by H. Kalbacher (IFIB, University of Tübingen) using solid-phase chemistry and the *N*-(9-fluorenyl)methoxycarbonyl (Fmoc) strategy on a SyroII synthesizer (MultiSynTech, Witten, Germany) as described in [135]. Peptides were purified with a C18 column. Purity was confirmed by analytical HPLC, matrix-assisted laser desorption/ionization time of flight mass spectrometry (MALDI-TOF-MS), and electrospray ionization mass spectrometry (ESI-MS).

2.3.3 Protein analysis

2.3.3.1 SDS-PAGE

Heterogeneous protein solutions can be separated using discontinuous sodium dodecyl sulfate polyacrylamide gel electrophoresis (SDS-PAGE, [136]). In general, the proteins are denatured by incubating with a reductive reagent and SDS, an anionic detergent that charges proteins with a constant mass ratio of 1.4 $mg_{SDS}/mg_{protein}$ and additional boiling for 5 min. The protein solution is then loaded onto an acryl-/bisacrylamide gel that forms a network of defined pores and separates the different proteins by molecular mass using an electric field.

In this thesis, protein fractions were tested for purity with SDS-PAGE analysis. Therefore, a 10 % separating gel with a 5 % stacking gel was cast with components listed in Table 8. Samples (5 µL) were mixed with 5 µL 2x SDS loading dye without boiling before loading on the gel. Electrophoresis was carried out at 140 V for 1 hour at room temperature using SDS running buffer. Gels were incubated with Coomassie staining solution and heated to 80 °C in a microwave for 30 seconds before they were incubated for 10-20 minutes at room temperature. After removing the staining solution, gels were destained in Coomassie destaining solution for 1 hour at room temperature.

Table 8: Composition of SDS gels.

	10 % separating gel (mL)		5 % stacking gel (mL)
H$_2$O	1.9	H$_2$O	1.4
Acrylamide-bisacrylamid (37.5:1)	1.7	Acrylamide-bisacrylamide (37.5:1)	0.33
1.5 M Tris, pH 8.8	1.3	1.5 M Tris, pH 6.8	0.25
10 % SDS	0.05	10 % SDS	0.02
10 % APS	0.05	10 % APS	0.02
TEMED	0.002	TEMED	0.002

2.3.3.2 Native PAGE

A native PAGE is carried out under non-reducing and non-denaturing conditions to detect possible oligomerization states of a protein or protein-protein interactions. In this thesis, a native PAGE was done to characterize the molar ratio of the PEX3-PEX19 complex formation. Therefore, protein solutions were separated on an 8 % native gel without addition of SDS. nPEX3 and PEX19 were used at a concentration of 10 µM each and mixed in different molar ratios. 15 µL protein samples were incubated with 2x

loading dye (native) before electrophoresis was done at 50 V for 3-4 hours under ice cooling using SDS running buffer without the addition of SDS. The gel was then further analyzed by Western blotting (see section 2.3.3.3).

2.3.3.3 Western Blotting

Western blotting identifies proteins using specific immunodetection with antibodies against the target protein. Therefore, proteins are separated by electrophoresis and electroblotted onto a membrane to make protein epitopes accessible to the antibodies [137]. The antibody itself is detected indirectly with a secondary antibody that is coupled to horseradish peroxidase. In the presence of H_2O_2 and the substrate luminol, photons are generated, which react with a light sensitive film at the positions of the proteins.

In this thesis, nPEX3:PEX19 protein solutions of different molar ratios (2:1, 1:1, 1:2) were separated with a native PAGE (section 2.3.3.2) before the gel was blotted onto a PVDF membrane (GE Healthcare, München, Germany) that was activated before in 100 % methanol. The proteins were transferred at 20 V for 1 hour at room temperature in a semidry blotting system (Bio-Rad, München, Germany) using WB buffer. The membrane was blocked with 10 % milk powder in PBS-Tween at 4 °C overnight with gentle shaking. Primary antibodies were either directed against PEX3 (GDA7, 1:15000 in 5 % milk powder in PBS-ST) or PEX19 (PEX19-1, 1:10000 in 5 % milk powder in PBS-ST), and were used at the indicated dilutions to decorate the membrane for 2 hours at room temperature under gentle shaking. After 5 washing steps with 10 mL PBS-ST for 10 minutes, the membrane was incubated with secondary antibodies (α-rabbit IgG coupled to horseradish peroxidase, 1:15000 in 5 % milk powder in PBS-ST) for 1 hour at room temperature. After washing 5 times with 10 mL PBS-ST for 10 minutes, the membrane was washed once with 10 mL PBS. The protein bands were detected with the ECL (enhanced chemoluminescence) system (Pierce/Thermo Fisher Scientific, Bonn, Germany) according to the manufacturer's instructions. A light sensitive film (Amersham Hyperfilm™ ECL, GE Healthcare, München, Germany) was then placed onto the membrane for 10-30 seconds and was processed in an automated film-developing machine (Konica, Langenhagen, Germany).

2.3.3.4 Protein concentration

The concentration of homogeneous protein solutions can be determined by measurements of absorbance at 280 nm according to the Lambert-Beer equation (Eq. 1).

$$c \left(^{mg}/_{mL} \right) = \left. A_{280} \, M_r \, (Da) \middle/ \varepsilon_{280} \, (M^{-1}cm^{-1}) d \right. \tag{1}$$

A$_{280}$ absorption at 280 nm
M$_r$ molecular mass
ε_{280} molar extinction coefficient at 280 nm
d   optical path length

The molar extinction coefficient at 280 nm can be calculated using the amino acid sequence of the corresponding proteins, as mainly tryptophans, tyrosines and cysteines are absorbing in the UV range [138].

In this thesis, the measurements of absorption were carried out using a NanoDrop ND-100 (Peqlab, Erlangen, Germany) and the ε_{280} values were determined using the software *ProtParam* ([139, 140], Table 9).

Table 9: Extinction coefficients at 280 nm and molecular masses.

Protein	ε_{280} (M^{-1}cm^{-1})	M$_r$ (kDa)
nPEX3	26275	39.3
sPEX3	23295	37.5
PEX19	10220	32.8

2.3.3.5 CD spectroscopy

The folding characteristics of a purified protein can be analyzed using circular dichroism (CD) spectroscopy. The secondary structure elements (α-helices, β-sheets) interact with circular polarized light and exhibit specific minima or maxima of ellipticity at distinct wavelengths in the recorded spectrum. Therefore, a CD spectrum can be used to differentiate between folded or unfolded proteins and to estimate the amount of α-helices and β-sheets within the protein fold. Additionally, the melting point of a protein can be determined with a CD spectrometer by recording the ellipticity at a specific wavelength in a defined temperature range. The change of the signal indicates unfolding of the protein structure. The melting point of a protein is defined as the inflection point in the data curve.

In this work, CD spectra were recorded on a JASCO J-720 spectropolarimeter. Proteins were present at a concentration of 10-15 µM in CD buffer. The mean of 8 protein spectra was corrected by subtracting the buffer spectrum. For the determination of protein

melting points, a JASCO J-810 spectropolarimeter was used. The scan rate was 1 °C/min in a temperature range of 20 to 95 °C. The CD signal was measured at 208 nm and the proteins were present at a concentration of 10-15 µM in T_m buffer.

2.3.3.6 ITC experiments

Isothermal titration calorimetry (ITC) is used to determine the thermodynamic parameters ΔH, ΔS and ΔG of an interaction between two molecules. With Equation 2, the dissociation constant (K_d-value) of the binding process can be calculated.

$$\Delta G = -RT \cdot \ln K_a \qquad \text{with } K_a = 1/K_d \qquad (2)$$

ΔG   free energy (J/mol)
R   gas constant (8.314 J/mol·K)
T   absolute temperature (K)
K_a association constant (1/M)
K_d dissociation constant (M)

During the experiment, a ligand is titrated into a protein solution. The heat (enthalpy, ΔH), which is released or consumed during the reaction, is measured. The data points are fitted to a sigmoidal curve, which leads to the calculation of the entropy ΔS, the free energy ΔG and stoichiometry of binding. For an interpretable experiment, the concentration of the ligand should be 10-times higher than the protein concentration.

Table 10: Protein concentrations for ITC experiments.

PEX3	Concentration [µM]	PEX19	Concentration [µM]
nPEX3	8.2	Full-length	92.0
sPEX3	10.1	Full-length	83.2
sPEX3	17.2	PEX19^{Pep}	275.1
sPEX3	17.2	PEX19^{Pep} F29A	184.6
sPEX3	17.2	PEX19^{Pep} A25L	156.3
sPEX3	17.2	PEX19^{Pep} A25Y	153.7
sPEX3	17.2	PEX19 124-136	101.6
sPEX3 L93N	25.9	Full-length	274.3
sPEX3 K324A	12.0	Full-length	147.2
sPEX3 E266A	9.3	Full-length	92.2
sPEX3 I140N	8.0	Full-length	96.3
sPEX3 L165N	10.1	Full-length	95.4

Affinity measurements between nPEX3, sPEX3, sPEX3 mutants and full-length PEX19 were recorded on a VP-ITC calorimeter (Microcal/GE Healthcare, München, Germany) at the Max Planck Institute (MPI), Tübingen. Binding studies of sPEX3 in complex with a PEX19-derived peptide were carried out with an ITC200 system (Microcal/GE Healthcare, München, Germany) at the Paul Scherrer Institute (PSI) in Villigen,

Switzerland. The concentrations used in the different experiments can be found in Table 10. PEX19 or PEX19[Pep] was titrated in 29 distinct steps to the corresponding PEX3 solutions. All measurements were done once at 25 °C in ITC buffer, with the exception of the binding analysis of nPEX3 with full-length PEX19, which was carried out in SEC buffer. Data were fitted in Microcal Origin® version 7.0 according to one binding site model.

2.3.3.7 In vitro transcription/translation

TNT experiments followed by coimmunoprecipitation (CoIP, section 2.3.3.8) were done to analyze the ability of PEX3 mutants to interact with PEX19. In vitro transcription and translation experiments were carried out with the TNT® Coupled Reticulocyte Lysate System (Promega, Mannheim, Germany) according to the manufacturer's instructions. The reaction was carried out in the presence of ^{35}S-methionine (37 TBq/mmol, Hartmann Analytic, Braunschweig, Germany) to label the translation products for detection. The empty vector pcDNA3 was used as a negative control. 10 µL of translated PEX19 were mixed with 10 µL of translated PEX3-myc, the corresponding PEX3-myc mutants or with the negative control. The samples were incubated at 30 °C for 1 hour, before they were subjected to CoIP experiments.

2.3.3.8 Coimmunoprecipitation

50 µL of Dynabeads® M-280 sheep α-mouse IgG (Invitrogen, Darmstadt, Germany) were prepared according to the manufacturer's instructions using CoIP buffer B for washing. The beads were then loaded with mouse α-myc antibodies (Cell Signalling/NEB, Frankfurt a.M., Germany; 1:200) in the presence of 0.1 % (w/v) BSA overnight at 4 °C. After washing with CoIP buffer B, the beads were resuspended in 130 µL CoIP buffer C before the translation mixtures obtained by TNT assays (section 2.3.3.7) were added. The samples were incubated under slight rotation for 2 hours at 4 °C and then placed on a magnet to separate the magnetic beads from the solvent. The supernatant was removed, immediately mixed with SDS-loading buffer and heated to 80 °C for 5 minutes. The beads were washed with CoIP buffer C, resuspended in 25 µL SDS-loading buffer and heated to 80 °C for 5 minutes. The tubes were then again placed onto the magnet to obtain the elution fraction. The samples were analyzed on a 10 % SDS-PAGE before the gels were incubated in 0.5 M Na-salicylate for 20 minutes. The gels were dried onto Whatman paper and exposed to an autoradiography film (BioMax MR film, Kodak)

overnight, which was then processed in an automated film-developing machine (Konica, Langenhagen, Germany).

2.4 Cell culture experiments

All cell culture reagents were purchased from PAA (Cölbe, Germany), Nunc (Fisher Scientific, Langenselbold, Germany) or BD Biosciences (Heidelberg, Germany), unless indicated otherwise. Cells were cultured in Dulbecco's modified Eagle's medium (DMEM) supplemented with 10 % (v/v) fetal calf serum (FCS), 2 mM glutamine and 0.1 mM (50 mg/mL) gentamicin. Cells were incubated at 37 °C in the presence of 8.5 % CO_2. All other experiments (transfection, immunofluorescence) were carried out at room temperature.

2.4.1 Cell lines

Human fibroblast cells were used for cell culture experiments. The cell line GM5756T, which represents transformed normal human fibroblasts, was provided by Stephen Gould (John Hopkins University, Baltimore). PEX3-deficient cells (ΔPEX3) were obtained from Barbara Paton (Women's and Children's Hospital, Adelaide; patient 1 in [141]), whereas the PEX19-deficient cells (ΔPEX19) were a gift by Ron Wanders (Academic Medical Centre, University of Amsterdam). Both cells have been transformed with large T-antigen of SV40 as described in [142] and are referred to as ΔPEX3T and ΔPEX19T fibroblasts, respectively.

2.4.2 Transfection of human fibroblasts

The uptake of plasmids in mammalian cells is known as transfection. There are different techniques for a transient transfection using electroporation, $Ca_3(PO_4)_2$ precipitation, or lipofection. In the latter technique, polyethyleneimine and DNA form positively charged particles, which interact with proteoglycans at the cell surface. These complexes enter the cell by endocytosis. The plasmid is then transferred to the nucleus, where protein expression is initiated. The cell density should range between 60-70 % for optimal transfection results. The ratio of plasmid DNA to transfection reagents and the incubation time should be optimized for every cell line.

In this thesis, human fibroblasts were transfected using the corresponding plasmid DNA (Table 3) and the transfection reagent jetPEI (PeqLab, Erlangen, Germany) according to the manufacturer's instructions. GM5756T and ΔPEX19T cells were seeded onto cover

slides 24 hours prior to transfection. ΔPEX3T cells were transfected in 25 cm² culture flasks. In each case, the jetPEI to plasmid ratio was 2 µL/1 µg with an incubation time of 3-4 hours.

2.4.3 Immunofluorescence microscopy

Proteins within a cell can be visualized with immunofluorescence using fluorescence-labeled antibodies against the target protein. Therefore, the cells have to be fixed on a surface with formaldehyde before cells are permeabilized with a detergent to allow the antibody to enter the interior of the cell. Indirect immunofluorescence uses a secondary antibody, which is directed against the primary antibody and is labeled with a fluorescent dye. The detection is carried out with a microscope, which excites the fluorescence label with a specific wavelength. The fluorescence itself can be extracted out of the entire spectrum by filters, which are permeable for a defined wavelength range.

Table 11: Antibodies and their dilutions in D-PBS used in immunofluorescence microscopy.

Primary antibody	Dilution
α-myc, mouse (Cell Signaling/NEB, Frankfurt a.M., Germany)	1:200
α-PEX13, rabbit (Marc Fransen, KU Leuven, Belgium)	1:250
α-PEX14, rabbit [143]	1:400
α-AFP, mouse (3E6) (QBiogene/MP Biomedicals, Illkirch, France)	1:400
α-PEX16, rabbit (JH290) (Stephen Gould, John Hopkins University, Baltimore)	1:100
α-PMP70, sheep (Stephen Gould, John Hopkins University, Baltimore)	1:100
α-catalase, sheep (The Binding Site, Schwetzingen, Germany)	1:100
Secondary antibodies	
AlexaFluor-488 (Molecular Probes/Invitrogen, Darmstadt, Germany)	1:300
AlexaFluor-596 (Molecular Probes/Invitrogen, Darmstadt, Germany)	1:200

After transient transfection, cells were subjected to immunofluorescence analysis one day (ΔPEX19T), two days (GM5757T), or seven days (ΔPEX3T) after transfection. Cells (density: ~60 %) on cover slides were washed three times with Dulbecco's PBS (D-PBS, Gibco/Invitrogen, Darmstadt, Germany) before they were fixed with formaldehyde (3 %

(v/v) in D-PBS) for 20 minutes. After permeabilization with Triton-X100 (1 % (v/v) in D-PBS) for 5 minutes, cells were again washed three times with D-PBS and incubated with 30 µL primary antibodies upside down on parafilm for 30 minutes. After washing for ten times with D-PBS, cells were incubated with 30 µL secondary antibodies upside down on parafilm for 10 minutes and washed again ten times with D-PBS. In the end, cells were embedded in mowiol (100 mg/ml; Callbiochem/Merck, Darmstadt, Germany) with n-propylgallate (2.5 mg/mL; Fluka/Sigma Aldrich, München, Germany) and dried overnight in the dark before cells were analyzed with a fluorescence microscope (Axiovert 200M; Zeiss, Jena, Germany). The antibodies used and their corresponding dilutions in D-PBS are listed in Table 11.

2.5 Protein crystallization

The vapor diffusion technique is the most widely used method to obtain protein crystals and can be performed in two experimental setups: the sitting drop or the hanging drop technique (Figure 2.1). In this method, a concentration difference between the reservoir and the protein solution is overcome by solvent diffusion through the gas phase.
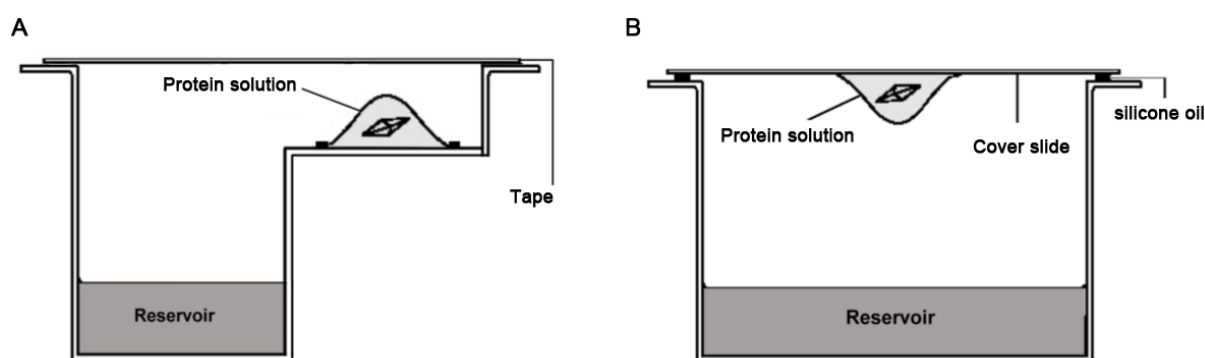
Figure 2.1: Schematic drawings of the sitting (A) and hanging drop (B) vapour diffusion techniques. Image modified from [144].

The solubility of the protein is decreased by organic compounds such as polyethylene glycols (PEGs) or inorganic compounds such as ammonium sulfate. With increasing protein concentration, the clear protein solution will reach a metastable region, where a nucleation seed initiates the growth of a protein crystal (Figure 2.2). This procedure is dependent on many factors including temperature, purity and concentration of the protein, concentration of precipitants, pH of buffers, and the presence of additives. As protein crystallization is an empiric process, all these different parameters have to be optimized to find suitable crystallization conditions.

Screening for initial crystallization conditions was carried out with a crystallization robot (Freedom Evo, Tecan, Switzerland) using the sitting drop technique. All crystallization screens were purchased from Hampton Research (Aliso Viejo, USA), Emerald Biosciences (Bainbridge Island, USA) or Qiagen (Hilden, Germany).
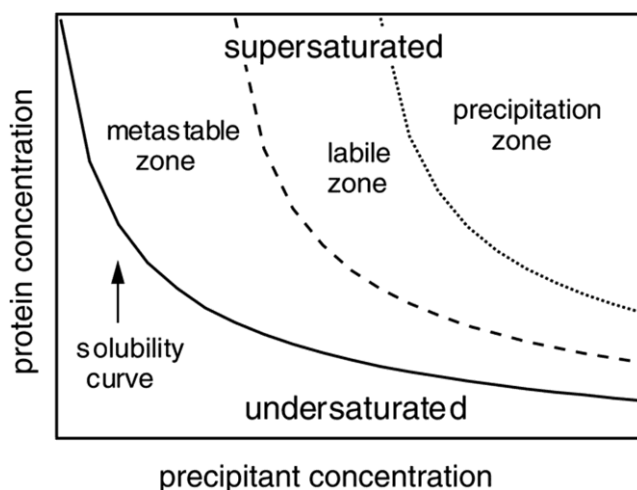
Figure 2.2: Phase diagram of a protein solution dependent on the protein and precipitant concentration. Image taken from [145].

Screening was carried out for nPEX3, nPEX3+PEX19, sPEX3 and sPEX3+PEX19[Pep] with all samples being present in SEC buffer. For nPEX3+PEX19, the proteins were purified separately, mixed in a molar 1:1 ratio and again applied to SEC. For sPEX3+PEX19[Pep], sPEX3 was purified and PEX19[Pep] was added in a molar 1:1 ratio before being cocrystallized without further purification. The screens tested, the protein concentrations and the incubation temperatures can be found in section 9.5. Initial crystals were only found for nPEX3 and sPEX3+PEX19[Pep] and were refined concerning the pH of the buffer, the concentration of protein, precipitants and salts using the hanging drop vapor diffusion method. The initial and refined conditions are listed in section 9.6. Crystallization plates were incubated at 4 or 20 °C and examined daily for the appearance of crystals. Crystals of nPEX3 were detected 10-14 days incubation time at 4 or 20 °C, whereas crystals of the sPEX3+PEX19[Pep]-complex appeared after 24 hours at 4 or 20 °C. Crystals were prepared for data collection by fishing with an appropriate loop and flash freezing in liquid nitrogen. In case of nPEX3, 25 % (v/v) glycerol was added as cryoprotectant. The crystals of sPEX3+PEX19[Pep] were frozen without any use of cryo protectant.

2.6 X-ray crystallography

This chapter was written with the help of the textbooks *Biomolecular Crystallography* [146] and *Outline of Crystallography for Biologists* [147].

2.6.1 X-ray sources and protein crystals

Protein crystallography is applied to produce a magnified image of a protein molecule. To achieve atomic resolution, an appropriate wavelength in the atomic range (1-2 Å) must be used for the diffraction experiment. These X-rays are electromagnetic waves, which have energies in the range of 6-12 kV and are able to ionize atoms. X-rays can be generated with metal anodes such as copper, chromium or molybdenum. Accelerated electrons hit the metal leading to gaps in the low-energy electron shell. These gaps are then filled with electrons of high-energy levels under emission of radiation. The radiation is focused and filtered to obtain suitable monochromatic radiation of a specific wavelength, *e.g.* CuKα: 1.54 Å. Much more intense X-ray sources are generated in synchrotron devices such as the SLS (Swiss Light Source; Villigen) or the BESSY (Berliner Elektronenspeicherringgesellschaft für Synchrotronstrahlung, Berlin). There, electrons are accelerated to a velocity near the speed of light in a vacuum. Strong electromagnetic fields keep the electrons moving circularly while radiation is emitted in a tangential direction. This X-ray beam can be easily adjusted to wavelengths between 0.5-2 Å, which is very useful for experimental phasing.

For structure determination with X-ray crystallography, single protein crystals of an appropriate size are required. Crystals are formed by a three dimensional repetition of a unit cell that is defined by the length of its axis (*a, b, c*) and the angles between these axis (α, β, γ). The unit cell can be further divided into smaller parts and the smallest volume that is able to generate the complete unit cell by symmetry elements, such as translation vectors or rotation axis, is called asymmetric unit (ASU). The entire symmetry of the crystalline lattice is represented with the space group, which includes information about the crystal system, the lattice centering and the crystallographic symmetry operators. In protein crystals, only 65 space groups can be found due to chirality of amino acids.

2.6.2 Diffraction

When X-ray radiation hits matter, for example a protein crystal, it is diffracted by interacting with the electrons of the protein molecules. The oscillating electrons emit X-ray radiation of the same frequency as the monochromatic incident beam.

Crystallographic structure determination is based on this coherent scattering. As the wavelength is similar to the atomic distances in the crystal (C-C bond: 1.5 Å), interference occurs. Constructive interference only emerges when the scattered waves have the same phases so that their amplitudes can accumulate. This process is dependent on the distribution of scatterers in a considered volume, which is the electron density. The sum of amplitudes can be measured by an X-ray detector and corresponds to the intensity of reflections on a diffraction image.

A simplified description for the diffraction of radiation by a lattice is provided by Bragg's law (Figure 2.3, [148]). Here, a model is used that devides the crystal into many parallel lattice planes. A reflection corresponds to an X-ray, which is diffracted by such a set of planes in the crystal lattice under a specific angle θ. The position of the planes within the unit cell is described by the reciprocal Miller indices (*hkl*) that represent the intersection of the lattice planes with the unit cell edges. According to Equation 3, positive interference of the diffracted X-rays is produced when the path difference *2dsinθ* is a multiple of the wavelength λ.

$$n\lambda = 2d_{hkl} \sin \theta_{hkl} \qquad (3)$$

n	integer
λ	wavelength
d	spacing between lattice planes
θ	glancing angle
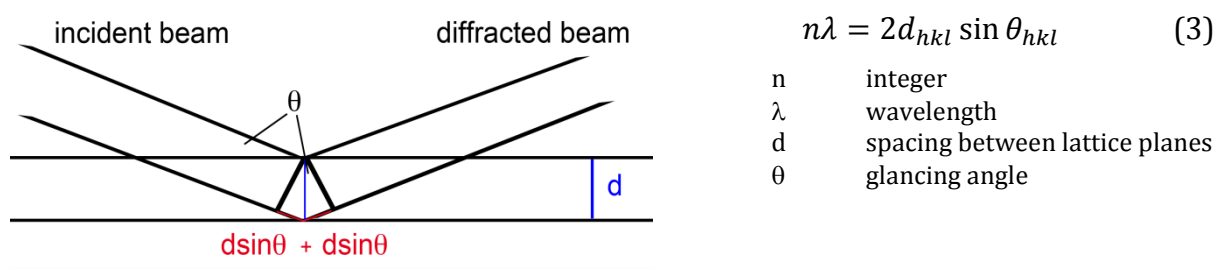
Figure 2.3: Geometric description of Bragg's law. Constructive interference occurs when the path difference $2d_{hkl} \cdot \sin\theta_{hkl}$ of two diffracted beams is a multiple of the wavelength λ.

The Ewald construction illustrates the connection between real lattice and reciprocal lattice and translates Bragg's law into three dimensions [149]. The Ewald sphere represents a sphere with a radius of *1/λ* and a crystal in the center (Figure 2.4). The origin O of the reciprocal lattice is the intersection between the incident beam and the surface of the Ewald sphere. Bragg's law is fulfilled when a reciprocal lattice point P*(hkl)* is located on the surface of the Ewald sphere and thus, a reflection occurs. In practice, the crystal is rotated along an axis perpendicular to the incident beam to cover more and more lattice points fulfilling Bragg's law. The reflections can be measured with an X-ray detector and result in the diffraction patterns. The symmetry of the produced diffraction

image is related to the symmetry of the crystal lattice and thus leads to the determination of the geometric parameters of the unit cell.
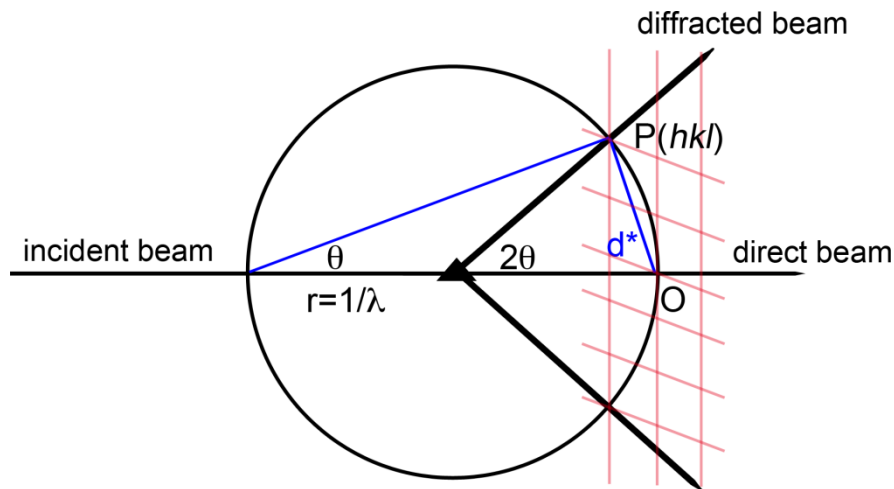
Figure 2.4: The Ewald sphere. Two dimensional representation of the Ewald sphere of reflection. Constructive interference occurs if a lattice point P(hkl) is located on the surface of the sphere. θ: glancing angle, λ: wavelength, d*: reciprocal spacing between lattices 1/d, O: origin.

2.6.3 Data processing

Information about the amplitudes and the phases of the scattered X-rays has to be extracted from the diffraction data. The amplitude is proportional to the intensity of the reflections on the detector (see below), whereas additional experiments need to be done to identify the phases. However, several initial parameters of a unit cell can be calculated just based on the diffraction patterns without any phase information. After collecting diffraction data, the initial steps in data processing are indexing, integration and scaling. Indexing uses the distances and angles of the reflection spots together with experimental parameters (origin of the image, detector distance, wavelength) to determine the parameters of the unit cell. Then, the spots are integrated in order to obtain intensities for each diffraction point. During scaling, the intensities of only partially recorded reflections are adjusted and symmetry related reflections are merged [150]. In addition, scaling is done to adjust the intensity levels of diffraction data recorded at different time points, which might differ due to radiation damage or fluctuations in the X-ray beam. In the end, a list of all unique reflections including their coordinates (hkl), their intensities and the corresponding signal to noise ratio (I/σI) is generated. Moreover, statistics are calculated to estimate the quality for the entire data set as well as for several resolution bins.

There are several reliability factors (R-factors) that indicate the quality of a data set. R-factors use the ratio of mean differences between values, which should be the same and mean magnitude of measured values to determine a value for accuracy. The linear merging R-value, R_{merge}, is defined in Equation 4.

$$R_{merge} = \left. \sum_{hkl} \sum_{i=1}^{N} |I_{hkl}^{i} - \bar{I}_{hkl}| \middle/ \sum_{hkl} \sum_{i=1}^{N} I_{hkl}^{i} \right. \tag{4}$$

I_{hkl}^{i} is the intensity of a redundant reflection (*hkl*), $\bar{I}_{hkl}$ is the mean intensity of a measured reflection. The summation is done over N redundant reflections and is thus dependent on redundancy. If a reflection is measured many times the value of the linear R_{merge} increases. To introduce a redundancy independent merging R-factor, the R_{meas} is defined [151], which weighs every reflection with a function of its multiplicity (Eq. 5).

$$R_{meas=} \left. \sum_{hkl} (\frac{N}{N-1})^{\frac{1}{2}} \sum_{i=1}^{N} |I_{hkl}^{i} - \bar{I}_{hkl}| \middle/ \sum_{hkl} \sum_{i=1}^{N} I_{hkl}^{i} \right. \tag{5}$$

An acceptable data set has an overall R_{meas} below 10% and an R_{meas} in the range of 50 % in the highest resolution bin. Furthermore, the signal to noise ratio of the measured intensities gives a cut-off value for the resolution limit. It is defined as the ratio of the mean intensity and the mean standard deviation of the measurements. A reasonable value for $I/\sigma(I)$, where a spot can be clearly distinguished from the background, is around 2. However, the reflection intensities decrease with higher resolution. This can be displayed by plotting the mean intensity against the resolution expressed as $(sin\theta/\lambda)^2$ [152]. The resulting characteristic curve is called Wilson plot, which approximates linearity in regions below 3.5 Å. The Wilson B-factor can be calculated from the linear slope and describes the decrease of diffraction intensities due to thermal vibration of atoms or atomic disorders in the crystalline lattice. In addition, the data should be as complete as possible. The map will become noisy if only 50-60% of the data is used in the highest resolution bin. Taken together, a set of parameters (R_{merge}, R_{meas}, $I/\sigma(I)$, completeness) indicates the quality of a data set.

2.6.4 Matthews parameter

The solvent content of protein crystals usually ranges between 30 to 70 %. Therefore, the number of molecules in the asymmetric unit can be estimated although the crystal structure is not known [153]. The packaging parameter V_M (Matthews parameter) can

be calculated if the geometric parameters of the unit cell are known (Eq. 6). The value of V_M usually lies in the range of 1.7 – 3.5 $Å^3$/Da with a mean around 2.5 $Å^3$/Da and a solvent percentage of 50 %.

$$V_M = V/_{M_r\, z\, n} \qquad (6)$$

V	volume of the unit cell ($Å^3$)
M_r	molecular mass (Da)
z	number of ASU in the unit cell
n	number of molecules in the ASU

2.6.5 Twinning

Defects and imperfections in growth lead to a protein crystal that is not a perfect entity but is built up by different subcrystals. The orientations of the domains to each other are related by twinning operations towards a defined crystallographic axis. Normally, twinned crystals look like perfect single crystals. Epitaxial twinning can be recognized in the diffraction pattern as it exhibits spots of two different interpenetrating lattices. In case of merohedral twinning, the reflections of the distinct crystal domains exactly overlap resulting in an unsuspicious diffraction pattern. The diffraction pattern looks more symmetric and leads to space group determinations with apparent higher symmetry. In fact, the measured reflections correspond to the sum of two individual intensities, which are weighted by the twinning fraction α (Eq. 7).

$$I_{obs} = \alpha I_1 + (1 - \alpha)I_2 \qquad (7)$$

The individual contributions to the measured intensities can often be determined with computational programs. However, if the twinning fraction α is 0.5, a perfect twin occurs and it is more challenging to separate the measured intensities. The entire data set must be examined for irregularities in intensity distribution. The H-test examines the ratio of $<I^2>/<I>^2$ which is 1.5 for perfectly twinned data and 2.0 for untwinned data [154]. The twinning fraction α is determined by comparison of the actually observed data with the statistical distribution.

2.6.6 Structure determination

Every reflection can be described with a structure factor F_{hkl}. F_{hkl} is a complex number, expressed by a vector representing the diffracted X-rays with the length of the vector corresponding to the amplitude ($|F_{hkl}|$) and the angle of the vector corresponding to the phase (φ_{hkl}) (Eq. 8). The structure factor itself is a summation over all scattering atoms

in the unit cell. If the atomic scattering factor f_j and the atomic coordinates x, y, z are known, the structure factor of the scattered beam can be calculated for each reflection (Eq. 9). Thus, each atom in the unit cell contributes to the structure factor of each single reflection.

$$F_{hkl} = |F_{hkl}|(\cos\varphi_{hkl} + i\sin\varphi_{hkl}) = |F_{hkl}|e^{i\varphi_{hkl}} \tag{8}$$

$$F_{hkl} = \sum_{j=1}^{N} f_j e^{2\pi i(hx_j + ky_j + lz_j)} = |F_{hkl}|e^{i\varphi_{hkl}} \tag{9}$$

The structure factor amplitudes $|F_{hkl}|$ can be directly extracted from the diffraction data, as $|F_{hkl}|$ is proportional to the square root of the measured reflection intensity I_{hkl} (Eq. 10). However, reflections do not contain any phase information. This circumstance is known as the phase problem. Therefore, different experiments must be done to determine the phases (see chapter 2.6.7).

$$I_{hkl} \sim F_{hkl}^2 = |F_{hkl}^2| \tag{10}$$

Equation 8 is a mathematical description for transforming information of real space into reciprocal space. This Fourier transformation connects the amplitudes and phases of the scattered beams (reciprocal space) to the distribution of scattering atoms in the unit cell (real space). In contrast, an inverse Fourier transformation can be applied to obtain information about the electron density $\rho(xyz)$ in the unit cell if structure factors are known (Eq. 11).

$$\varrho(xyz) = \frac{1}{V}\sum F_{hkl}\ e^{-2\pi i(hx+ky+lz)} = \frac{1}{V}\sum |F_{hkl}|\ e^{-2\pi\varphi_{hkl}(hx+ky+lz)} \tag{11}$$

2.6.7 Phasing and molecular replacement

A native data set of a diffraction experiment only contains information about the amplitudes of the diffracted X-rays, and not about their phases. However, for electron density calculation (Eq. 11), knowledge about phases is essential. There are two possibilities in protein crystallography to gain phase information. Experimental phasing is used for *de novo* phase determination in an individual experiment. Therefore, a marker atom substructure must be generated within the crystal. This can be done by soaking heavy atoms into the native crystal or by using scatterers such as Se-methionine or sulfur, which can be already incorporated in the protein. Ideally, this derivative crystal is isomorphous to the native crystal, that means, the geometric parameters of the

crystal are conserved. The introduction of marker atoms leads to electronic differences between the native crystal and its derivative. The diffraction data of the native and the derivative crystals and the localization of the marker atoms lead to phase determination of the native and the derivative crystals. However, the solutions are ambiguous and additional derivatives are needed to define the correct phases.

In contrast to experimental phasing, the method of molecular replacement uses a known structurally similar model for determining starting phases. Usually, this search model must exhibit at least 30 % sequence identity with the unknown protein structure [155]. For molecular replacement, the correct position of the molecule in the crystals has to be identified. The known structure is moved within the asymmetric unit until the calculated diffraction data from the search model and the experimental diffraction data from the unknown protein coincide. The process is split into a 3D-translational and a 3D-rotational Patterson search [156]. The Patterson function is an autocorrelation of the electron density and is the product of the structure factor amplitude F_{hkl} with its conjugate complex $F_{hkl}{}^{*}$, with the same amplitude but the negative phase $-\varphi_{hkl}$. According to Equation 12, the product yields a real number, which is the square of the amplitude. As $F_{hkl}{}^{2}$ is used as Fourier coefficients to generate the Patterson map, no phases are needed for this purpose.

$$F_{hkl} \, F_{hkl}^{*} = \left| F_{hkl} \right| e^{i\varphi_{hkl}} \cdot \left| F_{hkl} \right| e^{-i\varphi_{hkl}} = \left| F_{hkl} \right|^{2} e^{(i\varphi_{hkl} - i\varphi_{hkl})} = \left| F_{hkl} \right|^{2} \quad (12)$$

The Patterson space unit cell is populated with $N(N-1)$ peaks corresponding to interatomic distance vectors between N different atoms. The map exhibits specific distances in the low resolution range (10 – 4 Å) representing intramolecular vectors that are characteristic for the relative locations of secondary structure elements. In proteins with the same fold, these distances should be similar and their distribution only depends on the orientation of the molecule. This is the basis for Patterson rotation searches. The map of the search model is calculated only with intramolecular vectors. This map is then rotated and the fit between calculated and observed Patterson maps is calculated after each increment and expressed as a correlation coefficient. Once the relative orientation of the molecule is found, its actual position within the unit cell is determined with a Patterson translation search. The procedure is the same as described for rotation searches, this time using intermolecular Patterson vectors as characteristic for correctly oriented molecules in the unit cell.

2.6.8 Structure refinement

Once starting phases are obtained and an initial map is generated, the structure must be improved and refined. Again, better phases are calculated from the new model, which in turn leads to more interpretable electron density. This iterative procedure requires computational programs as well as manual model building to adjust the model to the experimental data. The model improvement can be monitored with crystallographic R-factors. The R-factor describes the difference between calculated and observed structure factor amplitudes (Eq. 13).

$$R = \frac{\sum_{hkl} \left| |F_{obs}| - |F_{calc}| \right|}{\sum_{hkl} |F_{obs}|} \tag{13}$$

During refinement, the R-value should converge. However, overrefinement is usually a problem, when the R-factor still decreases without any gain in model improvement. Therefore, 2-10 % of randomly selected reflections are excluded from the refinement process to calculate an autonomous R-value. This R_{free} is unbiased and used to perform a cross-validation of the model to estimate the model improvement [157, 158]. The difference between the R- and the R_{free}- values should not exceed 5 %, as this might be an indication for overfitting.

The general parameters describing the model are the atomic coordinates (*xyz*) and the atomic *B-factor* (atomic displacement parameter, Eq. 14). The B-factor describes the positional displacement of scattering atoms due to thermal motion. The value of the B-factor is often limited because of covalent bonds, which provide more rigidity to the neighboring atoms. Therefore, backbone atoms exhibit lower B-factors than solvent exposed, long amino acid side chains. Isotropic B-factor refinement uses only one parameter according to the same atomic motion in every direction. Anisotropic refinement correlates different atomic movements with different directions, leading to a more complex calculation for individual B-factors.

$$B = 8\pi^2 <u>^2 \tag{14}$$

<u>: mean displacement of a vibrating atom

Stereochemical restraints such as bond lengths, bond angles, torsion angles, planarity or non-bonded interactions limit the geometric orientation of the peptide backbone as well as the amino acid side chains to find the best fit between experimental data and the computed model.

2.6.9 Experimental procedures

2.6.9.1 Data collection

In this work, synchrotron experiments were carried out at beamline BL14.1 at BESSY. Crystals of nPEX3 were exposed to the X-ray beam (λ = 0.91841 Å) for 2 sec at a detector distance of 330 mm. The crystal was rotated in 1 ° steps for 120 °. In total, four data sets were collected with the resolution limit in the range of 4.0-3.3 Å. Crystals of sPEX3+PEX19[Pep] were exposed to radiation with a wavelength of 1.00001 Å at a detector distance of 215 mm for 1.5 sec and rotated in 1 ° steps for 180 °. In total three native data sets were collected and the best crystal diffracted to 2.4 Å.

2.6.9.2 Data processing and molecular replacement

Indexing, integrating and scaling, was carried out using the program XDS [159]. For sPEX3+PEX19[Pep], molecular replacement was carried out with the program *Phaser* [160] implemented in the *CCP4* suite [161]. The solutions of the molecular replacement search are evaluated with maximum likelihood methods. The likelihood is the probability that a value is actually observed under the assumption of a given model. The log likelihood gain (LLG) distinguishes a solution from the average of solutions and results in an increasing *Z-score* ("signal to noise ratio"). Translational Z-scores of 6-8 indicate a probable a correct solution, whereas the rotational Z-scores do not exhibit large differences among the solutions.

2.6.9.3 Model building and refinement

The model of sPEX3+PEX19[Pep] was built manually with the software *Coot* [162] and refinement was done with the program *REFMAC5* [163] implemented in *CCP4* [161]. The refined model was used to calculate more accurate phases and in turn an improved electron density map. In addition, geometric parameters were validated in *Coot* or *REFMAC5*. Anisotropic B-factor refinement was done using TLS analysis (translation, libration, screw) [164], where entire protein domains are defined as rigid bodies that are refined with correlated vibrational movement. TLS groups of sPEX3+PEX19[Pep] were separated with the help of the TLS server [165] and were analyzed using *TLSANL* [166] within *CCP4*. To minimize model bias, a simulated annealing omit map was generated in Phenix [167, 168]. Here, part of the structure is removed before the rest of the structure is treated with simulated annealing, where the structure is heated up and slowly cooled down to reach the lowest energy state. In this thesis, the PEX19-derived peptide was

omitted from the complex structure. Then, simulated annealing was performed with the rest of the structure and refinement was carried out before a new unbiased electron density map was calculated.

3 RESULTS

The human peroxins PEX3 and PEX19 are involved in the early steps of peroxisomal biogenesis and the import of PMPs. PEX3 is anchored in the peroxisome membrane with its first 33 amino acids. The rest of the protein protrudes out in the cytosol and mediates the interaction with the N-terminus of PEX19, the cytosolic receptor for newly synthesized PMPs. After insertion of the PMP into the lipid bilayer, PEX19 is recycled back to the cytosol to start another round of protein import.

In order to elucidate the parameters underlying the PEX3-PEX19 interaction, structural and functional studies were undertaken. In the first part of this work, different constructs of PEX3 and full-length PEX19 were expressed in *E. coli* and purified to homogeneity. Purification and characterization of the recombinantly expressed proteins is described, including an initial analysis of the PEX3-PEX19 complex. To obtain structural information, the PEX3 variants were subjected to crystallization alone and in the presence of full-length PEX19 or a synthesized PEX19-derived peptide. The second part focuses on the crystal structure of a truncated version of PEX3 in complex with a PEX19-derived peptide. Furthermore, the molar ratio and the affinity of the PEX3-PEX19 complex were characterized by biochemical experiments. Based on conservation analysis, several mutations were introduced on the surface of PEX3. The third part addresses the role of these mutations in PEX19-binding and in peroxisome biogenesis by applying *in vitro* and *in vivo* studies.

3.1 Purification of PEX3 and PEX19

3.1.1 Purification of nPEX3

The nPEX3 protein comprising residues 26-373 of human PEX3 and a cysteine to serine exchange at position 235 was expressed in *E. coli* Rosetta2 cells. The expression system is based on the plasmid pET32a, resulting in nPEX3 N-terminally fused to thioredoxin followed by a hexahistidine tag that is cleavable with TEV protease. The purification protocol was established previously [129, 144] and comprised the following steps: 1. affinity chromatography using a nickel column, 2. TEV protease cleavage, 3. a second Ni^{2+} affinity chromatography step and 4. size exclusion chromatography (SEC). A single purification yielded 3-4 mg pure nPEX3 protein from 1 L bacterial culture.

A

B

C
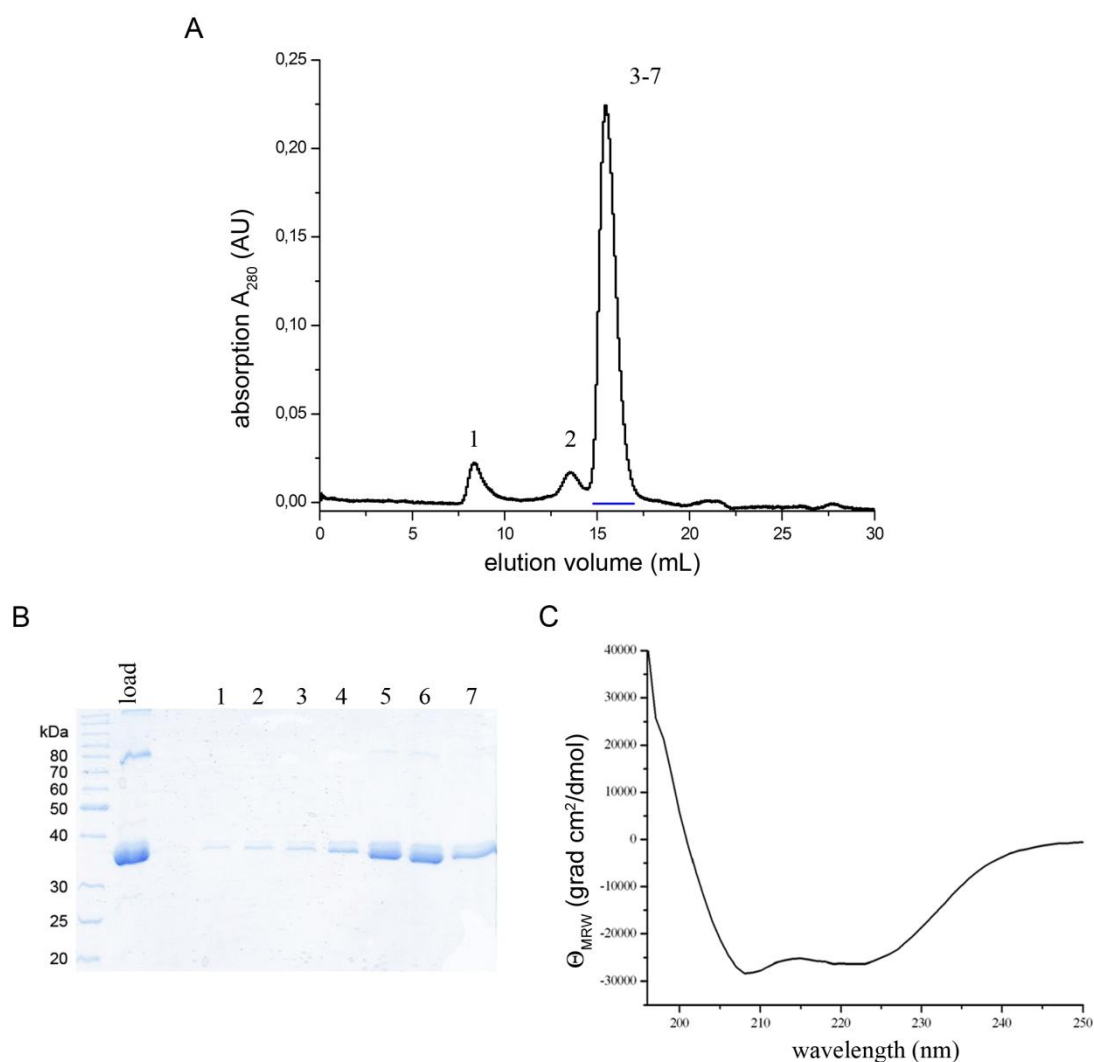
Figure 3.1: Purification and CD spectrum of nPEX3. (A) Elution profile of a preparative SEC of 3 mg protein in SEC buffer shows one major peak at 15.4 mL corresponding to a molecular mass of 52 kDa. The fractions marked with a blue bar were used for further analysis and crystallization attempts. (B) 15 µl samples were subjected to SDS-PAGE analysis. The band below the 40 kDa marker band represents nPEX3, which appears as a slight double band. The faint band at 80 kDa corresponds to a dimer of nPEX3. (C) CD spectrum of folded nPEX3 (10 µM in CD buffer) reveals characteristic α-helical properties with two minima of ellipticity at 208 and 220 nm.

SEC results in one major peak at 15.4 mL, corresponding to an apparent molecular mass of 52 kDa (Figure 3.1 A). The molecular mass of nPEX3 was calculated with the online tool *ProtParam* [139, 140] to be 39.3 kDa. As proteins might adopt a non-globular form in solution, the elution volume can sometimes correspond to a higher molecular mass than that determined based on the amino acid sequence. Thus, nPEX3 is a monomer in solution. Additionally, two minor peaks are detected in the chromatogram, which correspond to the void volume (peak 1) and the dimer of nPEX3. SDS-PAGE analysis shows pure protein with a band slightly below the 40 kDa marker (Figure 3.1 B). The faint band at 80 kDa corresponds to protein dimer formation that was previously verified by N-terminal sequencing [129] and which is likely due to an artefact in SDS-

PAGE. The CD spectrum of nPEX3 exhibits clear α-helical features, including the characteristic two minima of ellipticity at 208 and 220 nm (Figure 3.1 C).

3.1.2 Purification of PEX19

Full-length human PEX19 fused to an N-terminal hexahistidine tag followed by a TEV protease cleavage site was expressed in *E. coli* BL21(DE3) cells. The expression system uses the plasmid pColdI, in which protein expression is inducible by addition of IPTG and/or by reduced temperature. The purification protocol was established by N. Treiber [129] and consists of the following steps: 1. affinity chromatography using a nickel column, 2. TEV protease cleavage, 3. a second Ni^{2+} affinity chromatography step to remove uncleaved protein and His_6-tagged TEV protease, 4. SEC. A single purification yielded 10 mg pure PEX19 protein from 1 L bacterial culture.
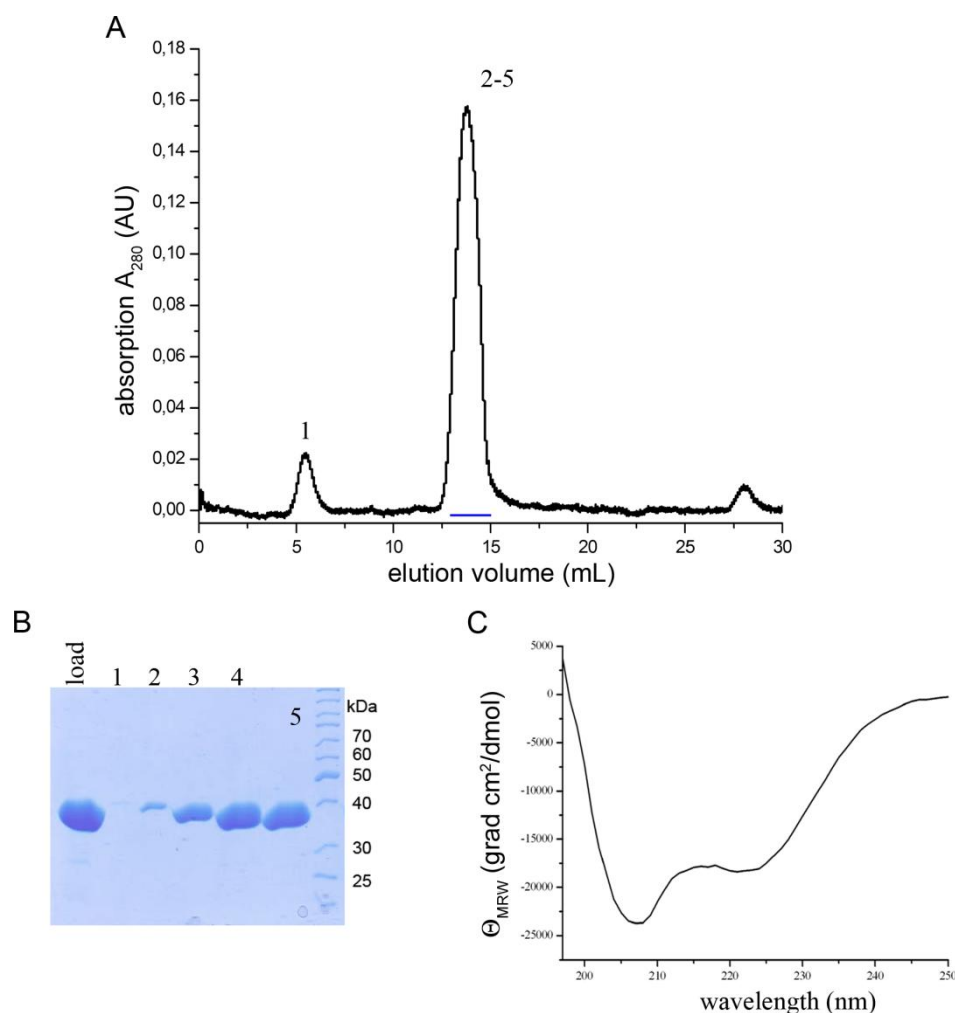

Figure 3.2: Purification and CD spectrum of PEX19. (A) Elution profile of a preparative SEC of 5 mg protein using SEC buffer reveals one major peak at 13.8 mL, corresponding to a molecular mass of 112 kDa. The fractions marked with a blue bar were used for further analysis and crystallization attempts. (B) 15 µl samples were subjected to SDS-PAGE analysis, which shows pure protein slightly below the 40 kDa marker band. (C) CD spectrum of PEX19 (10 µM in CD buffer) reveals folded protein with α-helical features.

Two peaks are observed in SEC with the first one corresponding to the void volume of the column (peak 1). The main peak in SEC elutes at 13.8 mL, which corresponds to a molecular mass of 112 kDa (Figure 3.2 A). The molecular mass of PEX19 calculated on the primary structure with the program *ProtParam* [139, 140] is 32.8 kDa. As a similar version of PEX19 was shown to be monomeric in solution by analytical ultracentrifugation [123], the difference in calculated molecular mass and experimentally determined molecular mass is probably due to the highly extended conformation of the N-terminal domain of PEX19 [118]. PEX19 migrates with the 40 kDa marker band on SDS-PAGE (Figure 3.2 B). The pure protein was shown to be folded using CD spectroscopy, and it exhibits α-helical features with two minima of ellipticity at 208 and 220 nm (Figure 3.2 C).

3.1.3 Molar ratio of the PEX3-PEX19 complex

Pure nPEX3 and PEX19 were used to determine the stoichiometry of the PEX3-PEX19 complex by mixing different molar ratios of of the two proteins followed by analytical SEC experiments. The individual nPEX3 and PEX19 proteins elute at 1.59 and 1.43 mL, respectively, on an analytical SEC column.
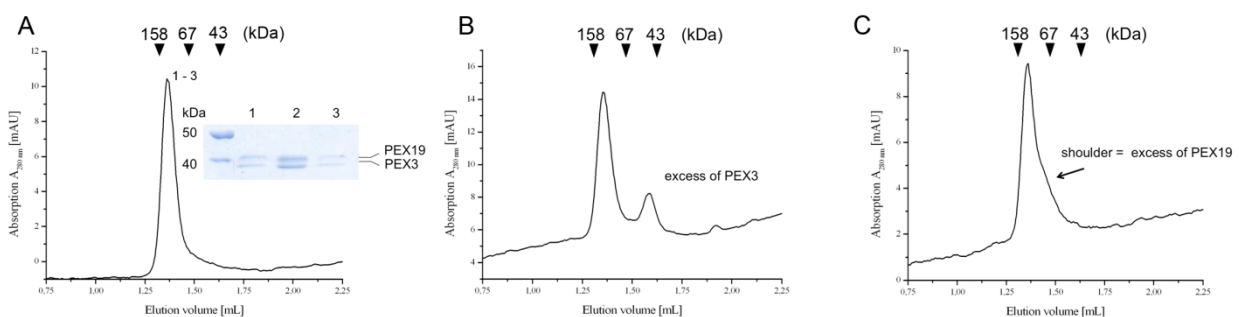
Figure 3.3: Analytical SEC runs of PEX3-PEX19 complex formation. nPEX3 and PEX19 were used at 25 µM; 50 µL of protein mixture were separated on analytical scale in SEC-buffer. (A) nPEX3 and PEX19 mixed at a molar ratio of 1:1 result in a single peak that corresponds to the PEX3-PEX19 complex. The corresponding SDS-PAGE is shown on the right. (B) nPEX3 and PEX19 mixed at a molar ratio of 2:1 result in two distinct peaks, which represent the PEX3-PEX19 complex and excess of unbound PEX3. (C) nPEX3 and PEX19 mixed at a molar ratio of 1:2 result in one peak that tails towards lower molecular masses.

The corresponding molecular masses refer to 44.4 kDa for nPEX3 and 95.2 kDa for PEX19. For the equimolar mixture, a single peak at 1.36 mL is observed, indicating a shift to a higher molecular mass of 132.9 kDa (Figure 3.3 A). This fits well with the sum of the molecular masses of the individual proteins, indicating a 1:1 complex formation. If nPEX3 is added in 2-fold excess, two peaks are observed. These correspond to a 1:1

complex (1.36 mL) and remaining unbound nPEX3 (1.59 mL; Figure 3.3 B). Excess of PEX19 results in one peak at 1.36 mL, which exhibits a slight tailing towards lower molecular masses (Figure 3.3 C). This shoulder likely corresponds to residual unbound PEX19, which cannot be completely separated from the PEX3-PEX19 complex on the SEC column used here.

In addition, the protein mixtures of different molar ratios were separated with native PAGE followed by western blotting analysis (Figure 3.4). The α-PEX3 antibody detects nPEX3 (left panel, lane 5) as a broad smear on the film. This is probably due to the pI of the protein (6.3), which is close to the pH of the stacking gel. Therefore, nPEX3 is only slightly negatively charged and needs longer to reach the separating gel with a pH of 8.8. However, the band corresponding to the nPEX3-PEX19 complex (*) appears as a distinct band, which is also detected by antibodies against PEX19 (right panel). The band corresponding to the nPEX3-PEX19 complex (*) is shifted towards higher molecular masses compared to PEX19. The bands of the individual proteins nPEX3 and PEX19 almost disappear if both proteins are present at equimolar ratio (lane 3) indicating a 1:1 complex formation.
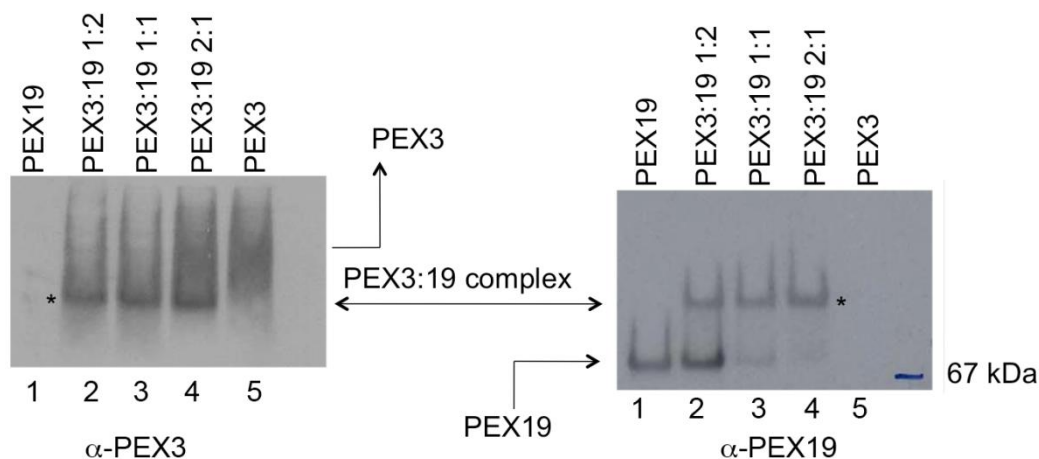
Figure 3.4: Western blot analysis of PEX3-PEX19 complex formation. nPEX3 and PEX19 were present at a concentration of 10 μM. 15 μL of protein mixtures in different molar ratios were separated by native PAGE and analyzed with western blotting using antibodies against PEX3 (left panel) and PEX19 (right panel). The PEX3-PEX19 complex (*) is detected by both antibodies and indicates a molar 1:1 ratio between PEX3 and PEX19.

For crystallization attempts, nPEX3 and PEX19 were purified separately (section 3.1.1 and 3.1.2) and mixed in a 1:1 molar ratio. The protein mixture was then subjected to SEC resulting in a single peak at 12.9 mL (Figure 3.5). This corresponds to a molecular mass of 171 kDa and fits with the sum of the individual molecular masses of nPEX3 (52 kDa)

48

and PEX19 (112 kDa) in SEC experiments. The fractions containing pure protein complex were concentrated to 5 mg/mL in SEC buffer and screened for initial crystallization conditions at 4 and 20 °C. However, initial protein crystals of the complex could never be obtained in any of the utilized screens.
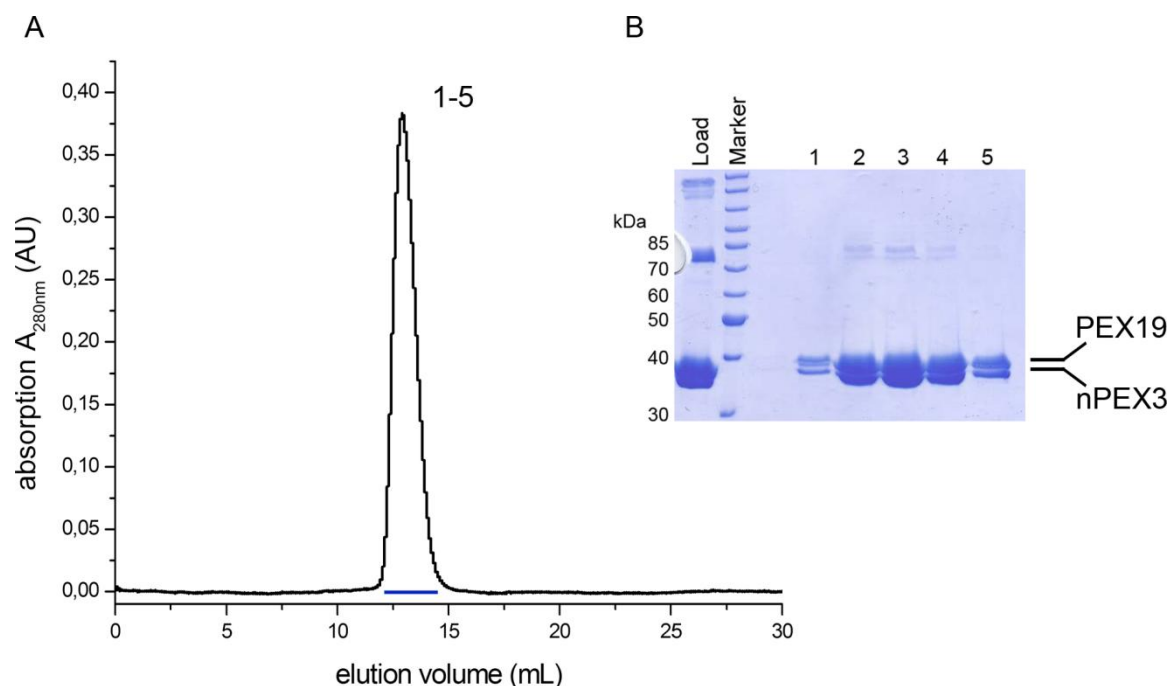
Figure 3.5: SEC of nPEX3+PEX19. (A) Elution profile of a preparative SEC of 4 mg protein using SEC-buffer reveals one major peak at 12.9 mL, corresponding to a molecular mass of 171 kDa. The fractions marked with a blue bar were used for crystallization. (B) 15 µl samples were loaded on the SDS-PAGE, which shows two protein bands slightly below the 40 kDa marker band. The upper band corresponds to PEX19, the lower one corresponds to nPEX3.

3.2 Crystallization of nPEX3

The purified nPEX3 solution obtained after SEC (Figure 3.1) was concentrated and used to screen for new crystallization conditions at two different concentrations of 3 and 4 mg/mL in SEC buffer. In total, six initial conditions could be identified (see section 9.5). The conditions were refined concerning the pH, the precipitant concentration and the protein concentration (see section 9.6). For crystal refinement, the hanging drop vapour diffusion method was used by mixing 1 µL of nPEX3 solution with 1 µL of reservoir solution. Only in two of the initial conditions (pHClearI_27 and pHClearI_34), crystal refinement was successful, leading to crystals of 100-200 µm in length (Figure 3.6). The crystals appeared after 10-14 days at 4 or 20 °C and were flash frozen in liquid nitrogen using 25 % glycerol as cryo protectant for data collection.
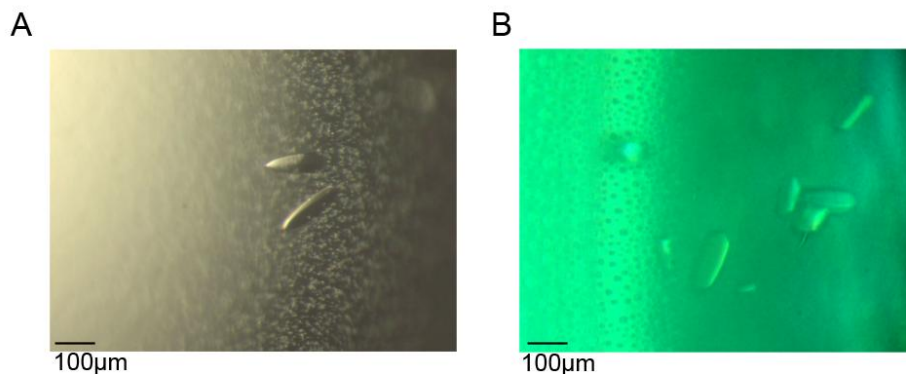
Figure 3.6: Refined nPEX3 crystals. nPEX3 was crystallized at a concentration of 3.1 mg/mL in SEC-buffer. (A) Crystals grown in refined condition of pHClear_27 (0.1 M MES, pH 6.2, 4 % PEG 6000) at 20 °C. (B) Crystals grown in refined condition of pHClear_34 (0.1 M HEPES, pH 6.5, 7 % PEG 6000) at 4 °C.

Several nPEX3 crystals were tested at the beamline BL14.1 at BESSY. Four native datasets in the resolution range of 4-3.3 Å were collected. Indexing, integrating and scaling, was carried out using the program XDS [159]. The crystals belong to hexagonal symmetry (a=b=258.1 Å, c=98.1 Å; $\alpha=\beta=90°$, $\gamma=120°$), but the correct space group could not be identified definitely. The best data set was processed and scaled in all possible space groups, which resulted in similar statistics and an overall R_{meas} of 16 % and 65 % in the highest resolution bin. All datasets show a high twinning factor of 0.45. The crystal form, the ambiguous space group determination and the high twinning factors are similar to previous results, which has led to an unrefined model of nPEX3 [129]. Therefore, new PEX3 constructs were designed in order to obtain non-twinned crystals.

3.3 Purification of sPEX3

As nPEX3 produced highly twinned crystals, new PEX3 constructs were designed to generate alternate crystal packing. The unrefined model of nPEX3 revealed that the crystal contacts involve the N-terminal α-helix [129]. Thus, the N-terminus of PEX3 was further truncated. The resulting PCR product was cloned into the *Nco*I, *Sal*I sites of the plasmid pET32a. The new construct comprises residue 41-373 of human PEX3, retains the cysteine to serine mutation at position 235 and is referred to as sPEX3.

The expression and purification procedure was the same as described for nPEX3 (section 3.1.1). A single purification yielded 4-5 mg pure sPEX3 from 1 L bacterial culture. SEC results in a major peak at an elution volume of 15.6 mL (Figure 3.7 A). This corresponds to an apparent molecular mass of 48 kDa and indicates monomeric sPEX3

in solution (calculated molecular mass: 37.5 kDa). The two minor peaks correspond to the void volume (peak 1) and sPEX3 dimer (peak 2). The corresponding SDS-PAGE analysis shows pure sPEX3 (Figure 3.7 B). As for nPEX3, a dimer band of sPEX3 can be observed, which is attributed to an artefact occurring in SDS gels.
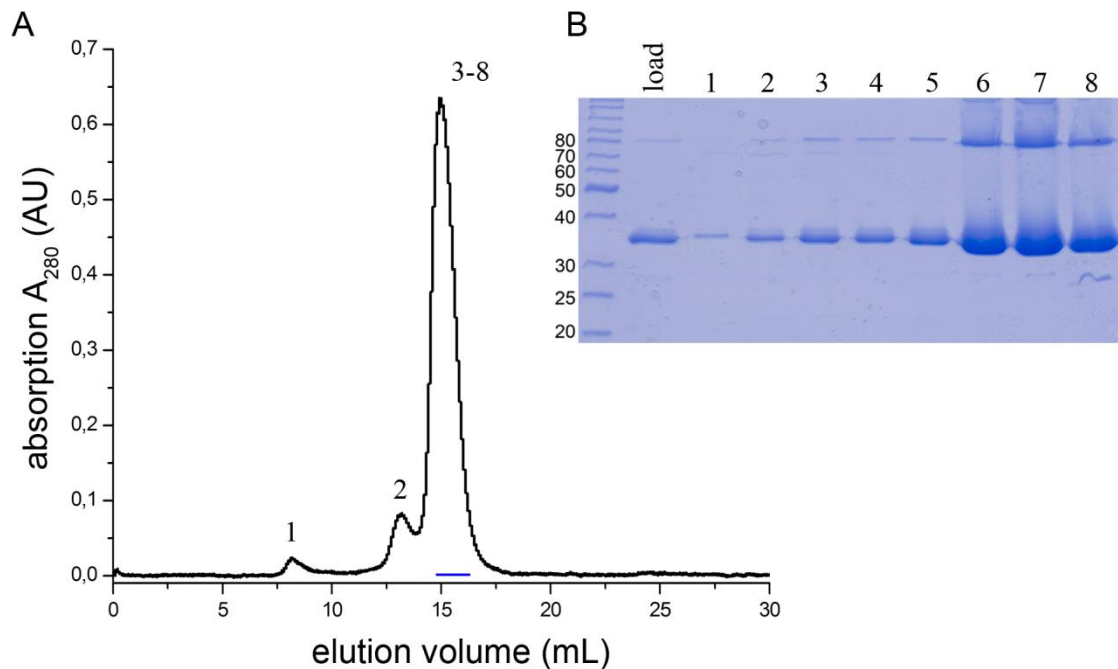
Figure 3.7: Purification and SDS-PAGE analysis of sPEX3. (A) Preparative SEC of 6 mg protein using SEC buffer results in one major peak at 15.6 mL corresponding to a molecular mass of 48 kDa. The fractions marked with a blue bar were used for further analysis and crystallization attempts. (B) 15 µl samples of the SEC were subjected to SDS-PAGE analysis. Pure sPEX3 can be detected with a monomer band below the 40 kDa marker and a dimer band at the 80 kDa marker.

3.4 Crystallization of sPEX3+PEX19^{Pep}

The homogenous sPEX3 solution was concentrated to 2.6 mg/mL in SEC buffer and subjected to initial crystallization experiments with the screens listed in section 9.5. In parallel, structural information about the PEX3-PEX19 complex was tried to obtain by crystallizing the protein complex. Crystallization attempts did not lead to initial crystals for nPEX3 in complex with full-length PEX19 (section 3.1.3), which might be due to the highly flexible N-terminal domain of PEX19 [118] that prevents successful crystallization. Therefore, sPEX3 was cocrystallized only with a fragment of PEX19, which was predicted to be α-helical [65]. The PEX19 peptide spans residues 14-33 (PEX19^{Pep}) and lies within the PEX3-binding region of the first 56 amino acid residues of PEX19 [65, 70, 76]. For initial screening, pure sPEX3 was concentrated to 2.8 mg/mL in

SEC buffer and mixed with the synthesized PEX19-derived peptide in a 1:1 molar ratio. The screens used are listed in section 9.5.

sPEX3 alone did not lead to any initial crystals. However, crystals of sPEX3+PEX19[Pep] are detected within 24 hours at 20 °C in five initial conditions that were refined by varying the pH of the buffers and the precipitant concentration (see section 9.6). The hanging drop vapour diffusion technique was used for set up refined crystals. sPEX3 was present at a concentration of 2.5 mg/mL and was mixed with the equimolar amount of the PEX19-derived peptide. Crystals appeared after 24 hours at 4 and 20 °C in four refined conditions. As an example, refined crystals of the initial condition JCSG_92 (0.1 M Bis-Tris, pH 5.5, 25 % (w/v) PEG 3350, 0.2 M NaCl) are shown in Figure 3.8.
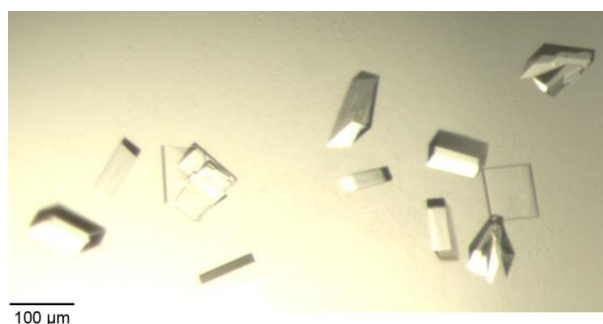
Figure 3.8: Refined crystals of sPEX3+PEX19Pep. sPEX3 was present at a concentration of 2.5 mg/ml in SEC buffer and was mixed at a molar 1:1 ratio with PEX19[Pep]. Crystals grew in 0.1 M Bis-Tris (pH 5.6), 24 % (w/v) PEG 3350, 0.2 M NaCl and appeared after 24 hours at 20 °C.

In total, 20 crystals from all refined conditions were flash frozen in liquid nitrogen without any cryo protectant and were tested at the BESSY. Three native data sets of three different crystals were collected, which diffracted around 2.6 Å. The space group was determined as P2$_1$ for all three crystals. Data was cut at $I/\sigma I$ of 3.0 and data statistics were similar for all three data sets. However, one crystal diffracted to 2.4 Å and resulted in slightly better data statistics (Table 12) with an overall R_{meas} of 5.9 %. The Matthews parameter was calculated to 2.07 Å^3/Da and one monomer per ASU, which corresponds to a solvent content of 41 %.

Structure determination of sPEX3+PEX19[Pep] was done with molecular replacement. Therefore, an unrefined model of nPEX3 that was obtained previously [129] was used as search model. In this model, the core of nPEX3 could be built into the electron density map. However, the initial model could not be refined due to high twinning factors ($\alpha \approx$ 0.4). The resulting high R-values of 40 % are probably due to remaining electron density, which could not be assigned definitely [129]. Molecular replacement led to a

unique solution with Z-scores for the rotation and translation functions of 14.3 and 18.3, respectively. The initial phases were used to calculate a first electron density map for sPEX3+PEX19^{Pep}. Clear positive electron density for the PEX19-derived peptide was observed in the difference map (F_{obs}-F_{calc}). The peptide and several parts of sPEX3, which were not included in the search model, could be built manually with the software *Coot* [162]. Geometric and stereochemical parameters were validated in *Coot*, resulting in 96.9 % of residues located in favorable regions of the Ramachandran plot and 3.1 % located in allowed regions. In addition, anisotropic B-factor refinement was done using TLS analysis. Refinement statistics are listed in Table 12.

Table 12: Data statistics for sPEX3+PEX19^{Pep}.

Parameter	Value
Data collection	
Space group	P2$_1$
Cell dimensions	a=38.48 Å, b=65.68 Å, c=61.59 Å
	α=90°, β=91.52°, γ=90°
Resolution (Å)	25-2.4 (2.48-2.42)*
R$_{meas}$ (%)	5.9 (55.9)
I/σI	20.2 (3.0)
Completeness (%)	99.8 (99.8)
Redundancy	3.7 (3.7)
Wilson B (Å^2)	46.7
Refinement	
Resolution (Å)	25-2.42
Unique reflections	11779 (848)*
R$_{work}$/R$_{free}$ (%)	19.4/23.4 (28.9/29.0)
No. of atoms	
Protein	2249
Peptide	122
Water	67
B-factors (Å^2)	
Protein	39.2
Peptide	58.7
Water	40.8
Rmsd	
Bond length (Å)	0.01
Bond angles (°)	1.08

* Values in parentheses correspond to the highest resolution shell.

3.5   Crystal structure of sPEX3 in complex with PEX19^{Pep}

This research was originally published in The Journal of Biological Chemistry, [169], © the American Society for Biochemistry and Molecular Biology. Here, the key findings are recapitulated with the indicated figures and tables referring to the original publication, which can be found directly following this section (page 58).

Insights into peroxisome function from the structure of PEX3 in complex with a soluble fragment of PEX19. Schmidt F, Treiber N, Zocher G, Bjelic S, Steinmetz MO, Kalbacher H, Stehle T, Dodt G (2010). J Biol Chem 285, 25410-25417.

Peroxisomal matrix protein import has been elucidated in detail, including several structures of the matrix protein receptor PEX5 and its cargos [85, 170]. However, structural information about the proteins involved in peroxisomal membrane protein import is rather scarce. X-ray data is available of the C-terminal domain of PEX19 [66] (PDB: 2WL8). Furthermore, an NMR structure of a PEX14 peptide in complex with a PEX19 peptide was published [171] (PDB: 2W85). Here, one of the first crystal structures of a peroxin complex involved in PMP import is presented. The structure of human PEX3 in complex with a peptide derived from its interaction partner PEX19 was determined at 2.4 Å using molecular replacement (Table 1). Affinity measurements and conservation analysis provide insights into the atomic details mediating the PEX3-PEX19 interaction. Furthermore, three conserved regions within PEX3 were identified that might represent additional binding sites for other proteins during peroxisome biogenesis.

Structural features of sPEX3

The cytosolic domain of PEX3, sPEX3, folds into an all helical bundle composed of ten α-helices and one short 3_{10}-helix (Figure 2C and 2D). The structure exhibits a novel fold according to computer-based structural homology searches [172, 173], which could identify only a similarity to subsets of α-helical regions of proteins but not to their correct three-dimensional arrangements. The helical bundle is 80 Å long, has a diameter of 30 Å, and is composed of slightly twisted helices that encircle a central helix, α3 (Figure 2A). Some helical segments include proline residues, resulting in kinked helical structures. The long N-terminal helix projects from the protein core and represents the elongation of the transmembrane region (Figure 2B). *In vivo*, both the N- and C-termini

would be oriented towards the peroxisomal membrane. The inner core of the protein is stabilized by mainly hydrophobic interactions between the individual helices and the central α3-helix, excluding any water molecules from the protein interior. The α3-helix has been proposed previously to mediate the binding to PEX19. Cell culture experiments showed that this part of PEX3, comprising residues 120-136, colocalizes with PEX19 to the nucleus when PEX19 is equipped with a nuclear localization signal [70]. According to the sPEX3 crystal structure, the α3-helix is not able to interact with PEX19 unless a rearrangement of the entire protein takes place that would expose the helix. However, such a rearrangement is unlikely. Thus, the previously observed colocalization is probably due to the characteristic feature of PEX19 to bind hydrophobic protein segments, which applies to the α3-helix.

Characteristics of the PEX19-binding groove

The PEX19-binding groove is located at the top of the helical bundle and is composed of three distinct regions within sPEX3 (Figure 3). The PEX19-derived peptide forms a single α-helix that exhibits amphipathic properties. The non-polar side represents the main interaction surface with sPEX3, burying a total area of 580 Å^2 from solvent. On the solvent exposed side, additional hydrogen bonds and salt bridges mediate interactions of the peptide with sPEX3. The largest contact area (42 % of buried surface area, BSA) is located between residues Thr90 and Lys108. This region forms a helix-loop-helix motif comprising helix α2 and α3 (Figure 3B). The central residue is a tryptophan placed at position 104, which is surrounded by hydrophobic residues Leu22, Ala25, Leu26 and Phe29 of PEX19. The significance of Trp104 can be deduced from its strict conservation throughout organisms (Figures 4 and S4A) and its essential role in peroxisome biogenesis [123]. The second contact region involves only two residues of sPEX3, Leu196 and Lys197, and represents 21 % of the BSA (Figure 3A). The residues lie in a loop that connects helices α4 and α5 of sPEX3, and they interact with the N-terminus of PEX19[Pep]. Leu196 is engaged in hydrophobic interactions with three leucine residues of PEX19 (Leu18, Leu21, Leu22). The side chain of Lys197 mediates two salt bridges to Asp15 and Glu17 of PEX19 and several van-der-Waals contacts with Leu18. The third contact region ranges from Pro321 to Pro327 and involves helix α8 and the preceding loop (Figure 3C). The BSA counts for 37 % of the total contact area. Lys324 forms one salt bridge to Asp28 and a hydrogen bond with Ser24 of the PEX19 peptide. Pro321 interacts with Leu21 and Leu22 of PEX19. The short side chain of Ala323 is involved in

hydrophobic contacts with Leu21, Leu22 and Ala25 of PEX19[Pep]. The ring of Pro327 packs against the aromatic side chain of Phe29 at the C-terminus of the peptide, which further contacts the residues Ile326 and Asn330 of sPEX3.

Electrostatic surface potential

The electrostatic potential of the PEX19[Pep]-binding groove is positive due to several lysine residues (Lys94, Lys100, Lys197, Lys324), and it matches the negatively charged glutamates (Glu17, Glu19) and aspartates (Asp15, Asp28) within the PEX19-derived peptide (Figure S2). Furthermore, the electrostatic surface of the PEX19-binding groove can explain the previous observation that PEX3 binds membrane lipids but only in the absence of PEX19 [174]. The PEX19-binding groove is likely able to generate charge-charge interactions with phospholipids, forming high molecular mass aggregates of PEX3. The high affinity of PEX19 (see below) disrupts these unspecific PEX3-lipid-complexes, which are unlikely to play a significant role under physiological conditions.

Affinity of the PEX3-PEX19 interaction

The K_d-value for the sPEX3-PEX19[Pep] complex was determined with ITC experiments to 330 nM (Figure 1B). This high-affinity interaction can be attributed to the features of the fing groove described above. Another ITC experiment revealed an even lower K_d-value of 10 nM for the interaction of PEX3[26-373](C235S), nPEX3, with full-length PEX19 (Figure 1A). In all cases, the complex is formed with an 1:1 molar ratio. Surface plasmon resonance data from independent measurements are consistent with these findings [123, 124]. The difference in affinity of PEX3 for full-length PEX19 or the N-terminal peptide might be assigned to additional contributions of residues within the full-length protein. A putative second binding site for PEX3, spanning residues 124-140 of PEX19, was postulated based on peptide scanning mutagenesis [65]. However, this fragment did not show any affinity for sPEX3 in ITC experiments (Table S1). As the enthalpy of the sPEX3+PEX19[Pep] complex is 70 % of the enthalpy calculated for the binding to full-length PEX19, binding of the peptide produces the main energetic force. Thus, the identified PEX19-binding groove represents the major interaction site of PEX3.

Surface conservation analysis

Surface analysis of PEX3 revealed several evolutionary conserved regions within the amino acid sequence (Figure S4A). Mapping of solvent-exposed residues identified three strikingly conserved patches on the surface of sPEX3 (Figure 4A). In addition to the

PEX19^{Pep}-binding groove, there is a hydrophobic groove lining the base of the molecule, and a cluster of several acidic residues on the opposite side of the protein. The binding groove for the peptide is built of several strictly conserved residues (Figure 4B), of which tryptophan at position 104 has already shown to be essential for the function of PEX3 in peroxisomal biogenesis and for the interaction with PEX19 [123]. The high degree of conservation within the binding groove throughout species emphasizes the crucial role of the PEX3-PEX19-complex during membrane protein import into peroxisomes. Thus, it is possible that the two other conserved regions, the hydrophobic groove and the acidic cluster, are engaged in peroxisome biogenesis, perhaps by mediating contacts with other proteins or molecules.

Conservation analysis was also carried out for the N-terminus of PEX19 (Figure S4B). The majority of residues involved in the interaction with PEX3 are highly conserved throughout species, with the C-terminally located amino acids being more conserved than the residues within the N-terminal part (Figure 4B). Phenylalanine at position 29 closes the binding groove with its bulky side chain and is crucial for binding to PEX3, as a mutation to alanine (PEX19^{Pep} F29A) results in a loss of affinity for sPEX3 (Figure 1C). This is consistent with the *in vivo* finding that the F29A mutation completely abolishes the complementation ability of full-length PEX19 in ΔPEX19 cells [124]. Another highly conserved residue is Ala 25. Mutagenesis experiments revealed that a leucine, which is present in some yeast at this position, is tolerated at this position, revealing a K_d of 410 nM calculated by ITC measurements. In contrast, the substitution to a tyrosine results in loss of binding, probably because the big aromatic side chain prevents complex formation (Table S1).

A similar PEX3-PEX19 complex structure

At the same time as these results were published, a competing group published a similar structure of a PEX3-PEX19 complex [124]. They used a shorter version of PEX3, starting at amino acid 49, and the first 44 N-terminal amino acids of PEX19 for crystallization. The crystals belong to space group P6$_5$22 and the structure was solved with MAD phasing of a seleno-methionine derivative. The hexagonal space group is reminiscent of the twinned crystals obtained for nPEX3. An overlay of the present structure with the complex structure of the other group reveals no significant differences in the overall fold, with an rmsd of 1.4 Å for the Cα-backbone (Figure 3.9) as determined with least square superposition in Coot [162]. The largest deviations can be found in some loops

and surface-exposed regions, which indicates flexibility. The PEX19-binding groove is highly similar in both structures, with good agreement of the side chain positions. The PEX19 fragment shows an rmsd of 0.6 Å for the Cα-backbone. The high similarity of two independently determined structures provides additional support for the PEX3-PEX19 complex structure determined in this thesis.
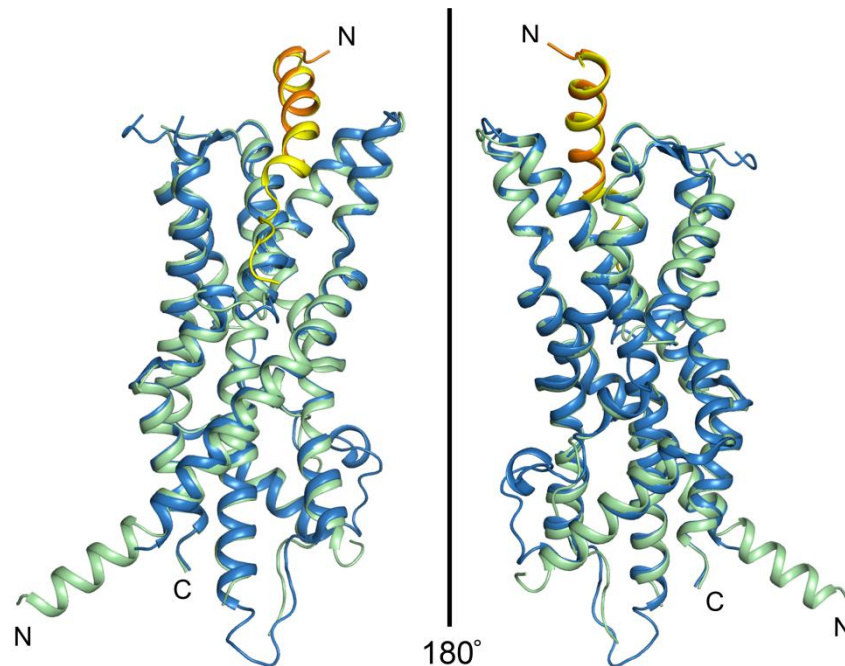
Figure 3.9: Superposition of two similar PEX3-PEX19-complex structures. The structure of sPEX3 (green cartoon) with a PEX19-derived peptide (orange cartoon) is superimposed with a similar complex structure published in [124] (PDB: 3AJB) with a shorter version of PEX3 depicted as a blue and a longer version of PEX19 depicted as a yellow cartoon, respectively. The rmsd values for the Cα-backbone are 1.4 Å for the PEX3 molecules and 0.6 Å for the PEX19 peptides, respectively.

The sPEX3+PEX19^{Pep} structure presented in this thesis provides insights into the mechanisms underlying the PEX3-PEX19 interaction and enables further functional analysis. The conservation of the PEX19-binding groove and the PEX19-derived peptide supports the crucial role of the PEX3-PEX19-complex during peroxisome biogenesis. The nanomolar affinity of the PEX3-PEX19 interaction ensures a correct initiation point for an essential step in peroxisome biogenesis, the insertion of peroxisomal membrane proteins. The biological relevance of the identified conserved regions on the surface of PEX3 has to be validated, especially applying *in vivo* studies. Furthermore, the functions of the conserved hydrophobic groove and the acidic patch, which both might represent the second PEX19-binding site as proposed earlier [65], remain to be elucidated.

Insights into Peroxisome Function from the Structure of PEX3 in Complex with a Soluble Fragment of PEX19*[S]

Friederike Schmidt[‡1], Nora Treiber[§1,2], Georg Zocher[‡], Sasa Bjelic[¶], Michel O. Steinmetz[¶], Hubert Kalbacher[‡], Thilo Stehle[‡||3], and Gabriele Dodt[‡4]

From the [‡]Interfaculty Institute for Biochemistry, University of Tübingen, 72076 Tübingen, Germany, the [§]Institute for Organic Chemistry and Biochemistry, University of Freiburg, 79106 Freiburg, Germany, the [¶]Laboratory of Biomolecular Research, Structural Biology, Paul Scherrer Institut, 5232 Villigen PSI, Switzerland, and the [||]Department of Pediatrics, Vanderbilt University School of Medicine, Nashville, Tennessee 37232

The human peroxins PEX3 and PEX19 play a central role in peroxisomal membrane biogenesis. The membrane-anchored PEX3 serves as the receptor for cytosolic PEX19, which in turn recognizes newly synthesized peroxisomal membrane proteins. After delivering these proteins to the peroxisomal membrane, PEX19 is recycled to the cytosol. The molecular mechanisms underlying these processes are not well understood. Here, we report the crystal structure of the cytosolic domain of PEX3 in complex with a PEX19-derived peptide. PEX3 adopts a novel fold that is best described as a large helical bundle. A hydrophobic groove at the membrane-distal end of PEX3 engages the PEX19 peptide with nanomolar affinity. Mutagenesis experiments identify phenylalanine 29 in PEX19 as critical for this interaction. Because key PEX3 residues involved in complex formation are highly conserved across species, the observed binding mechanism is of general biological relevance.

Peroxisomes are single membrane-bound organelles that carry out a variety of metabolic processes. In addition to the degradation of H_2O_2, the β-oxidation of very long chain or branched chain fatty acids and the synthesis of ether lipids are performed in these subcellular compartments (1, 2). The biogenesis of peroxisomes, including their formation and proliferation, as well as the degradation of peroxisomes are highly dynamic processes that are adapted to metabolic needs (3). Defects in peroxisome biogenesis cause a number of severe inherited diseases, which are collectively referred to as peroxisome biogenesis disorders (4, 5). Studies in yeast and analysis of patients affected by these disorders have led to the identification of specific proteins involved in peroxisomal formation and

maintenance (6). Fifteen such proteins, which are named peroxins, are currently known in humans and the corresponding genes (*PEX* genes) are highly conserved throughout the eukaryotic kingdom (7, 8).

All matrix proteins and most membrane proteins are imported post-translationally into peroxisomes. The machinery of peroxins that mediates the import of matrix proteins bearing a peroxisomal targeting signal is far better understood than the machinery that mediates the recognition and import of membrane proteins (9, 10). The peroxins PEX3,[5] PEX16, and PEX19 are known to be essential for peroxisomal membrane biogenesis as a loss of any of these proteins leads to the complete absence of detectable peroxisomal membrane structures (11). However, *de novo* formation of peroxisomes was observed in cells deficient for each of these peroxins upon complementation with the wild type gene, raising an intriguing question about the origin of the peroxisomal membrane (11–15). The endoplasmic reticulum membrane as the obvious source was disputed for a long time as several studies indicate that this process does not involve the classical coat protein I- and coat protein II-dependent pathways (16–18). Recently, new evidence for an involvement of the endoplasmic reticulum as a peroxisomal precursor has been reported in yeast (19–21) and in mammalian cells (22–24), although the details of this process remain to be elucidated.

PEX19 is a farnesylated but hydrophilic protein that is predominantly found in the cytosol, with a smaller fraction transiently located at the peroxisomal membrane (12, 25). In the cytoplasm, PEX19 can act as a chaperone for newly synthesized peroxisomal membrane proteins (PMPs) by binding them during or after translation and keeping them in an import-competent form (26, 27). For the majority of PMPs, the PEX19-binding site matches the proposed membrane-targeting signal (11, 28). Cargo-loaded PEX19 is directed to the peroxisomal membrane by docking to PEX3 (29). The predicted PEX3-binding domain of PEX19 is located within its first 56 amino acid residues, whereas the C-terminal part harbors the binding sites for other peroxisomal membrane proteins (11, 26, 30, 31). After insertion of the PMP, PEX19 is released into the cytosol to initiate another import cycle (32).

---

[5] The abbreviations used are: PEX, peroxisomal biogenesis factor; PMP, peroxisomal membrane protein; ITC, isothermal titration calorimetry; HPLC, high pressure liquid chromatography; Bis-Tris, 2-(bis(2-hydroxyethyl)amino)-2-(hydroxymethyl)propane-1,3-diol.

The peroxin PEX3 is anchored in the peroxisomal membrane via a short hydrophobic transmembrane segment within its N-terminal 33 residues, a region that is necessary and sufficient for targeting PEX3 to peroxisomes (33, 34). The cytosolic domain mediates the interaction with PEX19 (11). PEX3 is imported into peroxisomes in a PEX19-independent manner and hence defines a separate import pathway (26). The role of PEX16 during the import of peroxisomal membrane proteins is less well defined, but it is thought to function as a docking site for PEX3 (35).

To define the parameters that underlie the interaction of PEX3 with PEX19, we solved the structure of a soluble domain of PEX3 in complex with a peptide corresponding to an N-terminal region of PEX19 (PEX19^{Pep}). The soluble PEX3 domain comprises residues 41–373 and contains a cysteine to serine mutation at position 235 (sPEX3). In combination with affinity measurements and mutagenesis experiments, this structure provides insights into the determinants of recognition of the PEX3-PEX19 complex. As residues in the contact area are highly conserved among eukaryotes, our structure can serve as a general model for understanding the functions of PEX3 and PEX19 in peroxisomal biogenesis. Moreover, the structure presented here provides one of the first views of any interaction between two peroxins at high resolution.

EXPERIMENTAL PROCEDURES

Protein Expression—Two human PEX3 fragments, comprising residues 26–373 and 41–373, were expressed in *Escherichia coli*. The corresponding DNA regions including a preceding tobacco etch virus protease cleavage site were cloned into the vector pET32a (Novagen), which includes an N-terminal His$_6$ tag. Site-directed mutagenesis (QuikChange®, Stratagene) was used to generate Cys-Ser mutations at position 235 in both cases. These constructs were transformed into *E. coli* Rosetta2 (DE3) cells and grown at 37 °C to an A_{600} of 0.6 before protein expression was induced with 1 mM isopropyl-β-thiogalactopyranoside. Cells were grown for an additional 16 h at 18 °C before harvesting. DNA coding for full-length human PEX19 with a preceding tobacco etch virus protease cleavage site was cloned into the vector pColdI (Takara Bioscience), which includes an N-terminal His$_6$ tag. The construct was transformed into *E. coli* BL21 (DE3) cells. Cells were grown at 37 °C to an A_{600} of 0.4, at which point the temperature was lowered to 15 °C before protein expression was additionally induced with 1 mM isopropyl-β-thiogalactopyranoside. Cells were then incubated for 16 h at 15 °C.

Protein Purification—All three proteins (PEX3$^{26-373}$(C235S), PEX3$^{41-373}$(C235S), and PEX19$^{1-299}$) were purified using the same protocol. PEX3$^{41-373}$(C235S) is referred to as sPEX3. In each case, 10 g of cells were resuspended in 50 ml of buffer A (20 mM NaH$_2$PO$_4$, 300 mM NaCl, 10 mM imidazole, 5 mM β-mercaptoethanol, pH 8.0) and lysed with an EmulsiFlex®-C3 system (Avestin). After centrifugation (28,000 × g, 30 min, 4 °C), the supernatant was loaded onto a 5-ml HisTrap HP column (GE Healthcare). Protein was eluted using a linear gradient of buffer B (20 mM NaH$_2$PO$_4$, 300 mM NaCl, 500 mM imidazole, 5 mM β-mercaptoethanol, pH 8.0). Cleavage was carried out in a membrane tube (Spectra/Por®, Spectrumlabs) overnight at

4 °C with 1 mg of tobacco etch virus protease/40 mg of protein while dialyzing against 1 liter of buffer A. A second Ni^{2+} column removed residual uncleaved protein. Cleaved protein was then concentrated and applied to a Superdex^{TM} 200 10/300 (GE Healthcare) size exclusion column using buffer C (50 mM Tris, 200 mM NaCl, 0.5 mM Tris-(2-carboxyethyl)phosphine, pH 8.0). Purity and homogeneity of the proteins were confirmed by SDS-PAGE, native PAGE, and dynamic light scattering. Protein folding was analyzed with circular dichroism spectroscopy using a JASCO J-720 spectrophotometer. Protein concentrations were determined by measurements of absorption at 280 nm with a NanoDrop ND-1000 (PeqLab).

Peptide Synthesis—PEX19-derived peptides were prepared using solid-phase synthesis based on the *N*-(9-fluorenyl)methoxycarbonyl (Fmoc) strategy on a SyroII synthesizer (MultiSynTech, Witten, Germany) as described (36). Peptides were purified by HPLC using a C18 column, resulting in a purity of 95%. Purity and identity of the products were confirmed by analytical HPLC, matrix-assisted laser desorption/ionization time of flight mass spectrometry, and electrospray ionization mass spectrometry.

Affinity Measurements Using Isothermal Titration Calorimetry (ITC)—Affinity measurements for PEX3$^{26-373}$(C235S) with full-length PEX19 were carried out in buffer C at 25 °C with a VP-ITC system (Microcal). Purified PEX3$^{26-373}$(C235S) was present in 8 μM concentration, and PEX19 was injected stepwise in 92 μM concentration. For binding studies between sPEX3 and different PEX19-derived peptides, an ITC200 system (Microcal) was used. The protein was present in 17 μM concentration, while the peptide fragments were injected stepwise (1 μl/s) in a 5–15-fold higher concentration. ITC experiments with PEX19-derived peptides were performed at 25 °C in buffer D (10 mM Na$_2$HPO$_4$, 1.8 mM KH$_2$PO$_4$, 140 mM NaCl, 2.7 mM KCl, 0.5 mM Tris-(2-carboxyethyl)phosphine, pH 7.4). Binding isotherms were integrated and analyzed using Origin® 7 software supplied with the instrument according to a "one binding site" model.

Crystallization and Structure Determination—Purified sPEX3 at 2.5 mg/ml in buffer C was co-crystallized with PEX19^{Pep} (residues 14–33) in a molar 1:1 ratio using the hanging drop vapor diffusion method at 20 °C. The final crystallization condition was optimized to 10 mM Bis-Tris, pH 5.6, 24% (w/v) polyethylene glycol 3350, 200 mM NaCl. Crystals appeared within 24 h and were flash-frozen in liquid nitrogen without adding cryoprotectant. X-ray diffraction data were collected at beamline BL14.1 (Berliner Elektronenspeicherringgesellschaft für Synchrotronstrahlung (BESSY), Berlin, Germany). They belong to space group P2$_1$ and contain one complex in the asymmetric unit. Data were processed and scaled using the XDS package (37). Molecular replacement was carried out with PHASER (38, 39) using a highly twinned structure of PEX3$^{26-373}$(C235S) as the search model (40). This produced a clear solution and unambiguous difference electron density for the bound PEX19 peptide (supplemental Fig. S3) and regions of sPEX3 that had not been included in the search model. Model building and refinement were carried out using COOT (41) and Refmac5 (38, 42), respectively. TLS (translation/libration/screw) groups suggested by the TLS Motion Determination server (43) were

employed in the refinement process. According to stereochemical analysis within COOT, 96.9% of residues are located in favorable regions of the Ramachandran plot, whereas 3.1% are located in allowed regions. Data collection and refinement statistics are given in Table 1. Buried surface areas were calculated using CCP4 programs (38). Electrostatic surface potentials were computed with APBS (44) in PyMOL. The simulated annealing omit map was calculated in Phenix (45). The stereo view of the overall fold was displayed using Molscript (46). Coordinates and structure factors have been deposited with the RCSB Protein Data Bank (accession code 3MK4).

RESULTS

A PEX19-derived Peptide Binds sPEX3 with High Affinity—The interaction of the two peroxins PEX3 and PEX19 is required for the import of all peroxisomal membrane proteins. To define the structure-function relationships that underlie this interaction, we expressed and purified a soluble version of human PEX3 that comprises most of its predicted cytosolic domain (sPEX3) as well as a slightly longer version starting at residue 26 (PEX3$^{26-373}$). A solvent-exposed cysteine at position 235 was mutated to serine in both proteins to prevent non-native oxidation. Earlier crystallization trials of the larger version of PEX3 in complex with full-length PEX19 failed. We therefore pursued co-crystallization experiments of sPEX3 with a PEX19-derived peptide that spans residues 14–33 (PEX19^{Pep}). The design was based on a predicted α-helix in the proposed PEX3-binding region (30) that is located within the first 56 amino acid residues of PEX19 (29).

Affinity measurements using ITC demonstrate that sPEX3 binds PEX19^{Pep} with high affinity (K_d = 330 nM, Fig. 1). The affinity of PEX3$^{26-373}$(C235S) for full-length PEX19 is still higher (K_d = 10 nM, Fig. 1). The molar ratio was calculated to be 1:1 for both complexes (supplemental Table S1). A comparison of the ITC data shows that the enthalpy for binding PEX19^{Pep} is 70% of the enthalpy released upon binding full-length PEX19 (supplemental Table S1). This indicates that most of the specificity of the PEX3-PEX19 interaction can be attributed to contacts with PEX19^{Pep}.

Overall Structure of sPEX3 in Complex with PEX19^{Pep}—The structure of the sPEX3-PEX19^{Pep} complex was determined by molecular replacement at 2.42 Å resolution (Table 1 and "Experimental Procedures"). As a search model, we used the core structure of the previously obtained, unrefined model of PEX3 comprising residues 26–373 (40). This unliganded structure could be solved to a resolution of 3.3 Å with phases obtained from multiple anomalous diffraction data using seleno-methionine-derivatized crystals, but it could not be refined due to highly twinned x-ray data (twinning factor: 0.48). However, components of this model led to a unique solution for the structure presented here. Unambiguous difference electron density for the bound PEX19 peptide and regions of sPEX3 that had not been included in the search model provide confidence for the obtained solution. The cysteine residue at position 235 is located in a recessed, partially solvent-exposed area and would not be able to form intra- or intermolecular disulfide bridges in the wild type protein. Therefore, its mutation to serine is unlikely to alter the sPEX3 structure. The final structure has
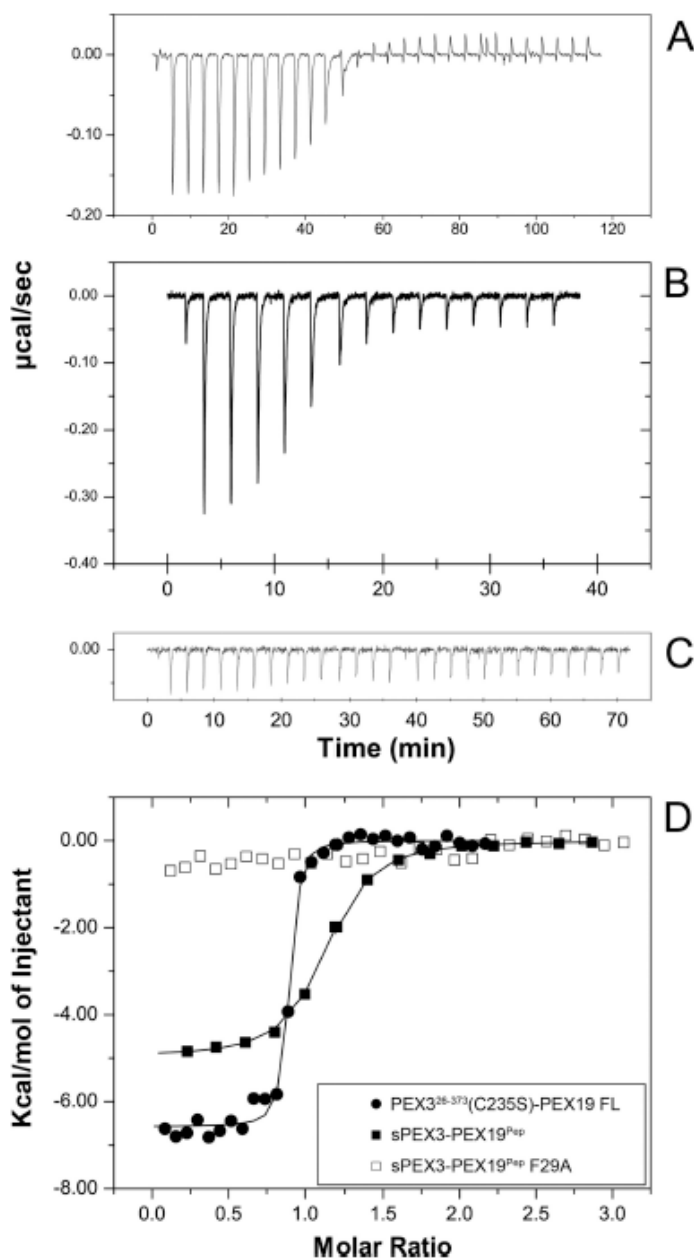
FIGURE 1. **ITC affinity measurements of complex formation between PEX3 and PEX19.** Single experiments were carried out at 25 °C. *A–C*, binding data for PEX3$^{26-373}$(C235S) with full-length PEX19 (*A*), sPEX3 with PEX19^{Pep} (*B*), and sPEX3 with Pex19^{Pep} F29A (*C*). *D*, integrated heat values for the different ITC experiments. *Closed circles*, PEX3$^{26-373}$(C235S) and full-length PEX19; *closed squares*, sPEX3 and PEX19^{Pep}; *open squares*, sPEX3 and Pex19^{Pep} F29A; see also supplemental Table S1.

excellent geometry and agrees very well with the experimental data (R_{free} = 23.4%, Table 1).

sPEX3 adopts a new fold that is composed of 10 α-helices and one short 3_{10}-helix (Fig. 2 and supplemental Fig. S1). Searches for structural homologs with the programs DALI (47) and GANGSTA+ (48) revealed no significant matches. Although portions of several proteins that contain multiple parallel helices can be aligned with the sPEX3 structure, the overall folds of these proteins clearly differ from the sPEX3 fold, confirming that sPEX3 exhibits a new fold.

The long α3-helix forms the core of the structure, and the remaining helices are arranged circularly around it in five segments (Fig. 2*A*). As all helical axes are aligned in roughly the

TABLE 1

Data collection and refinement statistics

Parameter	Value
Data collection	
Beamline	BL14.1, BESSY
Wavelength (Å)	0.91841
Space group	P2$_1$
Cell dimensions	
a, b, c (Å)	38.48, 65.68, 61.59
α, β, γ (°)	90.0, 91.52, 90.0
Resolution (Å)	25-2.42 (2.48-2.42)^a
R$_{meas}$	5.9 (55.9)^a
I/σI	20.2 (3.0)^a
Completeness (%)	99.8 (99.8)^a
Redundancy	3.7 (3.7)^a
Wilson B (Å^2)	46.7
Refinement	
Resolution (Å)	25-2.42
Unique reflections	11779 (848)^a
R$_{work}$/R$_{free}$	0.194/0.234 (0.289/0.290)^a
No. of atoms	
Protein	2249
Peptide	122
Water	67
B-factors (Å^2)	
Protein	39.2
Peptide	58.7
Water	40.8
r.m.s.^{b} deviations	
Bond lengths (Å)	0.01
Bond angles (°)	1.08

^{a} Values in parentheses are for highest-resolution shell.
^{b} r.m.s., root mean square.
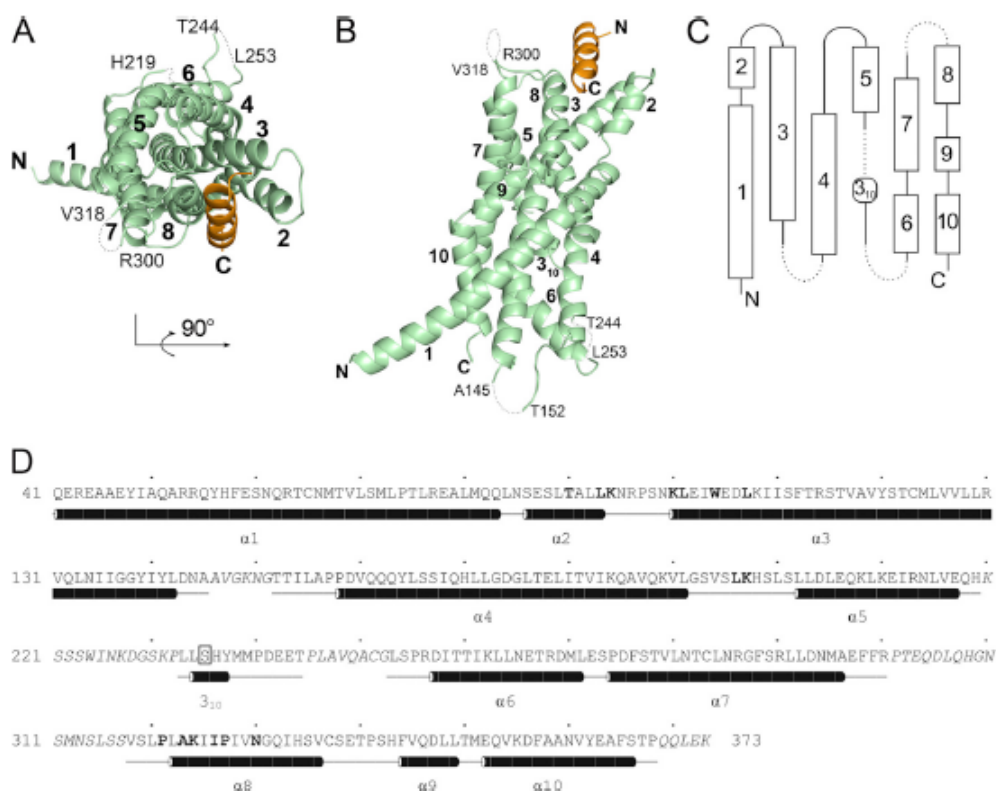
FIGURE 2. **Overall structure of sPEX3 (*green*) in complex with PEX19^{Pep} (*orange*).** sPEX3 folds into an all-helical bundle, with one central helix α3 surrounded by nine α-helices and a short 3$_{10}$-helix. The N terminus of helix α1 faces toward the peroxisomal membrane. Helices were assigned with DSSP (53) and numbered sequentially. *A*, top view of the sPEX3-PEX19^{Pep} complex. *B*, side view of the sPEX3-PEX19^{Pep} complex. Representation in *A* is rotated 90 degrees around a horizontal axis. *C*, topology of sPEX3. Helices 1–10 are represented as *cylinders*. The central helix α3 is surrounded by five helical segments (α1+α2, α4, α5 + 3$_{10}$, α6+α7, α8+α9+α10) arranged in nearly parallel fashion. Regions not included in the structure are shown as *dashed lines*. *D*, schematic view of the secondary structure elements of sPEX3. Residues involved in PEX19^{Pep} binding are highlighted in **bold**, and residues not present in the crystal structure are shown in *italics*. The cysteine-serine mutation at position 235 is *boxed*.

same direction, the structure can be described as a large helical bundle (Fig. 2*B*). The bundle is about 80 Å tall and 30 Å wide. Interfaces between the helices are mostly hydrophobic and devoid of water molecules, providing stability to the bundle. In contrast, the exterior of the bundle is predominantly hydrophilic. The C-terminal region of sPEX3 is oriented toward the N terminus and would thus face the peroxisomal membrane. Several of the helices in the bundle are kinked due to insertions or the presence of residues such as proline, which are not compatible with a regular helical structure. These kinks are probably needed to allow for tight packing between helices. Although the helical bundle is rigid and well defined by electron density, the positions of residues in several loop regions could not be determined due to their high mobility. Regions missing from the model are: Ala[146]–Gly[151], Lys[220]–Pro[232], Pro[245]–Gly[252], Pro[301]–Ser[317], and Gln[369]–Lys[373] at the C terminus. None of these regions are close to the site of interaction with PEX19^{Pep}.

Residues 14–30 of PEX19^{Pep} are well defined by electron density and permitted accurate model building. The C-terminal three amino acids (Lys[31]–Lys[33]) are not visible in the electron density maps and are not included in the model. The N terminus of the peptide is involved in crystal contacts that are distant from the PEX3-binding groove. PEX19^{Pep} forms a single amphipathic α-helix that binds into a groove at the top of the helical bundle, opposite the N terminus of sPEX3 (Fig. 2, *A* and *B*). One side of the groove is shaped by helices α2 and α3, whereas the other side is formed by the loop that connects helices α4 and α5 and by a portion of helix α8.

The PEX19^{Pep}-binding Site Reveals Three Distinct Interaction Regions within sPEX3—The contact interface is formed by surfaces in sPEX3 and PEX19^{Pep} that are complementary in shape, producing an uninterrupted, contiguous interface that is devoid of water molecules and gaps and buries a total area of 580 Å^2 from solvent. To facilitate the discussion of interactions, we have divided this interface into three contact areas along the sPEX3-binding groove (Fig. 3). The first and largest contact area (Fig. 3*B* and supplemental Fig. S3) is formed by sPEX3 residues located at the C-terminal end of helix α2 and the N-terminal region of helix α3. This helix-loop-helix motif of sPEX3 packs tightly against the C-terminal end of the PEX19^{Pep} helix. Contacts are predominantly hydrophobic and account for 42% of the total surface buried in the complex. A key interaction is centered at sPEX3 residue Trp[104], which is strictly conserved in all eukaryotic organisms
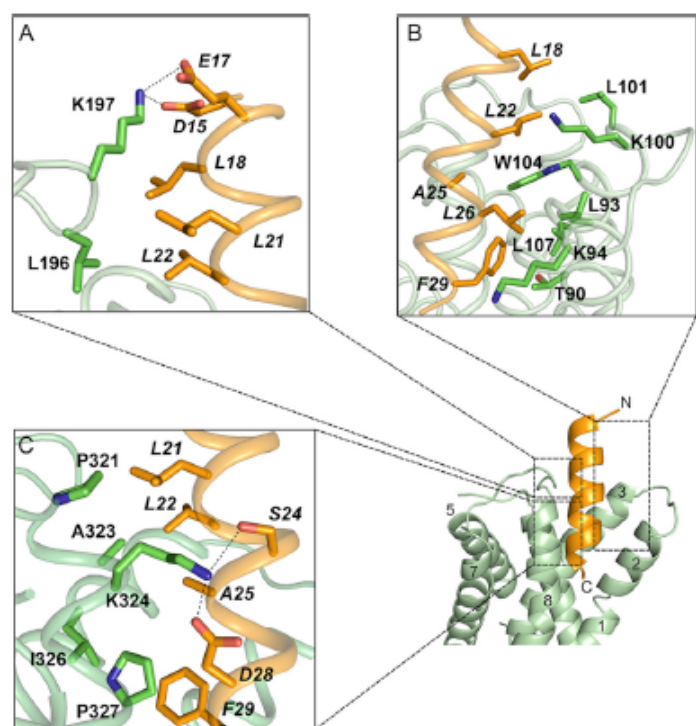
FIGURE 3. **Interactions between sPEX3 (*green*) and PEX19^{Pep} (*orange*).** *A–C*, the magnified regions show details of the three major contact areas. Labels in *regular font* correspond to sPEX3, and labels in *italics* correspond to PEX19^{Pep}.

FIGURE 4. **Surface distribution of conserved amino acid residues.** *A*, overall side views of surface representation of sPEX3 differing by 180 degrees along a vertical axis. PEX19^{Pep} is shown as an *orange ribbon*. *B*, magnified view of the binding groove. PEX19^{Pep} is displayed as a *ribbon*. Alignments were performed with ClustalW (54) and displayed in Jalview (55). Residues are colored according to the conservation score (supplemental Fig. S4) indicated at the *lower right*. Residues with a conservation score ≥ 9 (9, 10⁺, 11*) are displayed in the same color. Residues conserved in sPEX3 are colored in shades of *green*, and residues conserved in PEX19^{Pep} are colored in shades of *orange*.

(Fig. 4 and supplemental Fig. S4*A*) and was previously shown to be crucial for the interaction with PEX19 (49). Trp[104] inserts into a pocket formed by 4 PEX19^{Pep} residues: Leu[22], Ala[25], Leu[26], and Phe[29]. Additional hydrophobic contacts involving sPEX3 residues Thr[90], Leu[93], Lys[94], Lys[100], Leu[101], and Leu[107] also contribute to the interaction.
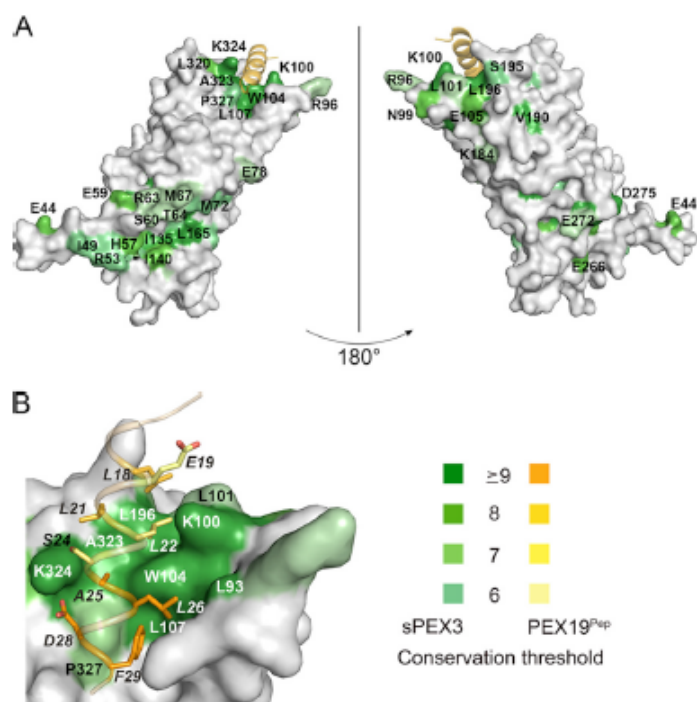
The second contact region is formed at the loop that connects helices α4 and α5 of sPEX3 (Fig. 3*A*) and accounts for 21% of the total buried surface area. Contacts in this region involve the side chains of Lys[197] and Leu[196] of sPEX3, which protrude from this loop and engage residues close to the N terminus of PEX19^{Pep}. Lys[197] forms salt bridges with Asp[15] and Glu[17] of the peptide, as well as hydrophobic interactions with Leu[18]. Leu[196] packs against Leu[18], Leu[21], and Leu[22], which all project from the same face of the PEX19^{Pep} helix.

The third contact region, which buries 37% of the total contact area, is located at the N terminus of helix α8 and the loop that precedes this helix (Fig. 3*C*). At the center of this region lies sPEX3 residue Lys[324], which forms salt bridges and hydrogen bonds with Asp[28] and Ser[24], respectively, of PEX19^{Pep}. The remaining contacts in this region are exclusively hydrophobic and involve 2 proline residues of sPEX3. Pro[321] faces toward peptide residues Leu[21] and Leu[22], whereas the ring of Pro[327] packs tightly against the Phe[29] side chain of the peptide. Located near the C terminus of PEX19^{Pep}, Phe[29] also interacts with the side chains of Ile[326] and Asn[330]. Additional contacts are formed with the methyl group of Ala[323], which faces toward Leu[21], Leu[22], and Ala[25] of PEX19^{Pep}.

Mutagenesis of Contact Residues—To analyze the impact of mutations in PEX19^{Pep} on sPEX3 binding, structure-guided mutagenesis experiments were performed. Select PEX19^{Pep}

amino acids that were judged to be critical for the interaction with sPEX3 were mutated, and the interactions between the peptide and sPEX3 were analyzed with ITC. Amino acid Phe[29], which contacts several sPEX3 residues via its hydrophobic side chain (Fig. 3, *B* and *C*), was replaced with alanine. This F29A mutation completely abolished binding to sPEX3 (Fig. 1 and supplemental Table S1). The presence of a phenylalanine at position 29 is therefore critical for PEX3-PEX19 complex formation, consistent with the strict conservation of this residue among the PEX19 sequences of eukaryotic species (Fig. 4 and supplemental Fig. S4*B*). Secondly, PEX19^{Pep} residue Ala[25] was mutated to leucine as well as tyrosine. The methyl group of Ala[25] interacts with hydrophobic residues of sPEX3 (Fig. 3, *B* and *C*). Inspection of the structure indicated that a leucine side chain might be able to form similar contacts, whereas a larger tyrosine side chain would not be tolerated. Consistent with this prediction, the K_d value for the A25L mutation is 410 nM, which is only slightly lower than the affinity of wild type PEX19^{Pep}. We note that a leucine is present at this position in some yeast PEX19 proteins. Not surprisingly, replacement of Ala[25] with tyrosine completely disrupted the interaction. The mutational data are summarized in supplemental Table S1.

Analysis of Surface Features and Conservation—To identify key surface features of sPEX3 and PEX19^{Pep}, we compared the sequences of both proteins from several organisms (supplemental Fig. S4) and displayed conserved surface residues, as depicted in Fig. 4. This analysis reveals that all residues lining the PEX19^{Pep}-binding groove at the membrane-distal end of

sPEX3 are well conserved (Fig. 4*A*). The structure of the complex identifies 2 key residues of sPEX3 that are involved in central contacts, Trp^{104} and Lys^{324}. Not surprisingly, these 2 residues exhibit the highest degree of conservation. A similar analysis of PEX19^{Pep} residues shows that Ala^{25}, Leu^{26}, Asp^{28}, and Phe^{29} are most highly conserved (Fig. 4*B*). Again, these residues all play central roles in complex formation (Fig. 3 and supplemental Table S1). An interesting finding is that the C-terminal region of PEX19^{Pep} (residues 25–29) is more conserved than residues that lie closer to the N terminus of the peptide (residues 18–24). This indicates that contacts formed by the C-terminal portion of PEX19^{Pep}, and especially residues Leu^{26} and Phe^{29}, are most important for a productive interaction and for conferring specificity.

Although most of the remaining sPEX3 surface is quite variable, our analysis reveals a second cluster of highly conserved residues at the base of the molecule, near the N-terminal helix α1. This cluster includes an unusual number of surface-exposed large, hydrophobic residues (Ile^{49}, Met^{67}, Met^{72}, Ile^{135}, and Ile^{140}). *In vivo*, this region would be located close to the peroxisomal membrane. It is tempting to speculate that it forms the site of interaction with a second region of PEX19 or with other peroxisomal proteins.

Analysis of surface charges of sPEX3 (supplemental Fig. S2*A*) reveals a polar surface with many small positively and negatively charged patches and two noticeably larger ones. The PEX19^{Pep}-binding groove exhibits a strong positive potential, consistent with several basic residues (Lys^{94}, Lys^{100}, Lys^{197}, and Lys^{324}) that line the groove and participate in PEX19^{Pep} binding. In contrast, the PEX19-derived peptide exhibits a highly negative surface potential due to exposed aspartic and glutamic acids (supplemental Fig. S2*B*). A less conserved region at the base of sPEX3 exhibits a strong negative potential, which is due to an accumulation of acidic residues (Asp^{257}, Glu^{266}, Asp^{269}, Glu^{272}, and Asp^{275}). Among these residues, Glu^{266}, Glu^{272}, and Asp^{275} are highly conserved in all eukaryotic species except yeasts. These features may indicate functional interactions of these residues with other proteins during peroxisomal biogenesis.

DISCUSSION

PEX3 has been reported to participate in different processes during peroxisomal biogenesis. In this study, we sought to define its structural features, as well as the specificity of its interaction with PEX19. Experiments performed in several laboratories have identified the N-terminal 56 amino acids of PEX19 as necessary and sufficient for the interaction with PEX3 and thus for docking PEX19 to the peroxisomal membrane (26, 29–31). Based on these studies, we have designed and synthesized a peptide that comprises the central part of this region of human PEX19 and determined the structure of the cytosolic domain of human PEX3 in complex with this peptide. sPEX3 folds into an elongated helical bundle that has no known structural homologs. Structural and functional analyses identified a single groove in sPEX3 as a high affinity binding site for PEX19. This region is highly conserved across eukaryotic species. Additional regions of surface conservation of sPEX3 indicate contact points for other molecules involved in peroxisomal biogenesis.

Several observations support our finding that the described binding region identified within PEX19 is indeed the main interaction surface with PEX3. Although the sPEX3-PEX19^{Pep} interaction buries only a comparatively small surface area of 580 Å^2, ITC measurements yield a high affinity of 330 nM for the sPEX3-PEX19^{Pep} complex. The K_d value for the interaction between PEX3$^{26-373}$(C235S) and PEX19 is 10 nM, indicating a 33-fold higher affinity for full-length PEX19. This value is consistent with previous surface plasmon resonance studies resulting in a K_d value in the low nanomolar range (3.4 nM) and a 1:1 molar ratio between PEX3 and PEX19 (49). The high affinity for PEX19^{Pep} can be attributed to an interacting surface that is complementary in shape, devoid of water molecules, and predominantly hydrophobic. The higher affinity for full-length PEX19 could be due to additional residues within the PEX19 N terminus, which were not included in the synthesized peptide but which contribute to binding at the identified interaction site. However, because both termini of the PEX19^{Pep} helix point away from sPEX3 and because the sPEX3 structure lacks additional conserved residues at the top of the bundle, we consider this possibility unlikely. The observation that the enthalpy for PEX19^{Pep} binding is 70% of the enthalpy for the full-length protein indicates that PEX19^{Pep} contributes significantly to the interaction. However, the difference in K_d also suggests that other residues of the full-length PEX19 protein are likely involved in contact formation. The conserved region at the base of sPEX3 is a possible candidate for additional interactions with full-length PEX19. A second binding site within residues 124–140 of PEX19 has been proposed previously (30). However, this region is unlikely to interact with PEX3 as our ITC measurements clearly show that a PEX19-derived peptide corresponding to these amino acids does not bind sPEX3 (supplemental Table S1).

The functional relevance of the observed interaction between sPEX3 and PEX19^{Pep} is further supported by the presence of highly conserved residues in the peptide-binding groove. A conserved region including PEX3 residues Lys^{100} to Arg^{114} was predicted to contribute to PEX19 binding (49). Our structure shows that many of these residues indeed form key contacts with PEX19^{Pep}. Residues Lys^{100}, Leu^{101}, Trp^{104}, and Leu^{107} are all part of the largest binding region (Fig. 3*B*). Trp^{104} can even be considered a central residue as it interacts with several hydrophobic PEX19^{Pep} side chains, including Phe^{29}. Furthermore, the tryptophan helps to orient side chains of additional sPEX3 residues (Leu^{93} and Lys^{100}) to form contacts with PEX19^{Pep}. Consistent with the central role of Trp^{104} in complex formation, it was reported that its replacement with alanine reduces the affinity of PEX3 for PEX19 significantly. Moreover, the W104A mutant of PEX3 was unable to restore peroxisomes in a *PEX3*-deficient cell line (49). Our surface analysis reveals that the PEX19^{Pep} residues involved in sPEX3 recognition are also highly conserved throughout eukaryotic species. The importance of these residues is emphasized by mutagenesis experiments and affinity measurements, identifying Phe^{29} as crucial for the formation of a PEX3-PEX19 complex (Fig. 1 and supplemental Table S1).

The observed contacts between sPEX3 and PEX19^{Pep} are in line with some, but not all, earlier studies that have sought to

identify PEX3 residues involved in the interaction with PEX19. Fang *et al.* (29) proposed that the highly conserved PEX3 residues 120–136 interact with PEX19 as this segment colocalizes with a nuclear localization sequence-tagged version of PEX19 to the nucleus. Furthermore, mutations in this region disrupted interactions with PEX19 and the ability of PEX3 to complement *PEX3*-deficient human cells. However, these PEX3 residues are in fact distant from the PEX19-binding site. They are located within helix α3, at the center of the protein, and are part of the solvent-inaccessible, hydrophobic core. These residues are therefore not able to interact with PEX19 in a physiological setting. The observed colocalization is probably due to unspecific binding of PEX19 to hydrophobic PEX3 regions. As sPEX3 residues 120–136 help to stabilize the protein fold, mutations in this region destabilize the entire α-helical bundle and are thus likely to abolish proper function of PEX3.

The surface analysis of sPEX3 reveals a mostly hydrophilic surface and strongly argues against the insertion of PEX3 into the peroxisomal membrane. Instead, our structure supports a model in which PEX3 is anchored to peroxisomes with a single sequence located at the N terminus but has no other direct contact with the lipid bilayer. An earlier study reported an interaction of the cytosolic domain of PEX3 with membrane lipids, based on the observation that PEX3 forms high molecular mass aggregates in the presence of mild detergents (50). This lipid binding property was assigned to hydrophobic residues in several predicted amphipathic helices. However, our structure shows that these hydrophobic residues are in fact part of the solvent-inaccessible core of the protein and are thus not available for interactions with lipids. As the lipid binding activity can be abolished by the addition of recombinant PEX19, a competing interaction between PEX3 and lipids on one side and PEX3 and PEX19 on the other side has been suggested (50). We note that the borders of the PEX19^Pep-binding groove, as well as a region just beyond the groove, exhibit a basic character due to the presence of highly conserved positively charged amino acids (Arg^{96}, Lys^{100}, and Lys^{324}) (Fig. 4 and supplemental Fig. S4). Thus, we cannot rule out the possibility that these 3 residues form favorable charge-charge interactions with membrane phospholipids, which are abolished once PEX19 engages PEX3 with high affinity. Although such interactions with phospholipids explain the observed lipid binding capacity of the cytosolic domain of PEX3 *in vitro*, they are not likely to be relevant under physiological conditions.

It is known that PEX19 is recycled back to the cytosol after cargo release into the peroxisomal membrane (32). Thus, the high affinity interaction between PEX3 and PEX19 must be disrupted to start a new insertion cycle. The structure of the complex does not offer any plausible scenarios for how this might occur. Subtle changes in pH are known to drive the association and dissociation of other large complexes. However, as the sPEX3-PEX19^Pep interface is largely hydrophobic, changes in pH are unlikely to affect its stability. Instead, we consider it more likely that other peroxins might play a role in this process.

Our results can serve as a model of the general mechanism of peroxisomal membrane protein import. Membrane insertion of PMPs has to involve the recruitment of PMP-loaded PEX19 to the peroxisome followed by positioning of the PMP directly adjacent to the membrane and its subsequent insertion. Although the PEX3-PEX19 complex formation is clearly explained by the structure presented here, the membrane positioning and insertion of PMPs remain speculative. It is known that PEX19 is composed of a flexible N-terminal domain and a compact, farnesylated C-terminal domain (51), with the farnesylation being crucial for correct PMP targeting to peroxisomes (52). It is likely that upon PEX19 binding to PEX3, the cargo-loaded C terminus of PEX19 is oriented close toward the peroxisomal membrane. This could involve either additional interactions with PEX3, perhaps mediated by the farnesyl group, or a direct insertion of the prenyl anchor into the peroxisomal membrane. The mechanism of PMP insertion could also involve PEX16. The release of cargo from PEX19 could be triggered by a conformational change in PEX19 or by binding of PMPs to PEX3. This might be sufficient for dissociation of the PEX3-PEX19 complex. One other possibility is that the affinity for PEX3 is reduced once PEX19 has unloaded its cargo. In support of this, it has been shown that the affinity of PEX3 for PEX19 carrying green fluorescent protein (GFP)-PMP24 is higher than for cargo-free PEX19 (27). Thus, cargo-loaded PEX19 could displace cargo-free PEX19 from PEX3 at the peroxisomal membrane to initiate a new insertion cycle.

In conclusion, our structure provides one of the first views of a complex between two peroxins at high resolution. It reveals essential structural features of sPEX3 and establishes a platform for understanding the parameters that guide its interactions with PEX19. Moreover, surface conservation analysis of sPEX3 provides a basis for potential interaction with other molecules and for the general role of PEX3 in peroxisomal membrane biogenesis.

REFERENCES

1. Wanders, R. J., and Waterham, H. R. (2006) *Biochim. Biophys. Acta* **1763**, 1707–1720
2. Schrader, M., and Fahimi, H. D. (2008) *Histochem. Cell Biol.* **129**, 421–440
3. Huybrechts, S. J., Van Veldhoven, P. P., Brees, C., Mannaerts, G. P., Los, G. V., and Fransen, M. (2009) *Traffic* **10**, 1722–1733
4. Weller, S., Gould, S. J., and Valle, D. (2003) *Annu. Rev. Genomics Hum. Genet.* **4**, 165–211
5. Steinberg, S. J., Dodt, G., Raymond, G. V., Braverman, N. E., Moser, A. B., and Moser, H. W. (2006) *Biochim. Biophys. Acta* **1763**, 1733–1748
6. Platta, H. W., and Erdmann, R. (2007) *Trends Cell Biol.* **17**, 474–484
7. Kiel, J. A., Veenhuis, M., and van der Klei, I. J. (2006) *Traffic* **7**, 1291–1303
8. Tabak, H. F., Hoepfner, D., Zand, A., Geuze, H. J., Braakman, I., and Huynen, M. A. (2006) *Biochim. Biophys. Acta* **1763**, 1647–1654
9. Girzalsky, W., Saffian, D., and Erdmann, R. (2010) *Biochim. Biophys. Acta* **1803**, 724–731
10. Alencastre, I. S., Rodrigues, T. A., Grou, C. P., Fransen, M., Sá-Miranda, C., and Azevedo, J. E. (2009) *J. Biol. Chem.* **284**, 27243–27251
11. Fujiki, Y., Matsuzono, Y., Matsuzaki, T., and Fransen, M. (2006) *Biochim. Biophys. Acta.* **1763**, 1639–1646

12. Matsuzono, Y., Kinoshita, N., Tamura, S., Shimozawa, N., Hamasaki, M., Ghaedi, K., Wanders, R. J., Suzuki, Y., Kondo, N., and Fujiki, Y. (1999) *Proc. Natl. Acad. Sci. U.S.A.* **96,** 2116–2121

13. South, S. T., and Gould, S. J. (1999) *J. Cell Biol.* **144,** 255–266

14. Ghaedi, K., Tamura, S., Okumoto, K., Matsuzono, Y., and Fujiki, Y. (2000) *Mol. Biol. Cell* **11,** 2085–2102

15. Muntau, A. C., Mayerhofer, P. U., Paton, B. C., Kammerer, S., and Roscher, A. A. (2000) *Am. J. Hum. Genet.* **67,** 967–975

16. South, S. T., Sacksteder, K. A., Li, X., Liu, Y., and Gould, S. J. (2000) *J. Cell Biol.* **149,** 1345–1360

17. Voorn-Brouwer, T., Kragt, A., Tabak, H. F., and Distel, B. (2001) *J. Cell Sci.* **114,** 2199–2204

18. Toro, A., Arredondo, C., Córdova, G., Araya, C., Palacios, J. L., Venegas, A., Morita, M., Imanaka, T., and Santos, M. J. (2007) *Biol. Res.* **40,** 231–249

19. Hoepfner, D., Schildknegt, D., Braakman, I., Philippsen, P., and Tabak, H. F. (2005) *Cell* **122,** 85–95

20. Kragt, A., Voorn-Brouwer, T., van den Berg, M., and Distel, B. (2005) *J. Biol. Chem.* **280,** 34350–34357

21. Tam, Y. Y., Fagarasanu, A., Fagarasanu, M., and Rachubinski, R. A. (2005) *J. Biol. Chem.* **280,** 34933–34939

22. Kim, P. K., Mullen, R. T., Schumann, U., and Lippincott-Schwartz, J. (2006) *J. Cell Biol.* **173,** 521–532

23. Toro, A. A., Araya, C. A., Córdova, G. J., Arredondo, C. A., Cárdenas, H. G., Moreno, R. E., Venegas, A., Koenig, C. S., Cancino, J., Gonzalez, A., and Santos, M. J. (2009) *J. Cell. Biochem.* **107,** 1083–1096

24. Geuze, H. J., Murk, J. L., Stroobants, A. K., Griffith, J. M., Kleijmeer, M. J., Koster, A. J., Verkleij, A. J., Distel, B., and Tabak, H. F. (2003) *Mol. Biol. Cell* **14,** 2900–2907

25. Sacksteder, K. A., Jones, J. M., South, S. T., Li, X., Liu, Y., and Gould, S. J. (2000) *J. Cell Biol.* **148,** 931–944

26. Jones, J. M., Morrell, J. C., and Gould, S. J. (2004) *J. Cell Biol.* **164,** 57–67

27. Pinto, M. P., Grou, C. P., Alencastre, I. S., Oliveira, M. E., Sá-Miranda, C., Fransen, M., and Azevedo, J. E. (2006) *J. Biol. Chem.* **281,** 34492–34502

28. Rottensteiner, H., Kramer, A., Lorenzen, S., Stein, K., Landgraf, C., Volkmer-Engert, R., and Erdmann, R. (2004) *Mol. Biol. Cell* **15,** 3406–3417

29. Fang, Y., Morrell, J. C., Jones, J. M., and Gould, S. J. (2004) *J. Cell Biol.* **164,** 863–875

30. Fransen, M., Vastiau, I., Brees, C., Brys, V., Mannaerts, G. P., and Van Veldhoven, P. P. (2005) *J. Mol. Biol.* **346,** 1275–1286

31. Matsuzono, Y., Matsuzaki, T., and Fujiki, Y. (2006) *J. Cell Sci.* **119,** 3539–3550

32. Matsuzono, Y., and Fujiki, Y. (2006) *J. Biol. Chem.* **281,** 36–42

33. Kammerer, S., Holzinger, A., Welsch, U., and Roscher, A. A. (1998) *FEBS Lett.* **429,** 53–60

34. Soukupova, M., Sprenger, C., Gorgas, K., Kunau, W. H., and Dodt, G. (1999) *Eur. J. Cell Biol.* **78,** 357–374

35. Matsuzaki, T., and Fujiki, Y. (2008) *J. Cell Biol.* **183,** 1275–1286

36. Lützner, N., Pätzold, B., Zoll, S., Stehle, T., and Kalbacher, H. (2009) *Biochem. Biophys. Res. Commun.* **380,** 554–558

37. Kabsch, W. (1993) *J. Appl. Crystallogr.* **26,** 795–800

38. Collaborative Computational Project Number 4 (1994) *Acta Crystallogr. D Biol. Crystallogr.* **50,** 760–763

39. Storoni, L. C., McCoy, A. J., and Read, R. J. (2004) *Acta Crystallogr. D Biol. Crystallogr.* **60,** 432–438

40. Treiber, N. (2008) *De novo generation and structural analysis of a protein-protein contact; towards structural characterisation of the peroxins PEX19 and PEX3; crystal structure of a mosquitocidal holotoxin and an aromatic flavin monooxygenase.* Ph. D. thesis, Albert-Ludwigs-Universität, Freiburg, Germany

41. Emsley, P., and Cowtan, K. (2004) *Acta Crystallogr. D Biol. Crystallogr.* **60,** 2126–2132

42. Murshudov, G. N., Vagin, A. A., and Dodson, E. J. (1997) *Acta Crystallogr. D Biol. Crystallogr.* **53,** 240–255

43. Painter, J., and Merritt, E. A. (2006) *Acta Crystallogr. D Biol. Crystallogr.* **62,** 439–450

44. Baker, N. A., Sept, D., Joseph, S., Holst, M. J., and McCammon, J. A. (2001) *Proc. Natl. Acad. Sci. U.S.A.* **98,** 10037–10041

45. Adams, P. D., Afonine, P. V., Bunkóczi, G., Chen, V. B., Davis, I. W., Echols, N., Headd, J. J., Hung, L. W., Kapral, G. J., Grosse-Kunstleve, R. W., McCoy, A. J., Moriarty, N. W., Oeffner, R., Read, R. J., Richardson, D. C., Richardson, J. S., Terwilliger, T. C., and Zwart, P. H. (2010) *Acta Crystallogr. D Biol. Crystallogr.* **66,** 213–221

46. Kraulis, P. (1991) *J. Appl. Crystallogr.* **24,** 946–950

47. Holm, L., Kääriäinen, S., Rosenström, P., and Schenkel, A. (2008) *Bioinformatics* **24,** 2780–2781

48. Guerler, A., and Knapp, E. W. (2008) *Protein Sci.* **17,** 1374–1382

49. Sato, Y., Shibata, H., Nakano, H., Matsuzono, Y., Kashiwayama, Y., Kobayashi, Y., Fujiki, Y., Imanaka, T., and Kato, H. (2008) *J. Biol. Chem.* **283,** 6136–6144

50. Pinto, M. P., Grou, C. P., Fransen, M., Sá-Miranda, C., and Azevedo, J. E. (2009) *Biochim. Biophys. Acta* **1793,** 1669–1675

51. Shibata, H., Kashiwayama, Y., Imanaka, T., and Kato, H. (2004) *J. Biol. Chem.* **279,** 38486–38494

52. Rucktäschel, R., Thoms, S., Sidorovitch, V., Halbach, A., Pechlivanis, M., Volkmer, R., Alexandrov, K., Kuhlmann, J., Rottensteiner, H., and Erdmann, R. (2009) *J. Biol. Chem.* **284,** 20885–20896

53. Kabsch, W., and Sander, C. (1983) *Biopolymers* **22,** 2577–2637

54. Larkin, M. A., Blackshields, G., Brown, N. P., Chenna, R., McGettigan, P. A., McWilliam, H., Valentin, F., Wallace, I. M., Wilm, A., Lopez, R., Thompson, J. D., Gibson, T. J., and Higgins, D. G. (2007) *Bioinformatics* **23,** 2947–2948

55. Waterhouse, A. M., Procter, J. B., Martin, D. M., Clamp, M., and Barton, G. J. (2009) *Bioinformatics* **25,** 1189–1191

Insights into Peroxisome Function from the Structure of PEX3 in Complex with a Soluble Fragment of PEX19

Friederike Schmidt[1,5], Nora Treiber[2,5,6], Georg Zocher[1], Sasa Bjelic[3], Michel O. Steinmetz[3], Hubert Kalbacher[1], Thilo Stehle[1,4*]and Gabriele Dodt[1*]

From the [1]Interfaculty Institute for Biochemistry, University of Tübingen, 72076 Tübingen, Germany, the [2]Institute for Organic Chemistry and Biochemistry, University of Freiburg, 79106 Freiburg,Germany, the [3]Biomolecular Research, Structural Biology, Paul Scherrer Institut, 5232 Villigen PSI, Switzerland, and the [4]Department of Pediatrics, Vanderbilt University School of Medicine, Nashville, TN 37232, USA

[5] These authors contributed equally to this work.

[6] Current address: Max-Planck Institute of Immunobiology, Department of Cellular and Molecular Immunology, 79108 Freiburg, Germany

Supplementary Information
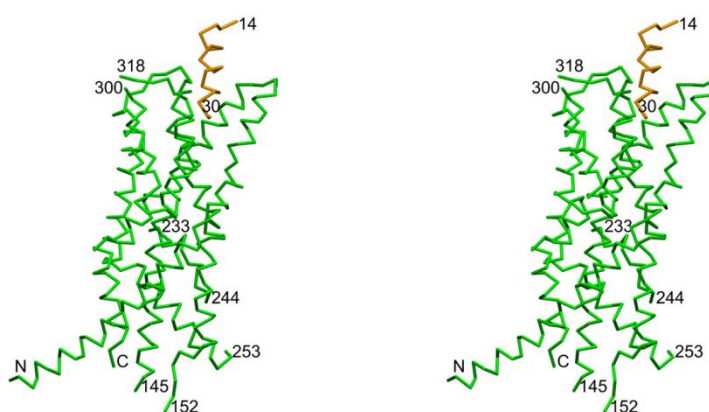
FIGURE S1. **Overall structure of the sPEX3-PEX19^Pep complex.** Stereo view of sPEX3 (green) in complex with PEX19^Pep (orange). The termini of loops missing in the electron density maps are labelled. The stereo view was made using molscript (46).
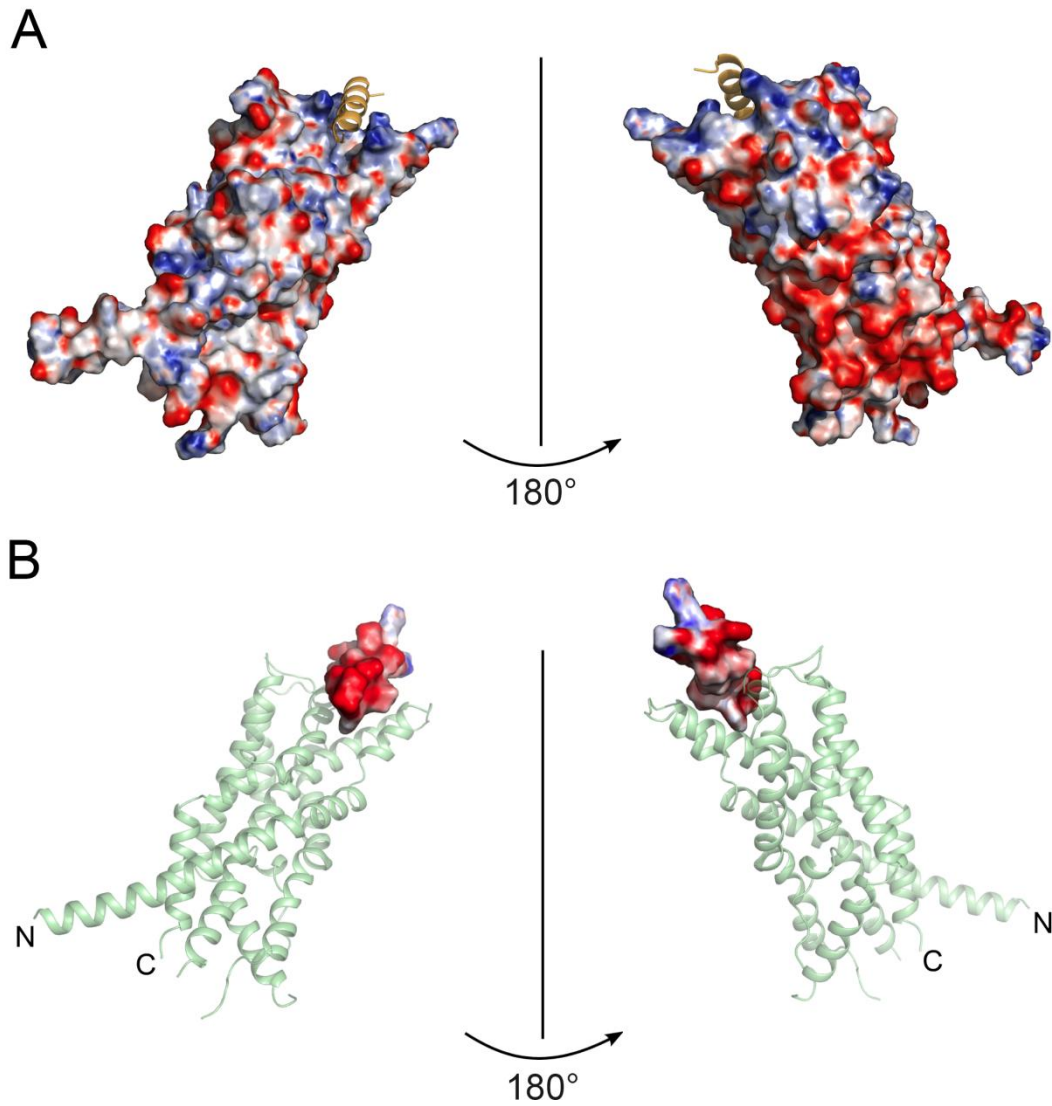
FIGURE S2. **Electrostatic surface potentials of sPEX3 and PEX19^{Pep}.** Two views, differing by 180 degrees along a vertical axis, are shown for each protein. The color scheme ranges from red (-12 kT) to blue (12 kT). The maps were calculated using APBS (44) in Pymol. *A* Electrostatic surface potential of sPEX3. PEX19^{Pep} is shown as an orange ribbon. The view on the right hand side reveals a highly negative electrostatic potential at the base of sPEX3. *B* Electrostatic surface potential of PEX19^{Pep}. sPEX3 is shown as a pale green ribbon. PEX19^{Pep} displays a highly negative electrostatic surface potential.
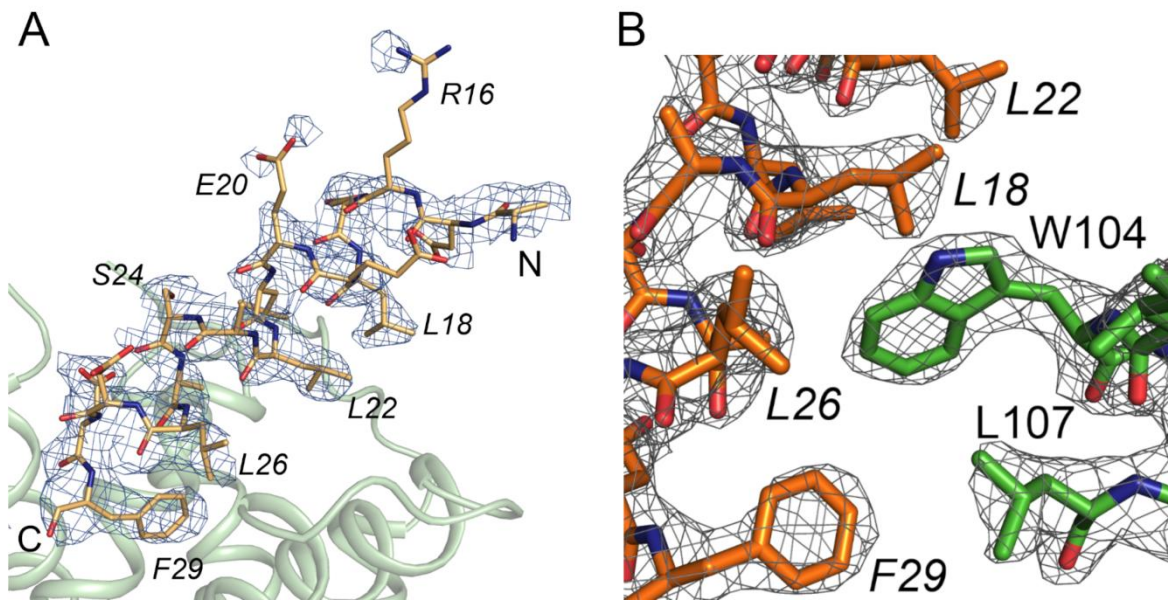
FIGURE S3. **Experimental electron densities.** *A* Simulated annealing omit map for PEX19[Pep], contoured at a σ-level of 1.0. sPEX3 is shown as a pale green ribbon, and PEX19[Pep] is represented with a stick model. *B* Final 2Fo-Fc electron density map, centered at Trp104 and contoured at a σ-level of 1.0. Labels in italics correspond to PEX19[Pep], labels in regular font correspond to sPEX3.

A

Homo_sapiens 1 --MLRSVWNFLKRHKKKCIFLGTVLGGVYILGKYGQKKIRETQERE-------AAEYIAQARRQYHFESNQRTCNMT--------------VLSMLPT75
Mus_musculus 1 --MLRSMWNFLKRHKKKCIFLGTVLGGVYILGKYGQKKIRETQERE-------AAEYIAQARRQYHFESNQRTCNMT--------------VLSMLPT75
Ornithorhynchus_anatinus 1 ----MWNGAFPAKEQ-------GVYILGKYGQKKIKETQERE-------AAEYIAQARRQYHFESNQRTCNMT--------------VLSMLPA62
Gallus_gallus 1 --MLRSLWSFLKRHKKKCLVLGTFLGGVYILGKYGQKKIRETQERE-------AAEYIAQARRQYHFESNQRTCNMT--------------VLSMLPT75
Taeniopygia_guttata 1 ----MEIHNESDEGGSDPQEKRVYLLGKYGQKKIRETQERE-------AAEYIAQARRQYHFESNQRTCNMT--------------VLSMLPT68
Xenopus_laevis 1 ----MLSMWNFLKRHKKKFIIFVGAFAGSVYILGKYAQRKIRETQERE-------AAEYIAQARRQYHFESNQRTCNMT--------------VLSMLPA74
Danio_rerio 1 ----MLSSTWNFIKRHRKFITTGVFVGGVYILGKYAQRKIQEMQERE-------AAEYIAQARRQFHFESNQRTCNMT--------------VLSMLPT75
Pediculus_corporis 1 --MFTRFKNFFSRHRNKFITGVLGGVVLFLKIIQYKLREFQERQ-----AKEFLERARKQQHYDSIEKTCNLT--------------AMTLASTT74
Culex_quinquefasciatus 1 --MLAAVKNFFTRHRKFVVTGIVLGSGVFLIKIIQYKLREFQERQ-----AKEIAERFKRMQHYSTERTCNQT--------------VGLLAPT75
Tribolium_castaneum 1 MSVFSKVRNFFSRHRNKFIVGGVIIGGSIFLTRYAQQKLREWQEKE-----ALEFLDRNRKHQHFESIGRTCNQT--------------ILNLALA77
Nasonia_vitripennis 1 --MFTRIRNFFYNHRRKFLFSGVFFGTLIILARYARSKLREWQEKE-----VNELLERSRRQHFESTERTCDQT--------------VLMLSKN75
Anopheles_gambia 1 --MWSSIKDFIYRHRRKFITTGVVIGGSVFLLKWLQYKLRELQERQ-----AKEIGEKLKRMQHYECTDRTCNQT--------------LGLLSPA75
Apis_melifera 1 --MFSRLRGFVNRHRRKFIVGGIVVGS-IIFIRYTARRLREWQEKE-----IKDMLDRSKRRQYFECNERTCSQM--------------IVSLTST74
Branchiostoma_floridae 1 --MLGAVWNFIKRHKKKLIFAGVVVGGAVFLGKYAETKLRELQEKE-------MAEQLENARKKHHFDNNQRTCNMT--------------VLSMIPS75
Arabidopsis_thaliana 1 ---MDLVRGLWRKHRRKILVTTTCLGSGYLLYKLYNAHTRKLADLERELANERENDEIIKTOMKAHFDNIQMIADTT--------------TLPHAIHH82
Oryza_sativa 1 --MLASARGFWGRHRRKILVSLGVAGAGYAAYRYLDSHRRQLVRVEQRALEERAAEEIIKNQLQTHFENVQKISDTT--------------TLPFAMHY83
Ricinus_communis 1 ---MLSLRDFWRRHRRKILSLQLYKKGGPP--NALTPSEKLEILKSFTRLVVSLWAMTMLSLYIRVTQVNILGRHLYLATARVLGSSDLIEDIDLIERDG179
Strongylocentrotus_purpuratus 1 --MLGSIWNFVKRHRRKFLVLGAVAGGASLLYKYAEWKLKEWRETE-------EAECLAMARRAHHFESNQRTCNMT--------------VLSMIPK75
Nematostella_vectensis 1 --MWESIKGFFRRHRVKFVVGGIVITGIYIVSRYARWRLDEWRANQ-------ELEYIAQARKQHHFESNQRTCHLT--------------LYSLSPV75
Trichoplax_adhaerens 1 MTFMNAMYNFFNRHRRKIIISSAIAGGVVVLVKYSQWRLQKYIEGE-------TTLQMTRARMENHFNNNQKTCHLTSKTNSSIHTLISILTIISLLPN92

Conservation
---10001162233745010000000040466947430844467333 8-------32437353743189865466736 7---------------7437513

Homo_sapiens 76 LREALMQQINSESLTALIK---------NRPSNKLEIWEDLKIISFTRSTVAVYSTCMLVVLLRVQLNIIGGYIYLDNAAVGKNGT----TILAPPDV160
Mus_musculus 76 QQQYLSSIQHLLGDGLTEIIVTIIKQAVQKVLGSVSIKHSLSLLDEQKLKEIRILVE--QHQSS-W-----NDKDVSRSSLCQYMMPDEETPLA----246

Conservation
9563524 1+35439643-4----------3352896 35-84+96468675553+9+369-455996-7899-448753--0012400-----0060003

Homo_sapiens 161 QQQYLSSIQHLLGDGLTEIITVIKQAVQKVLGSVSIKHSLSLLDEQKLKEIRNLVE--QHKSSSW------INKDGSKPLLCHYMMPDEETPLA----247

Conservation
5539975544872240285226623523953147-44073324512362293235 2--02110--------------000723968200---------

Homo_sapiens 248 -----VQACGLSPRDITTIKILLNETRDMLESPDFSTVLNTCLNRGFSRLLDNMAEFFRPTEQDLQHGNSMN--------------------SLSSV318

Conservation
------02210000-151495287238960943195126642563275433234300--0000000--------------------------0014

Homo_sapiens 319 SLPLAKIIPIVNGQIHSVCS-------------ETPSHFVQDLLTMEQVKDFAANVYEAFSTPQQLEK-----------373

Conservation
4658-97974844545410000--------------------4222259528413222423646258445 30------------------

B

FIGURE S4. **Sequence conservation for PEX3 and PEX19 in different eukaryotic species.** *A*, Alignment of PEX3 sequences from different eukaryotic species. Conserved residues are shown in shades of green. Conservation scores ≥ 9 (9, 10[+], 11*) are displayed in the same color. *B*, N-terminal sequence alignment of PEX19. Conserved residues are shown in shades of orange. Conservation scores ≥ 9 (9, 10[+], 11*) are displayed in the same color. The alignments were performed with ClustalW (54) and displayed in Jalview (55).

Table S1. ITC affinity measurements

Summarized binding data for ITC experiments with different PEX3 and PEX19 proteins. F29A, A25L and A25Y denote single point mutations of PEX19[Pep], whereas 120-134 defines a PEX19 derived peptide, spanning amino acids 120-134, that was proposed as a second PEX3 binding region (30). Single measurements were done at 25 °C.

Binding partners	K_d [nM]	$\Delta H_{Binding}$ [kcal/mol]	Molar ratio
PEX3[26-373](C235S)-PEX19 FL[a]	9.3	-6.7	0.86
sPEX3[b]-PEX19[Pep]	330	-4.9	1.06
sPEX3-PEX19[Pep] F29A	n.b.[c]	n.b.	n.b.
sPEX3-PEX19[Pep] A25L	410	-1.9	1.10
sPEX3-PEX19[Pep] A25Y	n.b.	n.b.	n.b.
sPEX3-PEX19[Pep] 120-134	n.b.	n.b.	n.b.

[a] full-length, [b] PEX3[41-373](C235S), [c] no binding,

3.6 Functional analysis of conserved PEX3 regions

The data presented in this section were used to prepare a manuscript for publication. The obtained results and conclusions are summarized here. The figures and tables refer to the publication manuscript, which is placed directly after this section (page 65).

The role of conserved PEX3 regions in PEX19-binding and peroxisome biogenesis. Schmidt F, Dietrich D, Eylenstein R, Groemping Y, Stehle T, Dodt G. Manuscript submitted.

The crystal structure of sPEX3 in complex with a PEX19-derived peptide has been determined at 2.4 Å resolution. Based on this structure, a mapping of conserved residues identified three highly conserved regions on the surface of sPEX3: the PEX19-binding groove, a hydrophobic groove and an acidic cluster. Mutagenesis experiments elucidated the functional relevance of these regions during different steps in peroxisomal membrane biogenesis *in vitro* and *in vivo*. For this, selected amino acids were mutated within sPEX3 and full-length, C-terminally myc-tagged PEX3 (PEX3-myc, Figure 1). The obtained results provide insights into peroxisome membrane biogenesis and define a direct participation of PEX3 during insertion of peroxisomal membrane proteins. Finally, the combined data lead to an improved model for the multi-step process of peroxisome membrane biogenesis.

Experimental prerequisites

The analysis of functional PEX3 can be easily performed in PEX3-deficient fibroblasts. These cells are completely lacking peroxisomes or peroxisomal ghosts. If these ΔPEX3T cells are transiently transfected with a plasmid coding for *PEX3* carrying a C-terminal myc-tag, the complemented cells are able to develop peroxisomes *de novo*. 24 hours after transfection, first membrane vesicles, the so-called preperoxisomes, can be detected. These preperoxisomes exhibit positive staining for PEX3 or PEX16 (Figure 8) but lack other membrane proteins such as PEX14 (Figure 8). Membrane proteins and other proteins necessary for the import of matrix proteins are imported before matrix proteins are transported to peroxisomes. Import competent peroxisomes, which exhibit a positive staining for the matrix protein catalase, are detected 5-7 days after transfection. In this thesis, PEX16-YFP was cotransfected with PEX3 variants to induce preperoxisome formation and to better visualize these early membrane structures. omplementation rates are calculated 7 days after transfection by counting the number of

cells that show a positive peroxisomal staining for PEX14. Transfection rates are determined 2 days after transfection in human fibroblasts by counting all cells that feature a positive peroxisomal myc staining due to expression of PEX3-myc. All *in vitro* experiments were carried out with sPEX3, which exhibits a cysteine to serine mutation at position 235. To test for any impact of this mutation on PEX3 function, the same mutation was also introduced in the mammalian expression vector and the complementation rate was determined in ΔPEX3T cells. As the complementation ability of PEX3-myc C235S lies in the range of normal PEX3-myc (4.5 % vs. 4.7 %, respectively), any influence of the C235S mutation can be excluded.

Folding and stability of PEX3 mutants

First, CD-spectroscopy and thermal denaturation assays were performed with the sPEX3 variants that have been successfully mutated within the *E. coli* expression vector. In the CD-spectra, all proteins exhibit the same α-helical folding characteristics as sPEX3 (Figure S1A). Furthermore, the protein melting points were determined using a thermal denaturation assay by recording the CD-signal at 208 nm and simultaneously heating the samples to 95 °C. The melting points of the mutants lie in the same range or even higher compared with sPEX3 (Figure S1B). These results indicate that the inserted mutations interfere neither with protein folding nor with protein stability, and that the effects observed in subsequent experiments are not due to misfolded or *per se* instable protein.

Mutations in the PEX19-binding groove

The PEX19-binding groove is one of the three conserved regions on the surface of PEX3 (Figure 1). It is located on the top of the helical bundle and is composed of three distinct areas of PEX3. Within the groove, a leucine at position 93 was mutated to an asparagine, which has a similar size but a more hydrophilic character. This mutation diminished the affinity for full-length PEX19 as determined with ITC experiments (Figure 2B and 2E). The K_d-value for the L93N mutant is 3.7 µM, compared to sPEX3 with 14 nM (Figure 2A and 2E). The reduced affinity of sPEX3 L93N for PEX19 can be also detected by analytical SEC, where both proteins elute as individual species and do not form a complex anymore (Figure S2D). *In vivo*, the ~270-fold decrease in affinity is sufficient to abolish the complementation ability of PEX3-myc L93N in ΔPEX3T cells, where the peroxisomal membrane marker PEX14 is mislocalized to mitochondria (Figure 6A).

Lys324, which is also located in the PEX19-binding region, was exchanged to an alanine. The reduction in affinity for full-length PEX19 is less severe than that observed for the L93N mutant, with a K_d-value of 270 nM (Figure 2C and 2E). sPEX3 K324A is able to form a complex with PEX19 in solution that elutes as a single peak in gel filtration experiments (Figure S2D). As the data were obtained with a truncated version of PEX3 lacking the first 40 amino acids, full-length PEX3 was used in a transcription/translation experiment followed by coimmunoprecipitation to test for a possible interaction of PEX19 with the N-terminus of PEX3. In contrast to PEX3-myc, the mutant PEX3-myc L93N is no longer able to interact with PEX19 (Figure 2F, compare lane 1 and 3). This finding excludes a high affinity binding of PEX3 N-terminus to PEX19. The affinity of PEX3-myc K324A is high enough to detect the PEX3-PEX19 complex in the CoIP gel (Figure 2F, lane 4), although the PEX19 band is weaker than that for normal PEX3-myc. *In vivo*, however, the reduced affinity of the PEX3-myc mutant K324A becomes noticeable through a reduced ability to complement ΔPEX3T cells (Figure 6A and 6B). The complementation rate of PEX3-myc K324A (2.0 %) is reduced about 60 % compared to PEX3-myc (4.7 %).

Stabilization of PEX3 upon PEX19-binding

It is worth mentioning that both PEX3-myc variants with mutations in the PEX19-binding groove are expressed at lower levels in normal human fibroblasts compared to PEX3-myc (Figure 3A and 3B). As the mRNA levels of the overexpressed PEX3-myc mutants L93N and K342A are ~200-fold higher than for endogenous PEX3 (Figure S3B), it is likely that these mutants are also present at protein level. The transfection rates for PEX3-myc L93N and K324A are 2.7 % and 6.4 %, respectively, compared to a transfection rate of 12.4 % for PEX3-myc. As both mutants are properly folded and stable at least *in vitro* as analyzed with CD and thermal denaturation assays, this observation might be due to impaired PEX19-binding. To further support this hypothesis, a thermal denaturation assay was performed (Figure 4A). The melting point of sPEX3 in the presence of a PEX19-derived peptide, PEX19[Pep], is 54 °C, an increase about 10 °C compared to sPEX3 alone. The membrane-distal end of sPEX3 is fixed upon peptide binding, which provides rigidity and stability to the entire helical bundle, resulting in a higher melting point of the sPEX3-PEX19[Pep] complex. As binding to PEX19 stabilizes PEX3, the PEX3-myc mutants with the mutations in the PEX19-binding groove lose a stabilizing element. The stabilization effect on PEX3 upon PEX19-binding is

further supported by the fact that in PEX19-deficient cells, the PEX3 protein is almost not detectable (Figure 4B, lower panel), while the mRNA level is comparable to that of normal cells (P. Krensel, Dodt lab). The same is true for PEX19-knockdown cells, where PEX3 at protein level is reduced about 80 % compared to control cells (Figure 4B, lower panel). The reduced cellular protein levels of PEX3 in ΔPEX19T or PEX19 knock-down cells and PEX3-myc mutants L93N and K324A in normal cells may be explained by an increased degradation of unstable protein. Thus, the instability of the PEX3 protein can likely be attributed to either the impaired PEX19-binding or the complete absence of PEX19 in ΔPEX19T cells.

PEX3 targeting to peroxisomes

The two PEX3 mutants impaired in PEX19-binding (L93N, K324A) are still correctly targeted to peroxisomes in human fibroblasts (Figure 3A). To further investigate, whether PEX3 is localized to peroxisomes independently of PEX19, human fibroblasts were treated with siRNA against PEX19 and subsequently transfected with PEX3-myc or PMP70-myc plasmids to analyze their import competence (Figure 5). YFP-PTS1 was cotransfected to normalize for transfection efficiencies. In PEX19-knockdown cells, the endogenous PEX19 protein level is reduced about 83 % compared to control cells (Figure 4B, upper panel). PEX3-myc and PMP70-myc are exclusively found in peroxisomes in control cells and in knockdown cells without any mislocalization to other organelles (Figure 5A). However, there are fewer cells exhibiting a positive peroxisomal staining for PMP70-myc in PEX19-knockdown cells, probably due to a PMP import defect and subsequent degradation of not imported PMP70-myc (Figure 5B). On the other hand, PEX3-myc is imported to peroxisomes in PEX19-knockdown cells to the same extent as in control cells (Figure 5A), implying a PEX19-independent peroxisomal localization of PEX3. These results contradict previous findings of a PEX19-dependent PEX3 targeting to peroxisomes [75].

Mutations in the acidic cluster

A glutamate and an aspartate in the acidic cluster were each mutated to an alanine to abolish possible charge-charge interactions with a yet undefined binding partner (Figure 1). PEX3-myc E266A is expressed in normal fibroblasts to the same extent as PEX3-myc (12.6 %) (Figures 3B and S3A). Furthermore, the E266A mutation does not interfere with the abilities to complement ΔPEX3T cells (4.6 %; Figures 6B and S4) or to

bind full-length PEX19 (K_d=18 nM; Figure S2B and S2C). This indicates that the glutamate at position 266 is not involved in an additional, previously proposed PEX19-binding site [169]. In contrast, PEX3-myc D275A shows a 50 % reduced complementation ability in ΔPEX3T cells (Figures 6B and S4), although the expression levels in normal fibroblasts lie in the range of PEX3-myc (9.3 %; Figures 3B and S3A). As ITC experiments of sPEX3 D275A with full-length PEX19 are not available, a putative additional PEX3-PEX19 interaction via this aspartate cannot be excluded. However, the PEX3-myc mutants E266A and D275A are able to interact with PEX19 in a CoIP assay (Figure 2F, lane 8 and 9) implying that the PEX3-PEX19 interaction remains unaffected in both mutants.

Mutations in the hydrophobic groove

An isoleucine at position 140 and a leucine at position 165 in the hydrophobic groove were both mutated to an asparagine, which has a similarly sized amino acid side chain but exhibits more hydrophilic features (Figure 1). A double mutant carrying both mutations was also analyzed in cell culture experiments. sPEX3 I140N and sPEX3 L165N have the same affinity for full-length PEX19 as sPEX3, with a K_d-value of 18.3 and 20.9 nM, respectively (Figures 2D, 2E, S2A and S2C). Thus, a participation of the hydrophobic groove in a second PEX19-binding site can be excluded. In addition, CoIP experiments reveal that the PEX3-myc mutants I140N, L165N and the double mutant I140N*L165N are able to precipitate PEX19 (Figure 2F, lane 5-7). The transfection efficiency in human fibroblasts is lowered for PEX3-myc L165N (3.5 %; Figure 3A and 3B), but not for the PEX3-myc mutants I140N (10.4 %; Figures 3B and S3A) and I140N*L165N (13.7 %; Figures 3B and S3A). The decreased protein level for PEX3-myc L165N in human fibroblasts cannot be explained at the moment. As the mRNA level of PEX3-myc L165N is 170-fold higher than for endogenous PEX3 and correlates to 70 % of overexpressed PEX3-myc mRNA (Figure S3B), the reduced protein level is not due to a transcription defect. Surprisingly, PEX3-myc L165N and the I140N*L165N double mutant exhibit a reduced complementation rate for ΔPEX3T cells (0.8 and 0.9 %, respectively; Figures 6A, 6B and S4), whereas PEX3-myc I140N remains unaffected (3.9 %; Figures 6B and S4). This indicates, that the leucine to asparagine exchange at position 165 is responsible for the observed results. As sPEX3 L165N is not impaired in PEX19-binding, the reduced complementation efficiency of the correspondent PEX3-myc mutant must be caused by a different factor. There are two possibilities, which might

both explain the present findings: 1. The hydrophobic groove is involved in PMP insertion into the lipid phase of the peroxisomal membrane. Here, peroxisomal membranes can be formed but cannot be complemented with membrane proteins. 2. The hydrophobic groove is required for *de novo* peroxisome formation. In this case, the defect occurs in the very early stages of peroxisomal biogenesis, as peroxisomal membrane structures are not developed at all.

The role of the hydrophobic groove during peroxisome biogenesis

To further elucidate these two hypotheses, ΔPEX3T cells were cotransfected with PEX3-myc or different PEX3 mutants (L93N, K324A, E266A, L165N) in the presence of PEX16-YFP to better visualize newly formed peroxisomes (Figure 7A and B). The cells were analyzed for preperoxisome formation 24 hours after transfection. PEX3-myc exhibits an YFP-positive punctate staining pattern in 24.8 % of transfected cells. The two mutations located in the PEX19-binding groove (L93N, K324A) are impaired in preperoxisome formation as they show YFP-positive structures only in 8.2 and 9.9 % of transfected cells, respectively. This defect in *de novo* peroxisome biogenesis can probably be linked to the reduced PEX19-binding affinity. The requirement of an intact PEX3-PEX19 complex for *de novo* peroxisome formation has been shown previously in *S. cerevisiae* [38, 40, 41]. The E266A mutant is able to form preperoxisomes comparable to PEX3-myc (17.4 % of transfected cells), indicating a negligible role of the acidic cluster in the very early stages of *de novo* peroxisome biogenesis. Interestingly, PEX3-myc L165N, which carries the mutation in the hydrophobic groove, is capable of developing preperoxisomes to the same extent as PEX3-myc (19.2 % of transfected cells). Thus, the reduced complementation ability of PEX3-myc L165N can be rather attributed to a defect in inserting PMPs into the peroxisomal membrane than to a defect in preperoxisome formation.

The PEX3-PEX16 interaction

In mammalian cells, the only other known interaction partner of PEX3 is PEX16 [52, 75, 76]. To identify the regions of PEX3 involved in PEX16-binding, PEX19-deficient fibroblasts (ΔPEX19T) were transfected with different GFP-tagged versions of PEX3 in the absence or presence of PEX16-myc (Figure 9A and 9B). Twenty-four hours after transfection, cells were analyzed with immunofluorescence for cellular localization of the corresponding proteins. As ΔPEX19T cells do not contain peroxisomes, PEX16 is

found in the ER and in the cytosol. The N-terminus of PEX3, PEX3$^{1-33}$-GFP is detected mainly in mitochondria in the absence of PEX16-myc. In the presence of PEX16-myc, its cellular localization is partly shifted to the ER, where a colocalization with PEX16 is observed. The C-terminal domain of PEX3, PEX3$^{34-373}$-GFP, is exclusively located in the cytosol independent of the presence of PEX16-myc. These findings indicate that the first N-terminal 33 amino acids of PEX3, the peroxisomal targeting signal and membrane anchor of PEX3, interact with PEX16. As the hydrophobic groove and the acidic cluster are both present on the cytosolic domain of PEX3, these regions are likely not involved in PEX16-binding.

Taken together, these results support a dual function of the PEX3-PEX19 complex in peroxisome biogenesis. In addition to its role in PMP insertion, a functional PEX3-PEX19 interaction is also required for *de novo* peroxisome biogenesis. Furthermore, the role of PEX16 as an interaction partner of PEX3 in the peroxisomal membrane was further evaluated and confirmed. Although PEX3 is localized to peroxisomes independently of PEX19, the stabilization of PEX3 upon PEX19-binding is quite striking. A more detailed model of peroxisome membrane biogenesis is discussed in section 4.

The role of conserved PEX3 regions in PEX19-binding and peroxisome biogenesis

Friederike Schmidt[1], Denise Dietrich[1], Roy Eylenstein[2], Yvonne Groemping[2], Thilo Stehle[1,3,*], and Gabriele Dodt[1,*]

[1] Interfaculty Institute of Biochemistry, University of Tübingen, D-72076 Tübingen, Germany

[2] Max-Planck Institute of Developmental Biology, Department of Protein Evolution, D-72076 Tübingen, Germany

[3] Department of Pediatrics, Vanderbilt University School of Medicine, Nashville, TN 37232, USA

ABSTRACT

The human peroxins PEX3 and PEX19 are essential for peroxisome biogenesis. They are involved in the posttranslational import of membrane proteins and in *de novo* formation of peroxisomes. PEX19 binds newly synthesized PMPs posttranslationally and directs them to peroxisomes by engaging PEX3, a protein anchored in the peroxisomal membrane. After protein insertion into the lipid bilayer, PEX19 is released back to the cytosol. Crystallographic analysis provided detailed insights into the PEX3-PEX19 interaction and identified three highly conserved regions on the surface of PEX3, the PEX19-binding groove, a hydrophobic groove and an acidic cluster. Here, we used site-directed mutagenesis to elucidate the role of these regions in PEX19-binding and in peroxisome biogenesis. We find that binding to PEX19 stabilizes PEX3. This interaction is however not essential for targeting PEX3 to peroxisomes via the classical posttranslational import pathway. Furthermore, we provide evidence for a crucial function of the PEX3-PEX19 complex during *de novo* formation of peroxisomes in peroxisome deficient cells. These findings support a dual function of the PEX3-PEX19 interaction in peroxisome biogenesis. The maturation of preperoxisomes appears to require the hydrophobic groove of PEX3, presumably by its involvement in peroxisomal membrane protein insertion.

INTRODUCTION

Peroxisomes have long been known for their essential contributions to a multitude of metabolic pathways, such as the beta-oxidation of very long and branched chained fatty acids, plasmalogen biosynthesis, or the degradation of H_2O_2 (1, 2). Defects in peroxisome biogenesis can be linked to mutations in *PEX* genes and form a group of inherited diseases, the peroxisome biogenesis disorders (3-7). Loss of one of the three peroxins PEX3, PEX16 or PEX19 results in severe cellular phenotypes in which cells are not able to develop detectable peroxisomal membrane structures but can be complemented by reintroduction of the corresponding cDNA (8-12). The phenomenon of peroxisomal *de novo* formation has been intensively investigated in yeast. In PEX3-deficient cells, newly synthesized PEX3 is first located in concentrated foci on the endoplasmic reticulum (ER) before new peroxisomes are formed in the presence of PEX19 (13-15). While this ER-dependent route has been found to occur in peroxisome-deficient cells, peroxisomes can multiply by growth and division in wild-type cells (16). Recently, it was proposed that ER-dependent peroxisome biogenesis is not restricted to *de novo* synthesis in mutant cells but serves as the main pathway in peroxisome biogenesis in all cells (17, 18). However, it is not known whether these findings can be generalized to mammalian cells. Although it has been described that newly synthesized PEX16 or PEX3 travels via the ER in PEX16- or PEX3-deficient cells, respectively (19, 20), it still is debated whether and to what extend this pathway is actually used when peroxisomes are present (21).

Posttranslational import of peroxisomal membrane proteins (PMPs) is initiated by the cytosolic receptor PEX19 (22), which binds to the membrane peroxisomal targeting sequence (mPTS) (23) of PMPs with its C-terminal domain (24). In addition, PEX19 acts as a chaperone for newly synthesized PMPs by shielding hydrophobic patches from the aqueous environment (25, 26). The N-terminus of PEX19 is sufficient and necessary to localize cargo-loaded PEX19 to peroxisomes (25, 27, 28), where it interacts with PEX3 (29-31). The cytosolic C-terminal domain of PEX3 forms an α-helical bundle and mediates the high affinity binding to PEX19 (32-34). PEX3 is anchored in the peroxisomal membrane with its first 34 N-terminal amino acid residues, which also harbor the information for its targeting to peroxisomes (35, 36). The mechanism of membrane insertion of PMPs and the role of ATP in PMP import remain to be elucidated. Whereas one study detected an ATP-dependent targeting of PEX19 to peroxisomes (22), other findings indicate a negligible role of ATP during the whole process (37, 38). In

addition to ATP hydrolysis, the thermodynamically favored embedding of transmembrane segments into the lipid bilayer might present a driving force for PMP insertion.

Based on the crystal structure of the cytosolic domain of PEX3 in complex with a PEX19-derived peptide (33), several surface mutations have been inserted into conserved regions of PEX3. These mutants were expressed in *E. coli*, purified and analyzed with respect to their folding characteristics and their ability to bind PEX19 *in vitro*. In addition, the full-length proteins were analyzed *in vivo* to define their localization in normal fibroblasts and their functionality in *de novo* peroxisome formation in PEX3-deficient cells. Our findings lead to a more detailed model for protein import into the peroxisomal membrane.

RESULTS

The soluble domain of human PEX3, which was crystallized in complex with a peptide derived from its interaction partner PEX19, folds into an elongated, α-helical bundle (33). At the peroxisome surface, the long N-terminal helix would be connected to a transmembrane-spanning segment that was not included in the crystallized protein (33, 34). The mostly hydrophobic PEX19-binding groove is located at the top of the helical bundle, distant from the membrane anchor. Analysis of the protein surface identified three highly conserved regions within PEX3: the binding groove for PEX19 at the top of the helical bundle, a hydrophobic groove near the base of the protein, and a cluster of acidic residues also near the base of PEX3 but on a different side (Figure 1) (33). Reasoning that conserved regions are rather likely to play a role in peroxisome biogenesis and binding to peroxisomal or other proteins, we mutated single amino acids in all three areas (Figure 1). Two mutations, K324A and L93N, are located in the binding region for PEX19. The K324 side chain interacts with PEX19 primarily via a hydrogen bond and a salt bridge, while L93 mediates hydrophobic interactions. Residues I140 and L165 were each mutated to an asparagine, a more hydrophilic residue of a similar size, in order to change the physical properties of the conserved hydrophobic groove. A double mutant (I140N*L165N) was also produced to further reduce the hydrophobicity in this area. Finally, residues E266 and D275 were individually mutated to alanine to probe the putative function of the acidic cluster by reducing its overall electrostatic potential.

Mutations do not influence the overall fold and the stability of recombinant sPEX3.

The mutations were introduced into an *E. coli* expression vector coding for human PEX3[41-373] with a cysteine to serine exchange at position 235. The corresponding protein (PEX3[41-373] C235S) is hereafter referred to as sPEX3 and is identical to the protein crystallized earlier (33). Six sPEX3 mutants (L93N, K324A, E266A, I140N, L165N and the double mutant I140N*L165N) were expressed in *E. coli* and purified to homogeneity using an established protocol (33). To test whether the mutations affect the overall fold of sPEX3, all mutants were subjected to circular dichroism (CD) spectroscopy. sPEX3 and the six mutants show similar spectra, with clear α-helical features represented by two minima of ellipticity at 208 and 220 nm (Figure S1A). This indicates that the mutagenesis did not alter the overall fold of the protein. However, CD spectroscopy can only reveal larger changes in the folding of a protein, and is not sensitive enough to detect smaller structural rearrangements or local unfolding. Therefore, the stabilities of the mutants were also analyzed using a thermal denaturation assay, in which a CD-signal was recorded at 208 nm while the sample was simultaneously heated to 95 °C. The melting point of sPEX3 was determined as 43 °C. As all mutants melt at similar or even higher temperatures (Figure S1B), we conclude that introduction of the mutations has no adverse effect on either fold or stability of sPEX3.

Mutations in the PEX19-binding region reduce the affinity of sPEX3 for PEX19.

The binding affinities of sPEX3 and the sPEX3 mutants for full-length PEX19 were determined using isothermal titration calorimetry (ITC). sPEX3 binds PEX19 with nanomolar affinity (K_d = 14 nM, Figure 2A, E), consistent with previous findings (32, 33). The mutations I140N, L165N and E266A do not result in significant changes of affinity, as the K_d values lie in the range of 20 nM for all three proteins (Figure 2D, Table 1 and Figure S2A-C). However, the mutations located in the PEX19-binding region influence the PEX3-PEX19 interaction properties. The K324A mutation lowers the affinity for PEX19 about 20-fold (K_d = 270 nM). This decrease is in agreement with the expected loss of one salt bridge and one hydrogen bond upon complex formation. The binding constant is still high enough to detect the complex formation between the K324A mutant and PEX19 in solution (Figure S2D). With a K_d value of 3.7 μM, the L93N mutant is severely impaired in PEX19-binding (Figure 2B, E). This decrease corresponds to a 250-fold affinity reduction compared to sPEX3. The observation that the complex of the

sPEX3 L93N mutant and PEX19 cannot be detected by gel filtration experiments (Figure S2D) confirms these results. The thermodynamic parameters of the interaction of sPEX3 mutants with PEX19 are listed in Table 1.

The N-terminus of PEX3 is not involved in high affinity PEX19-binding.
To exclude that the N-terminus of PEX3, which is absent in sPEX3 and the mutant proteins, influences the interaction with PEX19, we tested full-length PEX3 for the ability to bind PEX19 by coimmunoprecipitation (CoIP). All mutations (L93N, K324A, E266A, D275A, I140N, L165N and I140N*L165N) were introduced into the mammalian expression vector PEX3-myc, which encodes human full-length PEX3 with a C-terminal myc-tag. PEX19 and all PEX3-myc mutants were first transcribed and translated separately *in vitro*, then mixed, incubated for one hour and subjected to coimmunoprecipitation using beads coupled to α-myc antibodies. The translation products, the supernatants and the elution fractions were separated by SDS-PAGE prior to autoradiographic detection of the ^{35}S-methionine labeled proteins (Figure 2F). Full-length PEX3-myc and the mutants K324A, I140N, L165N, I140N*L165N, E266A and D275A are able to interact with PEX19, as indicated by its detection in the eluate. PEX3-myc L93N is no longer able to precipitate PEX19, as the corresponding PEX19-band is absent in the eluate (lane 3). In case of PEX3-myc K324A, PEX19 can be indeed detected in the eluated fraction (lane 4), however the corresponding band is weaker compared to PEX3-myc. The negative control (lane 2), where PEX19 was mock treated in the absence of PEX3-myc, excludes any unspecific binding of PEX19 to the beads. Thus, it is likely that the N-terminus of PEX3 is not involved in a high affinity interaction with PEX19.

All PEX3 mutants localize correctly to peroxisomes in human fibroblasts.
The different *PEX3-myc* plasmids used for CoIP experiments were also transfected in human fibroblast cells and the expressed proteins were tested for peroxisomal localization using indirect immunofluorescence microscopy. PEX3-myc and all mutants showed an unambiguous peroxisomal staining pattern and colocalized with the peroxisomal membrane protein PEX14 (Figure 3A and Figure S3A). However, the transfection rates differ significantly among some of the mutants (Figure 3B). The amount of transfected cells for the mutations E266A, D275A, I140N and the double mutation I140N*L165N lies in the same range as quantified for PEX3-myc (9-12 % of

total cells). With a transfection level of 3.5 %, a three-fold reduction was observed for the PEX3-myc L165N mutant. Interestingly, the two mutations located in the PEX19-binding region, L93N and K324A, both have decreased transfection rates of 2.7 % and 6.4 %, respectively, compared to PEX3-myc. As all PEX3-myc mutants are transcribed at the mRNA levels in amounts that are 120-250-fold higher than the mRNA of endogenous PEX3 (Figure S3B), it is likely that the PEX3-myc mutants were also present at the protein level.

The two PEX3 mutants L93N and K324A that are impaired in binding to PEX19 might be less stable in a cellular environment, resulting in a lower transfection rate compared to PEX3-myc. To further investigate this possibility *in vitro*, we analyzed the stability of recombinant sPEX3 in the presence of a PEX19-derived peptide comprising residues 14-33 (PEX19[Pep]), which has previously been shown to bind sPEX3 with high affinity (33). Thermal denaturation curves for sPEX3 alone and in combination with PEX19[Pep] were determined by recording the CD-signal at 208 nm (Figure 4A). The melting point of the sPEX3-PEX19[Pep]-complex is significantly shifted towards higher temperatures, indicating a higher thermal stability of almost 10 °C upon peptide-binding. Thus, PEX19-binding stabilizes PEX3 *in vitro.*

The postranslational import of newly synthesized PEX3 into peroxisomes is independent of PEX19.

As the two PEX3 mutants impaired in PEX19-binding still localized correctly to peroxisomes, we investigated whether newly synthesized PEX3 is imported into peroxisomes independently of PEX19. Normal human fibroblasts were treated either with siRNA against PEX19 (25) or with control siRNA. Immunoblotting against PEX19 revealed a severe reduction of the endogenous PEX19 protein level of 83 % compared to control cells (Figure 4B). Interestingly, PEX3 was also reduced in these PEX19-knockdown cells and in PEX19-deficient cells (Figure 4B), indicating that PEX3 is indeed more stable in the presence of PEX19. The siRNA-treated cells were subsequently transfected either with PEX3-myc or PMP70-myc. In both cases, YFP-PTS1 was cotransfected for normalization of transfection efficiency. Colocalization of PEX3-myc and PMP70-myc with the peroxisomal matrix marker YFP-PTS1 revealed a distinct peroxisomal staining in control cells as well as in PEX19-knockdown cells. PEX3-myc and PMP70-myc were exclusively detected in peroxisomes and were not mislocalized to

other organelles (Figure 5A). However, PMP70-myc was less frequently detected in cells treated with PEX19 siRNA, likely due to an import defect and subsequent degradation. These cells showed an 1.5-fold reduction in the ratio of PMP70-myc to YFP-PTS1 transfection rates compared to control cells (Figure 5B). However, this PEX19 reduction does not interfere with PEX3-myc import, as PEX3 was localized to peroxisomes to the same extent in control and PEX19-knockdown cells (Figure 5B). These findings support a discrete import pathway for PEX3 to peroxisomes that is independent of PEX19.

The PEX3 mutants differ in their efficiency to complement PEX3-deficient human fibroblasts.

As PEX3-deficient cells lack any detectable peroxisomes, PMPs are either mistargeted to other organelles or degraded (8, 9). For example, the peroxisomal membrane protein PEX14 is mislocalized to mitochondria in *ΔPEX3T* cells (Figure 6A, (8)), and analysis of PEX14 localization therefore can be used as an assay to study PEX3 function. A characteristic feature of functional PEX3 is the ability to induce formation of new peroxisomes in these PEX3-deficient cells. In complemented cells, PEX14 is detected in the restored peroxisomes. To determine the functionality of the different PEX3-myc mutants, *ΔPEX3T* cells were transfected with the corresponding plasmids and analyzed for restoration of peroxisomes 7 days after transfection. The amount of complemented cells for the PEX3-myc mutants I140N and E266A did not differ from the complementation level of PEX3-myc (4-5 % of total cells), whereas the mutant D275A lowered the complementation rate about 50 %. The import competence of these new peroxisomes was validated by immunofluorescence staining against the matrix protein catalase, which colocalizes with the peroxisomal membrane marker PEX14 (Figure S4). The PEX3-myc mutant K324A showed a significantly reduced complementation rate (2 % of total cells, Figure 6B). However, distinct peroxisomes that are import-competent for catalase were detected (Figure 6A). This reduced complementation efficiency may be explained by the reduced PEX19-binding affinity. In case of the L93N mutation, the complementation ability is lost, showing the typical mitochondrial mistargeting of PEX14 (Figure 6A) in *ΔPEX3T* cells (8). This observation is consistent with the severe impact of the PEX3 L93N mutation on PEX19-binding affinity. Interestingly, a defect in complementing PEX3-deficient human cells was also observed for the mutant L165N and the double mutant I140N*L165N (about 1 % of total cells, Figure 6B). Quantitative

analysis of complementation rates for PEX3-myc and all PEX3-myc mutants is shown in Figure 6B. The *in vitro* studies described above, used sPEX3, which carries a cysteine to serine mutation at position 235. The same mutation was now introduced into the PEX3-myc plasmid and then transfected into *ΔPEX3T* cells. As PEX3-myc C235S is able to complement *ΔPEX3T* cells to the same extent as PEX3-myc (4.2 %, Figure S4), we can exclude any negative impact of the C235S mutation on essential functions of PEX3.

Binding to PEX19 is important for the formation of preperoxisomes.
The overall complementation rate does not reflect the influence of PEX3 on the different steps necessary to create new peroxisomes. Cotransfection of PEX3 and PEX16 plasmids into *ΔPEX3T* cells leads to the formation of preperoxisomal structures within 24 hours. These vesicles do not contain the peroxisomal membrane marker PEX14, but exhibit a positive staining for PEX3 and PEX16 (see Figure 8). Here, these structures are defined as preperoxisomes. Later, these preperoxisomes import PEX14 and other membrane proteins, followed by the translocation of matrix proteins, finally leading to fully functional peroxisomes within 3-7 days (8, 39). We now investigated the impact of the PEX3-myc mutants L93N, K324A, E266A and L165N on the early stages of complementation in PEX3-deficient fibroblasts. PEX3-myc coexpressed with PEX16-YFP is able to form YFP-positive preperoxisomes (24,8 % of transfected cells) after 24 hours, while few YFP-positive punctate structures were detected with the control vector (4,2 % of transfected cells, Figure 7A, B). For the E266A mutant, 17.4 % of transfected cells exhibit YFP-positive punctate staining patterns. The L93N mutant shows a three-fold reduction in forming preperoxisomes compared to PEX3-myc (8,2 % of transfected cells). Additionally, the second mutation in the PEX19-binding groove, K324A, reduces the formation of preperoxisomes about 60 % (9,9 % of transfected cells, Figure 7B). Interestingly, the L165N mutant, which carries the mutation in the hydrophobic groove, reveals only a small reduction in preperoxisome formation (19,2 % of transfected cells), but is severely impaired in overall complementation efficiency of PEX3-deficient cells (Figure 6B). This implies that the hydrophobic groove is involved later in membrane biogenesis, presumably in the import of proteins into the peroxisomal membrane.

PMPs are imported posttranslationally into preperoxisomes.

The PEX3-PEX19-complex appears to be required for the formation of preperoxisomes that mature into peroxisomes by importing PMPs posttranslationally. To further support this hypothesis, PEX3-deficient cells were transfected with a PEX16-myc construct together with PEX3-YFP, PEX3-YFP L93N or PEX3-YFP L165N. For this experiment, the tags on the proteins were swapped so that the expression of the PEX3-YFP mutants could be easily monitored. The cells were subjected to immunofluorescence analysis one, two and three days after transfection. In case of PEX3-YFP, punctate preperoxisomes were detected after 24 hours. These structures were labeled with α-YFP and α-PEX16 antibodies (Figure 8A), but were negative for the PMPs PEX14 and PEX13. After 2-3 days, these preperoxisomal structures developed into functional peroxisomes harbouring PEX3-YFP, PEX14 and catalase (data not shown). PEX3-YFP L93N was primarily detected in the cytosol (Figure 8B) and failed to generate peroxisomes after 2-3 days, indicating a crucial function of the PEX3-PEX19 complex in the early stages of *de novo* biogenesis. The PEX3-YFP mutant L165N colocalized with PEX16 in preperoxisomes after 24 hours (Figure 8C), while PEX14 was only detected in mitochondria. After 2-3 days, the number of PEX3-YFP L16N-positive punctate structures has decreased remarkably perhaps due to degradation of import-defective preperoxisomes. However, the cells that exhibited a punctate YFP-staining after 3 days also showed a punctate PEX14 staining indicating new peroxisomes. These cells probably represent the small amount of complemented cells detected after 7 days (Figure 6).

The N-terminus of PEX3 colocalizes with PEX16 in the ER.

In addition to PEX19, only one other peroxin, PEX16, has been shown to interact with PEX3 in mammalian cells (20, 40). The observation that transfection of PEX16 into PEX19-deficient cells leads to a partial ER-localization of PEX16 (20) was used to test for a possible PEX3-PEX16 interaction visualized by colocalization of PEX3 and PEX16 in the ER. Therefore, PEX16-myc was coexpressed with truncated versions of PEX3 (PEX3[1-33]-GFP and PEX3[34-373]-GFP) in *ΔPEX19T* cells. The N-terminus of PEX3 colocalized with PEX16 in the ER (Figure 9A). However, when individually expressed in *ΔPEX19T* cells, this PEX3 variant was primarily detected in mitochondria (Figure 9A, B) and in the cytosol. The cytosolic domain of PEX3 (residues 34-373) is exclusively found in the

cytosol independent of PEX16-myc coexpression and therefore does not superpose with PEX16 localization in the ER. These findings suggest that the N-terminus of PEX3 mediates the interaction to PEX16 in the ER, which is consistent with previous studies that found direct PEX16 binding to the mPTS of PEX3 using immunoprecipitation assays (40). Furthermore, we can now exclude that the hydrophobic groove on the surface of PEX3 is involved in binding to PEX16, as reasoned previously (33). As all tested point mutations reside in the cytosolic domain, it is unlikely that the observed complementation defect of the L93N or the L165N mutants results from an impaired PEX3-PEX16 interaction.

DISCUSSION

The human peroxins PEX3 and PEX19 are essential for peroxisome membrane biogenesis including the posttranslational import of PMPs and the *de novo* peroxisome formation in peroxisome deficient cells. sPEX3 folds into an elongated α-helical bundle that engages a PEX19-derived peptide with high affinity in a conserved region at the membrane-distal end of the protein (33). However, little is known about additional interactions of these proteins with each other and also about their mode of interaction with other peroxisomal and non-peroxisomal proteins. Surface analysis of the sPEX3 structure identified two other regions with high levels of conservation in addition to the PEX19-binding groove: a hydrophobic groove at one side of sPEX3, and a cluster of acidic residues at a different side. It is tempting to speculate that the observed evolutionary conservation translates into specific functions of these three regions in peroxisome biogenesis. We have therefore probed the putative functions of all three regions using site-directed mutagenesis, *in vitro* binding assays and *in vivo* localization experiments. We find that mutations in the PEX19-binding groove destabilize PEX3 at the cellular level, but do not interfere with PEX3 targeting to the peroxisomal membrane. In addition, the interaction between the two peroxins is essential for preperoxisome formation. One mutant in the hydrophobic groove is selectively impaired in later stages of peroxisome biogenesis, most likely in posttranslational membrane protein import. The E266A mutation in the cluster of acidic residues did not affect either PEX19-binding or other stages in peroxisome biogenesis.

Based on the observation that full-length PEX19 binds PEX3 with a higher affinity than an N-terminal PEX19-derived peptide, a second PEX19-binding site was proposed to

exist in PEX3 (33). Due to their conservation, the hydrophobic groove and the acidic cluster were thought to be possible candidates for such a binding site (33). However, as mutations in either region (I140N, L165N, E266A) result in affinities for PEX19, which are comparable to sPEX3 (K_d = 15-20 nM) this possibility can now be excluded, at least for nonfarnesylated PEX19 used in this study. Furthermore, ITC measurements demonstrate that PEX3 mutations located in the PEX19-binding groove (L93N and K324A) reduce the affinity for PEX19 about 250- and 20-fold, respectively. However, the PEX3 protein used for K_d-value determination did not include the N-terminal transmembrane region. This region was proposed earlier to form a possible additional PEX19-binding site using pull-down assays with different splice variants of PEX19 (41). As the corresponding full-length PEX3 L93N mutant did not bind PEX19 in CoIP experiments, an interaction of the N-terminal transmembrane region of PEX3 with PEX19 is unlikely. However, the method used here and in previous studies (as reviewed in (31)) are not suitable to detect low affinity binding of the N-terminal first 34 amino acids of PEX3 and PEX19.

Pulse-chase experiments in CHO cells demonstrated that the presence of PEX19 extends the half-life of PEX3 (40). Our *in vitro* findings support this observation as binding to a PEX19-derived peptide leads to a significant increase in PEX3 stability. The interaction with PEX19 shields hydrophobic PEX3 residues from the aqueous environment (33). By inserting into the PEX3 groove, the PEX19-derived peptide also crosslinks the walls of the groove, limiting their thermal mobility. A comparable effect in terms of temperature stability has been observed in major histocompatibility complexes, which also become more stable upon peptide-binding to a groove that is similar in length to the one present in sPEX3 (42, 43). Remarkably, the mutations in the PEX19-binding region (L93N, K324A) exhibit a reduced cellular expression level. As both mutants are properly folded and stable *in vitro*, a destabilizing effect induced by the amino acids changes within PEX3 can be excluded. However, additional factors such as proteases or chaperones that might influence protein integrity and stability *in vivo* have to be considered. As the mRNA levels of these PEX3 mutants in fibroblasts are 200-fold higher than that of endogenous PEX3, the reduced expression levels are unlikely to be linked to mRNA instability. The diminished PEX19-binding may lower the stability of PEX3 and the more unstable protein undergoes subsequent degradation. Our findings that the PEX3 protein level is reduced in PEX19-knockdown and *ΔPEX19T* cells support this scenario. The mutations

in the acidic cluster are expressed in fibroblasts comparable to PEX3-myc. In addition, the E266A variant is neither impaired in complementation efficiency nor in preperoxisome formation. This leads to the conclusion that the glutamate at position 266 plays a negligible role in peroxisome biogenesis.

Recent siRNA experiments in HEK293 cells implicate PEX19 as a targeting receptor not only for PMPs, but also for PEX3 (40). We have employed a similar gene silencing approach using fibroblast cells and find that in this case, posttranslational PEX3 import into existing peroxisomes is independent of PEX19. In our case the PEX19 protein level is at least reduced by 83% and the import of PMP70 is impaired, while the PEX3-myc import seems unaffected. Our observation that PEX3 is targeted to peroxisomes independently of PEX19 is further supported by an unambiguous peroxisomal staining pattern in normal fibroblasts for the two PEX3 proteins that bear mutations in the PEX19-binding groove. These mutations severely decrease the affinity of PEX3 for PEX19, and in one case even prevent formation of a stable complex.

Our studies also reveal a strikingly reduced complementation level for PEX3 variants carrying mutations in the PEX19-binding groove. The PEX3 mutant L93N has lost the ability to complement PEX3-deficient human fibroblasts, while the corresponding ability of the K324A mutant is lowered by 60 %. These results agree with our *in vitro* PEX19 affinity studies for these two mutants (see above). A similar loss in complementing PEX19-deficient cells has been described for a PEX19 mutant in which F29, a residue involved in PEX3 binding, is replaced with an alanine (34). In that case, the mutation led to a 300-fold decrease in affinity compared to original PEX19 (32), consistent with our observation that a 250-fold affinity reduction for the interaction of the PEX3 L93N mutant with PEX19 is also sufficient to prevent complementation. Furthermore, the L93N mutant is not able to form preperoxisomes to the same extent as PEX3-myc. This suggests a crucial function of the PEX3-PEX19 complex already in the very first steps of peroxisome membrane biogenesis similar as described for yeast cells (13, 15, 44) and not only in the direct import of proteins into the peroxisomal membrane.

Surprisingly, the L165N and I140N*L165N mutants are severely impaired in the reconstitution of peroxisomes in *ΔPEX3T* cells. As the number of complemented cells for the single mutant at position 140 is comparable to PEX3-myc, we conclude that the observed effect is due to the amino acid change at position 165. Although the PEX3

L165N protein has a low expression level in normal fibroblasts, the mRNA is indeed generated. Furthermore, the double mutant I140N*L165N is highly expressed in normal cells but exhibits the same complementation defect. Thus, the reduced complementation efficiency of PEX3-myc L165N is unlikely due to the low expression levels. The PEX3 mutant L165N is still able to generate preperoxisomes at day one to almost the same extent as PEX3-myc. However, in most cells these preperoxisomes cannot be retained at the second and third day. Presumably they cannot import further membrane proteins, and the PEX3 proteins are localized to the cytosol or to mitochondria. Thus, the defect in complementation is more likely linked to a reduced import of PMPs into the peroxisomal membrane and not to a dysfunction in the early stages of membrane biogenesis.

Our results lead to a more informative model of PMP import by providing support for a specific role of PEX3 during PMP insertion (Figure 10). PEX19 directs newly synthesized PMPs in an import-competent form to the peroxisomal membrane. Here, PEX3, which is anchored to the peroxisomal membrane via its N-terminal region, is able to bind to PEX19 using its cytosolic domain. It is tempting to speculate that structural rearrangements within the PEX19-PMP complex upon binding to PEX3 allow access to previously covered hydrophobic patches of the PMP. Such rearrangements might explain why only ternary complexes comprising PEX3, PEX19 and a PMP have been described so far (22, 37). PEX3 likely adopts an active role in PMP import by offering the hydrophobic groove as a channel for the polypeptide chain that has to be inserted into the peroxisomal membrane. As depicted in Figure 1, the leucine at position 165 is located at the top of the hydrophobic groove. Mutation to an asparagine could interfere with PMP import because the channel entrance would feature a more polar residue. However, the insertion and the folding process of the PMP into the peroxisomal membrane need to be clarified in detail.

The present study leads to a more detailed view of peroxisome biogenesis and provides evidence for a dual role of the PEX3-PEX19 complex in *de novo* formation of peroxisomes and in posttranslational import of PMPs for the investigated mammalian system. Moreover, PEX3 is highly stabilized upon binding to PEX19 in solution. However, interaction with PEX19 is not essential for PEX3 targeting to peroxisomes, which implies a PEX19-independent posttranslational import of PEX3. These findings support the coexistence of *de novo* formation of peroxisomes in peroxisome-deficient cells and the

posttranslational import of membrane proteins in existing peroxisomes that proliferate and divide independently of *de novo* formation (18, 21, 45, 46).

MATERIALS AND METHODS

Plasmids

The plasmids containing the coding sequence for human sPEX3 (*HsPEX3$^{41-373}$* (C235S) in pET32a) and for human PEX19 (full-length *HsPEX19* in pColdI) used for expression in *E. coli* have been described previously (33). For expression studies in human fibroblasts full-length *HsPEX3* encoding a C-terminal myc-tag and two truncated versions with a C-terminal GFP-tag (PEX3$^{1-33}$-GFP and PEX3$^{34-373}$-GFP) (35), or a C-terminal YFP-tag (PEX3-YFP$^{1-373}$) (30) have been used. The PEX16-myc construct was generated by amplifying the ORF with the forward (5'-CCGGTACCAGGAATTCACCATGGAGAAGCTGCGGCTCC-3', GD119) and reverse primers (5'-CGGAGATCTGCCCCAACTGTAGAAGTAG-3'). The PCR product was cloned into the Acc65I and BamHI site of pcDNA3.1Zeo-myc followed by the coding sequence of the c-myc epitope. The PCR product amplified with GD119 and the reverse primer (5'-CGTCGACGCGCCCCAACTGTAGAAGTAD-3') using the PEX16-myc construct as template was cloned into the EcoRI and SalI site of pEYFP-N1 (Clontech) to generate PEX16-YFP. The plasmid PMP70-myc in pcDNA3 encoding the *HsPMP70* (*ABCD3*) with a C-terminal myc-epitope is a generous gift of Stephen Gould. YFP-PTS1 refers to pEYFP-Peroxi (Clontech).

Site-directed mutagenesis

Primers used for inserting point mutations in sPEX3, PEX3-myc or PEX3-YFP are listed in Table S1. *sPEX3* (sPEX3 in pET32a), *PEX3-myc* (PEX3-myc in pcDNA3.1zeo) and PEX3-YFP (PEX3 in pEYFP-N1) were used as template DNA for PCR amplification. The PCR products were digested overnight with DpnI (Fermentas) at 37 °C to remove parental methylated DNA. 2 μL of each PCR sample were transformed into *E. coli* DH5α cells and plasmid-containing clones were selected via ampicillin resistance on LB-agar plates. Several overnight cultures of LB-medium containing ampicillin were inoculated with individual clones. DNA preparation was carried out with *mi-Plasmid Miniprep Kit*

(Metabion) according to manufacturer's instructions. DNA was sent for sequencing (MWG Operon) to test for successful mutagenesis.

Protein expression and purification

PEX19 full-length protein, sPEX3 and the sPEX3 mutants were expressed and purified as described previously (33). Protein concentrations were determined by measurements of absorption at 280 nm using a NanoDrop ND-1000 (PeqLab). Analytical size exclusion chromatography was carried out with a Superdex™ 200 PC 3.2/30 (GE Healtchcare) in buffer A (10 mM Na_2HPO_4, 1.8 mM KH_2PO_4, 140 mM NaCl, 2.7 mM KCl, 0.5 mM tris-2-carboxyethyl-phosphine, pH 7.2).

Circular dichroism (CD) analysis

CD spectra were recorded with a Jasco J-720 spectropolarimeter. All purified proteins were used at concentrations of 10-15 μM in buffer B (5 mM Na_2HPO_4, 0.9 mM KH_2PO_4, 70 mM NaCl, 1.35 mM KCl, 0.25 mM tris-2-carboxyethyl-phosphine, pH 7.2). The spectra were recorded 8 times and corrected with the buffer spectrum. Thermal denaturation curves were recorded on a Jasco J-810 spectropolarimeter. The proteins were denatured with a scan rate of 1 °C/min from 20 to 95 °C measuring the CD signal at 208 nm. The purified proteins were used at concentrations of 10-15 μM in buffer C (10 mM Na_2HPO_4, 1.8 mM KH_2PO_4, 5 mM NaCl, pH 7.4).

Affinity measurements using isothermal titration calorimetry (ITC)

Binding studies between full-length PEX19 and different mutants of sPEX3 were carried out with a VP-ITC calorimeter (GE Healthcare). Six PEX3 proteins (sPEX3, K324A, E266A, I140N, L165N, I140N*L165N) were present in ~10 μM concentrations, whereas sPEX3 L93N was used at 25 μM concentration. PEX19 was injected stepwise at an 8- to 12-fold higher concentration (Table S2). All ITC experiments were performed once at 25 °C in buffer A. Data were fitted by least-squares procedures according to a one bindig site model using Microcal Origin® version 7.0.

In vitro transcription/translation and Coimmuno-precipitation (CoIP)

In vitro transcription and translation experiments were carried out with the TNT® Coupled Reticulocyte Lysate Systems (Promega) according to manufacturer's

instructions. The translation products were labeled with ^{35}S-methionine (37 TBq/mmol, Hartmann Analytik) for detection. The empty vector pcDNA3 was used as a negative control. 10 µL of the translated PEX19 were mixed with 10 µL of PEX3-myc, with the corresponding PEX3-myc mutants or with the negative control. The mixtures were incubated at 30 °C for 1 hour, and then subjected to CoIP experiments. 50 µL of Dynabeads® M-280 sheep α-mouse IgG (Invitrogen) were prepared according to the manufacturer's instructions using buffer D (20 mM HEPES, 110 mM KAc, 5 mM NaAc, 2 mM MgAc, 1 mM EDTA, pH 7.3) and loaded with mouse α-myc antibodies (Cell Signalling, 1:200) in the presence of 0.1 % (w/v) BSA overnight at 4 °C. After washing with buffer D, the beads were resuspended in 130 µL buffer E (buffer D with 0.5 % (v/v) Triton X100 and protease inhibitor cocktail (Sigma, 1:200)) and the translation mixtures were added. The samples were incubated under slight rotation for 2 hours at 4 °C and then placed on a magnet to separate the magnetic beads from the solvent. The supernatant was removed, immediately mixed with SDS-loading buffer and heated to 80 °C for 5 minutes. The beads were washed with buffer E, resuspended in 25 µL SDS-loading buffer and heated to 80 °C for 5 minutes. The tubes were then again placed onto the magnet to obtain the eluate. The samples were analyzed by 10 % SDS-PAGE. The gels were incubated in 0.5 M Na-salicylate (AppliChem) for 20 minutes, dried onto Whatman paper and exposed to an autoradiography film (BioMax MR film, Kodak) overnight.

Cell culture and transient transfection of human fibroblasts

The transformed human fibroblasts (GM5657T) were provided by Stephen Gould (Baltimore). The *PEX3*-deficient human fibroblasts (47) were a kind gift by Barbara Paton. The *PEX19*-deficient cells were obtained from Ron Wanders (Amsterdam). These fibroblasts were transformed with pRSV-SV40T as described (48) and referred to as *ΔPEX3T* and *ΔPEX19T* fibroblasts, respectively. Cells were cultured in Dulbecco's modified Eagle's medium (DMEM) containing 10 % fetal calf serum, 2 mM glutamine and 0.1 mM (50 mg/L) gentamicin at 37 °C and 8.5 % CO_2. In general, cells were seeded onto cover slips 24 hours before transfection, whereas *ΔPEX3T* cells used for complementation studies were grown in 25 cm^2 culture flasks. The cells were transfected transiently with the corresponding plasmid DNA using jetPEI (PeqLab) according to the manufacturer's instruction and prepared for indirect immunofluorescence microscopy one day *(ΔPEX19T*, *ΔPEX3T*), two days (GM5756T) or

seven days (*ΔPEX3T*) after transfection, respectively, unless otherwise indicated in the figure legend.

Indirect immunofluorescence microscopy

After washing three times with Dulbecco's-PBS (D-PBS, Gibco), cells on cover slips were fixed with formaldehyde (3 % in D-PBS) for 20 minutes. The fixed cells were permeabilized with Triton-X100 (1 % in D-PBS) for 5 minutes and washed three times with D-PBS. Incubation with primary antibodies was carried out for 30 minutes. After extensive washing with D-PBS, cells were incubated with secondary antibodies for 10 minutes. Following ten additional washing steps with D-PBS, cells were embedded in mowiol (100 mg/mL, Calbiochem) containing 2.5 mg/ml n-propylgallate (Fluka) prior to analysis by fluorescence microscopy. All steps were carried out at room temperature. Mouse primary antibodies against the C-terminal myc-tag were purchased from Cell Signalling and diluted 1:200. Rabbit polyclonal antibodies detecting PEX14 were raised against the first N-terminal 133 amino acids of human PEX14 and were used at an 1:400 dilution (49). Monoclonal α-AFP mouse antibodies (3E6) detecting all GFP variants (1:400 dilution) were purchased from QBiogene. The polyclonal antibodies against HsPEX16 (JH290) were a kind gift of Stephen Gould and used at an 1:100 dilution. Catalase antibodies produced in sheep were obtained from Binding Site and used at an 1:100 dilution. Antibodies against PEX13 (rabbit) were kindly provided by Marc Fransen (50) and used at an 1:250 dilution. Corresponding secondary antibodies were either donkey or goat IgGs conjugated with AlexaFluor-596 or AlexaFluor-488 (Molecular Probes, Invitrogen). Immunofluorescence images were acquired using a Zeiss Axiovert 200M fluorescence microscope equipped with an AxioPlan Apochromat 1.4 63x oil objective, an AxioPlan Neofluar 1.3 100x oil objective, and an AxioCam MRm camera in combination with AxioVision 4.7.2 software.

Knockdown of endogenous PEX19 with siRNA

Human skin fibroblasts (GM5756T) were electroporated twice either with 1 nmol (20 μM) siRNA against endogenous PEX19 (sense 5'-GAGAUCGCCAGGAGACACUTT-3'; (25) or with 1 nmol (20 μM) Negative Control siRNA (Qiagen) at an interval of 24 hours. For siRNA transfection cells were resuspended in DMEM and treated with 230 V for 25 ms. Afterwards, knockdown cells and control cells were transfected transiently either

with PEX3-myc or PMP70-myc using jetPEI (PeqLab) 24 hours after the second electroporation. In both cases, YFP-PTS1 was cotransfected in order to form the ratio of transfection rates. Indirect immunofluorescence staining was performed 6, 12 and 24 hours after plasmid transfection.

Immunoblotting

The siRNA transfected fibroblasts were harvested for immunoblotting 48 hours after the second electroporation. 20 µg of total protein were separated on a 12 % SDS-PAGE gel and transferred onto a polivinylidene fluoride membrane (GE healthcare) using a semidry blotting system (Biorad). Blots were blocked for 2 hours with 10 % (w/v) non-fat dry milk. The membranes were decorated for 2 hours with polyclonal rabbit α-PEX19 antibodies raised against the recombinant full-length PEX19 (see Protein expression and purification) at a dilution of 1:10000 in PBS-ST (10 mM Na_2HPO_4, 1.8 mM KH_2PO_4, 140 mM NaCl, 2.7 mM KCl, 0.02 % (w/v) SDS, 0.1 % (v/v) Triton-X100), polyclonal rabbit α-PEX3.1 antibodies (raised against $PEX3^{26-373}$ C235S purified as described in (33)) at a dilution of 1:1000 in PBS-ST, α-Tubulin-ß I+II antibodies (monoclonal mouse, Sigma) at a dilution of 1:2000 in TBS-T (100 mM Tris, 100 mM NaCl, pH7.4, 0.1 % (v/v) Tween) or α-Tubulin-α antibodies (monoclonal mouse, Sigma) at a dilution of 1:2000 in TBS-T. After washing, the membranes were incubated for 1 hour either with horseradish peroxidase-conjugated goat α-mouse IgGs or horseradish peroxidase-conjugated goat α-rabbit IgGs at a 1:15000 dilution (Sigma). The blots were washed and developed using enhanced chemoluminescence Western Blotting substrate (Thermo Scientific). All steps were carried out at room temperature.

Quantification of PEX3 mRNA levels

Human skin fibroblasts were transfected with PEX3-myc or the mutated PEX3-myc variants with jetPEI and harvested 24 hours after transfection. Total RNA was extracted (RNA spin Kit, PrepEase, USB) and subjected to cDNA synthesis (iScript, BioRad) according to the manufacturer's instruction. Quantitative real-time PCR was performed using Maxima SYBR Green/ROX qPCR Master Mix (Fermentas) and primers for PEX3 (forward 5'-GGCTGAGTTCTTTCGACCTACTG-3', reverse 5'-TCACTGCAAACTGAATGGATCTG-3') or Glyceraldehyde 3-phosphate dehydrogenase (GAPDH, forward 5'-CATCAAGAAGGTGGTGAAGCAG-3', reverse 5'-

CAAAGTGGTCGTTGAGGGGCAATG-3'). The PCR reactions were carried out in the StepOne Plus Real-time PCR System (Applied Biosystems) under following conditions: 50°C for 2 min, 95°C for 10 min, 40 cycles at 95°C for 15 sec and 60°C for 1 min followed by melting curve analysis. Data were collected at the 60°C step. The mRNA levels of PEX3-myc and PEX3-myc mutants compared to endogenous PEX3 were calculated via the $2^{-\Delta\Delta ct}$ Method (51).

ACKNOWLEDGMENTS

REFERENCES

1.   Schrader M, Fahimi HD. The peroxisome: still a mysterious organelle. Histochem Cell Biol 2008;129(4):421-440.

2.   Wanders RJ, Waterham HR. Biochemistry of mammalian peroxisomes revisited. Annu Rev Biochem 2006;75:295-332.

3.   Steinberg SJ, Dodt G, Raymond GV, Braverman NE, Moser AB, Moser HW. Peroxisome biogenesis disorders. Biochim Biophys Acta 2006;1763(12):1733-1748.

4.   Wanders RJ, Waterham HR. Peroxisomal disorders I: biochemistry and genetics of peroxisome biogenesis disorders. Clin Genet 2005;67(2):107-133.

5.   Wanders RJ, van Grunsven EG, Jansen GA. Lipid metabolism in peroxisomes: enzymology, functions and dysfunctions of the fatty acid alpha- and beta-oxidation systems in humans. Biochem Soc Trans 2000;28(2):141-149.

6.   Weller S, Gould SJ, Valle D. Peroxisome biogenesis disorders. Annu Rev Genomics Hum Genet 2003;4:165-211.

7.   Sacksteder KA, Gould SJ. The genetics of peroxisome biogenesis. Annu Rev Genet 2000;34:623-652.

8.   Muntau AC, Mayerhofer PU, Paton BC, Kammerer S, Roscher AA. Defective peroxisome membrane synthesis due to mutations in human PEX3 causes Zellweger syndrome, complementation group G. Am J Hum Genet 2000;67(4):967-975.

9.   Ghaedi K, Honsho M, Shimozawa N, Suzuki Y, Kondo N, Fujiki Y. PEX3 is the causal gene responsible for peroxisome membrane assembly-defective Zellweger syndrome of complementation group G. Am J Hum Genet 2000;67(4):976-981.

10.   South ST, Gould SJ. Peroxisome synthesis in the absence of preexisting peroxisomes. J Cell Biol 1999;144(2):255-266.

11.   Matsuzono Y, Kinoshita N, Tamura S, Shimozawa N, Hamasaki M, Ghaedi K, Wanders RJ, Suzuki Y, Kondo N, Fujiki Y. Human PEX19: cDNA cloning by functional complementation, mutation analysis in a patient with Zellweger syndrome, and potential role in peroxisomal membrane assembly. Proc Natl Acad Sci U S A 1999;96(5):2116-2121.

12.   Honsho M, Tamura S, Shimozawa N, Suzuki Y, Kondo N, Fujiki Y. Mutation in PEX16 is causal in the peroxisome-deficient Zellweger syndrome of complementation group D. Am J Hum Genet 1998;63(6):1622-1630.

13.   Lam SK, Yoda N, Schekman R. A vesicle carrier that mediates peroxisome protein traffic from the endoplasmic reticulum. Proc Natl Acad Sci U S A 2010;107(50):21523-21528.

14.   Tam YY, Fagarasanu A, Fagarasanu M, Rachubinski RA. Pex3p initiates the formation of a preperoxisomal compartment from a subdomain of the endoplasmic reticulum in Saccharomyces cerevisiae. J Biol Chem 2005;280(41):34933-34939.

15.   Hoepfner D, Schildknegt D, Braakman I, Philippsen P, Tabak HF. Contribution of the endoplasmic reticulum to peroxisome formation. Cell 2005;122(1):85-95.

16.   Motley AM, Ward GP, Hettema EH. Dnm1p-dependent peroxisome fission requires Caf4p, Mdv1p and Fis1p. J Cell Sci 2008;121(10):1633-1640.

17.   van der Zand A, Braakman I, Tabak HF. Peroxisomal membrane proteins insert into the endoplasmic reticulum. Mol Biol Cell 2010;21(12):2057-2065.

18.   Ma C, Agrawal G, Subramani S. Peroxisome assembly: matrix and membrane protein biogenesis. J Cell Biol 2011;193(1):7-16.

19.   Toro AA, Araya CA, Cordova GJ, Arredondo CA, Cardenas HG, Moreno RE, Venegas A, Koenig CS, Cancino J, Gonzalez A, Santos MJ. Pex3p-dependent peroxisomal biogenesis initiates in the endoplasmic reticulum of human fibroblasts. J Cell Biochem 2009;107(6):1083-1096.

20.   Kim PK, Mullen RT, Schumann U, Lippincott-Schwartz J. The origin and maintenance of mammalian peroxisomes involves a de novo PEX16-dependent pathway from the ER. J Cell Biol 2006;173(4):521-532.

21.   Huybrechts SJ, Van Veldhoven PP, Brees C, Mannaerts GP, Los GV, Fransen M. Peroxisome dynamics in cultured mammalian cells. Traffic 2009;10(11):1722-1733.

22.   Matsuzono Y, Fujiki Y. In vitro transport of membrane proteins to peroxisomes by shuttling receptor Pex19p. J Biol Chem 2006;281(1):36-42.

23.   Rottensteiner H, Kramer A, Lorenzen S, Stein K, Landgraf C, Volkmer-Engert R, Erdmann R. Peroxisomal membrane proteins contain common Pex19p-binding sites that are an integral part of their targeting signals. Mol Biol Cell 2004;15(7):3406-3417.

24.   Schueller N, Holton SJ, Fodor K, Milewski M, Konarev P, Stanley WA, Wolf J, Erdmann R, Schliebs W, Song YH, Wilmanns M. The peroxisomal receptor Pex19p forms a helical mPTS recognition domain. EMBO J 2010;29(15):2491-2500.

25.   Jones JM, Morrell JC, Gould SJ. PEX19 is a predominantly cytosolic chaperone and import receptor for class 1 peroxisomal membrane proteins. J Cell Biol 2004;164(1):57-67.

26.   Shibata H, Kashiwayama Y, Imanaka T, Kato H. Domain architecture and activity of human Pex19p, a chaperone-like protein for intracellular trafficking of peroxisomal membrane proteins. J Biol Chem 2004;279(37):38486-38494.

27.   Fransen M, Vastiau I, Brees C, Brys V, Mannaerts GP, Van Veldhoven PP. Analysis of human Pex19p's domain structure by pentapeptide scanning mutagenesis. J Mol Biol 2005;346(5):1275-1286.

28.   Matsuzono Y, Matsuzaki T, Fujiki Y. Functional domain mapping of peroxin Pex19p: interaction with Pex3p is essential for function and translocation. J Cell Sci 2006;119(17):3539-3550.

29.   Fang Y, Morrell JC, Jones JM, Gould SJ. PEX3 functions as a PEX19 docking factor in the import of class I peroxisomal membrane proteins. J Cell Biol 2004;164(6):863-875.

30.   Muntau AC, Roscher AA, Kunau WH, Dodt G. The interaction between human PEX3 and PEX19 characterized by fluorescence resonance energy transfer (FRET) analysis. Eur J Cell Biol 2003;82(7):333-342.

31.   Fujiki Y, Matsuzono Y, Matsuzaki T, Fransen M. Import of peroxisomal membrane proteins: the interplay of Pex3p- and Pex19p-mediated interactions. Biochim Biophys Acta 2006;1763(12):1639-1646.

32.   Sato Y, Shibata H, Nakano H, Matsuzono Y, Kashiwayama Y, Kobayashi Y, Fujiki Y, Imanaka T, Kato H. Characterization of the interaction between recombinant human peroxin Pex3p and Pex19p: identification of Trp-104 in Pex3p as a critical residue for the interaction. J Biol Chem 2008;283(10):6136-6144.

33.   Schmidt F, Treiber N, Zocher G, Bjelic S, Steinmetz MO, Kalbacher H, Stehle T, Dodt G. Insights into peroxisome function from the structure of PEX3 in complex with a soluble fragment of PEX19. J Biol Chem 2010;285(33):25410-25417.

34.   Sato Y, Shibata H, Nakatsu T, Nakano H, Kashiwayama Y, Imanaka T, Kato H. Structural basis for docking of peroxisomal membrane protein carrier Pex19p onto its receptor Pex3p. EMBO J 2010;29(24):4083-4093.

35.   Soukupova M, Sprenger C, Gorgas K, Kunau WH, Dodt G. Identification and characterization of the human peroxin PEX3. Eur J Cell Biol 1999;78(6):357-374.

36.   Kammerer S, Holzinger A, Welsch U, Roscher AA. Cloning and characterization of the gene encoding the human peroxisomal assembly protein Pex3p. FEBS Lett 1998;429(1):53-60.

37.   Pinto MP, Grou CP, Alencastre IS, Oliveira ME, Sa-Miranda C, Fransen M, Azevedo JE. The import competence of a peroxisomal membrane protein is determined by Pex19p before the docking step. J Biol Chem 2006;281(45):34492-34502.

38.   Diestelkötter P, Just WW. In vitro insertion of the 22-kD peroxisomal membrane protein into isolated rat liver peroxisomes. J Cell Biol 1993;123(6):1717-1725.

39.   Ghaedi K, Tamura S, Okumoto K, Matsuzono Y, Fujiki Y. The peroxin pex3p initiates membrane assembly in peroxisome biogenesis. Mol Biol Cell 2000;11(6):2085-2102.

40.   Matsuzaki T, Fujiki Y. The peroxisomal membrane protein import receptor Pex3p is directly transported to peroxisomes by a novel Pex19p- and Pex16p-dependent pathway. J Cell Biol 2008;183(7):1275-1286.

41.   Mayerhofer PU, Kattenfeld T, Roscher AA, Muntau AC. Two splice variants of human PEX19 exhibit distinct functions in peroxisomal assembly. Biochem Biophys Res Commun 2002;291(5):1180-1186.

42.   Fahnestock ML, Tamir I, Narhi L, Bjorkman PJ. Thermal stability comparison of purified empty and peptide-filled forms of a class I MHC molecule. Science 1992;258(5088):1658-1662.

43.   Bouvier M, Wiley DC. Structural characterization of a soluble and partially folded class I major histocompatibility heavy chain/beta 2m heterodimer. Nat Struct Biol 1998;5(5):377-384.

44.   Agrawal G, Joshi S, Subramani S. Cell-free sorting of peroxisomal membrane proteins from the endoplasmic reticulum. Proc Natl Acad Sci U S A 2011;108(22):9113-9118.

45.   Delille HK, Agricola B, Guimaraes SC, Borta H, Luers GH, Fransen M, Schrader M. Pex11pbeta-mediated growth and division of mammalian peroxisomes follows a maturation pathway. J Cell Sci 2010;123(16):2750-2762.

46.   Koch J, Pranjic K, Huber A, Ellinger A, Hartig A, Kragler F, Brocard C. PEX11 family members are membrane elongation factors that coordinate peroxisome proliferation and maintenance. J Cell Sci 2010;123(19):3389-3400.

47.   Poulos A, Christodoulou J, Chow CW, Goldblatt J, Paton BC, Orii T, Suzuki Y, Shimozawa N. Peroxisomal assembly defects: clinical, pathologic, and biochemical findings in two patients in a newly identified complementation group. J Pediatr 1995;127(4):596-599.

48.   Dodt G, Braverman N, Wong C, Moser A, Moser HW, Watkins P, Valle D, Gould SJ. Mutations in the PTS1 receptor gene, PXR1, define complementation group 2 of the peroxisome biogenesis disorders. Nat Genet 1995;9(2):115-125.

49.   Will GK, Soukupova M, Hong X, Erdmann KS, Kiel JA, Dodt G, Kunau WH, Erdmann R. Identification and characterization of the human orthologue of yeast Pex14p. Mol Cell Biol 1999;19(3):2265-2277.

50.   Fransen M, Wylin T, Brees C, Mannaerts GP, Van Veldhoven PP. Human pex19p binds peroxisomal integral membrane proteins at regions distinct from their sorting sequences. Mol Cell Biol 2001;21(13):4413-4424.

51.   Livak KJ, Schmittgen TD. Analysis of relative gene expression data using real-time quantitative PCR and the 2(-Delta Delta C(T)) Method. Methods 2001;25(4):402-408.

TABLES

Table 1. Thermodynamic parameters for the interaction of sPEX3 proteins and full-length PEX19.

Protein	K_d [nM]	ΔH [kcal/mol]	Molar ratio
sPEX3[a]	14.8	-9.3	0.89
sPEX3 L93N	3750	-10.4	0.90
sPEX3 K324A	270.3	-8.0	1.03
sPEX3 E266A	17.9	-9.4	0.94
sPEX3 I140N	18.3	-7.8	1.25
sPEX3 L165N	20.9	-5.6	0.87

[a]PEX3[41-373] C235S. All experiments were carried out at 25 °C and data were fit to a single binding isotherm.
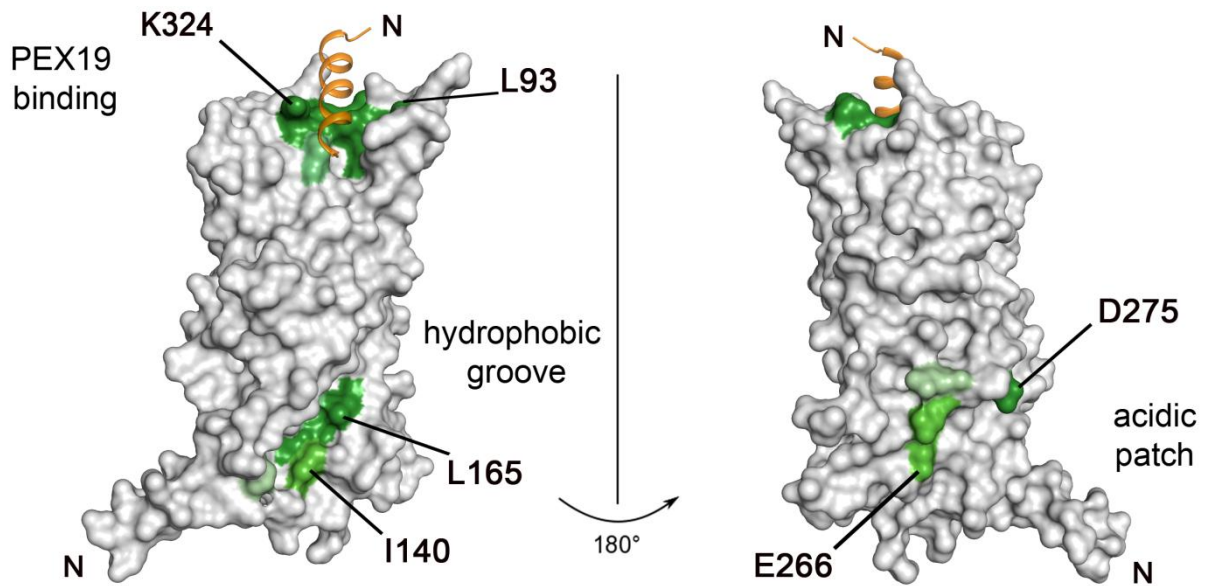
Figure 1. Distribution of conserved amino acids on the surface of sPEX3. Surface representations of sPEX3 with the bound PEX19-derived peptide depicted as an orange ribbon (PDB entry 3MK4, (33)) differ by 180°C along the indicated vertical axis. Conservation analysis of surface exposed residues revealed three conserved regions within sPEX3, which are highlighted in shades of green: The PEX19-binding groove at the top of the helical bundle, where amino acids L93 and K324 are located; a hydrophobic groove that includes amino acids I140 and L165; and an acidic cluster that is delineated by residues E266 and D275. The color code is the same as used in (33). Mutations in all three regions were inserted into sPEX3 for *in vitro* analysis and into PEX3-myc or PEX3-YFP for *in vivo* experiments.
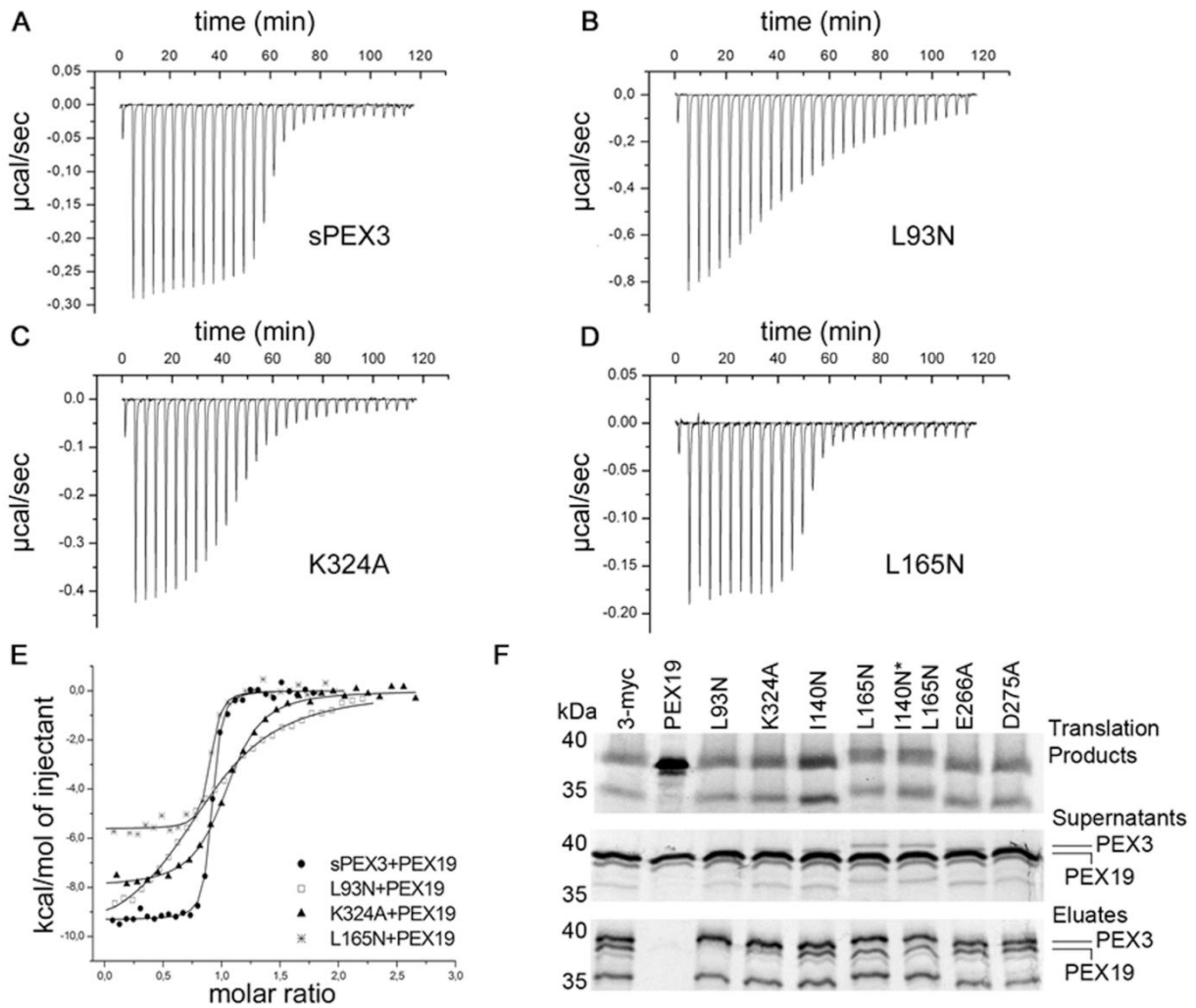
Figure 2. Analysis of complex formation between different sPEX3 mutants and PEX19 using ITC and CoIP experiments. Raw ITC-data for titrations of sPEX3 with PEX19 (A), sPEX3 L93N with PEX19 (B), sPEX3 K324A with PEX19 (C) and sPEX3 L165N with PEX19 (D) are shown. (E) Integrated heat values for the different ITC experiments showing fits to a single binding isotherm for the respective titrations. The data for affinity measurements of the mutants E266A and I140N with PEX19 are displayed in Supplemental Figure S2. (F) Autoradiography of CoIP experiments using full-length PEX3-myc and full-length PEX19. PEX3-myc, the corresponding mutants and PEX19 were obtained by an *in vitro* TNT assay, mixed and subjected to coimmunoprecipitations using α-myc antibodies coupled to magnetic beads. The translation products, the supernatants and the eluates are shown separately for each PEX3-myc mutant. All PEX3-myc mutants except PEX3-myc L93N precipitate PEX19. Note that the corresponding PEX19-band is lacking in the eluated fraction (lane 3) for PEX3-myc L93N.
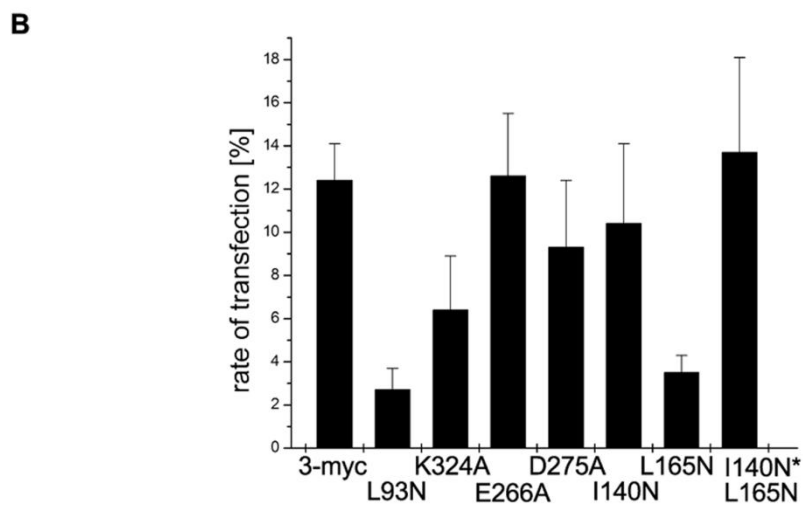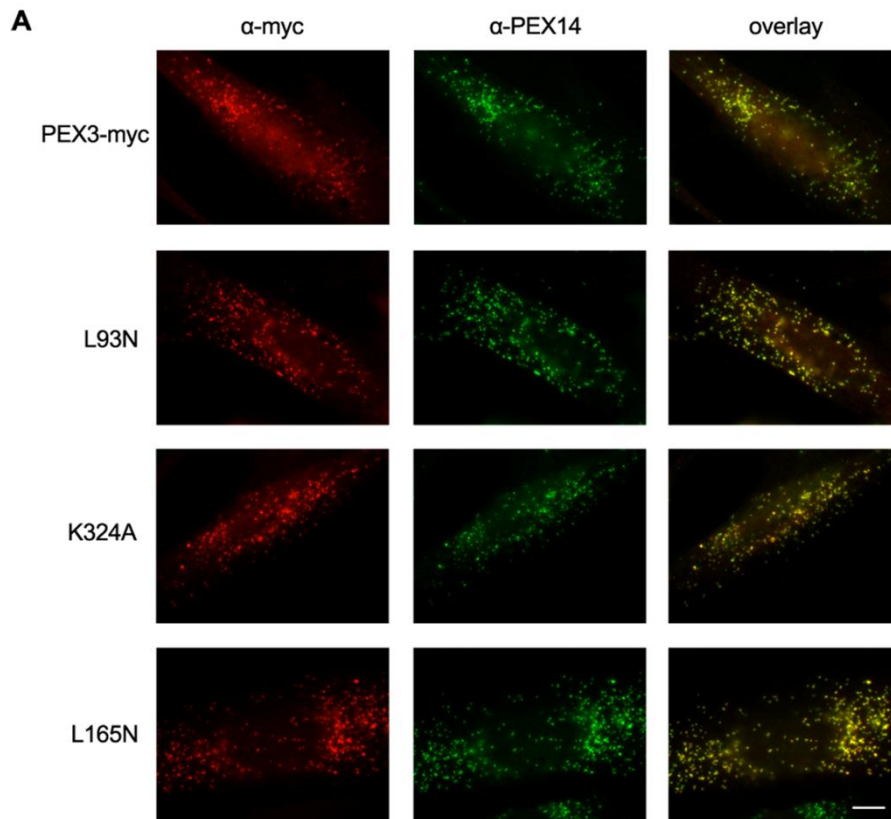
Figure 3. Peroxisomal localization of different PEX3-myc mutants in human fibroblasts. Normal fibroblasts (GM5756T) were transfected with the corresponding PEX3-myc plasmids. (A) Cellular localization of the expressed mutants was detected using α-myc antibodies two days after transfection. Peroxisomes were visualized using α-PEX14 antibodies. All PEX3-myc mutants reveal a peroxisomal distribution pattern validated by colocalization with PEX14. The pictures for PEX3-myc and for the representative mutants L93N, K324A and L165N are shown here, the mutants E266A, D275A, I140N and I140N*L165N are displayed in Supplemental Figure S3. Scale bar: 10 μm. (B) Rates of transfection, determined by the amount of cells that display a myc-positve peroxisomal staining, are quantified for the individual PEX3-myc mutants. For each of the three independent experiments, at least 500 cells were counted for calculation. Values were represented as means with standard deviations.
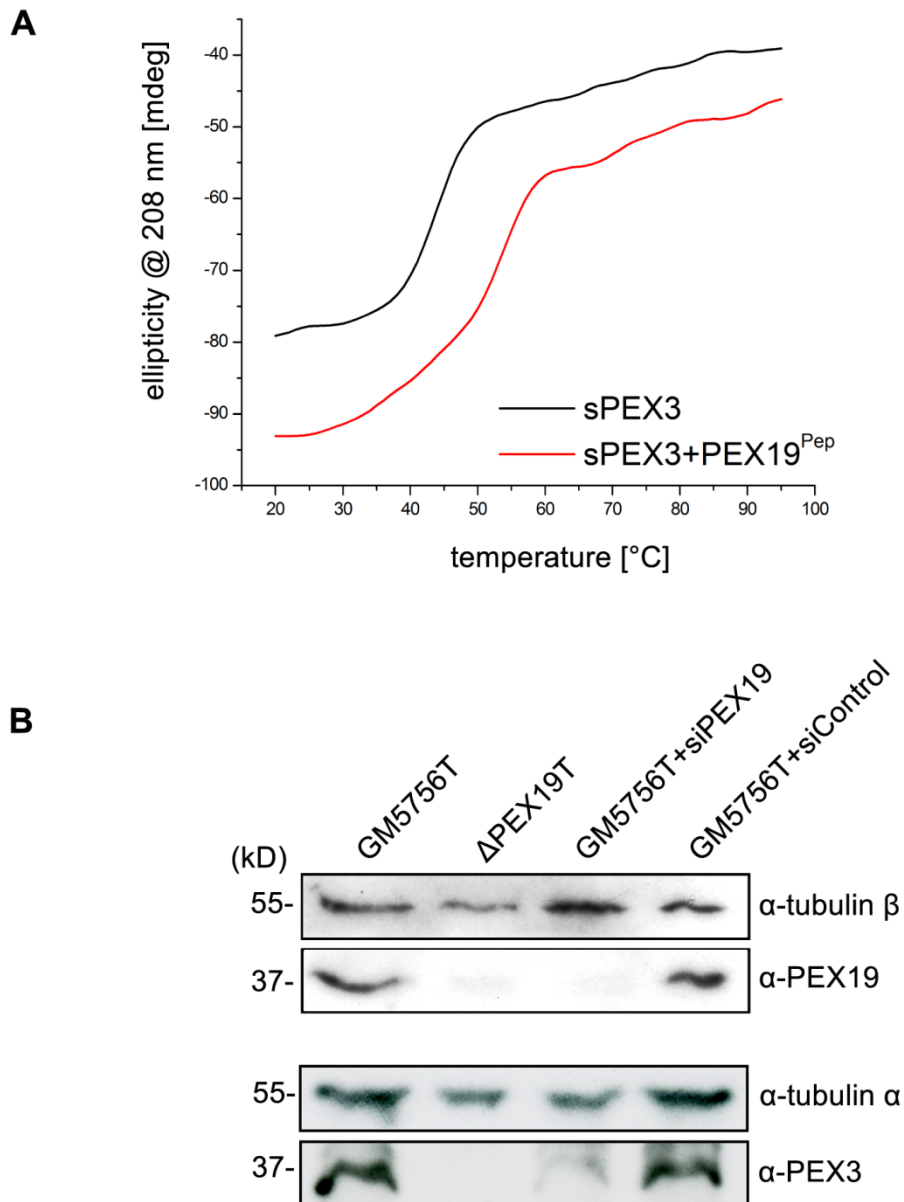
Figure 4. PEX3 is stabilized upon PEX19-binding. (A) Thermal denaturation curves for sPEX3 (black) and sPEX3+PEX19[Pep] (red). Protein solutions were used at a concentration of 12 μM. Melting curves were recorded with a scan rate of 1 °C/min at 208 nm to detect α-helical protein content. The temperature was raised stepwise to 95°C. The inflection point indicates the melting temperature of the protein, which is clearly shifted to higher temperatures in the presence of the PEX19-derived peptide. (B) Human fibroblasts (GM5756T) were electroporated twice either with siRNA against endogenous PEX19 or with control siRNA. To control the efficiency of PEX19 knockdown, cells were harvested 48 hours after the second electroporation. Equal amounts of total protein were separated by SDS-PAGE and analyzed by immunoblotting using antibodies against PEX19 and PEX3 and against tubulin-β and tubulin-α as protein loading controls. Quantification reveals an 83% reduction of PEX19 protein and an 87% reduction of PEX3 protein in PEX19-knockdown cells compared to control cells.
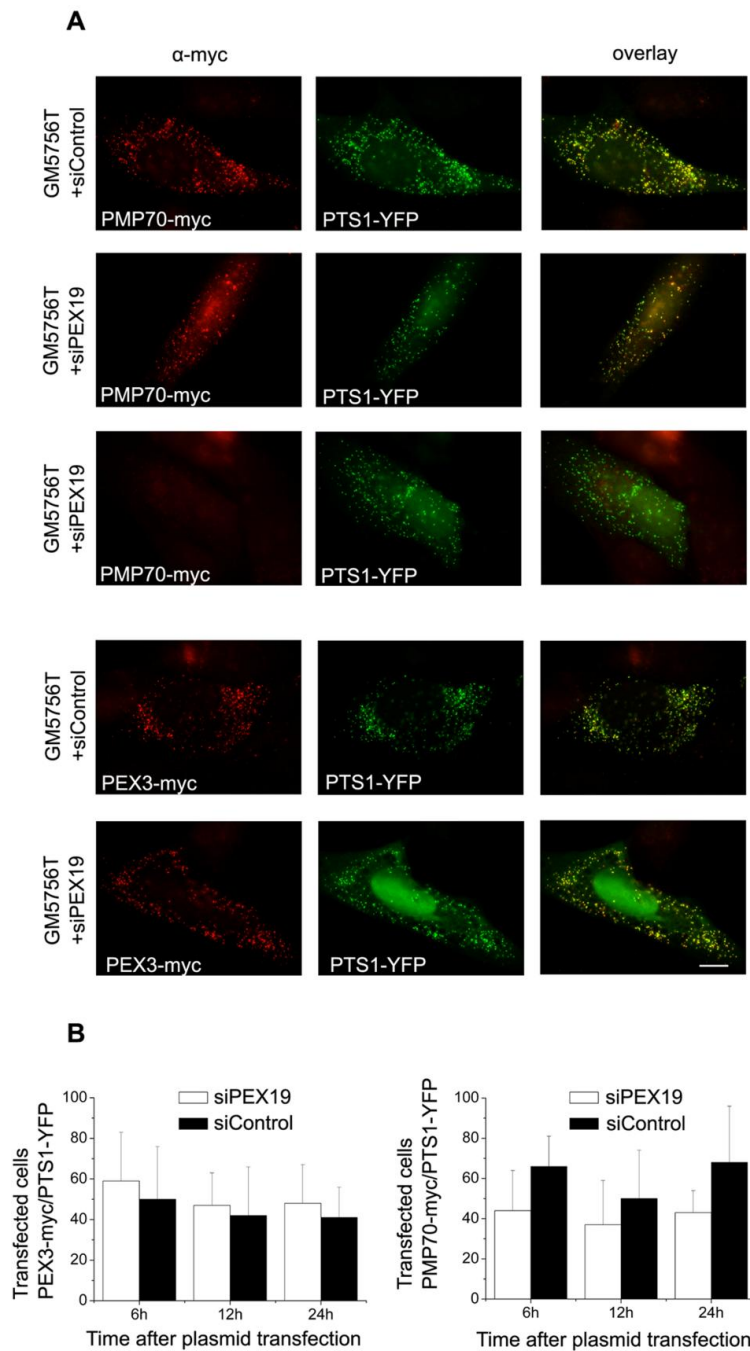
Figure 5. Newly synthesized PEX3 is imported into peroxisomes independently of PEX19. Human fibroblasts (GM5756T) were electroporated twice either with siRNA against endogenous PEX19 or with control siRNA. (A) The siRNA treated fibroblasts were transfected transiently with plasmid DNA coding for PEX3-myc or PMP70-myc and were processed for indirect immunofluorescence at the indicated time points post transfection using α-myc antibodies. In both cases, YFP-PTS1 was cotransfected to normalize for cell transfection efficiency. PMP70-myc and Pex3-myc were exclusively detected in peroxisomes validated by colocalization with YFP-PTS1, scale bar: 10 μm. (B) The ratios of transfection rates for PEX3-myc or PMP70-myc to YFP-PTS1 are displayed as a diagram, showing a peroxisomal import defect in the case of PMP70-myc, but not for PEX3-myc in PEX19-knockdown cells. Means of three independent experiments are presented with standard deviations; at least 1000 cells were counted for each experiment.
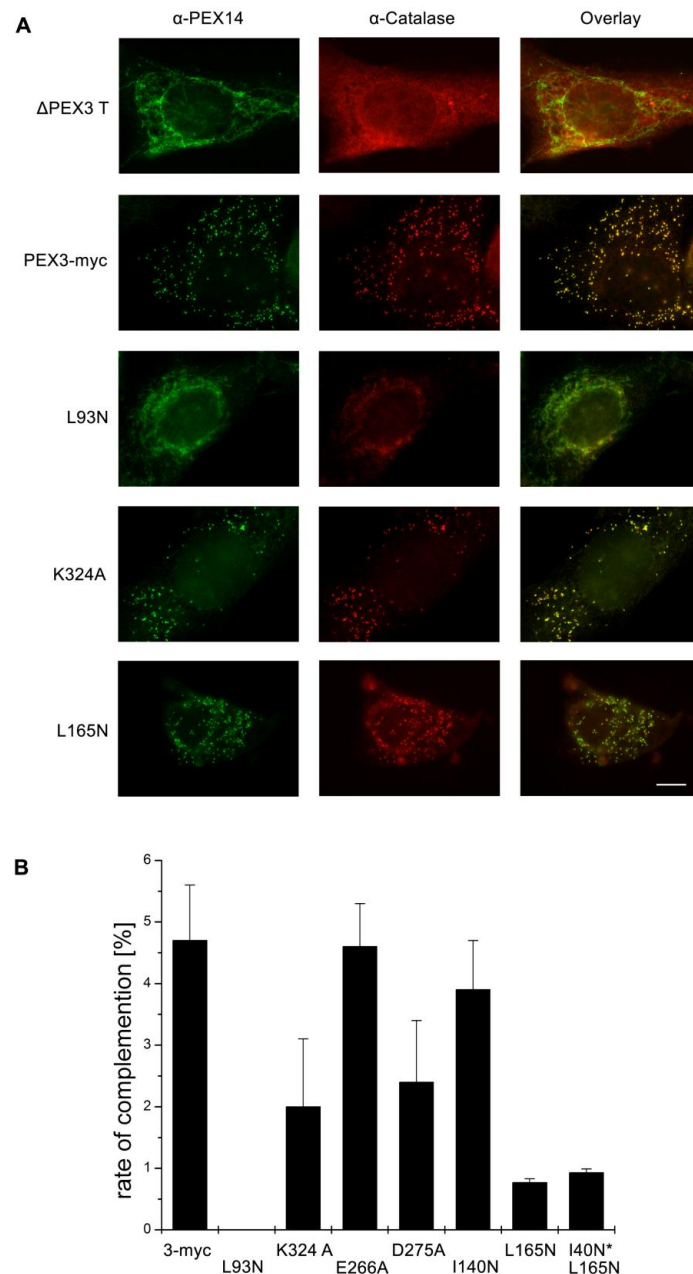
Figure 6. Complementation of PEX3-deficient human fibroblasts. *ΔPEX3T* cells were transfected with plasmids coding for different PEX3-myc mutants. For comparison, untransfected cells are displayed in the first lane. (A) The corresponding complementation efficiency was determined 7 days after transfection using α-PEX14 antibodies to detect newly formed peroxisomes. The import competence of these organelles was tested with α-catalase antibodies. The mutation L93N abolishes the ability of PEX3 to complement *ΔPEX3T* cells showing a mitochondrial localization of PEX14. The other PEX3 mutants are still able to complement *ΔPEX3T* cells. *ΔPEX3T* transfected with PEX3-myc including the mutations L93N, K324A and L165N are shown here exemplarily, the mutants E266A, D275A, I140N and I140N*L165N are displayed in Supplemental Figure S4. Scale bar: 10 µm. The image for the L165N mutant was acquired using a z-stack overlay. (B) Complementation rates for all mutants were calculated by counting cells that exhibit PEX14-positive peroxisomal structures. In each of the three independent experiments at least 500 cells were counted for quantification. Values were represented as means with standard deviations.
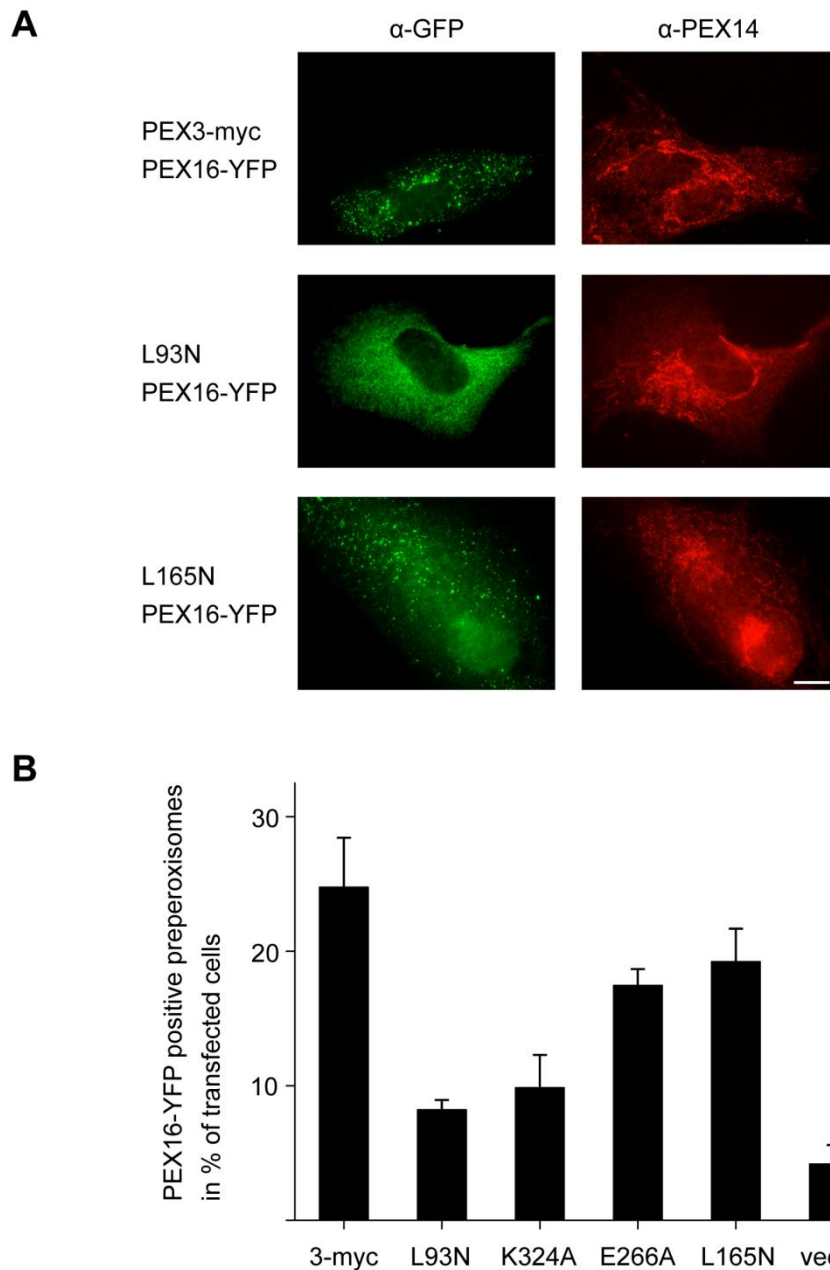
Figure 7. Early stage of complementation in PEX3-deficient cells. *ΔPEX3T* cells were cotransfected with plasmids coding for different PEX3-myc mutants and PEX16-YFP. (A) Cells were labeled with α-GFP antibodies and α-PEX14 antibodies 24 hours post transfection to visualize early stages in peroxisome biogenesis. Punctate preperoxisomal structures that are positive for PEX16-YFP could be detected in cells transfected with PEX3-myc and with the L165N mutant, but were barely found in cells transfected with PEX3-myc L93N. In all cells endogenous PEX14 is localized to mitochondria; scale bar: 10 μm. (B) The number of cells with YFP-positive preperoxisomes was counted and is represented in % of transfected cells. For each of the three independent experiments at least 500 cells were included in the calculation. Values were represented as means with standard deviations.
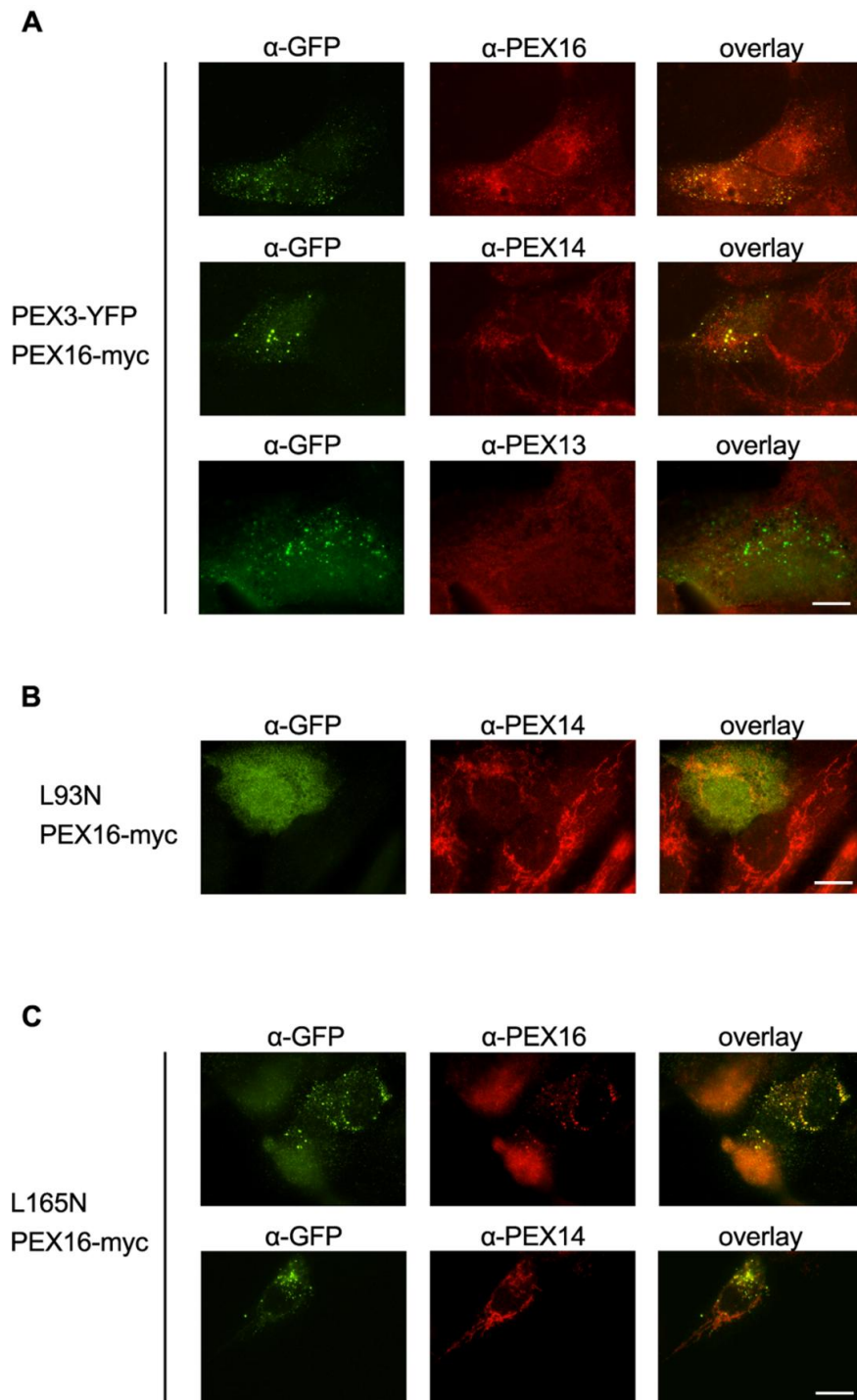
Figure 8. Preperoxisomal maturation. ΔPEX3T cells were cotransfected with plasmids coding for different PEX3-YFP mutants and PEX16-myc. (A) Cells were subjected to immunostaining 24 hours post transfection and labeled with α-GFP antibodies, α-PEX16 antibodies, α-PEX14 antibodies and α-PEX13 antibodies to visualize early stages in peroxisome biogenesis. The punctate YFP-staining colocalizes with PEX16 but not with PEX14 or PEX13, indicating preperoxisomes that are not import competent for PMPs yet. (B) PEX3-YFP L93N is mainly detected in the cytosol 2 days after transfection. Preperoxisomal structures are barely detectable. (C) One day after transfection, PEX3-YFP L165N colocalizes with PEX16 in preperoxisomes, whereas PEX14 is found in mitochondria. A small amount of these preperoxisomes can mature into peroxisomes import competent for PEX14 and catalase after 2-3 days.
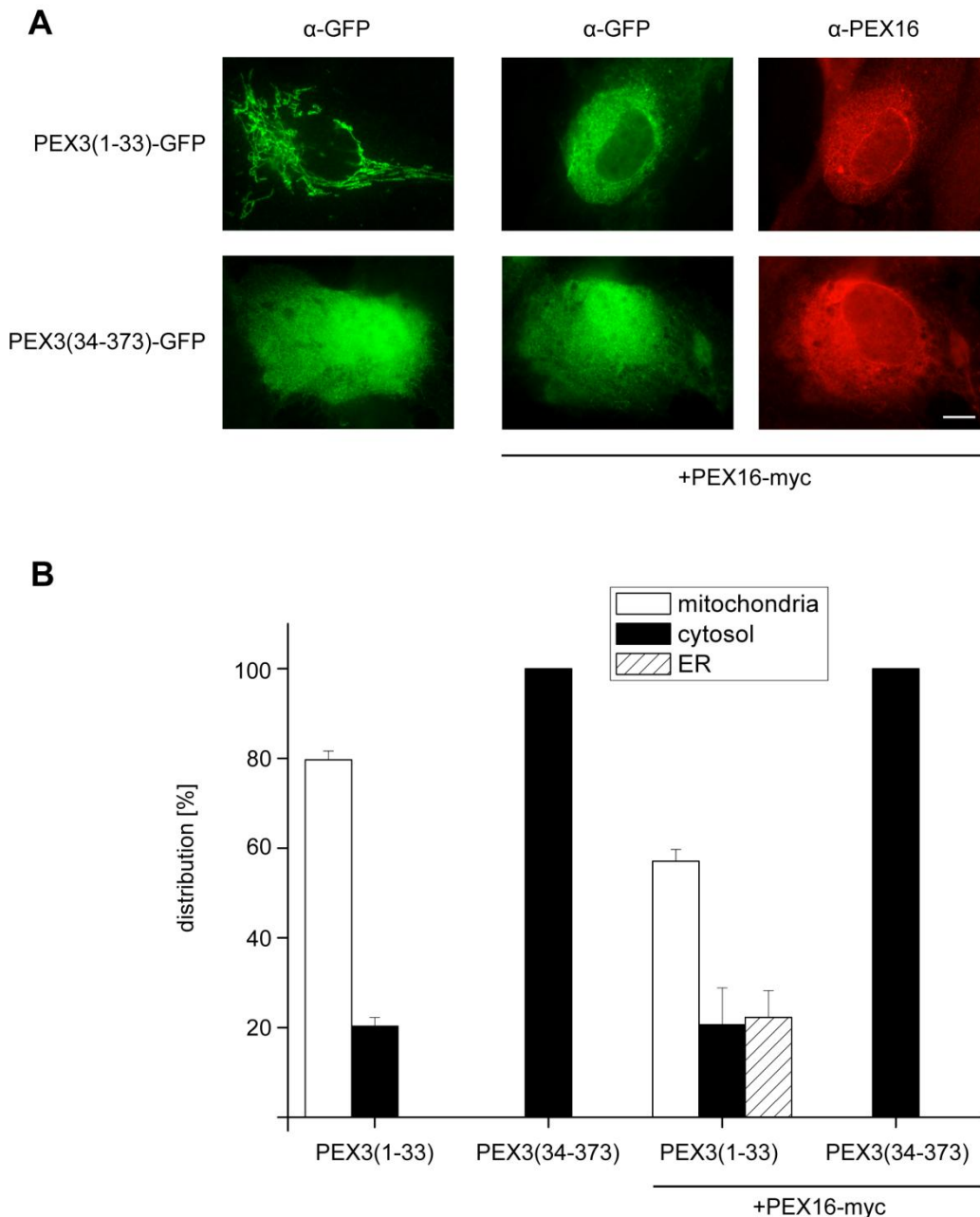
Figure 9. The N-terminus of PEX3 colocalizes with PEX16 to the ER in PEX19-deficient cells. *ΔPEX19T* cells were transfected with plasmids coding for different GFP-tagged PEX3 variants. Additionally, either the control vector pcDNA3.1Zeo or PEX16-myc was cotransfected. (A) Cells were analyzed by immunofluorescence microscopy 24 hours after transfection. PEX3 localization was detected using α-GFP antibodies; PEX16 was visualized with α-myc antibodies, respectively. In the absence of PEX16-myc, the N-terminus of PEX3 is mainly found in mitochondria. In the presence of PEX16-myc that is partially localized in the ER, this PEX3 variant exhibits a partial ER staining. The C-terminal domain of PEX3 (PEX3$^{34-373}$) is exclusively found in the cytosol independently of PEX16-myc coexpression; scale bar: 10 μm. (B) The distribution of the different PEX3-GFP constructs within the cell in the absence or presence of PEX16-myc was evaluated and plotted as a diagram. For each of the three independent experiments at least 500 cells were counted. Values were represented as means with standard deviations.

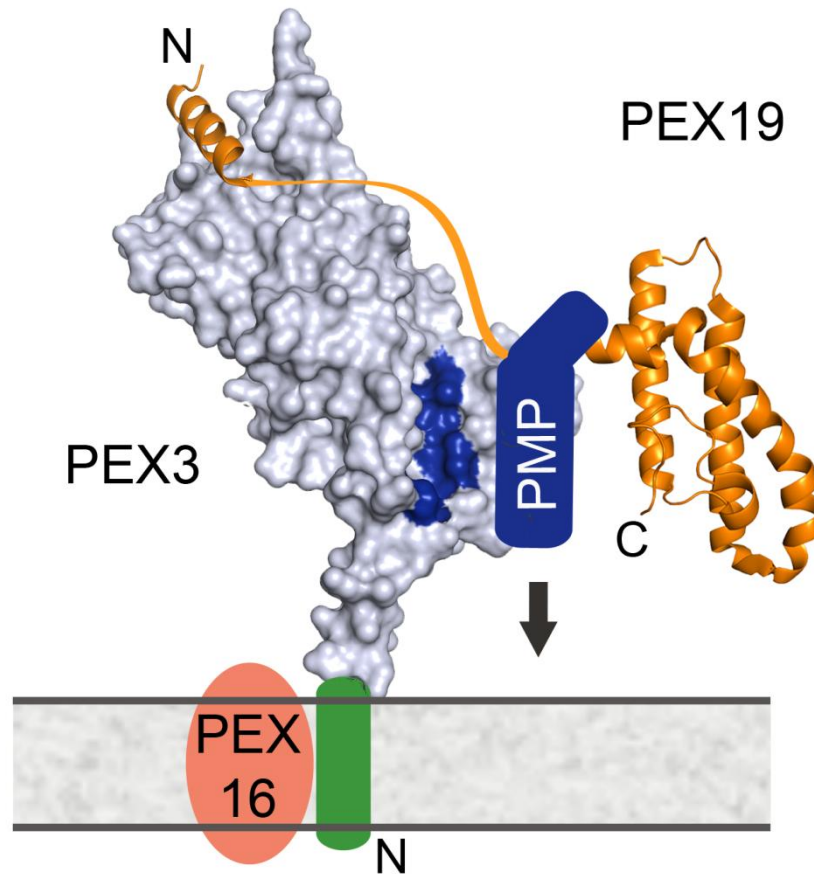**Figure 10.** Model for PMP import into peroxisomes. Surface representation of PEX3 (light gray) with the hydrophobic groove highlighted in blue. The structures of the N- and C-terminal domains of PEX19 are depicted as cartoon (orange), whereas the flexible part in between is shown as a solid line. The PEX19 C-terminal helix bundle refers to PDB entry 2WL8 (24). PEX3 is anchored in the peroxisomal membrane with its N-terminus (green) that mediates the interaction to PEX16 (red). PEX19 binds to the PMP with its C-terminal domain. The N-terminal helix of PEX19 directs the cargo-loaded PEX19-PMP-complex to peroxisomes by binding to PEX3. After PMP insertion into the peroxisomal membrane, PEX19 is released back to the cytosol to initiate another round of PMP import.

SUPPLEMENTAL MATERIAL

SUPPLEMENTAL TABLES

Table S1: Primers for inserting point mutations in *sPEX3*, *PEX3-myc* and *PEX3-YFP*.

Mutation	Primer forward 5'- 3'	Primer reverse 5'- 3'
L93N[a]	CCGAGAGCCTCACAGCTCTGAACAAAAACAGGCC	GGCCTGTTTTTGTTCAGAGCTGTAGGCTCTCGG
I140N	CATAATTGGTGGATATAACTACCTGGATAATGCAGC	GCTGCATTATCCAGGTAGTTATATCCACCAATTATG
L165N	CCAACAGCAGTATAATTCAAGTATTCAGCACC	GGTGCTGAATACTTGAATTATACTGCTGTTGG
E266A	CTATTAAACTTCTCAATGCAACTAGAGACATGTTGG	CCAAATGTCTCTAGTTGCATTGAGAAGTTTAATAG
D275A	GTTGGAAAGCCCAGCTTTTAGTACAGTTTTG	CAAAACTGTACTAAAAGCTGGGCTTTCCAAC
K324A	GTCAGCCTGCCTTTAGCTGCGATAATTCCAATAG	CTATTGGAATTATCGCAGCTAAAGGCAGGCTGAC
C235S	GGATCCAAACCTTTATTAAGCCATTATATGATGCC	GGCATCATATAATGGCTTAATAAAGGTTTGGATCC

[a]The corresponding mutation is underlined within the primer sequences.

Table S2: Protein concentrations used for ITC experiments.

Protein	Concentration sPEX3 [μM]	Concentration PEX19 [μM]
sPEX3[a]	10.1	83.2
sPEX3 L93N	25.9	274.3
sPEX3 K324A	12.0	147.2
sPEX3 E266A	9.3	92.2
sPEX3 I140N	8.0	96.3
sPEX3 L165N	10.1	95.4

[a] PEX3[41-373] C235S.
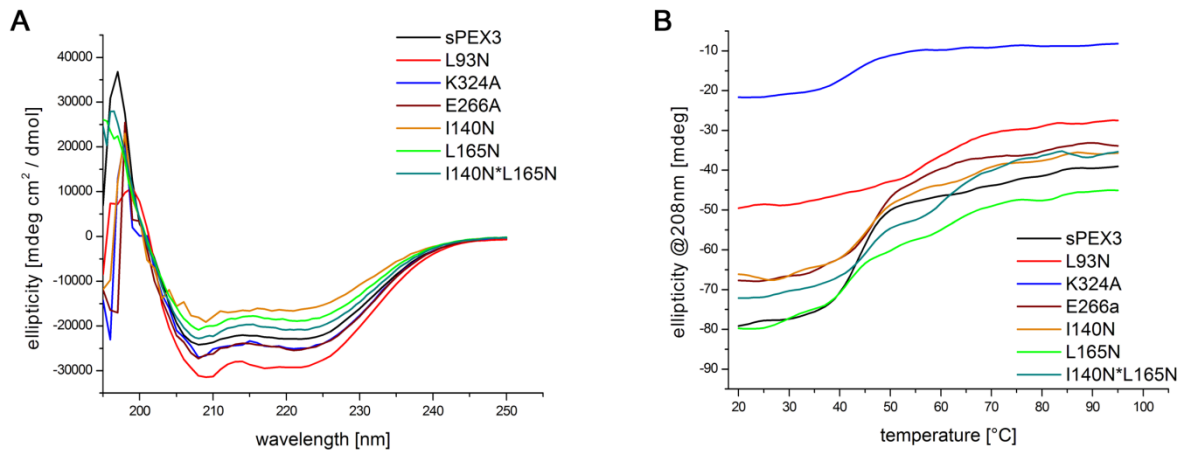
Figure S1. Folding studies and stability analysis of different sPEX3 mutants. (A) Circular dichroism spectroscopy of all sPEX3 mutants show an α-helical structural content, indicating no change in the overall fold of the protein compared to sPEX3. CD spectra were recorded with 12 µM protein solutions and corrected with the buffer spectrum. (B) Thermal stability analysis for sPEX3 mutants. Proteins were heated stepwise to 95°C with a scan rate of 1 °C/min. The CD signal at 208 nm was recorded during the whole denaturation process. Curves are displayed using a smoothing factor of 5. The inflection point represents the melting temperature of the protein. For all mutants, this melting point is somewhat higher than for sPEX3 (black), implicating no loss in stability upon introducing the mutations in sPEX3.
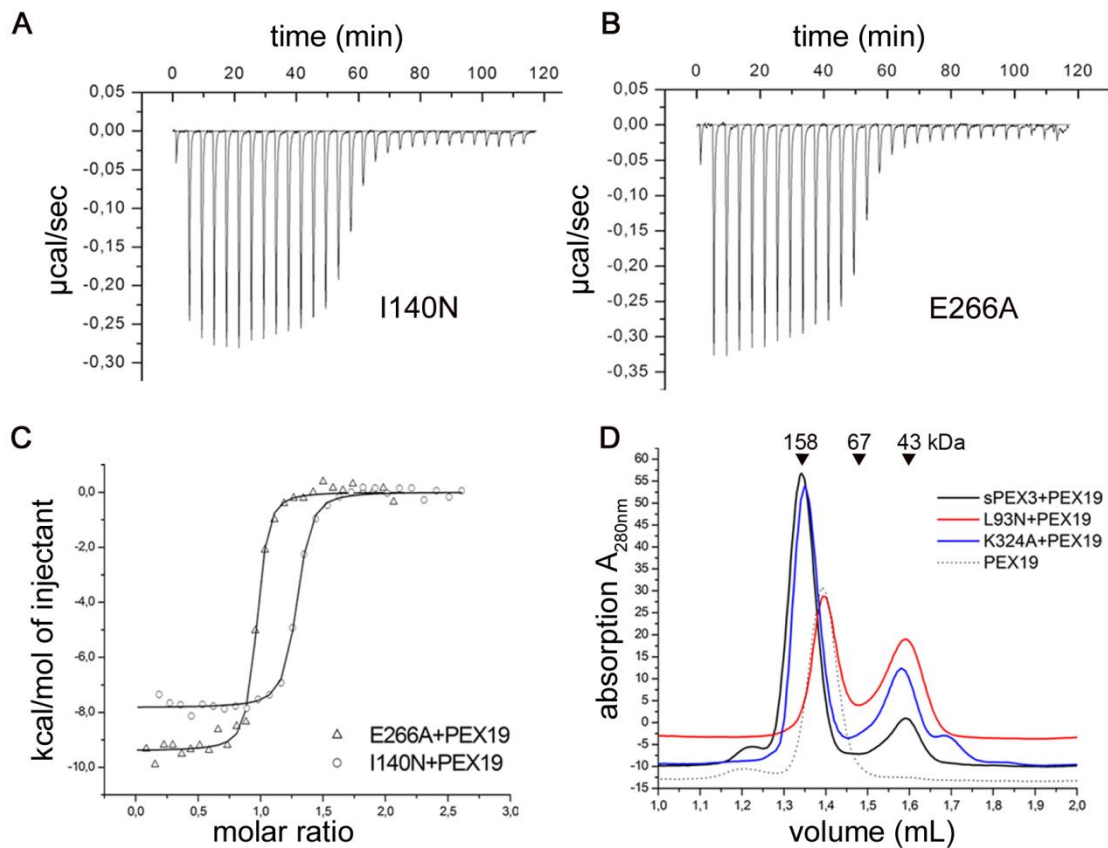
Figure S2. Affinity measurements of complex formation between different sPEX3 mutants and PEX19. Raw data for binding of sPEX3 I140N to PEX19 (A) and sPEX3 E266A to PEX19 (B). (C) Integrated heat values for the different ITC experiments showing fits to a single binding isotherm for the respective titrations. The thermodynamic parameters for each sample are listed in Table 1. (D) Analytical size exclusion chromatography for sPEX3+PEX19, L93N+PEX19, K324A+PEX19 and PEX19 alone are shown. It is known, that PEX19 exists as a monomer in solution but elutes at higher molecular weight mass in gel filtration (32). Here, PEX19 (molecular mass: 32.8 kDa) elutes at an apparent molecular mass of 115 kDa due to its extended conformation. The complex sPEX3+PEX19 represents a molecular mass of 160 kDa, corresponding to the total of the two monomers building a 1:1 complex. The second peak in the profile of the complex can be assigned to an excess of monomeric sPEX3 (molecular mass: 37.5 kDa). The elution profile for sPEX3 K324A+PEX19 overlays with the complex profile for sPEX3+PEX19. Two single peaks, corresponding to the individual proteins PEX19 and sPEX3 L93N, characterize the elution profile of a mixture of sPEX3 L93N and PEX19.
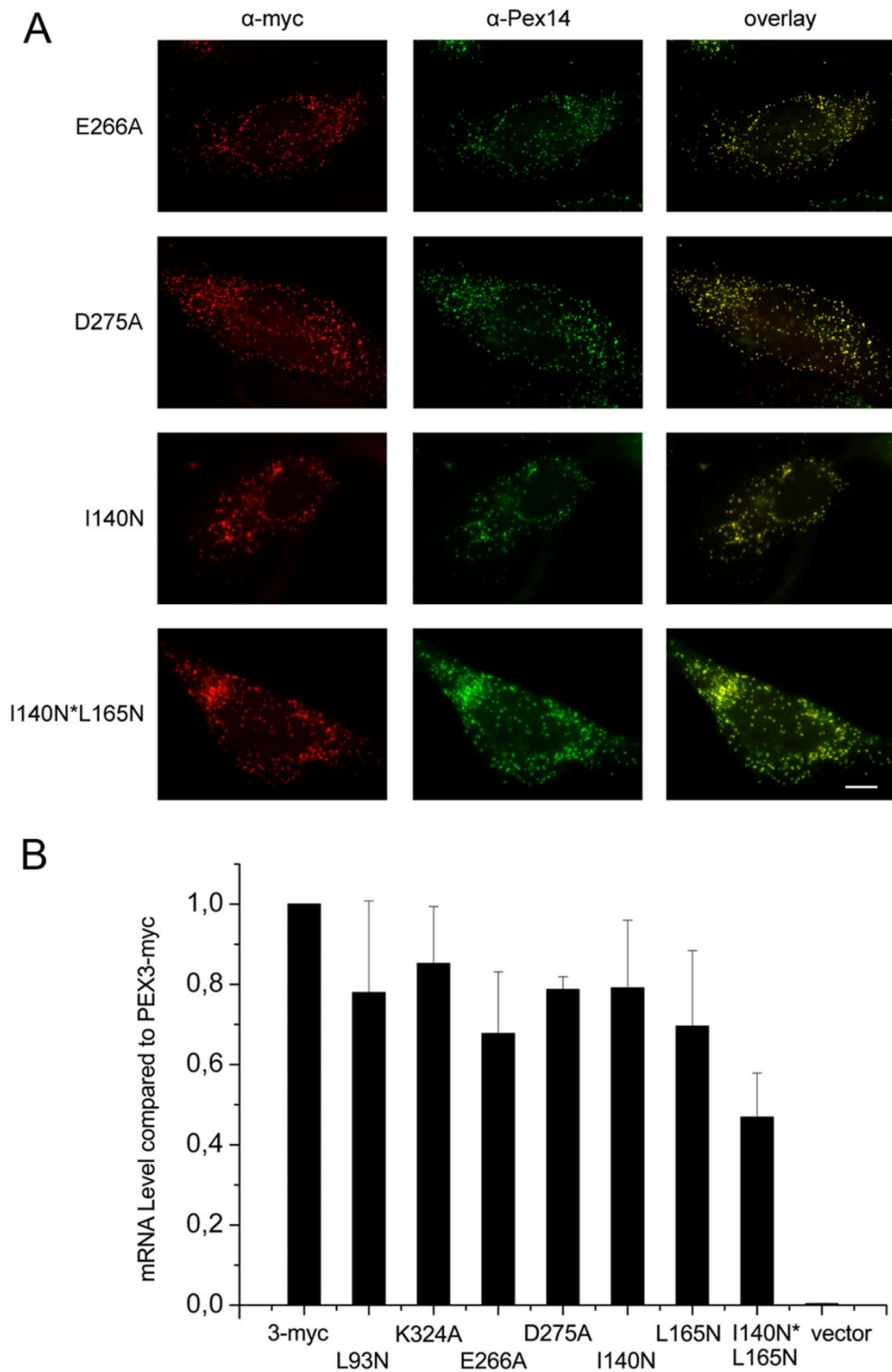
Figure S3. Peroxisomal localization of different PEX3-myc mutants in human fibroblasts. (A) Normal fibroblasts (GM5756T) were transfected with plasmids coding for the different PEX3-myc mutants E266A, D275A, I140N and I140N*L165N. The cellular localization of the expressed proteins was detected with α-myc antibodies two days after transfection. Peroxisomes were visualized with α-PEX14 antibodies. These PEX3-myc mutants reveal a peroxisomal distribution within the cell validated by colocalization with PEX14. Scale bar: 10 μm. (B) mRNA levels of endogenous PEX3 and the corresponding PEX3-myc mutants in relation to PEX3-myc, which was set to 1. Values represent the mean and range of two experiments.
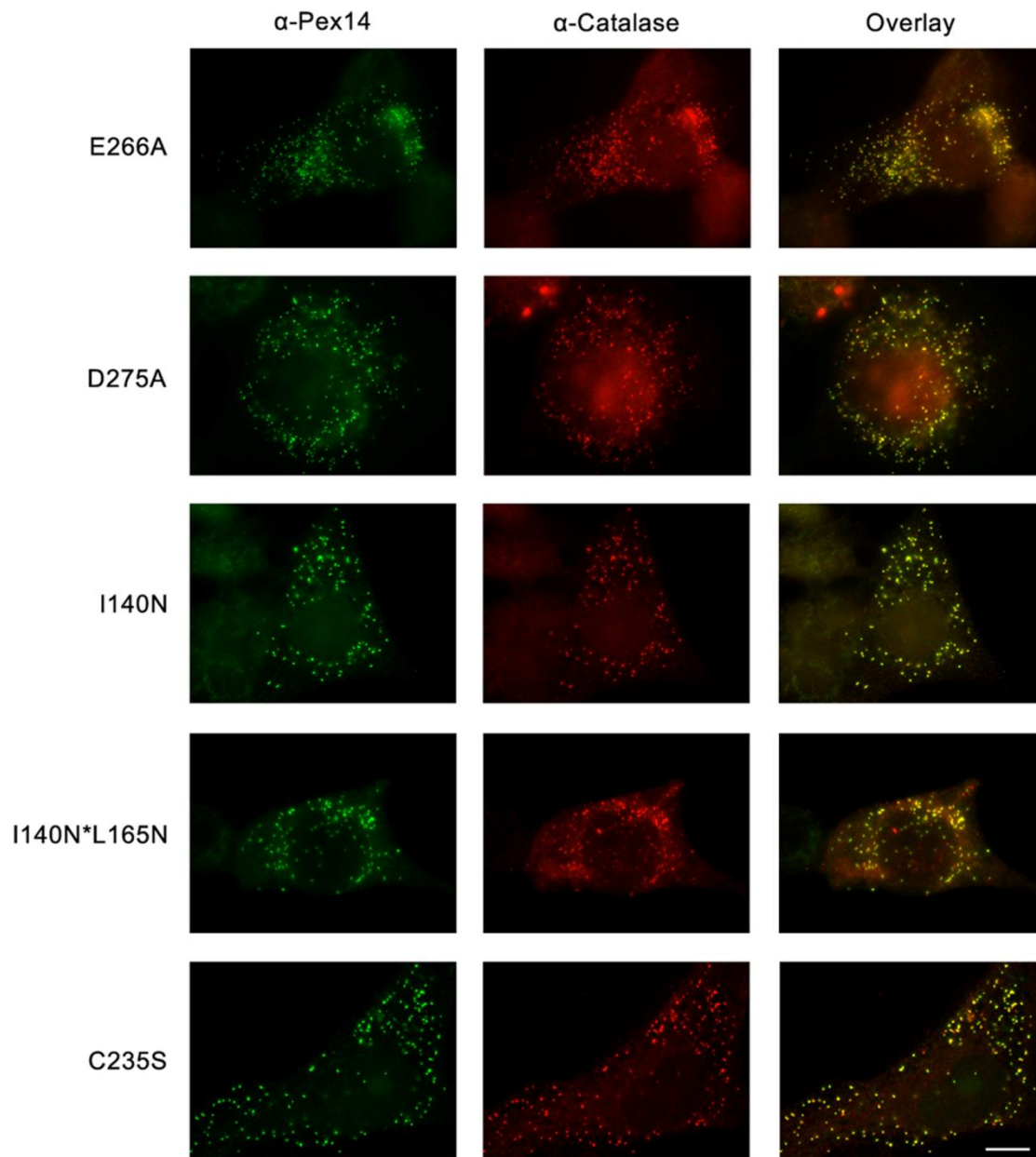
Figure S4. Complementation of PEX3-deficient human fibroblasts. *ΔPEX3T* cells were transfected with plasmids coding for the different PEX3-myc mutants E266A, D275A, I140N, I140N*L165N and C235S. The ability for complementation of *ΔPEX3T* cells was determined 7 days after transfection using α-PEX14 antibodies to detect newly formed peroxisomes. The import competence of these organelles was tested with αa-catalase antibodies. The PEX3-myc mutants are still able to complement *ΔPEX3T* cells, which is validated by the colocalization of PEX14 with catalase-positive punctate structures. Scale bar: 10 μ.

4 DISCUSSION

In this thesis, the parameters underlying the PEX3-PEX19 interaction were defined. The structure of sPEX3 in complex with a PEX19-derived peptide provides insights into the molecular details mediating the PEX3-PEX19 binding, which is essential in peroxisome biogenesis. Based on the crystal structure, surface analysis of PEX3 reveals three larger conserved regions. In addition to the PEX19-binding groove, a hydrophobic groove and a cluster of acidic residues feature high conservation, indicating a possible role in PEX3 function. Mutagenesis studies followed by affinity experiments determine two residues in the PEX19-binding groove, which are required for correct PEX19-binding and thus, for complementing PEX3-deficient cells. These residues are also essential for functional PEX3 in the early steps in peroxisome membrane biogenesis *in vivo*. Furthermore, the hydrophobic groove is likely involved in PMP insertion, which leads to a more detailed model of PMP insertion into the lipid bilayer. The cluster of acidic residues does not appear to play a critical role in PEX3 function in peroxisome biogenesis.

4.1 Characteristics of the PEX3-PEX19 interaction

4.1.1 Topology of PEX3

The crystal structure of sPEX3 in complex with a peptide fragment of its interaction partner PEX19 serves as a platform for understanding the process of PMP import (Figure 1.4). According to structural homology searches, the structure of sPEX3 exhibits a novel fold. The closest structural homologs are membrane-embedded helical proteins such as the β-adrenergic receptor or rhodopsin. However, the structural homology is not convincing with Z-scores below six (Z=5.5, β-adrenergic receptor; Z=5.3, rhodopsin) and high rmsd values of 5.5 and 4.3 Å, respectively. The similarity is rather found within the α-helical propensity of the proteins, but not within the arrangement of the helices towards each other and in space. Additionally, analysis of the electrostatic potential of sPEX3 reveals a hydrophilic surface with mostly randomly distributed positive and negative patches. These surface features make it unlikely that the bulk of PEX3 is inserted into the membrane. As only the inner core of the protein is highly hydrophobic (especially the central helix α3), the protein would have to undergo an immense conformational change to be able to insert into the lipid phase of the peroxisomal membrane. These findings support the view of PEX3 being anchored in the peroxisomal membrane only with its N-terminal TM domain and the rest of the protein projecting

into the cytosol. As no putative pore forming protein has been identified so far, it is unlikely that peroxisomal membrane protein import engages a protein pore to insert PMPs into the lipid bilayer. However, it has never been shown whether PEX3 is engaged in a protein import complex together with other peroxins (PEX16, PEX19). PEX16 was identified in this thesis and in other studies [52, 75] to interact with the N-terminal membrane anchor of PEX3 and might participate directly in the PMP insertion process. However, as a knockdown of PEX16 does not seem to result in an import defect of classI PMPs in human fibroblasts (D. Dietrich, Dodt lab), PEX16 might adopt a different function in peroxisome biogenesis.

4.1.2 Comparison of unliganded and PEX19-bound PEX3

So far, crystallization attempts of sPEX3 alone have not been successful. However, an unrefined structural model of a longer version of PEX3, nPEX3, alone is available [129], Although the model is somewhat unreliable because of crystal twinning, its core could be used for molecular replacement in this thesis. Hence, it is feasible to compare the overall fold of unliganded and PEX19-bound PEX3.
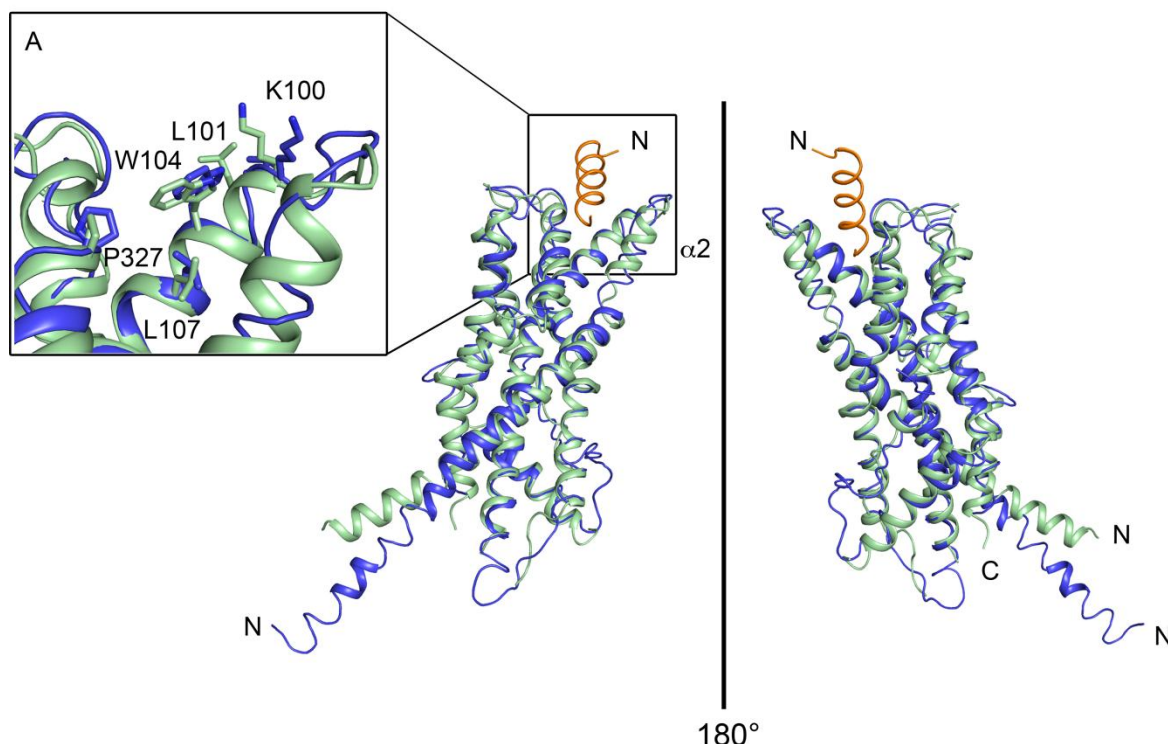
Figure 4.1: Superposition of unliganded PEX3 and PEX19-bound PEX3. The unrefined model of nPEX3 [129] alone is depicted as a blue cartoon, whereas sPEX3 from the PEX19-bound complex is shown in green. The variations within the N-terminal α-helix are most likely due to crystal contacts. The biggest deviations can be found in loop regions and within helix α2. (A) PEX19-binding groove with selected amino acids depicted as sticks. The other residues involved in PEX19^{Pep}-binding and the PEX19-derived peptide are not shown for reasons of clarity.

Least squares superposition of the two proteins (Figure 4.1) in Coot [162] results in an rmsd of 2.6 Å for the Cα-backbone. The most noticeable deviations (rmsd: ~2-4 Å) of the Cα-backbones can be detected in the N-terminus, in helix α2 and several loop regions. The divergence within the N-terminal α-helix is most likely due to different crystal contacts. The good alignment of the Cα-backbone and the majority of the side chain atoms within the PEX19-binding groove of cargo-loaded and unliganded PEX3 argues against an induced structural change in the PEX3 molecule upon PEX19-binding. It is thus likely that the complementary geometric shapes of PEX3 and PEX19 perfectly fit to each other with only minor structural adaptations accompanying complex formation.

4.1.3 The PEX19-binding groove

The crystal structure of sPEX3 in complex with PEX19[Pep] provides insights into the molecular details mediating the binding of PEX3 to PEX19. The complex is formed mainly by hydrophobic interactions involving highly conserved residues of PEX3 and PEX19, which indicates an essential function of the PEX3-PEX19 complex in peroxisome biogenesis. The stabilizing effect on sPEX3 upon peptide binding, which was determined here *in vitro* with a thermal denaturation assay, is probably not only due to a fixation of the helices in the bundle, but also to a protection of the hydrophobic PEX19-binding groove from the aqueous environment. Concerning the melting temperatures of proteins, a comparable impact of peptide binding was described for MHC molecules. In this case, a class I MHC molecule is stabilized about 12 °C upon peptide binding determined with a similar thermal denaturation assay [175]. In contrast to the specific PEX3-PEX19 interaction, MHC molecules are designed for binding a variety of antigen-derived peptides. Hence, the peptide-binding groove of MHC molecules is less conserved than the PEX19-binding groove and the peptide is in general bound via interactions with the N- and C-termini to guarantee a large diversity of presented antigens [176].

4.1.4 Is there a second PEX19-binding site?

The affinity of the PEX19-derived peptide for sPEX3 was calculated with ITC experiments to a K_d of 330 nM. However, the affinity of full-length PEX19 for sPEX3 is even higher, with a K_d of 14.8 nM. This 22-fold higher affinity can be due to long-range interactions, which contribute nonspecifically to the affinity, or to a specific second PEX19-binding site within PEX3. An additional PEX19-binding site has already been proposed earlier [65]. In this thesis, surface conservation analysis of sPEX3 identified

two conserved regions in addition to the PEX19-binding groove, which might represent the second PEX19 interaction site. However, mutagenesis and affinity measurements excluded that the conserved hydrophobic groove or the conserved glutamate at position 266 of PEX3 participate in PEX19-binding. The presence of a second PEX19-binding site is further supported by mutational analysis of a conserved phenylalanine at position 29 of PEX19, which is engaged in PEX3-binding. The mutation of Phe29 to an alanine within full-length PEX19 results in a K_d-value of ~1 µM for PEX3 compared to a K_d-value of 3.4 nM using native PEX19 calculated with SPR analysis [124]. The same F29A mutation within the PEX19-derived peptide completely abolishes binding to sPEX3 as determined with ITC experiments in the present thesis. Therefore, these results point towards a second PEX19-binding site of minor affinity on the surface of PEX3.

4.1.5 The hydrophobic groove

The complementation defect of the mutant PEX3 L165N indicates a direct participation of the conserved hydrophobic groove on the surface of sPEX3 in PMP insertion in peroxisome biogenesis. During the insertion of tail-anchored proteins into the ER membrane, a similar hydrophobic groove has been identified within the dimer interface of Get3 [177], which acts as a cytosolic receptor for TA proteins and directs them to the target membrane (see section 1.5.3). In that case, the groove is 15 Å wide and 30 Å long, and it is capable of binding an α-helix of 20 aars deeply within the groove (Figure 4.2A).
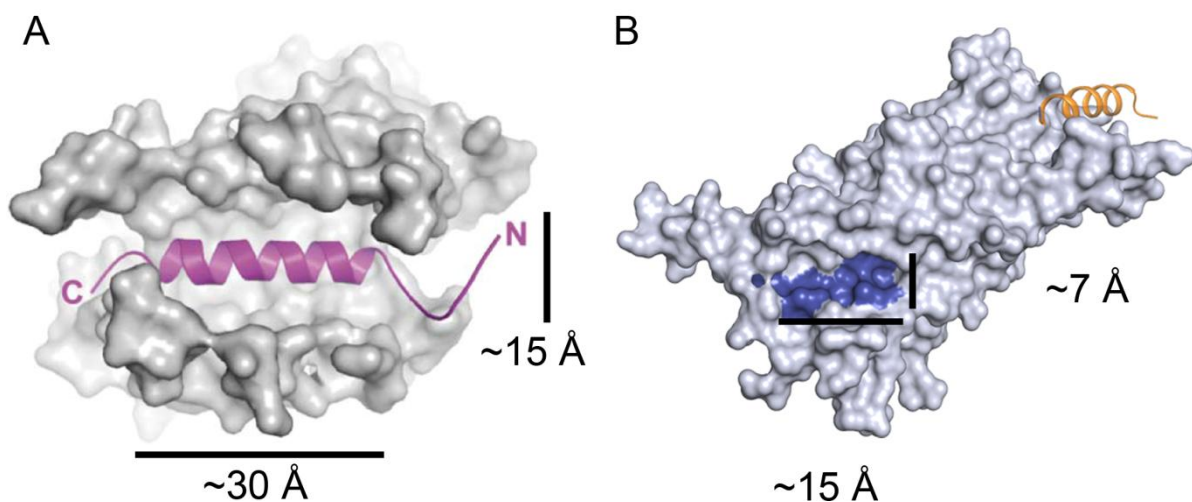
Figure 4.2: Dimensions of the hydrophobic groove. (A) Hydrophobic groove built by the interface of the Get3 dimer (light grey). The purple helix is modeled into the groove. Image modified from [177]. (B) The dimensions of the conserved hydrophobic groove (blue) on the surface of sPEX3 (grey). PEX19[Pep] is depicted as an orange cartoon.

In case of PEX3, the hydrophobic groove is ~7 Å wide and ~15 Å long (Figure 4.2B). Thus, an interaction between a shorter α-helix or a hydrophobic unstructured loop present within the PMP is imaginable. As the hydrophobic groove on the surface of PEX3 is not as deep as the groove of the Get3 dimer, the α-helix might not be completely lowered into the groove. Furthermore, the hydrophobic groove of PEX3 might also partly harbor the farnesyl moiety of PEX19 under *in vivo* conditions. As the affinity measurements were performed with nonfarnesylated PEX19 in this thesis, this possibility cannot be fully excluded.

4.1.6 The acidic cluster

Four residues are part of the acidic cluster, of which E266 and D275 are the most highly conserved. The PEX3 mutations E266A and D275A do not influence the interaction with PEX19. In addition, the complementation ability of PEX3 E266A is not impaired compared to normal PEX3. Thus, the glutamate at position 266 does not appear to have a specific biological function. In contrast, the complementation ability of PEX3 D275A is reduced about 50 % compared to normal PEX3. This observation might implicate a role of the aspartate in peroxisome biogenesis. However, the relevance and specificity as well as possible binding partners require further anaylses to be defined more precisely.

4.1.7 The roles of PEX3 and PEX19

There are two different scenarios describing the import of PMPs into peroxisomes. In the first one, PMPs are directly inserted into mature peroxisomes posttranslationally dependent on PEX3 and PEX19. The second scenario supports an indirect PMP pathway via the ER. Here, PEX3 and PEX19 are required for budding preperoxisomal vesicles from the ER, which already contain the majority of PMPs [45].
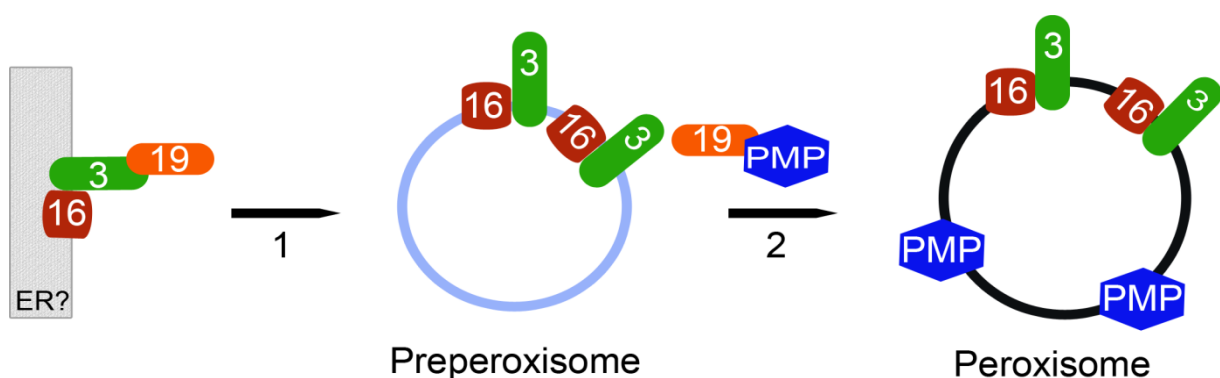
Figure 4.3: A dual function of PEX3 and PEX19. The PEX3-PEX19 complex is required for budding of preperoxisomes from a membrane system that likely is the ER (1). These preperoxisomes mature to peroxisomes by importing PMPs with the help of PEX3 and PEX19 (2).

The findings presented in this thesis favor a direct PMP import into peroxisomes over an exclusively ER-dependent route of PMPs. The PEX3 L165N mutant, which carries the mutation in the hydrophobic groove, showed a reduced ability to complement PEX3-deficient human fibroblasts. This is likely due to a defect in PMP insertion and not to an impaired preperoxisome formation. As these structures do not contain PEX14, PMP insertion is thought to occur after the budding of preperoxisomes. Furthermore, it was shown, that a functional PEX3-PEX19 interaction is required for the formation of preperoxisomes: The PEX3 L93N mutant, which is impaired in PEX19-binding, exhibits a defect in developing these early membrane structures. This is consistent with findings in yeast that the presence of PEX19 is essential for preperoxisomal vesicle budding [38, 40, 43]. This also implies that the PEX3-PEX19 interaction may have a dual function during peroxisome biogenesis (Figure 4.3).

4.2   A more detailed model of PMP import

In addition to gaining detailed insights into the basis of the PEX3-PEX19 complex formation, the combination of *in vitro* and *in vivo* experiments leads to a more detailed model of PMP import into peroxisomes (Figure 4.4). PEX19 recognizes newly synthesized PMPs in the cytosol posttranslationally [77] by binding to one or even multiple mPTSs [63, 69]. At the same time, PEX19-binding provides stability to the PMP probably by shielding hydrophobic patches from the aqueous environment and keeping the PMPs in an import-competent form [67]. The PMP-PEX19-complex is then directed to the peroxisomal membrane through the interaction of the PEX19 N-terminus with PEX3 [122].

The high affinity interaction ensures a precise initiation for the following steps of PMP insertion. The PMP-PEX19 complex must be oriented towards the peroxisomal membrane in such a way that the PMP can be inserted into the lipid phase correctly. As the very C-terminus of PEX19 can be oriented to face the peroxisome, the C-terminal farnesyl moiety might act as another membrane anchor, which was proposed previously [69]. This ancillary function of the lipid anchor has been shown independently for human and yeast cells [69, 128]. However, some studies favor an essential role of the farnesylation motif in peroxisome biogenesis and cell viability in eukaryotic cells [34, 59, 126]. Several reports have shown that the farnesyl anchor enhances binding to several PMPs [71, 126], in contradiction to other results that could not detect any difference in

PMP-binding of farnesylated or unmodified PEX19 [128, 178]. Thus, the importance and exact function of farnesylated PEX19 is still a matter of ongoing debate.

Furthermore, the hydrophobic groove of PEX3 represents an interaction site for the PMP, which probably helps to insert the PMP into the lipid bilayer. It is tempting to speculate that hydrophobic patches in the PMP are made accessible after docking the PEX19-PMP complex to the peroxisomal membrane. This scenario might involve a structural rearrangement within the PMP to be able to interact with PEX3. The indirect, PEX19-dependent complex formation of PEX3 and the PMP might explain the finding of only ternary complexes including PEX3, PEX19 and a PMP [76, 179]. However, it is not clear if PEX3, PEX19 and/or a yet unidentified factor promotes the insertion process. As the insertion process itself proceeds in the absence of ATP [180], the energy needed for crossing the membrane barrier could be (over-) compensated by the favorable interactions between the TM domains of the PMP with the lipid phase of the peroxisomal membrane.
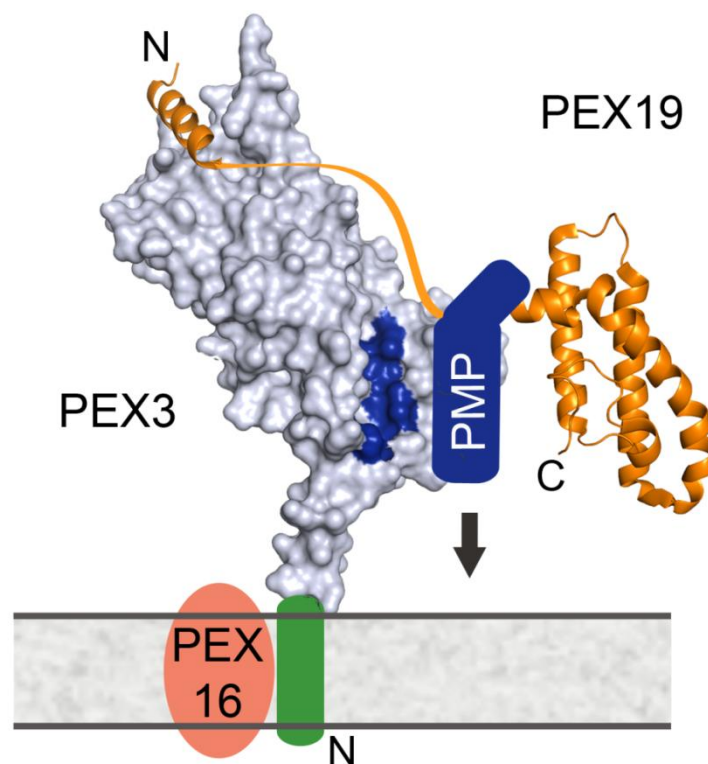
Figure 4.4: Model for PMP import into the peroxisomal membrane. Surface representation of PEX3 (light gray) with the hydrophobic groove highlighted in blue. The known structures of the PEX19 N- and C-terminal domains are depicted as cartoon (orange) with the flexible part shown as a solid line. The PEX19 C-terminal helical bundle refers to PDB entry 2WL8 [66]. PEX3 is anchored in the peroxisomal membrane with its N-terminus (green), which binds to PEX16 (red). The N-terminal PEX19 helix directs cargo-loaded PEX19 to peroxisomes by interacting with PEX3. After PMP insertion, PEX19 is recycled back to the cytosol to start another round of PMP import.

The high affinity interaction between PEX3 and PEX19 must be disrupted to start another round of PMP import. It has been shown that the affinity of PEX3 for cargo-free PEX19 is reduced compared to cargo-loaded PEX19 [179]. Thus, a PEX19-PMP complex would be able to displace unliganded PEX19 from PEX3. Another scenario might involve a cooperative process between PMP-insertion and PEX19 recycling. Here, a conformational change within PEX19 would break the PEX3-PEX19 interaction after cargo release into the peroxisomal membrane resulting in free cytosolic PEX19 prepared for another round of PMP import.

5   OUTLOOK

The combination of *in vitro* and *in vivo* experiments performed in this thesis has led to the structure-function analysis of the PEX3-PEX19 interaction. The crystal structure provided first insights into the basis of the PEX3-PEX19 complex formation and allowed to assess the impact of specific PEX3 mutations on PEX19-binding and in peroxisome biogenesis. In the end, a more precise model of PMP insertion into the peroxisomal membrane could be presented. However, many details about peroxisome membrane biogenesis remain to be clarified.

The first controversial issue is the role of the farnesyl moiety at the very C-terminus of PEX19. As recombinantly expressed PEX19 can be easily farnesylated *in vitro*, affinity measurements of modified PEX19 and PEX3 will determine a putative influence of the prenyl moiety on PEX3-binding. Furthermore, ITC experiments of PEX3 and PEX19 in the presence of a PMP might shed light on a replacement of unliganded PEX19 with cargo-loaded PEX19 on the binding site of PEX3. As full-length PMPs are hard to express in a soluble form and in an adequate amount, it might be sufficient to perform the experiments in the presence of a peptide, which is derived from a known mPTS of a PMP. However, a peptide might not be enough to detect a possible influence of PMP-binding on the PEX3-PEX19 interaction. Therefore, the PMP could be coexpressed in the presence of PEX19, which would help to keep the PMP in a soluble form and to prevent aggregation. If the PEX19-PMP complex can be expressed in sufficient amounts, it would be feasible to subject the protein complex to crystallization attempts.

Further experiments have to be carried out in order to confirm the role of the hydrophobic groove during PMP insertion. So far, the only PMP used to determine complementation abilities is PEX14. Other PMPs (PMP70, PEX13) could be tested to show if the reduced complementation ability of the PEX3 L165N mutant, which carries the mutation in the hydrophobic groove, is not restricted to PEX14. This might indicate a general function of the hydrophobic groove during PMP insertion into the peroxisomal membrane. Furthermore, a dominant negative effect of the PEX3 L165N mutant might be detected in normal fibroblast cells. Therefore, the PEX3 mutant and a PMP are coexpressed in normal cells and the ability to import newly synthesized PMP in cells expressing the PEX3 mutant is determined. This would help to elucidate a direct participation of the hydrophobic groove in the PMP insertion process.

It is also unclear how the PMP is inserted into the lipid phase of the peroxisomal membrane. Therefore, full-length PEX3 would be required to test for a putative import complex formation. Full-length PEX3 can be recombinantly expressed in *E. coli*. However, it is obtained as inclusion bodies that cannot be refolded [129]. Therefore, other expression systems, such as yeast or mammalian cells, which naturally contain peroxisomes, could be tested. Then, PEX3 could be extracted from the membranes in the presence of detergents. The same could be done for native PEX3, which could be isolated from peroxisomes, although the amount of protein might be too low as PEX3 is not overexpressed. Purified full-length PEX3 must then be subjected to analytical size exclusion chromatography to determine the oligomeric state in the presence of lipids or detergents. However, it is likely that additional factors are involved in PMP insertion into the lipid phase of the peroxisomal membrane, which have to be identified in further proteomic approaches.

6 Summary

Peroxisomes are eukaryotic cellular organelles involved in metabolic functions such as the β-oxidation of very long chain fatty acids, the synthesis of plasmalogens and the degradation of H_2O_2. The so-called peroxins (PEX) are proteins that mediate peroxisomal biogenesis. 14 human peroxins are known to date, of which PEX3, PEX16 and PEX19 belong to the early peroxins responsible for the formation of the peroxisomal membrane. Cells lacking one of these three peroxins do not exhibit any detectable peroxisomal membrane structures. All three variants (ΔPEX3-, ΔPEX16- or ΔPEX19-cells) can be complemented upon introduction of the missing gene and are then able to generate peroxisomes *de novo*.

PEX3 and PEX19 are engaged in the import of peroxisomal membrane proteins (PMPs). PEX19 serves as a cytosolic receptor for newly synthesized PMPs by binding to the membrane peroxisomal targeting sequence. In addition, PEX19 functions as a chaperone as it keeps PMPs in an import-competent form by shielding their hydrophobic regions from the aqueous environment. Cargo-loaded PEX19 is directed to the peroxisomal membrane, where its N-terminus interacts with the cytosolic domain of PEX3. PEX3 is anchored within the membrane via its N-terminus, which also serves as the peroxisomal targeting signal as well as the PEX16-binding site. In this work, the crystal structure of PEX3 in complex with a PEX19-derived peptide fragment was determined. Furthermore, the influence of specific mutations within surface exposed regions of PEX3 on PEX19-binding and during peroxisomal biogenesis was elucidated in detail using *in vitro* and *in vivo* experiments.

The crystal structure of the cytosolic part of PEX3 (sPEX3: aar 41-373, C235S) in complex with a PEX19-derived peptide (PEX19[Pep]: aar 14-33) provides first insights into the details of the PEX3-PEX19 complex formation at the peroxisome membrane. sPEX3 exhibits an all α-helical folding that lacks homology to previously known structures. Ten α-helices and one 3_{10}-helix build a compact bundle with the N-terminal helix projecting towards the peroxisomal membrane *in vivo*. PEX19[Pep] forms an amphipathic α-helix, which is engaged by sPEX3 with high affinity (K_d = 330 nM) calculated with isothermal titration calorimety. The PEX19-binding groove lies at the membrane-distal end and is composed of three distinct regions within sPEX3. The PEX3-PEX19 interaction is mainly mediated by hydrophobic interactions including several strictly conserved residues in both proteins. A thermal denaturation assay demonstrated that sPEX3 is stabilized upon

PEX19[Pep]-binding, shifting the melting point of sPEX3 about 10 °C towards higher temperatures.

Three conserved regions were identified on the surface of sPEX3. In addition to the PEX19-binding groove, a hydrophobic groove on the base of sPEX3 and a cluster of acidic residues on the opposite side could be defined. Several amino acids within these conserved regions were mutated and analyzed in order to examine their function in PEX19-binding and in peroxisome biogenesis. Two mutations in the PEX19-binding groove (L93N, K324A) lower the affinity for PEX19 but localize correctly to peroxisomes *in vivo*. The ability to complement ΔPEX3-cells is reduced for the mutant PEX3-myc K324A compared to native PEX3-myc, whereas PEX3-myc L93N has completely lost this characteristic feature. Furthermore, a functional PEX3-PEX19 complex is essential for *de novo* formation of preperoxisomal membranes. The mutation E266A, which is located in the acidic cluster, does not interfere with PEX19-binding. In addition, both mutations in the acidic cluster are properly targeted to peroxisomes and show either no (E266A) or only a small (D275A) effect on the complementation ability of ΔPEX3-cells. The mutations in the hydrophobic groove (I140N, L165N and the double mutant I140N*L165N) do not influence PEX19-binding or the exact peroxisomal localization of PEX3-myc. However, the ability to complement ΔPEX3-cells is reduced for PEX3-myc L165N and the double mutant compared to native PEX3-myc. As the mutation at position 165 is impaired neither in the formation of preperoxisomes in *de novo* biogenesis nor in the affinity to PEX19, the hydrophobic groove could conceivably mediate the insertion of PMPs into the lipid bilayer. This implies a direct participation of PEX3 during PMP insertion. The findings implicate a dual function of the PEX3-PEX19 complex in peroxisome biogenesis. Further experiments are required to clarify the exact function of PEX3 and the detailed mechanism of PMP insertion.

7   ZUSAMMENFASSUNG

Peroxisomen sind eukaryotische Zellorganellen, die wichtige metabolische Funktionen bei der β-Oxidation langkettiger Fettsäuren, bei der Synthese von Plasmologenen sowie beim Abbau von H_2O_2 ausüben. Die an der peroxisomalen Biogenese beteiligten Proteine werden Peroxine (PEX) genannt. Von den 14 bisher bekannten humanen Peroxinen, zählen PEX3, PEX16 und PEX19 zu den frühen Peroxinen, die bei der Entstehung der peroxisomalen Membran benötigt werden. Zellen, denen eines dieser drei Peroxine fehlt, weisen keine detektierbaren peroxisomalen Membranstrukturen auf. Diese PEX3-, PEX16- oder PEX19-defizienten Zellen (ΔPEX3-, ΔPEX16- oder ΔPEX19-Zellen) können durch Transfektion des entsprechenden Gens wieder komplementiert werden und sind danach in der Lage, *de novo* Peroxisomen zu bilden.

PEX3 und PEX19 sind am Import peroxisomaler Membranproteine (PMP) beteiligt. PEX19 dient hierbei als cytosolischer Rezeptor für neu synthetisierte PMPs, indem es die peroxisomale Membranzielsequenz bindet. Zusätzlich wird PEX19 die Rolle eines Chaperons zugeordnet, da es hydrophobe Bereiche des Membranproteins bindet und sie auf diese Weise in einer Import-kompetenten Form konserviert. Beladenes PEX19 wird an die peroxisomale Membran dirigiert, indem der N-Terminus von PEX19 mit der cytosolischen Domäne von PEX3 interagiert. PEX3 ist in der peroxisomalen Membran mittels seines N-Terminus verankert, der zugleich die peroxisomale Zielsequenz als auch die Bindungsstelle für PEX16 darstellt. In dieser Arbeit wurde die Struktur von PEX3 in Verbindung mit einem PEX19-Peptid mittels Röntgenstreuung gelöst. Des Weiteren wurde der Einfluss spezifischer Mutationen in konservierten Oberflächen-bereichen von PEX3 auf die Binding mit PEX19 *in vitro* sowie auf eine mögliche Beteiligung während der peroxisomalen Biogenese *in vivo* untersucht.

Die hier beschriebene Kristallstruktur des zytosolischen Teils von PEX3 (sPEX3: aar 41-373, C235S) im Komplex mit einem PEX19-Peptid (PEX19[Pep]: aar 14-33) ermöglicht einen ersten präzisen Einblick in die PEX3-PEX19-Binding an der peroxisomalen Membran. sPEX3 weist eine rein α-helikale Faltung auf, die keinerlei Homologien zu bisher bekannten Strukturen besitzt. Zehn α-Helices und eine 3_{10}-Helix lagern sich zu einem kompakten Bündel zusammen, aus dem eine lange N-terminale Helix herausragt. Ihre Verlängerung würde *in vivo* die Verbindung zur peroxisomalen Membran herstellen. PEX19[Pep] bildet eine amphipatische Helix, die von sPEX3 mit hoher Affinität gebunden wird (K_d = 330 nM). Dies konnte mit Hilfe von kalorimetrischen Messungen

ermittelt werden. Die PEX19-Bindetasche liegt auf der Membran-abgewandten Seite und wird von drei verschiedenen Bereichen innerhalb von PEX3 gebildet. PEX19[Pep] interagiert fast ausschließlich über hydrophobe Wechselwirkungen mit sPEX3. Mittels eines thermischen Denaturierungsexperiments konnte gezeigt werden, dass PEX3 durch die Bindung von PEX19 stabilisiert wird, da der Schmelzpunkt des sPEX3+PEX19[Pep]-Komplexes um 10 °C gegenüber freiem sPEX3 erhöht ist.

sPEX3 weist mehrere hoch konservierte Bereiche auf, von denen drei auf der Oberfläche liegende Regionen darstellen: neben der konservierten PEX19-Bindetasche konnte eine konservierte hydrophobe Furche und ein konservierter Bereich mit einer Gruppe saurer Aminosäurereste identifiziert werden. Durch Mutation ausgewählter Aminosäuren innerhalb dieser Regionen wurde deren Beteiligung in Bezug auf die Bindung zu PEX19 sowie ihre Rolle während der peroxisomalen Biogenese analysiert. Zwei Mutationen in der PEX19-Bindetasche (L93N, K324A) sind in ihrer Affinität zu PEX19 beeinträchtigt. Dennoch werden beide PEX3-Mutanten *in vivo* zu Peroxisomen gebracht. Im Vergleich zu nativem PEX3-myc ist die Fähigkeit von PEX3-myc K324A ΔPEX3T-Zellen zu komplementieren, reduziert, während PEX3-myc L93N diese Eigenschaft sogar komplett verloren hat. Des Weiteren konnte gezeigt werden, dass ein funktionsfähiger PEX3-PEX19-Komplex essentiell für die *de novo* Entstehung präperoxisomaler Membranen ist. Von den Mutationen im sauren Cluster (E266A, D275A) beeinträchtigt die Mutation E266A nicht die Affinität zu PEX19. Zusätzlich werden beide PEX3-myc Mutanten in Peroxisomen lokalisiert und zeigen keine (E266A) oder nur eine geringe (D275A) Auswirkung auf die Komplementationsfähigkeit von ΔPEX3T-Zellen. Die Mutationen in der hydrophoben Tasche (I140N, L165N und die Doppelmutante I140N*L165N) wirken sich weder auf eine mögliche zusätzliche PEX19-Bindung noch auf die korrekte peroxisomale Lokalisation von PEX3 aus. Allerdings weisen PEX3-myc L165N und die Doppelmutante eine verringerte Komplementationsfähigkeit von ΔPEX3T-Zellen auf. Da die Mutation an Position 165 keinen Einfluss auf die Bildung von Präperoxisomen während der *de novo* Biogenese hat und ebenso wenig die Affinität zu PEX19 beeinflusst, könnte die hydrophobe Furche die Insertion von PMPs in die peroxisomale Membran vermitteln. Da dies der erste Hinweis auf eine direkte Beteiligung von PEX3 während der Membraninsertion von PMPs ist, bedarf es weiterführender Experimente, um diese Ergebnisse zu untermauern und die genaue Aufgabe von PEX3 sowie den Mechanismus des PMP Imports zu klären.

8   REFERENCES

1.   Rhodin, J. (1954). Correlation of ultrastructural organization and function in normal and experimentally changed proximal convoluted tubule cells of the mouse kidney. PhD thesis, Karolinska Institute, Stockholm.

2.   De Duve, C., Baudhuin, P. (1966). Peroxisomes (microbodies and related particles). Physiol Revue 46, 323-357.

3.   Breidenbach, R. W., Beevers, H. (1967). Association of the glyoxylate cycle enzymes in a novel subcellular particle from castor bean endosperm. Biochem Biophys Res Commun 24, 462-469.

4.   Opperdoes, F. R., Borst, P. (1977). Localization of nine glycolytic enzymes in a microbody-like organells in Trypanosoma brucei: the glycosome. FEBS Lett 80, 360-364.

5.   Angermüller, S., and Fahimi, H. D. (1986). Ultrastructural cytochemical localization of uricase in peroxisomes of rat liver. J Histochem Cytochem 34, 159-165.

6.   Schrader, M., and Fahimi, H. D. (2008). The peroxisome: still a mysterious organelle. Histochem Cell Biol 129, 421-440.

7.   Hruban, Z., Rechcigl, M. (1969). Microbodies and related particles. Morphology, bicohemistry and physiology. Int Rev Cytol, Suppl 1:1, Suppl 296.

8.   Fahimi, H. D. (1968). Cytochemical localization of peroxidase activity in rat hepatic microbodies (peroxisomes). J Histochem Cytochem 16, 547-550.

9.   Fahimi, H. D. (1969). Cytochemical localization of peroxidatic activita of catalase in rat hepatic microbodies (peroxisomes) J Cell Biol 43, 275-288.

10.   Lazarow, P. B., De Duve, C. (1976). A fatty acid acyl-CoA oxidizing system in rat liver peroxisomes; enhancement by clofibrate, a hypolipidemic drug. Proc Natl Acad Sci USA 73, 2043-2046.

11.   Wanders, R. J., van Grunsven, E. G., and Jansen, G. A. (2000). Lipid metabolism in peroxisomes: enzymology, functions and dysfunctions of the fatty acid alpha- and beta-oxidation systems in humans. Biochem Soc Trans 28, 141-149.

12.   Hajra, A. K., Burke, C. L., Jones, C. L. (1979). Subcellular localizationof acyl coenzyme A: dihydroxyacetone phosphate acyltransferase in rat liver peroxisomes (microbodies). J Biol Chem 254, 10896-10900.

13.   Momoi, K., Fukui, K., Watanabe, F., and Miyake, Y. (1988). Molecular cloning and sequence analysis of cDNA encoding human kidney D-amino acid oxidase. FEBS Lett 238, 180-184.

14.   Krisans, S. K., Thompson, S. L., Pena, L. A., Kok, E., and Javitt, N. B. (1985). Bile acid synthesis in rat liver peroxisomes: metabolism of 26-hydroxycholesterol to 3 beta-hydroxy-5-cholenoic acid. J Lipid Res 26, 1324-1332.

15.   Brites, P., Waterham, H. R., and Wanders, R. J. (2004). Functions and biosynthesis of plasmalogens in health and disease. Biochim Biophys Acta 1636, 219-231.

16.   Krisans, S. K. (1992). The role of peroxisomes in cholesterol metabolism. Am J Respir Cell Mol Biol 7, 358-364.

17.   Mosser, J., Douar, A. M., Sarde, C. O., Kioschis, P., Feil, R., Moser, H., Poustka, A. M., Mandel, J. L., and Aubourg, P. (1993). Putative X-linked adrenoleukodystrophy gene shares unexpected homology with ABC transporters. Nature 361, 726-730.

18.   Moser, H. W. (1997). Adrenoleukodystrophy: phenotype, genetics, pathogenesis and therapy. Brain 120, 1485-1508.

19.   Wanders, R. J. (2004). Metabolic and molecular basis of peroxisomal disorders: a review. Am J Med Genet A 126A, 355-375.

20.   Wanders, R. J. (2004). Peroxisomes, lipid metabolism, and peroxisomal disorders. Mol Genet Metab 83, 16-27.

21.   Distel, B., Erdmann, R., Gould, S. J., Blobel, G., Crane, D. I., Cregg, J. M., Dodt, G., Fujiki, Y., Goodman, J. M., Just, W. W., Kiel, J. A., Kunau, W. H., Lazarow, P. B., Mannaerts, G. P., Moser, H. W., Osumi, T., Rachubinski, R. A., Roscher, A., Subramani, S., Tabak, H. F., Tsukamoto, T., Valle, D., van der Klei, I., van Veldhoven, P. P., and Veenhuis, M. (1996). A unified nomenclature for peroxisome biogenesis factors. J Cell Biol 135, 1-3.

22.   Zellweger, H., Lindenberg, P., Bowen, C. (1964). A familial syndrome of multiple congenital defects. Bull Johns Hopkins Hosp 114, 402-414.

23.   Kelley, R. I., Datta, N. S., Dobyns, W. B., Hajra, A. K., Moser, A. B., Noetzel, M. J., Zackai, E. H., Moser, H. W. (1986). Neonatal adrenoleukodystrophy: new cases, biochemical studies, and differentiation from Zellweger and related peroxisomal polydystrophy syndromes. Am J Med Genet 23, 869-901.

24.   Poll-The, B. T., Ogier, H., Saudubray, J. M., Schutgens, R. B., Wanders, R. J., van den Bosch, H., and Schrakamp, G. (1986). Impaired plasmalogen metabolism in infantile Refsum's disease. Eur J Pediatr 144, 513-514.

25.   Poll-The, B. T., Saudubray, J. M., Ogier, H., Schutgens, R. B. H., Wanders, R. J. A., Schrakamp, G., van den Bosch, H., Trijbels, J. M. F., Poulos, A., Moser, H. W., van Eldere, J., Eyssen, H. J. (1986). Infantile Refsum's disease: biochemical findings suggesting multiple peroxisomal dysfunction. J Inherit Metab Dis 9, 169-174.

26.   Heymans, H. S. A., Oorthuys, J. W. E., Nelck, G., Wanders, R. J. A., Schutgens, R. B. H. (1985). Rhizomelic chondrodysplasia punctata: another peroxisomal disorder. New Eng J Med 2, 187-188.

27.   Nagotu, S., Veenhuis, M., and van der Klei, I. J. Divide et impera: the dictum of peroxisomes. Traffic 11, 175-184.

28.   Sakai, Y., Oku, M., van der Klei, I. J., and Kiel, J. A. (2006). Pexophagy: autophagic degradation of peroxisomes. Biochim Biophys Acta 1763, 1767-1775.

29.   Platta, H. W., and Erdmann, R. (2007). Peroxisomal dynamics. Trends Cell Biol 17, 474-484.

30.   Novikoff, A. B., Shin, W.-Y. (1964). The endoplasmic reticulum in the golgi zone and its relations to microbodies, golgi apparatus and autophagic vacuoles in rat liver cells. J Mikros Oxford 3, 187-206.

31.   Fujiki, Y., Rachubinski, R. A., and Lazarow, P. B. (1984). Synthesis of a major integral membrane polypeptide of rat liver peroxisomes on free polysomes. Proc Natl Acad Sci U S A 81, 7127-7131.

32.   Lazarow, P. B., and Fujiki, Y. (1985). Biogenesis of peroxisomes. Annu Rev Cell Biol 1, 489-530.

33.   Höhfeld, J., Veenhuis, M., and Kunau, W. H. (1991). PAS3, a Saccharomyces cerevisiae gene encoding a peroxisomal integral membrane protein essential for peroxisome biogenesis. J Cell Biol 114, 1167-1178.

34.   Matsuzono, Y., Kinoshita, N., Tamura, S., Shimozawa, N., Hamasaki, M., Ghaedi, K., Wanders, R. J., Suzuki, Y., Kondo, N., and Fujiki, Y. (1999). Human PEX19: cDNA cloning by functional complementation, mutation analysis in a patient with Zellweger syndrome, and potential role in peroxisomal membrane assembly. Proc Natl Acad Sci U S A 96, 2116-2121.

35.   South, S. T., and Gould, S. J. (1999). Peroxisome synthesis in the absence of preexisting peroxisomes. J Cell Biol 144, 255-266.

36.   Titorenko, V. I., Chan, H., and Rachubinski, R. A. (2000). Fusion of small peroxisomal vesicles in vitro reconstructs an early step in the in vivo multistep peroxisome assembly pathway of Yarrowia lipolytica. J Cell Biol 148, 29-44.

37.   Tabak, H. F., Murk, J. L., Braakman, I., and Geuze, H. J. (2003). Peroxisomes start their life in the endoplasmic reticulum. Traffic 4, 512-518.

38.   Hoepfner, D., Schildknegt, D., Braakman, I., Philippsen, P., and Tabak, H. F. (2005). Contribution of the endoplasmic reticulum to peroxisome formation. Cell 122, 85-95.

39.   Titorenko, V. I., and Rachubinski, R. A. (1998). Mutants of the yeast Yarrowia lipolytica defective in protein exit from the endoplasmic reticulum are also defective in peroxisome biogenesis. Mol Cell Biol 18, 2789-2803.

40.   Lam, S. K., Yoda, N., and Schekman, R. (2010). A vesicle carrier that mediates peroxisome protein traffic from the endoplasmic reticulum. Proc Natl Acad Sci U S A 107, 21523-21528.

41.   Tam, Y. Y., Fagarasanu, A., Fagarasanu, M., and Rachubinski, R. A. (2005). Pex3p initiates the formation of a preperoxisomal compartment from a subdomain of the endoplasmic reticulum in Saccharomyces cerevisiae. J Biol Chem 280, 34933-34939.

42.   South, S. T., Baumgart, E., and Gould, S. J. (2001). Inactivation of the endoplasmic reticulum protein translocation factor, Sec61p, or its homolog, Ssh1p, does not affect peroxisome biogenesis. Proc Natl Acad Sci U S A 98, 12027-12031.

43.   Agrawal, G., Joshi, S., and Subramani, S. (2011). Cell-free sorting of peroxisomal membrane proteins from the endoplasmic reticulum. Proc Natl Acad Sci U S A 108, 9113-9118.

44.   Motley, A. M., and Hettema, E. H. (2007). Yeast peroxisomes multiply by growth and division. J Cell Biol 178, 399-410.

45.   van der Zand, A., Braakman, I., and Tabak, H. F. (2010). Peroxisomal membrane proteins insert into the endoplasmic reticulum. Mol Biol Cell 21, 2057-2065.

46.   Zipor, G., Haim-Vilmovsky, L., Gelin-Licht, R., Gadir, N., Brocard, C., and Gerst, J. E. (2009). Localization of mRNAs coding for peroxisomal proteins in the yeast, Saccharomyces cerevisiae. Proc Natl Acad Sci U S A 106, 19848-19853.

47.   Halbach, A., Rucktäschel, R., Rottensteiner, H., and Erdmann, R. (2009). The N-domain of Pex22p can functionally replace the Pex3p N-domain in targeting and peroxisome formation. J Biol Chem 284, 3906-3916.

48.   Rucktäschel, R., Halbach, A., Girzalsky, W., Rottensteiner, H., and Erdmann, R. (2010). De novo synthesis of peroxisomes upon mitochondrial targeting of Pex3p. Eur J Cell Biol 89, 947-954.

49.   Titorenko, V. I., and Rachubinski, R. A. (2000). Peroxisomal membrane fusion requires two AAA family ATPases, Pex1p and Pex6p. J Cell Biol 150, 881-886.

50.   Geuze, H. J., Murk, J. L., Stroobants, A. K., Griffith, J. M., Kleijmeer, M. J., Koster, A. J., Verkleij, A. J., Distel, B., and Tabak, H. F. (2003). Involvement of the endoplasmic reticulum in peroxisome formation. Mol Biol Cell 14, 2900-2907.

51.   Toro, A. A., Araya, C. A., Cordova, G. J., Arredondo, C. A., Cardenas, H. G., Moreno, R. E., Venegas, A., Koenig, C. S., Cancino, J., Gonzalez, A., and Santos, M. J. (2009). Pex3p-dependent peroxisomal biogenesis initiates in the endoplasmic reticulum of human fibroblasts. J Cell Biochem 107, 1083-1096.

52.   Kim, P. K., Mullen, R. T., Schumann, U., and Lippincott-Schwartz, J. (2006). The origin and maintenance of mammalian peroxisomes involves a de novo PEX16-dependent pathway from the ER. J Cell Biol 173, 521-532.

53.   Voorn-Brouwer, T., Kragt, A., Tabak, H. F., and Distel, B. (2001). Peroxisomal membrane proteins are properly targeted to peroxisomes in the absence of COPI- and COPII-mediated vesicular transport. J Cell Sci 114, 2199-2204.

54.   South, S. T., Sacksteder, K. A., Li, X., Liu, Y., and Gould, S. J. (2000). Inhibitors of COPI and COPII do not block PEX3-mediated peroxisome synthesis. J Cell Biol 149, 1345-1360.

55.   Yonekawa, S., Furuno, A., Baba, T., Fujiki, Y., Ogasawara, Y., Yamamoto, A., Tagaya, M., and Tani, K. (2011). Sec16B is involved in the endoplasmic reticulum export of the peroxisomal membrane biogenesis factor peroxin 16 (Pex16) in mammalian cells. Proc Natl Acad Sci U S A, Epub ahead of print.

56.   Ma, C., Agrawal, G., and Subramani, S. (2011). Peroxisome assembly: matrix and membrane protein biogenesis. J Cell Biol 193, 7-16.

57.   Hettema, E. H., Girzalsky, W., van Den Berg, M., Erdmann, R., and Distel, B. (2000). Saccharomyces cerevisiae pex3p and pex19p are required for proper localization and stability of peroxisomal membrane proteins. EMBO J 19, 223-233.

58.   Ghaedi, K., Tamura, S., Okumoto, K., Matsuzono, Y., and Fujiki, Y. (2000). The peroxin pex3p initiates membrane assembly in peroxisome biogenesis. Mol Biol Cell 11, 2085-2102.

59.   Götte, K., Girzalsky, W., Linkert, M., Baumgart, E., Kammerer, S., Kunau, W. H., and Erdmann, R. (1998). Pex19p, a farnesylated protein essential for peroxisome biogenesis. Mol Cell Biol 18, 616-628.

60.   Erdmann, R., and Blobel, G. (1996). Identification of Pex13p a peroxisomal membrane receptor for the PTS1 recognition factor. J Cell Biol 135, 111-121.

61.   Gould, S. J., Kalish, J. E., Morrell, J. C., Bjorkman, J., Urquhart, A. J., and Crane, D. I. (1996). Pex13p is an SH3 protein of the peroxisome membrane and a docking factor for the predominantly cytoplasmic PTs1 receptor. J Cell Biol 135, 85-95.

62.   Van Ael, E., and Fransen, M. (2006). Targeting signals in peroxisomal membrane proteins. Biochim Biophys Acta 1763, 1629-1638.

63.   Rottensteiner, H., Kramer, A., Lorenzen, S., Stein, K., Landgraf, C., Volkmer-Engert, R., and Erdmann, R. (2004). Peroxisomal membrane proteins contain common Pex19p-binding sites that are an integral part of their targeting signals. Mol Biol Cell 15, 3406-3417.

64.   Girzalsky, W., Saffian, D., and Erdmann, R. (2010). Peroxisomal protein translocation. Biochim Biophys Acta 1803, 724-731.

65.   Fransen, M., Vastiau, I., Brees, C., Brys, V., Mannaerts, G. P., and Van Veldhoven, P. P. (2005). Analysis of human Pex19p's domain structure by pentapeptide scanning mutagenesis. J Mol Biol 346, 1275-1286.

66.   Schueller, N., Holton, S. J., Fodor, K., Milewski, M., Konarev, P., Stanley, W. A., Wolf, J., Erdmann, R., Schliebs, W., Song, Y. H., and Wilmanns, M. (2010). The peroxisomal receptor Pex19p forms a helical mPTS recognition domain. EMBO J 29, 2491-2500.

67.   Jones, J. M., Morrell, J. C., and Gould, S. J. (2004). PEX19 is a predominantly cytosolic chaperone and import receptor for class 1 peroxisomal membrane proteins. J Cell Biol 164, 57-67.

68.   Snyder, W. B., Koller, A., Choy, A. J., and Subramani, S. (2000). The peroxin Pex19p interacts with multiple, integral membrane proteins at the peroxisomal membrane. J Cell Biol 149, 1171-1178.

69.   Sacksteder, K. A., Jones, J. M., South, S. T., Li, X., Liu, Y., and Gould, S. J. (2000). PEX19 binds multiple peroxisomal membrane proteins, is predominantly cytoplasmic, and is required for peroxisome membrane synthesis. J Cell Biol 148, 931-944.

70.   Fang, Y., Morrell, J. C., Jones, J. M., and Gould, S. J. (2004). PEX3 functions as a PEX19 docking factor in the import of class I peroxisomal membrane proteins. J Cell Biol 164, 863-875.

71.   Fransen, M., Wylin, T., Brees, C., Mannaerts, G. P., and Van Veldhoven, P. P. (2001). Human pex19p binds peroxisomal integral membrane proteins at regions distinct from their sorting sequences. Mol Cell Biol 21, 4413-4424.

72.   Rucktäschel, R., Girzalsky, W., and Erdmann, R. (2010). Protein import machineries of peroxisomes. Biochim Biophys Acta 1808, 892-900.

73.   Muntau, A. C., Roscher, A. A., Kunau, W. H., and Dodt, G. (2003). The interaction between human PEX3 and PEX19 characterized by fluorescence resonance energy transfer (FRET) analysis. Eur J Cell Biol 82, 333-342.

74.   Muntau, A. C., Roscher, A. A., Kunau, W. H., and Dodt, G. (2003). Interaction of PEX3 and PEX19 visualized by fluorescence resonance energy transfer (FRET). Adv Exp Med Biol 544, 221-224.

75.   Matsuzaki, T., and Fujiki, Y. (2008). The peroxisomal membrane protein import receptor Pex3p is directly transported to peroxisomes by a novel Pex19p- and Pex16p-dependent pathway. J Cell Biol 183, 1275-1286.

76.   Matsuzono, Y., and Fujiki, Y. (2006). In vitro transport of membrane proteins to peroxisomes by shuttling receptor Pex19p. J Biol Chem 281, 36-42.

77.   Diestelkötter, P., and Just, W. W. (1993). In vitro insertion of the 22-kD peroxisomal membrane protein into isolated rat liver peroxisomes. J Cell Biol 123, 1717-1725.

78.   Walton, P. A., Hill, P. E., and Subramani, S. (1995). Import of stably folded proteins into peroxisomes. Mol Biol Cell 6, 675-683.

79.   McNew, J. A., and Goodman, J. M. (1994). An oligomeric protein is imported into peroxisomes in vivo. J Cell Biol 127, 1245-1257.

80.   Leon, S., Goodman, J. M., and Subramani, S. (2006). Uniqueness of the mechanism of protein import into the peroxisome matrix: transport of folded, co-factor-bound and oligomeric proteins by shuttling receptors. Biochim Biophys Acta 1763, 1552-1564.

81.   Subramani, S. (1993). Protein import into peroxisomes and biogenesis of the organelle. Annu Rev Cell Biol 9, 445-478.

82.   Dammai, V., and Subramani, S. (2001). The human peroxisomal targeting signal receptor, Pex5p, is translocated into the peroxisomal matrix and recycled to the cytosol. Cell 105, 187-196.

83.   Gould, S. J., Keller, G. A., Hosken, N., Wilkinson, J., and Subramani, S. (1989). A conserved tripeptide sorts proteins to peroxisomes. J Cell Biol 108, 1657-1664.

84.   Brocard, C., and Hartig, A. (2006). Peroxisome targeting signal 1: is it really a simple tripeptide? Biochim Biophys Acta 1763, 1565-1573.

85.   Stanley, W. A., Filipp, F. V., Kursula, P., Schuller, N., Erdmann, R., Schliebs, W., Sattler, M., and Wilmanns, M. (2006). Recognition of a functional peroxisome type 1 target by the dynamic import receptor pex5p. Mol Cell 24, 653-663.

86.   Lazarow, P. B. (2006). The import receptor Pex7p and the PTS2 targeting sequence. Biochim Biophys Acta 1763, 1599-1604.

87.   Mukai, S., and Fujiki, Y. (2006). Molecular mechanisms of import of peroxisome-targeting signal type 2 (PTS2) proteins by PTS2 receptor Pex7p and PTS1 receptor Pex5pL. J Biol Chem 281, 37311-37320.

88.   Shepard, A. R., Jacobson, N., Millar, J. C., Pang, I. H., Steely, H. T., Searby, C. C., Sheffield, V. C., Stone, E. M., and Clark, A. F. (2007). Glaucoma-causing myocilin mutants require the Peroxisomal targeting signal-1 receptor (PTS1R) to elevate intraocular pressure. Hum Mol Genet 16, 609-617.

89.   Dodt, G., Warren, D., Becker, E., Rehling, P., and Gould, S. J. (2001). Domain mapping of human PEX5 reveals functional and structural similarities to Saccharomyces cerevisiae Pex18p and Pex21p. J Biol Chem 276, 41769-41781.

90.   Yang, X., Purdue, P. E., and Lazarow, P. B. (2001). Eci1p uses a PTS1 to enter peroxisomes: either its own or that of a partner, Dci1p. Eur J Cell Biol 80, 126-138.

91.   van der Klei, I. J., and Veenhuis, M. (2006). PTS1-independent sorting of peroxisomal matrix proteins by Pex5p. Biochim Biophys Acta 1763, 1794-1800.

92.   Rayapuram, N., and Subramani, S. (2006). The importomer--a peroxisomal membrane complex involved in protein translocation into the peroxisome matrix. Biochim Biophys Acta 1763, 1613-1619.

93.   Brocard, C., Lametschwandtner, G., Koudelka, R., and Hartig, A. (1997). Pex14p is a member of the protein linkage map of Pex5p. EMBO J 16, 5491-5500.

94.   Meinecke, M., Cizmowski, C., Schliebs, W., Kruger, V., Beck, S., Wagner, R., and Erdmann, R. (2010). The peroxisomal importomer constitutes a large and highly dynamic pore. Nat Cell Biol 12, 273-277.

95.   Gouveia, A. M., Reguenga, C., Oliveira, M. E., Sa-Miranda, C., and Azevedo, J. E. (2000). Characterization of peroxisomal Pex5p from rat liver. Pex5p in the Pex5p-Pex14p membrane complex is a transmembrane protein. J Biol Chem 275, 32444-32451.

96.   Platta, H. W., El Magraoui, F., Schlee, D., Grunau, S., Girzalsky, W., and Erdmann, R. (2007). Ubiquitination of the peroxisomal import receptor Pex5p is required for its recycling. J Cell Biol 177, 197-204.

97.   Carvalho, A. F., Pinto, M. P., Grou, C. P., Alencastre, I. S., Fransen, M., Sa-Miranda, C., and Azevedo, J. E. (2007). Ubiquitination of mammalian Pex5p, the peroxisomal import receptor. J Biol Chem 282, 31267-31272.

98.   Miyata, N., and Fujiki, Y. (2005). Shuttling mechanism of peroxisome targeting signal type 1 receptor Pex5: ATP-independent import and ATP-dependent export. Mol Cell Biol 25, 10822-10832.

99.   Platta, H. W., Grunau, S., Rosenkranz, K., Girzalsky, W., and Erdmann, R. (2005). Functional role of the AAA peroxins in dislocation of the cycling PTS1 receptor back to the cytosol. Nat Cell Biol 7, 817-822.

100.   Matsumoto, N., Tamura, S., and Fujiki, Y. (2003). The pathogenic peroxin Pex26p recruits the Pex1p-Pex6p AAA ATPase complexes to peroxisomes. Nat Cell Biol 5, 454-460.

101.   Platta, H. W., Girzalsky, W., and Erdmann, R. (2004). Ubiquitination of the peroxisomal import receptor Pex5p. Biochem J 384, 37-45.

102.   Kiel, J. A., Emmrich, K., Meyer, H. E., and Kunau, W. H. (2005). Ubiquitination of the peroxisomal targeting signal type 1 receptor, Pex5p, suggests the presence of a quality control mechanism during peroxisomal matrix protein import. J Biol Chem 280, 1921-1930.

103.   Wickner, W., and Schekman, R. (2005). Protein translocation across biological membranes. Science 310, 1452-1456.

104.   Santos, M. J., Imanaka, T., Shio, H., Small, G. M., and Lazarow, P. B. (1988). Peroxisomal membrane ghosts in Zellweger syndrome--aberrant organelle assembly. Science 239, 1536-1538.

105.   Santos, M. J., Imanaka, T., Shio, H., and Lazarow, P. B. (1988). Peroxisomal integral membrane proteins in control and Zellweger fibroblasts. J Biol Chem 263, 10502-10509.

106.   Chang, C. C., South, S., Warren, D., Jones, J., Moser, A. B., Moser, H. W., and Gould, S. J. (1999). Metabolic control of peroxisome abundance. J Cell Sci 112 (Pt 10), 1579-1590.

107.   Zimmermann, R., Eyrisch, S., Ahmad, M., and Helms, V. (2011). Protein translocation across the ER membrane. Biochim Biophys Acta 1808, 912-924.

108.   Gebert, N., Ryan, M. T., Pfanner, N., Wiedemann, N., and Stojanovski, D. (2011). Mitochondrial protein import machineries and lipids: a functional connection. Biochim Biophys Acta 1808, 1002-1011.

109.   Schwenkert, S., Soll, J., and Bolter, B. (2011). Protein import into chloroplasts--how chaperones feature into the game. Biochim Biophys Acta 1808, 901-911.

110.   Robinson, C., Matos, C. F., Beck, D., Ren, C., Lawrence, J., Vasisht, N., and Mendel, S. (2011). Transport and proofreading of proteins by the twin-arginine translocation (Tat) system in bacteria. Biochim Biophys Acta 1808, 876-884.

111.   Aldridge, C., Cain, P., and Robinson, C. (2009). Protein transport in organelles: Protein transport into and across the thylakoid membrane. FEBS J 276, 1177-1186.

112.   Dukanovic, J., and Rapaport, D. (2011). Multiple pathways in the integration of proteins into the mitochondrial outer membrane. Biochim Biophys Acta 1808, 971-980.

113.   Marom, M., Azem, A., and Mokranjac, D. (2011). Understanding the molecular mechanism of protein translocation across the mitochondrial inner membrane: still a long way to go. Biochim Biophys Acta 1808, 990-1001.

114.   Hofmann, N. R., and Theg, S. M. (2005). Chloroplast outer membrane protein targeting and insertion. Trends Plant Sci 10, 450-457.

115.   Borgese, N., and Fasana, E. (2011). Targeting pathways of C-tail-anchored proteins. Biochim Biophys Acta 1808, 937-946.

116.   Halbach, A., Landgraf, C., Lorenzen, S., Rosenkranz, K., Volkmer-Engert, R., Erdmann, R., and Rottensteiner, H. (2006). Targeting of the tail-anchored peroxisomal membrane proteins PEX26 and PEX15 occurs through C-terminal PEX19-binding sites. J Cell Sci 119, 2508-2517.

117.   Delille, H. K., and Schrader, M. (2008). Targeting of hFis1 to peroxisomes is mediated by Pex19p. J Biol Chem 283, 31107-31115.

118. Shibata, H., Kashiwayama, Y., Imanaka, T., and Kato, H. (2004). Domain architecture and activity of human Pex19p, a chaperone-like protein for intracellular trafficking of peroxisomal membrane proteins. J Biol Chem 279, 38486-38494.

119. Fujiki, Y., Matsuzono, Y., Matsuzaki, T., and Fransen, M. (2006). Import of peroxisomal membrane proteins: the interplay of Pex3p- and Pex19p-mediated interactions. Biochim Biophys Acta 1763, 1639-1646.

120. Soukupova, M., Sprenger, C., Gorgas, K., Kunau, W. H., and Dodt, G. (1999). Identification and characterization of the human peroxin PEX3. Eur J Cell Biol 78, 357-374.

121. Kammerer, S., Holzinger, A., Welsch, U., and Roscher, A. A. (1998). Cloning and characterization of the gene encoding the human peroxisomal assembly protein Pex3p. FEBS Lett 429, 53-60.

122. Matsuzono, Y., Matsuzaki, T., and Fujiki, Y. (2006). Functional domain mapping of peroxin Pex19p: interaction with Pex3p is essential for function and translocation. J Cell Sci 119, 3539-3550.

123. Sato, Y., Shibata, H., Nakano, H., Matsuzono, Y., Kashiwayama, Y., Kobayashi, Y., Fujiki, Y., Imanaka, T., and Kato, H. (2008). Characterization of the interaction between recombinant human peroxin Pex3p and Pex19p: identification of Trp-104 in Pex3p as a critical residue for the interaction. J Biol Chem 283, 6136-6144.

124. Sato, Y., Shibata, H., Nakatsu, T., Nakano, H., Kashiwayama, Y., Imanaka, T., and Kato, H. (2010). Structural basis for docking of peroxisomal membrane protein carrier Pex19p onto its receptor Pex3p. EMBO J 29, 4083-4093.

125. Kammerer, S., Arnold, N., Gutensohn, W., Mewes, H. W., Kunau, W. H., Hofler, G., Roscher, A. A., and Braun, A. (1997). Genomic organization and molecular characterization of a gene encoding HsPXF, a human peroxisomal farnesylated protein. Genomics 45, 200-210.

126. Rucktäschel, R., Thoms, S., Sidorovitch, V., Halbach, A., Pechlivanis, M., Volkmer, R., Alexandrov, K., Kuhlmann, J., Rottensteiner, H., and Erdmann, R. (2009). Farnesylation of pex19p is required for its structural integrity and function in peroxisome biogenesis. J Biol Chem 284, 20885-20896.

127. Fransen, M., Brees, C., Ghys, K., Amery, L., Mannaerts, G. P., Ladant, D., and Van Veldhoven, P. P. (2002). Analysis of mammalian peroxin interactions using a non-transcription-based bacterial two-hybrid assay. Mol Cell Proteomics 1, 243-252.

128. Vastiau, I. M., Anthonio, E. A., Brams, M., Brees, C., Young, S. G., Van de Velde, S., Wanders, R. J., Mannaerts, G. P., Baes, M., Van Veldhoven, P. P., and Fransen, M. (2006). Farnesylation of Pex19p is not essential for peroxisome biogenesis in yeast and mammalian cells. Cell Mol Life Sci 63, 1686-1699.

129. Treiber, N. (2008). De novo Erzeugung und Strukturanalyse eines Protein-Protein-Kontaktes und Versuche zur strukturellen Charakterisierung der Peroxine PEX19 und PEX3 sowie Kristallstrukturen eines moskitoziden Holotoxins und einer aromatischen Flavin-Monooxygenase. Promotionsarbeit, Universität Freiburg.

130.   Soukupova, M. (2000). Biogenese von Peroxisomen - Untersuchungen zu PEX3 und PEX5 Proteinen des Menschen. Promotionsarbeit, Universität Bochum.

131.   Mullis, K., Faloona, F., Scharf, S., Saiki, R., Horn, G., and Erlich, H. (1986). Specific enzymatic amplification of DNA in vitro: the polymerase chain reaction. Cold Spring Harb Symp Quant Biol 51, 263-273.

132.   Hutchison, C. A., 3rd, Phillips, S., Edgell, M. H., Gillam, S., Jahnke, P., and Smith, M. (1978). Mutagenesis at a specific position in a DNA sequence. J Biol Chem 253, 6551-6560.

133.   Sanger, F. (1981). Determination of nucleotide sequences in DNA. Science 214, 1205-1210.

134.   Porath, J., Carlsson, J., Olsson, I., and Belfrage, G. (1975). Metal chelate affinity chromatography, a new approach to protein fractionation. Nature 258, 598-599.

135.   Lützner, N., Pätzold, B., Zoll, S., Stehle, T., and Kalbacher, H. (2009). Development of a novel fluorescent substrate for Autolysin E, a bacterial type II amidase. Biochem Biophys Res Commun 380, 554-558.

136.   Laemmli, U. K. (1970). Cleavage of structural proteins during the assembly of the head of bacteriophage T4. Nature 227, 680-685.

137.   Renart, J., Reiser, J., and Stark, G. R. (1979). Transfer of proteins from gels to diazobenzyloxymethyl-paper and detection with antisera: a method for studying antibody specificity and antigen structure. Proc Natl Acad Sci U S A 76, 3116-3120.

138.   Gill, S. C., and von Hippel, P. H. (1989). Calculation of protein extinction coefficients from amino acid sequence data. Anal Biochem 182, 319-326.

139.   Gasteiger, E., Hoogland, C., Gattiker, A., Duvaud, S., Wilkins, M. R., Appel, R. D., and Bairoch, A. (2005) Protein Identification and Analysis Tools on the ExPASy Server. in The Proteomics Protocols Handbook, Humana Press. pp 571-607

140.   Gasteiger, E., Gattiker, A., Hoogland, C., Ivanyi, I., Appel, R. D., and Bairoch, A. (2003). ExPASy: The proteomics server for in-depth protein knowledge and analysis. Nucleic Acids Res 31, 3784-3788.

141.   Poulos, A., Christodoulou, J., Chow, C. W., Goldblatt, J., Paton, B. C., Orii, T., Suzuki, Y., and Shimozawa, N. (1995). Peroxisomal assembly defects: clinical, pathologic, and biochemical findings in two patients in a newly identified complementation group. J Pediatr 127, 596-599.

142.   Dodt, G., Braverman, N., Wong, C., Moser, A., Moser, H. W., Watkins, P., Valle, D., and Gould, S. J. (1995). Mutations in the PTS1 receptor gene, PXR1, define complementation group 2 of the peroxisome biogenesis disorders. Nat Genet 9, 115-125.

143.   Will, G. K., Soukupova, M., Hong, X., Erdmann, K. S., Kiel, J. A., Dodt, G., Kunau, W. H., and Erdmann, R. (1999). Identification and characterization of the human orthologue of yeast Pex14p. Mol Cell Biol 19, 2265-2277.

144. Schmidt, F. (2007). Reinigung, Kristallisation und röntgenographische Untersuchungen des Faktors 3 der humanen peroxisomalen Biogenese. Diplomarbeit, Universität Freiburg.

145. Asherie, N. (2004). Protein crystallization and phase diagrams. Methods 34, 266-272.

146. Rupp, B. (2010). Biomolecular Crystallography - Principles, Practice and Application to Structural Biology. Garland Science, New York.

147. Blow, D. (2002). Outline of Crystallography for Biologists. Oxford University Press, Oxford.

148. Bragg, W. H., Bragg, W. L. (1913). The reflection of X-rays by crystals: I. Proc Roy Soc (London) A 88, 428-438.

149. Ewald, P. P. (1917). Zur Begründung der Kristalloptik. Ann Phys Lpz 349, 519.

150. Evans, P. (2006). Scaling and assessment of data quality. Acta Crystallogr D Biol Crystallogr 62, 72-82.

151. Diederichs, K., and Karplus, P. A. (1997). Improved R-factors for diffraction data analysis in macromolecular crystallography. Nat Struct Biol 4, 269-275.

152. Wilson, A. J. C. (1949). X-ray diffraction by random layers: ideal profiles and determination of structure amplitudes from observed line profiles. Acta Crystallogr 2, 245.

153. Matthews, B. W. (1968). Solvent content of protein crystals. J Mol Biol 33, 491-497.

154. Yeates, T. O. (1997). Detecting and overcoming crystal twinning. Methods Enzymol 276, 344-358.

155. Sander, C., and Schneider, R. (1991). Database of homology-derived protein structures and the structural meaning of sequence alignment. Proteins 9, 56-68.

156. Rossmann, M. G., Blow, D. M. (1962). The detection of sub-units within the crystallographic asymmetric unit. Acta Crystallogr 15, 24-31.

157. Brunger, A. T. (1993). Assessment of phase accuracy by cross validation: the free R value. Methods and applications. Acta Crystallogr D Biol Crystallogr 49, 24-36.

158. Brunger, A. T. (1992). Free R value: a novel statistical quantity for assessing the accuracy of crystal structures. Nature 355, 472-475.

159. Kabsch, W. (1993). Automatic processing of rotation diffraction data from crystals of initially unknown symmetry and cell constants. J Appl Crystallogr 26, 795 - 800.

160. McCoy, A. J., Grosse-Kunstleve, R. W., Storoni, L. C., and Read, R. J. (2005). Likelihood-enhanced fast translation functions. Acta Crystallogr D Biol Crystallogr 61, 458-464.

161. CCP4. (1994). The CCP4 suite: programs for protein crystallography. Acta Crystallogr D Biol Crystallogr 50, 760-763.

162. Emsley, P., and Cowtan, K. (2004). Coot: model building tools for molecular graphics. Acta Crystallogr D Biol Crystallogr 60, 2126-2132.

163. Murshudov, G. N., Vagin, A. A., and Dodson, E. J. (1997). Refinement of macromolecular structures by the maximum-likelihood method. Acta Crystallogr D Biol Crystallogr 53, 240-255.

164. Painter, J., and Merritt, E. A. (2006). Optimal description of a protein structure in terms of multiple groups undergoing TLS motion. Acta Crystallogr D Biol Crystallogr 62, 439-450.

165. Painter, J., and Merrit, E. A. (2006). TLSMD web server for the generation of multi-group TLS models. J Appl Crystallogr 39, 109-111.

166. Howlin, B., Butler, S. A., Moss, D. S., Harris, G. W., Driessen, H. P. C. (1993). TLSANL: TLS parameter-analysis program for segmented anisotropic refinement of macromolecular strcutures. J Appl Crystallogr 26, 622-624.

167. Adams, P. D., Afonine, P. V., Bunkoczi, G., Chen, V. B., Davis, I. W., Echols, N., Headd, J. J., Hung, L. W., Kapral, G. J., Grosse-Kunstleve, R. W., McCoy, A. J., Moriarty, N. W., Oeffner, R., Read, R. J., Richardson, D. C., Richardson, J. S., Terwilliger, T. C., and Zwart, P. H. (2010). PHENIX: a comprehensive Python-based system for macromolecular structure solution. Acta Crystallogr D Biol Crystallogr 66, 213-221.

168. Adams, P. D., Grosse-Kunstleve, R. W., Hung, L. W., Ioerger, T. R., McCoy, A. J., Moriarty, N. W., Read, R. J., Sacchettini, J. C., Sauter, N. K., and Terwilliger, T. C. (2002). PHENIX: building new software for automated crystallographic structure determination. Acta Crystallogr D Biol Crystallogr 58, 1948-1954.

169. Schmidt, F., Treiber, N., Zocher, G., Bjelic, S., Steinmetz, M. O., Kalbacher, H., Stehle, T., and Dodt, G. (2010). Insights into peroxisome function from the structure of PEX3 in complex with a soluble fragment of PEX19. J Biol Chem 285, 25410-25417.

170. Gatto, G. J., Jr., Geisbrecht, B. V., Gould, S. J., and Berg, J. M. (2000). Peroxisomal targeting signal-1 recognition by the TPR domains of human PEX5. Nat Struct Biol 7, 1091-1095.

171. Neufeld, C., Filipp, F. V., Simon, B., Neuhaus, A., Schuller, N., David, C., Kooshapur, H., Madl, T., Erdmann, R., Schliebs, W., Wilmanns, M., and Sattler, M. (2009). Structural basis for competitive interactions of Pex14 with the import receptors Pex5 and Pex19. EMBO J 28, 745-754.

172. Guerler, A., and Knapp, E. W. (2008). Novel protein folds and their nonsequential structural analogs. Protein Sci 17, 1374-1382.

173. Holm, L., Kaariainen, S., Rosenstrom, P., and Schenkel, A. (2008). Searching protein structure databases with DaliLite v.3. Bioinformatics 24, 2780-2781.

174. Pinto, M. P., Grou, C. P., Fransen, M., Sa-Miranda, C., and Azevedo, J. E. (2009). The cytosolic domain of PEX3, a protein involved in the biogenesis of peroxisomes, binds membrane lipids. Biochim Biophys Acta 1793, 1669-1675.

175.   Fahnestock, M. L., Tamir, I., Narhi, L., and Bjorkman, P. J. (1992). Thermal stability comparison of purified empty and peptide-filled forms of a class I MHC molecule. Science 258, 1658-1662.

176.   Madden, D. R. (1995). The three-dimensional structure of peptide-MHC complexes. Annu Rev Immunol 13, 587-622.

177.   Mateja, A., Szlachcic, A., Downing, M. E., Dobosz, M., Mariappan, M., Hegde, R. S., and Keenan, R. J. (2009). The structural basis of tail-anchored membrane protein recognition by Get3. Nature 461, 361-366.

178.   Gloeckner, C. J., Mayerhofer, P. U., Landgraf, P., Muntau, A. C., Holzinger, A., Gerber, J. K., Kammerer, S., Adamski, J., and Roscher, A. A. (2000). Human adrenoleukodystrophy protein and related peroxisomal ABC transporters interact with the peroxisomal assembly protein PEX19p. Biochem Biophys Res Commun 271, 144-150.

179.   Pinto, M. P., Grou, C. P., Alencastre, I. S., Oliveira, M. E., Sa-Miranda, C., Fransen, M., and Azevedo, J. E. (2006). The import competence of a peroxisomal membrane protein is determined by Pex19p before the docking step. J Biol Chem 281, 34492-34502.

180.   Just, W. W., and Diestelkötter, P. (1996). Protein insertion into the peroxisomal membrane. Ann N Y Acad Sci 804, 60-75.

9 APPENDIX

9.1 Plasmids
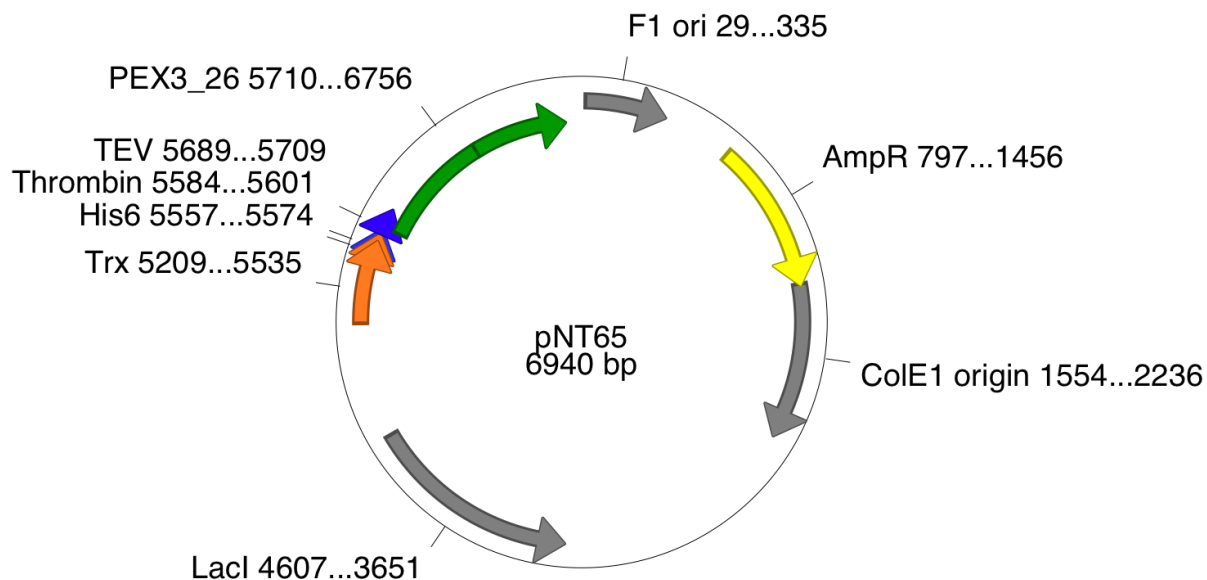
Figure 9.1: Plasmid pNT65. PEX3$^{26\text{-}373}$ (C235S) in pET32a with a preceding TEV protease cleavage site. The protein nPEX3 is expressed as an N-terminal His$_6$-tagged thioredoxin fusion protein.
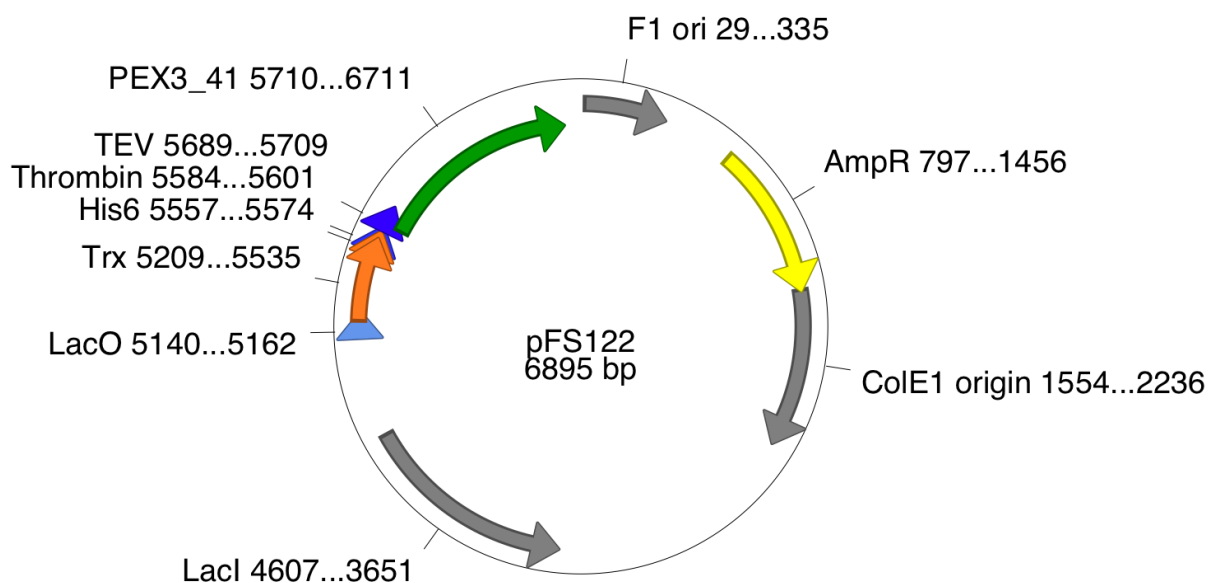
Figure 9.2: Plasmid pFS122. PEX3$^{41\text{-}373}$ (C235S) in pET32a with a preceding TEV protease cleavage site. The protein sPEX3 is expressed as an N-terminal His$_6$-tagged thioredoxin fusion protein.

His 271...288
TEV 307...327

PEX19 328...1226

pNT45
5312 bp

PEX19 328...1226

ColE1 origin 3231...3913

AmpR 2474...3133
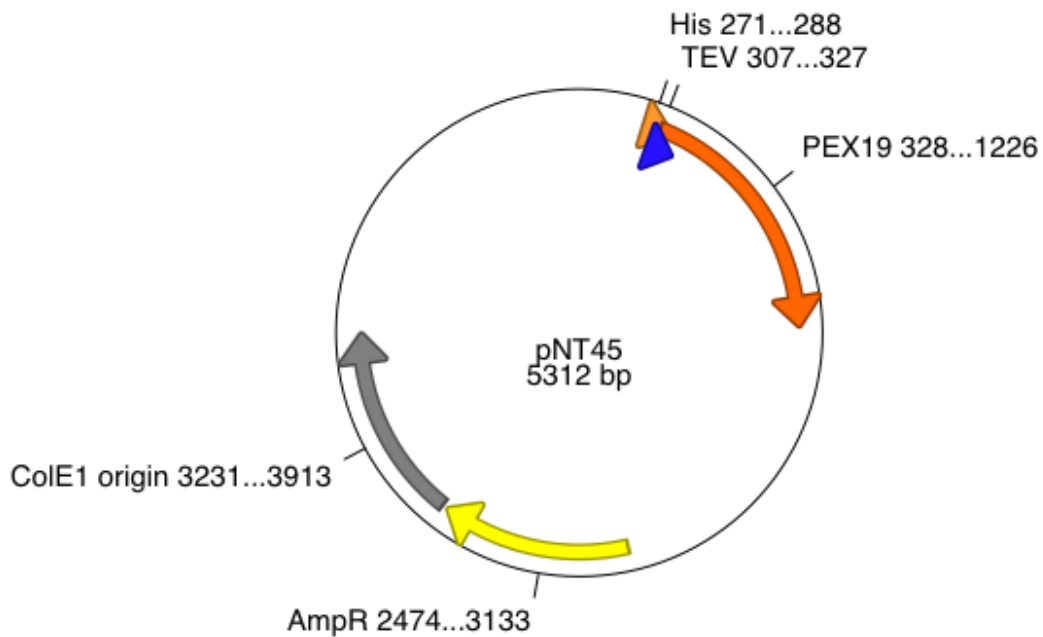
Figure 9.3: Plasmid pNT45. PEX19 in pCOLDI with a preceding TEV protease cleavage site. The full-length protein is expressed with a N-terminal His$_6$-tag.

9.2 DNA and protein sequences of PEX3 and PEX19

9.2.1 sPEX3

The DNA sequence and the amino acid sequence of the expressed fusion protein thioredoxin-His$_6$-TEV-sPEX3 are shown here. The TEV protease cleavage site is highlighted in blue. TEV protease cleaves between Gln and Gly (underlined), leaving the glycine residue at the target protein sPEX3. The sPEX3 amino acid sequence is highlighted in green and begins at the glutamine that follows the cleavage sequence and corresponds to position 41 in full-length PEX3. The cysteine to serine mutation at position 235 is underlined and highlighted in bold.

```
     atg agc gat aaa att att cac ctg act gac gac agt ttt gac acg
1    Met Ser Asp Lys Ile Ile His Leu Thr Asp Asp Ser Phe Asp Thr
     gat gta ctc aaa gcg gac ggg gcg atc ctc gtc gat ttc tgg gca
16   Asp Val Leu Lys Ala Asp Gly Ala Ile Leu Val Asp Phe Trp Ala
     gag tgg tgc ggt ccg tgc aaa atg atc gcc ccg att ctg gat gaa
31   Glu Trp Cys Gly Pro Cys Lys Met Ile Ala Pro Ile Leu Asp Glu
     atc gct gac gaa tat cag ggc aaa ctg acc gtt gca aaa ctg aac
46   Ile Ala Asp Glu Tyr Gln Gly Lys Leu Thr Val Ala Lys Leu Asn
     atc gat caa aac cct ggc act gcg ccg aaa tat ggc atc cgt ggt
61   Ile Asp Gln Asn Pro Gly Thr Ala Pro Lys Tyr Gly Ile Arg Gly
     atc ccg act ctg ctg ctg ttc aaa aac ggt gaa gtg gcg gca acc
76   Ile Pro Thr Leu Leu Leu Phe Lys Asn Gly Glu Val Ala Ala Thr
     aaa gtg ggt gca ctg tct aaa ggt cag ttg aaa gag ttc ctc gac
91   Lys Val Gly Ala Leu Ser Lys Gly Gln Leu Lys Glu Phe Leu Asp
```

```
        gct aac ctg gcc ggt tct ggt tct ggc cat atg cac cat cat cat
106     Ala Asn Leu Ala Gly Ser Gly Ser Gly His Met His His His His
        cat cat tct tct ggt ctg gtg cca cgc ggt tct ggt atg aaa gaa
121     His His Ser Ser Gly Leu Val Pro Arg Gly Ser Gly Met Lys Glu
        acc gct gct gct aaa ttc gaa cgc cag cac atg gac agc cca gat
136     Thr Ala Ala Ala Lys Phe Glu Arg Gln His Met Asp Ser Pro Asp
        ctg ggt acc gac gac gac gac aag gcc atg gaa aac ctg tat ttt
151     Leu Gly Thr Asp Asp Asp Asp Lys Ala Met Glu Asn Leu Tyr Phe
        cag gga cag gaa agg gag gct gca gaa tac att gcc caa gca cga
166     Gln Gly Gln Glu Arg Glu Ala Ala Glu Tyr Ile Ala Gln Ala Arg
        cga caa tat cat ttt gaa agt aac cag agg act tgc aat atg aca
181     Arg Gln Tyr His Phe Glu Ser Asn Gln Arg Thr Cys Asn Met Thr
        gtg ctg tcc atg ctt cca aca ctg aga gag gcc tta atg cag caa
196     Val Leu Ser Met Leu Pro Thr Leu Arg Glu Ala Leu Met Gln Gln
        ctg aat tcc gag agc ctc aca gct ctg cta aaa aac agg cct tca
211     Leu Asn Ser Glu Ser Leu Thr Ala Leu Leu Lys Asn Arg Pro Ser
        aac aag cta gaa ata tgg gag gat ctg aag ata ata agt ttc aca
226     Asn Lys Leu Glu Ile Trp Glu Asp Leu Lys Ile Ile Ser Phe Thr
        aga agt act gtg gct gta tac agt acc tgt atg ctg gtt gtt ctt
241     Arg Ser Thr Val Ala Val Tyr Ser Thr Cys Met Leu Val Val Leu
        ttg cgg gtc cag tta aac ata att ggt gga tat att tac ctg gat
256     Leu Arg Val Gln Leu Asn Ile Ile Gly Gly Tyr Ile Tyr Leu Asp
        aat gca gca gtt ggc aaa aat ggc act aca att ctt gct ccc cca
271     Asn Ala Ala Val Gly Lys Asn Gly Thr Thr Ile Leu Ala Pro Pro
        gat gtc caa cag cag tat tta tca agt att cag cac cta ctt gga
286     Asp Val Gln Gln Gln Tyr Leu Ser Ser Ile Gln His Leu Leu Gly
        gat ggc ctg aca gaa ttg atc act gtc att aaa caa gct gtg cag
301     Asp Gly Leu Thr Glu Leu Ile Thr Val Ile Lys Gln Ala Val Gln
        aag gtt tta gga agt gtt tct ctt aaa cat tct ttg tcc ctt ttg
316     Lys Val Leu Gly Ser Val Ser Leu Lys His Ser Leu Ser Leu Leu
        gac ttg gag caa aaa cta aaa gaa atc aga aat ctc gtt gag cag
331     Asp Leu Glu Gln Lys Leu Lys Glu Ile Arg Asn Leu Val Glu Gln
        cat aag tct tct tct tgg att aat aaa gat gga tcc aaa cct tta
346     His Lys Ser Ser Ser Trp Ile Asn Lys Asp Gly Ser Lys Pro Leu
        tta tcc cat tat atg atg cca gat gaa gaa act cca tta gca gtg
361     Leu Ser His Tyr Met Met Pro Asp Glu Glu Thr Pro Leu Ala Val
        cag gcc tgt gga ctt tct cct cga gac att acc act att aaa ctt
376     Gln Ala Cys Gly Leu Ser Pro Arg Asp Ile Thr Thr Ile Lys Leu
        ctc aat gaa act aga gac atg ttg gaa agc cca gat ttt agt aca
391     Leu Asn Glu Thr Arg Asp Met Leu Glu Ser Pro Asp Phe Ser Thr
        gtt ttg aat acc tgt tta aac cga ggt ttt agt aga ctt cta gac
406     Val Leu Asn Thr Cys Leu Asn Arg Gly Phe Ser Arg Leu Leu Asp
        aat atg gct gag ttc ttt cga cct act gaa cag gac ctg caa cat
421     Asn Met Ala Glu Phe Phe Arg Pro Thr Glu Gln Asp Leu Gln His
```

95

```
      ggt aac tct atg aat agt ctt tcc agt gtc agc ctg cct tta gct
436   Gly Asn Ser Met Asn Ser Leu Ser Ser Val Ser Leu Pro Leu Ala
      aag ata att cca ata gta aac gga cag atc cat tca gtt tgc agt
451   Lys Ile Ile Pro Ile Val Asn Gly Gln Ile His Ser Val Cys Ser
      gaa aca cct agt cat ttt gtt cag gat ctg ttg aca atg gag caa
466   Glu Thr Pro Ser His Phe Val Gln Asp Leu Leu Thr Met Glu Gln
      gtg aaa gac ttt gct gct aat gtg tat gaa gct ttt agt acc cct
481   Val Lys Asp Phe Ala Ala Asn Val Tyr Glu Ala Phe Ser Thr Pro
      cag caa ctg gag aaa tga
496   Gln Gln Leu Glu Lys *
```

9.2.2 PEX19

The DNA sequence and the amino acid sequence of the expressed fusion protein His$_6$-TEV-PEX19 are shown here. The TEV protease cleavage site is highlighted in blue. TEV protease cleaves between Gln and Gly (underlined), leaving the glycine residue at the target protein PEX19. The PEX19 amino acid sequence is highlighted in orange. The peptide sequence spanning Ala14 to Lys33 is underlined.

```
      atg aat cac aaa gtg cat cat cat cat cat cat atc gaa ggt agg
1     Met Asn His Lys Val His His His His His His Ile Glu Gly Arg
      cat atg GAA AAC CTG TAT TTT CAG GGA atg gcc gcc gct gag gaa
16    His Met Glu Asn Leu Tyr Phe Gln Gly Met Ala Ala Ala Glu Glu
      ggc tgt agt gtc ggg gcc gaa gcg gac agg gaa ttg gag gag ctt
31    Gly Cys Ser Val Gly Ala Glu Ala Asp Arg Glu Leu Glu Glu Leu
      ctg gaa agt gct ctt gat gat ttc gat aaa gcc aaa ccc tcc cca
46    Leu Glu Ser Ala Leu Asp Asp Phe Asp Lys Ala Lys Pro Ser Pro
      gca ccc cct tct acc acc acg gcc cct gat gct tcg ggg ccc cag
61    Ala Pro Pro Ser Thr Thr Thr Ala Pro Asp Ala Ser Gly Pro Gln
      aag aga tcg cca gga gac act gcc aaa gat gcc ctc ttc gct tcc
76    Lys Arg Ser Pro Gly Asp Thr Ala Lys Asp Ala Leu Phe Ala Ser
      caa gag aag ttt ttc cag gaa cta ttc gac agt gaa ctg gct tcc
91    Gln Glu Lys Phe Phe Gln Glu Leu Phe Asp Ser Glu Leu Ala Ser
      caa gcc act gcg gag ttc gag aag gca atg aag gag ttg gct gag
106   Gln Ala Thr Ala Glu Phe Glu Lys Ala Met Lys Glu Leu Ala Glu
      gaa gaa ccc cac ctg gtg gag cag ttc caa aag ctc tca gag gct
121   Glu Glu Pro His Leu Val Glu Gln Phe Gln Lys Leu Ser Glu Ala
      gca ggg aga gtg ggc agt gat atg acc tcc caa caa gaa ttc act
136   Ala Gly Arg Val Gly Ser Asp Met Thr Ser Gln Gln Glu Phe Thr
      tct tgc cta aag gaa aca cta agt gga tta gcc aaa aat gcc act
151   Ser Cys Leu Lys Glu Thr Leu Ser Gly Leu Ala Lys Asn Ala Thr
      gac ctt cag aac tcc agc atg tcg gaa gaa gag ctg acc aag gcc
166   Asp Leu Gln Asn Ser Ser Met Ser Glu Glu Glu Leu Thr Lys Ala
```

```
        atg gag ggg cta ggc atg gac gaa ggg gat ggg gaa ggg aac atc
181     Met Glu Gly Leu Gly Met Asp Glu Gly Asp Gly Glu Gly Asn Ile
        ctc ccc atc atg cag agt att atg cag aac cta ctc tcc aag gat
196     Leu Pro Ile Met Gln Ser Ile Met Gln Asn Leu Leu Ser Lys Asp
        gtg ctg tac cca tca ctg aag gag atc aca gaa aag tat cca gaa
211     Val Leu Tyr Pro Ser Leu Lys Glu Ile Thr Glu Lys Tyr Pro Glu
        tgg ttg cag agt cat cgg gaa tct cta cct cca gag cag ttt gaa
226     Trp Leu Gln Ser His Arg Glu Ser Leu Pro Pro Glu Gln Phe Glu
        aaa tat cag gag cag cac agc gtc atg tgc aaa ata tgt gag cag
241     Lys Tyr Gln Glu Gln His Ser Val Met Cys Lys Ile Cys Glu Gln
        ttt gag gca gag acc ccc aca gac agt gaa acc act caa aag gct
256     Phe Glu Ala Glu Thr Pro Thr Asp Ser Glu Thr Thr Gln Lys Ala
        cgt ttt gag atg gtg ctg gat ctt atg cag cag cta caa gat tta
271     Arg Phe Glu Met Val Leu Asp Leu Met Gln Gln Leu Gln Asp Leu
        ggc cat cct cca aaa gag ctg gct gga gag atg cct cct ggc ctc
286     Gly His Pro Pro Lys Glu Leu Ala Gly Glu Met Pro Pro Gly Leu
        aac ttt gac ctg gat gcc ctc aat ctt tcg ggc cca cca ggt gcc
301     Asn Phe Asp Leu Asp Ala Leu Asn Leu Ser Gly Pro Pro Gly Ala
        agt ggt gaa cag tgt ctg atc atg tga
316     Ser Gly Glu Gln Cys Leu Ile Met *
```
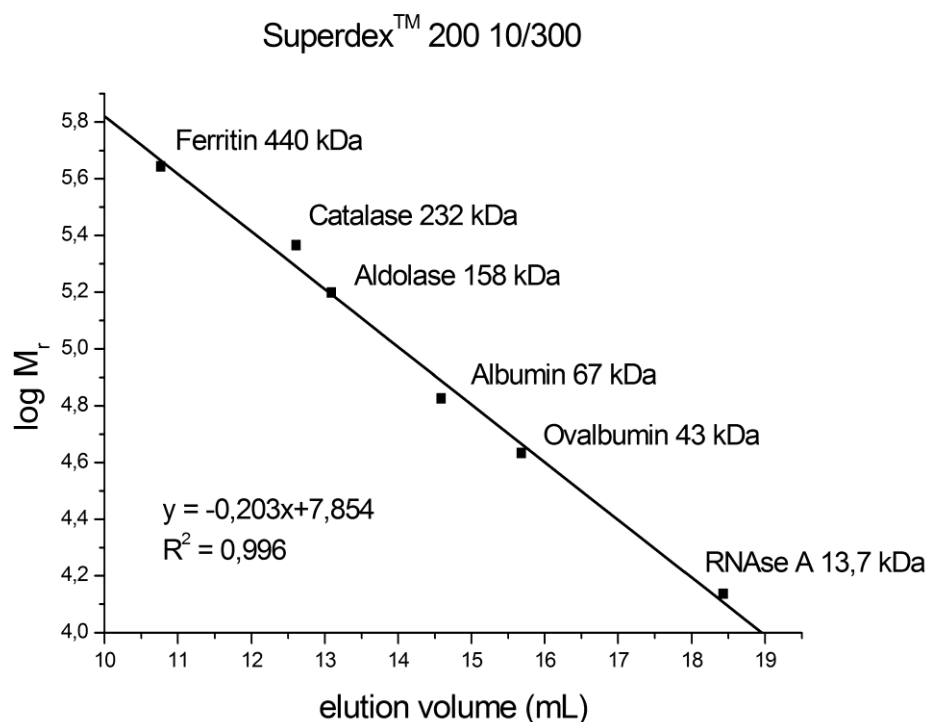
9.3   Calibration of SEC columns

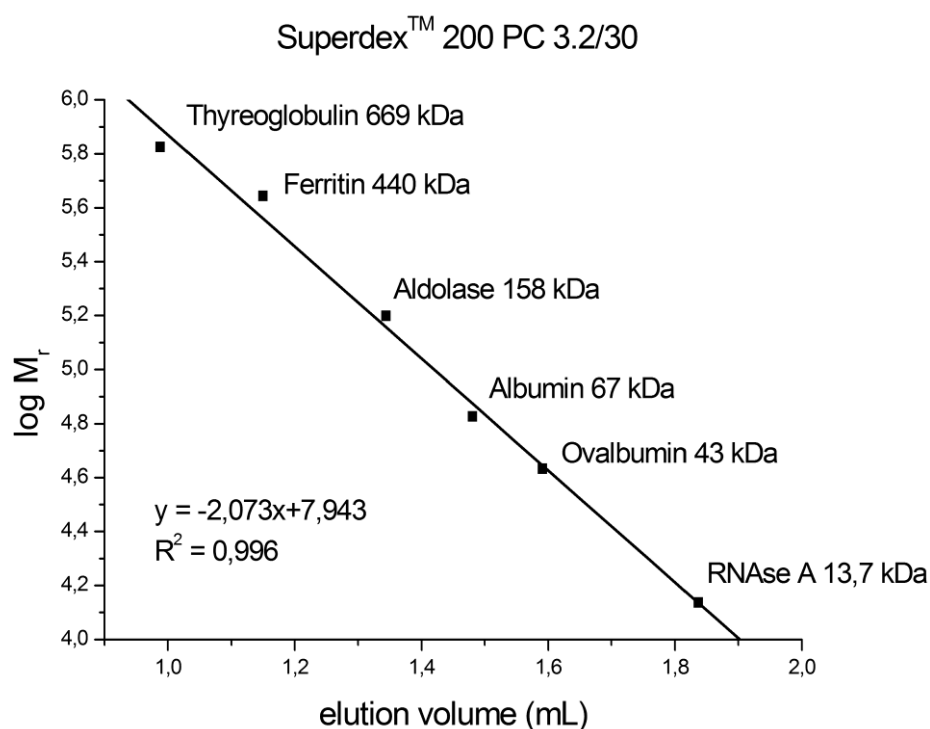**Figure 9.4: Calibration of Superdex™ 200 10/300 column.**

97

Figure 9.5: Calibration of Superdex™ 200 PC 3.2/30 column.

9.4 ITC experiments

Table 13: Thermodynamic parameters of the PEX3-PEX19 interaction.

PEX3	PEX19	K_d (nM)	$\Delta H_{Binding}$ (kcal/mol)	Molar ratio
nPEX3[a]	Full-length	9.3	-6.7	0.86
sPEX3[b]	Full-length	14.9	-9.3	0.89
sPEX3	PEX19[Pep c]	330	-4.9	1.06
sPEX3	PEX19[Pep] F29A	n.b.[d]	n.b.	n.b.
sPEX3	PEX19[Pep] A25L	410	-1.9	1.10
sPEX3	PEX19[Pep] A25Y	n.b.	n.b.	n.b.
sPEX3	PEX19 124-136	n.b.	n.b.	n.b.
sPEX3 L93N	Full-length	3750	-10.4	0.90
sPEX3 K324A	Full-length	270	-8.0	1.03
sPEX3 E266A	Full-length	17.9	-9.4	0.94
sPEX3 I140N	Full-length	18.3	-7.8	1.25
sPEX3 L165N	Full-length	20.9	-5.6	0.87

[a] PEX3[26-373] (C235S), [b] PEX3[41-373] (C235S), [c] PEX19[14-33], [d] no binding

9.5 Initial crystallization screens

Table 14: Screens tested for initial crystallization.

Screens	Temperature	Concentration
nPEX3		
Crystal Screen I, II	4 °C	3.0, 4.0 mg/mL
Crystal Lite Screen	4 °C	4.0 mg/mL
MembFac Screen	4 °C	4.0, 6.0 mg/mL
Wizard Screen I, II, III	4 °C	4.0 mg/mL
pHClear Screen I,II	4 °C, 20 °C	3.2 mg/mL
Cation Suite	4 °C, 20 °C	3.2 mg/mL
Anion Suite	4 °C, 20 °C	3.2 mg/mL
JCSG Screen	20 °C	3.2 mg/mL
nPEX3+PEX19		
Crystal Screen I, II	4 °C, 20 °C	5.0 mg/mL
Crystal Lite Screen	20 °C	5.0 mg/mL
Wizard Screen I, II, III	4 °C, 20 °C	5.0 mg/mL
MembFac Screen	20 °C	5.0 mg/mL
sPEX3		
Crystal Screen I, II	4 °C, 20 °C	2.6 mg/mL
Wizard Screen I, II	4 °C, 20 °C	2.6 mg/mL
pHClear Screen I, II	4 °C, 20 °C	2.6 mg/mL
JCSG Screen	20 °C	2.6 mg/mL
sPEX3+PEX19[Pep]		
Crystal Screen I, II	20 °C	2.8 mg/mL
Wizard Screen I, II	20 °C	2.8 mg/mL
pHClear Screen I, II	20 °C	2.8 mg/mL
JCSG Screen	20 °C	2.8 mg/mL

9.6 Crystallization conditions

Table 15: Initial and refined crystallization conditions for nPEX3 and sPEX3+PEX19^{Pep}.

Screen	Condition
nPEX3 (3.1 mg/mL)	
pHClearI_27	0.1 M MES, pH 6.0, 5 % (w/v) PEG 6000; 4 and 20 °C Refined: 0.1 M MES, pH 5.6-6.5, 2-12 % (w/v) PEG 6000; 4 and 20 °C
pHClearI_34	0.1 M HEPES, pH 7.0, 10 % (w/v) PEG 6000; 4 and 20 °C Refined: 0.1 M HEPES, pH 6.5-8.0, 5-15 % (w/v) PEG 6000; 4 and 20 °C
pHClearII_27	0.1 M MES, pH 6.0, 5 % (v/v) isopropanol; 4 and 20 °C Refined: 0.1 M MES, pH 5.6-6.5, 2-7 % (v/v) isopropanol, 4 and 20 °C
Cation_28	0.1 M NaAc, pH 4.6, 1.25 M LiAc; 4 °C
Anion_19	0.1 M Tris, pH 8.5, 2.5 M NaAc; 4 °C
Anion_25	0.1 M NaAc, pH 4.6, 3.5 M NaFormate; 4 °C
sPEX3+PEX19^{Pep} (2.5 mg/mL)	
JCSG_9	0.1 M NH$_4$Cl, 20 % (w/v) PEG 3350; 20 °C Refined: 0.1-0.25 M NH$_4$Cl; 17-20 % (w/v) PEG 3350
JCSG_20	0.1 M Tris, pH 7.0, 10 % (w/v) PEG 8000, 0.1 M MgCl$_2$; 20 °C Refined: 0.1 M Tris, pH 6.7-7.6; 7-12 % (w/v) PEG 8000, 0.1 M MgCl$_2$; 4 and 20 °C
JCSG_90	0.1 M Bis-Tris, pH 5.5, 17 % (w/v) PEG 10000, 0.1 M NH$_4$Ac; 20 °C Refined: 0.1 M Bis-Tris, pH 5.3-6.2, 14-19 % (w/v) PEG 10000, 0.1 M NH$_4$Ac; 4 and 20 °C
JCSG_92	0.1 M Bis-Tris, pH 5.5, 25 % (w/v) PEG 3350, 0.2 M NaCl; 20 °C Refined: 0.1 M Bis-Tris, pH 5.3-6.2, 22-27 % (w/v) PEG 3350, 0.1 M NaCl, 4 and 20 °C
JCSG_94	0.1 M Bis-Tris, pH 5.5, 25 % (w/v) PEG 3350, 0.2 M NH$_4$Ac; 20 °C Refined: 0.1 M Bis-Tris, pH 5.3-6.2, 22-27 % (w/v) PEG 3350, 0.2 M NH$_4$Ac, 4 and 20 °C

9.7 Transfection and complementation rates

Table 16: Transfection and complementation rates for different PEX3-myc mutants.

PEX3	Transfection[a] (%)	Complementation[b] (%)	Preperoxisomes[c] (%)
PEX3-myc	12.4 ± 1.7	4.7 ± 0.9	24.8 ± 3.7
PEX3-myc L93N	2.7 ± 1.0	0	8.2 ± 0.7
PEX3-myc K324A	6.4 ± 2.5	2.0 ± 1.1	9.8 ± 2.4
PEX3-myc E266A	12.6 ± 2.9	4.6 ± 0.7	17.5 ± 1.2
PEX3-myc D275A	9.3 ± 3.1	2.4 ± 1.0	n.d.[d]
PEX3-myc I140N	10.4 ± 3.7	3.9 ± 0.8	n.d.
PEX3-myc L165N	3.5 ± 0.8	0.77 ± 0.06	19.2 ± 2.4
PEX3-myc I140N*L165N	13.7 ± 4.4	0.93 ± 0.06	n.d.

[a] normal fibroblasts with myc-positive staining after 2 days, [b] ΔPEX3T fibroblasts with PEX14-positive staining after 7 days, [c] ΔPEX3T cells cotransfected with PEX16-YFP, YFP-positive punctate staining after 24 hours, [d] not determined. Values correspond to the mean of three independent experiments ± standard deviations.

PUBLICATIONS

Schmidt F, Treiber N, Zocher G, Bjelic S, Steinmetz MO, Kalbacher H, Stehle T, Dodt G (2010). Insights into peroxisome function from the structure of PEX3 in complex with a soluble fragment of PEX19. *J Biol Chem* **285**, 25410-7.

F.S. performed molecular cloning, protein purification, crystallization and structure determination with the help of G.Z., N.T. established protein purification and determined the initial model for molecular replacement, H.K. synthesized and purified the peptides, M.S. and B.S. carried out the affinity measurements, F.S., G.D. and T.S. wrote the manuscript, and G.D. and T.S. directed the project.

Schmidt F, Dietrich D, Eylenstein R, Groemping Y, Stehle T, Dodt G.
The role of conserved PEX3 regions in PEX19 binding and peroxisome biogenesis.
Manuscript submitted.

F.S. performed molecular cloning, protein purification, CD measurements, transfection and complementation studies, F.S., R.E. and Y.G. carried out and analyzed ITC measurements, D.D. performed siRNA experiments, F.S., D.D., G.D. and T.S. wrote the manuscript, and G.D. and T.S. directed the project.

PRESENTATION OF THE RESULTS

The results obtained in this thesis have been presented at the following conferences:

Oral presentations

- 1st Young Scientist IFIB Symposium, Blaubeuren   06/2010
- 24th Regio Meeting, Albé, France   09/2010
- Open European Peroxisome Meeting, Lunteren, The Netherlands   10/2010

Poster presentations

- Doctoral Poster Session, IFIB, Tübingen   06/2009
- The EMBO Meeting, Amsterdam   10/2009
- Doctoral Poster Session, IFIB, Tübingen   06/2010

CURRICULUM VITAE

Personal details

Name	Friederike Schmidt
Date of birth	18.09.1981
Place of birth	Basel/Switzerland
Nationality	German

DANKSAGUNG

Ich danke Thilo Stehle und Gabi Dodt für die Möglichkeit, die vorliegende Arbeit in ihren Laboren anfertigen zu können, ihr Interesse am Fortgang dieser Arbeit, die Finanzierung dieses Projektes und Thilos unglaublichen Optimismus.

Bei meinen Kooperationspartnern möchte ich mich für die gute Zusammenarbeit und ihre Hilfe bei aufkommenden Problemen bedanken: Hubert Kalbacher für die schnelle Synthese der Peptide, Sasa Bjelic und Michel Steinmetz für die ITC-Messungen am PSI (Villigen), Carsten Kintscher, Roy Eylenstein und Yvonne Groemping für zahlreiche ITC-Messungen am MPI, Tübingen.

Ein besonderer Dank geht an Nora Treiber und Georg Zocher für ihre Hilfe bei der Strukturlösung, für ihre Unterstützung bei aufkommenden Fragen und für die kompetente und freundschaftliche Beratung bei Problemen nicht nur wissenschaftlicher Art.

Patrick Schulte-Euler, Anne Dueck und Mathias Stotz danke ich für eine schöne und lustige Zeit im Labor, die mir den Anfang in Tübingen erleichtert hat.

Meinen Mädels aus dem Ladies-Lab, Yvonne, Vera und Denise, gilt ein besonders herzlicher Dank für eine wirklich angenehme und hilfsbereite Arbeitsatmoshpäre, unzählige Kaffeepausen, einige Sektfrühstücke, erlebnisreiche Tage in Amsterdam, aufmunternde Gespräche, unvergessliche Bossless-Abende und zahlreiche andere lustige Erlebnisse, die ich hier aus Platzgründen nicht alle erwähnen kann.

Allen Mitgliedern des Stehle-Labors danke ich für ihre Hilfsbereitschaft bei aufkommenden Laborproblemen. Insbesondere danke ich Johannes (JoBa), Sebastian, Kerstin, Bärbel, Luisa, Karolina, Dirk und Volker für erheiternde Gespräche, Philosophieren über Fußball, Fahrten zu Fußballspielen und viele witzige Stunden außerhalb des Labors.

Bei Karin Steiger, Andrea Barna, Hanna Leins und Julia Maier bedanke ich mich für die Hilfe bei der Durchführung von Experimenten.

Franzi möchte ich dafür danken, dass der Kontakt nie abgerissen ist und dass sie mir immer mit Tipps und Tricks und einem offenem Ohr zur Seite stand.

Meinen Eltern und meinen Geschwistern Katharina, Ulrich und Johannes, danke ich von ganzem Herzen für ihre Unterstützung und Motivation in den zurückliegenden Jahren.

Zu guter Letzt möchte ich mich bei Moritz bedanken, der immer für mich da war, mich in meinem Tun unterstützt hat und dafür gesorgt hat, dass auch nicht-wissenschaftliche Dinge ihre Wichtigkeit nicht verloren haben.